Dipole Dynamics in the Point Vortex Model

Karl Lydon

March, 2023

Abstract

Presented here is a thorough theoretical and numerical investigation into the dynamics of vortex dipoles in point vortex and point vortex adjacent systems. We begin by reviewing the basic laws of fluid flow and thus standard hydrodynamic turbulence after which, motivated by the vortex filament description of fluid flow, we introduce the intriguing phenomenon of quantum turbulence. From this quantum turbulence we motivate study of the point vortex model, including a description of the basic theory of point vortex systems. Using Kirchoff's Hamiltonian formulation of the 2D point vortex model in the infinite domain, we consider work done into dipole-vortex collisions, as well as extending this to consider the dipole-dipole collisions in both the integrable and non-integrable cases. Here we solve for important dynamical quantities such as the scattering angle, of great importance to the mixing of turbulent systems, and also the vortex separations at the dipole periapsis, as well as the extremum values of dipole separation, and we discuss the possibility of dipole creation in such systems. We consider this as a numerical analysis but also analyse each interaction regime theoretically where possible, finding perfect agreement between theoretical predictions and numerical results where this is done. The study then continues by considering the collisions of dipoles with same-signed rotating vortex clusters, and also analysing the possibility of approximating the dynamics of a dipole colliding with large vortex clusters by the dynamics of a dipole colliding with equivalently strong single point vortices, we find such an approximation is even more effective than may first be considered, with the dipole-vortex simulations often faithfully reproducing the dynamical quantities of the dipole-clusters. We also consider the scattering angles and dipole creation possibility as before, noting the highly chaotic behaviour found at impact parameters close to zero. We then move from the 2D infinite domain point vortex model in the strict sense in order to consider how point vortex systems may capture behaviour of standard turbulent systems; by considering large N periodic point vortex systems we realise the 2D turbulent phenomenon of the inverse

energy cascade through additional forcing and dampening mechanisms. Finally, we give a study on the effect of the interaction of sound waves with a vortex dipole. Investigating the notion that sound will lead to an eventual vortex collapse, we find this is highly dependent upon the initial conditions present, more specifically the initial sound distribution, as this behaviour although realised in Gaussian distributed sound is not realised in Rayleigh-Jean distributed sound. Therefore, it is speculated that the shrinkage and annihilation processes occur not due to the presence of sound alone but instead through the out-of-equilibrium motion as the system relaxes towards the eventual statistical equilibrium of vortex annihilation.

Contents

List of Figures

List of Tables

Chapter 1

Introduction

1.1 Research questions and objectives

The problem of turbulence throughout its history from the initial investigation by Reynolds [6], to the description of Kolmogorov [7], to the modern day is one of the greatest unsolved problems in classical physics. Due to the computational complexity involved in direct simulations of the fluid equations of motion, numerous approaches have thus been developed in trying to investigate turbulence; primary among these are the simulations and analysis of the underlying vortex motion which occurs. In this work we consider a subset of these; namely consideration of turbulence through the point vortex model, where continuous vortices (i.e. a continuous vorticity field) is replaced by discrete vortices at points of infinitesimal width. By themselves, point vortices have been used extensively in numerous applications throughout fluid dynamics and turbulence, most often in the analysis of quantum turbulence in particular, but with applications in classical turbulence also. We find this lacking for several reasons however, often the point vortex assemblies used to simplify greater problems are still considered complex problems to solve in themselves, and often an alternative description of point vortices would prove more useful than consideration of the "bare" point vortex model.

It is our hypothesis that a better alternative would be to consider the point vortex system as a statistical model, with the main driving agent of evolution being vortex dipoles rather than the evolution of singular point vortices, such that the entirety of the point vortex statistical evolution can be described in terms of the effects of these dipoles. Such a model would greatly simplify the analysis of point vortex dynamics, as complicated large point vortex evolutions

could be reduced into fundamental interactions undergone by dipoles (whether with other vortex structures or otherwise), certain dipole interactions will then have a higher probability of occurring than others, and through categorisation of which interactions are to occur with higher probability and the effects of such interactions we are thus left with a statistical description of dipoles that is much simpler than the standard point vortex model, yet can powerfully predict long-term statistical quantities.

The idea of point vortex statistics is not however a new one, it was Onsager [8] who first developed a statistical theory of these point vortices, through this, Onsager sought to provide explanation for the long-lived vortices at large length-scales found in quasi-2D turbulence. This seminal work led to the ingenious realisation that point vortices at high enough energy result in negative temperature states, causing large-scale vortices to form as smaller vortex clusters coalesce into larger clusters. This example elucidates the viability of considering point vortices in a statistical manner, and in considering the corollary of Onsager's finding, that positive temperature states result in a domination of point vortex dipoles in the fluid flow, presents the possibility of accomplishing this in terms of vortex dipoles.

The idea of statistical description of point vortices is further examined in the work of Campbell [9], whereupon vortex clustering in high energy states in the manner of Onsager is studied via the average interaction energy between negative and positive vortices (i.e. dipoles) and the addition of an annihilation mechanism of close vortex dipoles, with results observed to be similar to that seen in late-time 2D Navier-Stokes equations. Another interesting example of such statistical analysis is given by Chavanis [10], where under certain assumptions the general kinetic equation for the vorticity profile of the flow is given as a kinetic equation for $\partial\omega/\partial t$, it is then our hypothesis that a similar theory and eventually similar kinetic equations may be derived for point vortex dipoles.

Another significant example showing the statistical possibilities in describing point vortex dipoles is the kinetic theory developed by Carnevale et al. and extended to a theory of point vortex dipoles by Marmanis [11, 12], where here a full kinetic theory of point vortex dipoles is developed. Several assumptions are made in this work; first it is assumed that only direct scattering collisions are observed, as well as dilute vortex dipoles (vortex dipoles have an extended time of flight without interaction vs. time within interactions), and also that dipoles

can approach such that the distance between like-signed vortices are much less that the dipole distance and this can be considered as a single dipole of vortex clusters (which are then idealised as single vortices), resulting in a reduction of vortices in the system. From this the theory of Bogolyubov [13] the BBGKY hierarchy is derived, and a kinetic equation of dipole-dipole collisions using point vortices to model two-dimensional turbulence is formed as the eigenvalue problem

$$\left[\frac{1}{2\pi r_1^2}\frac{\partial}{\partial\theta_1}+\frac{1}{v_1}\left(\langle\frac{u_r^{(2)}}{r_2}\rangle+\langle\boldsymbol{u}^{(1)}\rangle\cdot\nabla\right)\right]g_1^{(0)}=\xi g_1^{(0)}. \tag{1.1}$$

Here ξ is a proposed parameter specifying all statistical properties of the system, that is related to the number of vortices per area, and the probability of finding a dipole somewhere in the plane as $f_1 = gt^{-\xi}$, where g is a function of ρ_1, ϕ_1, r_1, and θ_1. These are polar coordinates specifying dipole position; ϕ_1 gives the separation of one dipole vortex to the origin, r_1 gives the dipole separation, ϕ_1 gives angle of a dipole vortex to the origin, and θ_1 gives the orientation of the dipole. Also, subscripts specify which dipole is referred to in the interaction. Note also here u_r gives radial velocity of dipole vortices, $\boldsymbol{u}$ is the velocity vector of the polar parameters already mentioned, and superscripts are given to represent terms of expanded power series in the following form

$$g_1 = g_1^{(0)} + g_1^{(1)}\delta t + g_1^{(2)}\delta t^2 \ldots,$$

where a collision take place in time δt. This in effect validates the construction of a statistical system around dipoles, however this particular model is unattractive on account of the numerous assumptions made; such as being based around only direct scattering collisions, dipoles being dilute, the possibility of multiple dipoles coalescing, among others. Thus, we investigate the possibility of developing a dipole statistical model, with the end goal a kinetic description of dipoles similar to (1.1), without such restrictive assumptions.

These works on kinetic theory all have in common a starting point of the BBGKY hierarchy, in effect a coupled system of equations describing the statistics of the system. Given a Hamiltonian system of N particles we have the Hamiltonian in terms of generalised position p and momentum q coordinates as the sum of the energy of particles and pair interaction potentials

$\Phi_{i,j} = \Phi(|q_i - q_j|)$ as

$$H = \sum_{s=1}^{N} H_s(p_1, ..., p_s, q_1, ..., p_s), \quad H_s = \sum_{i=1}^{N} T(p_i) + \sum_{1 \leq i < j \leq s} \Phi_{i,j}. \tag{1.2}$$

Here T is the energy of the $i_t h$ particle, usually the kinetic energy. Given the probability density function of a quantity of interest $\mathcal{D} = \mathcal{D}(t, p_1, p_2, ..., p_N, q_1, q_1, ..., q_N)$ there then exists the s-particle functions F such that

$$F_s(t, q_1, ..., q_s, p_1, ..., p_s) = \int_{\Omega_V} \mathcal{D}(t, p_1, \ldots, p_N, q_1, \ldots, q_N) dp_{s+1} \ldots dp_N dq_{s+1} \ldots dq_N,$$

where F_s is the s particle distribution function of $\mathcal{D}$, and Ω_V is the entire phase space of a single particle. Through starting at the Liouville equation and this definition of the F_s functions the BBGKY hierarchy is then formed [14]

$$\frac{\partial F_s}{\partial t} = H_s, F_s + n \int_{\Omega} dq_{s+1} dp_{s+1} \left\{ \sum_{i=1}^{s} \Psi_{i,s+1}, F_{s+1} \right\},$$

with H_s defined as in (1.2) and $\{..., ...\}$ is the Poisson bracket defined as

$$\{f, g\} = \sum_{i=1}^{N} \left(\frac{\partial f}{\partial q_i} \frac{\partial g}{\partial p_i} - \frac{\partial f}{\partial p_i} \frac{\partial g}{\partial q_i} \right).$$

The above the results in a coupled chain of equations where the s-particle distribution is given in terms of the $s+1$-particle distribution until the N particle Liouville equation is reached. The solution to such a problem is equivalent to solution of the original Liouville equation, which can be approximated from the BBGKY by only considering a truncated chain of such F distribution functions.

This truncation process provides the justification for how we may construct statistical model based upon a chain of dipole interactions such that interactions with a lower probability of occurring are neglected in favour of the more common interactions. The application of such a model will be heavily dependent upon the effects of the particular dipole interactions that are identified, and so a preliminary investigation into the basic dipole interactions and the effects of these must be done. Firstly we must identify the basic interactions which we wish to form such a model around, it is natural that the first considered must be effects between point

vortex structures, of which three can be identified as primary; the interaction of a dipole with a lone stationary vortex, the interaction of a dipole with another dipole, and the interaction of a dipole with a rotating vortex cluster made up of many point vortices. It should be the case that these three collisions on the whole can already be thought to describe the majority of point vortex evolution, as we speculate that the collisions that are most likely to occur are those that are the simplest in terms of the interaction constituents. For an example to illustrate this, consider the interaction of two dipoles with a lone vortex; such a case relies upon two dipoles forming and interacting simultaneously at the same point in time with a lone vortex. Such an interaction is obviously very unlikely due to this, what is much more likely is a two-step interaction process, where the first dipole interacts with the lone vortex first, followed by a second interaction involving the second dipole. Thus, in this way complicated interactions between vortex structures can be reduced to these basic collisions, with any interactions not describable in terms of these collisions being so unlikely the effects of these are negligible in the context of a larger statistical theory. The effects of these basic interactions must then be considered, with special emphasis on those that will most affect the evolution of a larger point vortex system.

The first important consideration is the structural effects of such interactions; we consider a model in terms of vortex dipoles, so the resulting makeup of vortex dipoles after basic interactions, and the size of such dipoles, is of prime importance as it is this that will decide the agents of evolution at later time steps. We then must question what types of interaction are possible, and after interaction do dipoles persist? And do dipoles after interaction contain the same vortices post-interaction as in pre-interaction? We must also consider the scattering of dipoles due to such collisions, as it is this scattering that promotes mixing of the system, and which subsequent interactions will take place at later points in time. Specifically, it must be considered what interactions result in most/least scattering, and what regimes of each interaction result in most scattering also. These are all key quantities that a hypothesised statistical model should be able to predict. Also in considering a more typical turbulent fluid flow (which the proposed statistical point vortex model would hope to replicate), dipole phenomena exist that it is not possible to replicate in the standard point vortex model. These include the effect of sound on vortex dynamics in quantum turbulence that point vortices are typically used to

model, also mechanisms for vortex annihilation do not exist in the point vortex model, which are very important to the development of both classical and quantum turbulence. Additionally the existence one of the most fundamental ideas in the theory of turbulent flows; that of the direct and inverse energy cascade, is questionable in the point vortex model. It is then necessary that these effects are considered in formulating our model. The effects due to sound on a vortex dipole must be investigated as compared to no sound present. In particular, we consider the annihilation mechanisms that sound allows, and how sound may or may not lead to this process in systems where sound is present. Finally, large amounts of theory regarding turbulent flow centre around the notion of the energy cascade, this process is central to many turbulent flows, and is vastly important to the development of vortex structures in these systems. No consensus on whether this process is achievable in the point vortex model is found, so it presents an interesting case-study to consider how this may be possible through the dynamics of dipoles in the system and of vortex structure statistics involved. The overall objective of the current work is to provide an analysis of the basic dipole interactions in order to perhaps look towards using this in a future kinetic equation for dipole motion, before considering this in detail we first introduce the key concepts we develop upon in the remainder of this chapter.

1.2 Hydrodynamic turbulence

Even when discussing the phenomenon of turbulence it is often difficult to formulate a precise definition of turbulent fluid flow, with this being another debated topic within the fluid dynamics community. Rieutord gives a particularly useful description in forming what it means for fluid to be considered turbulent [15]; given a certain turbulent fluid flow and two points in the flow A and B, fluid velocities $\boldsymbol{v}_A, \boldsymbol{v}_B$ at the two points are statistically independent if A and B are separated by a distance greater than what is termed the correlation length; also at either of these points we note statistical independence between the velocity at a time t and a later time $t + T_c$, i.e. $\boldsymbol{v}(t)$ and $\boldsymbol{v}(t + T_c)$ are uncorrelated, with T_c called the correlation time. Given a fluid flow evolution is considered for length scales larger than the correlation length and for longer time than the correlation time we will observe both spatial and temporal randomness known more commonly as turbulence.

The first serious study of turbulent fluid motion can be attributed to the previously men-

tioned work of Reynolds [6], where the connection between "direct and sinuous" (in our parlance laminar and turbulent) fluid flows are explored, Half a century later, Kolmogorov set out a statistical theory of turbulence from which the famed Kolmogorov-Obukhov power law for the energy spectrum $E(k)$ was found later by Obukhov [16] which will be explored later in the current work. This with the other power laws developed as part of the famed Kolmogorov 1941 theory are some of the most developed theories regarding turbulent fluid flow that exist. An excellent introduction to the Kolmogorov statistical theory of turbulence can be found in [17], where the issues with the Kolmogorov formulation are also explored.

To this day the long-standing battle to understand turbulence wages on, continuing the great problem experienced by fluid dynamicists throughout history, as turbulent phenomena are fundamental to fluid motion and are frequently encountered in many fluid dynamics applications showing the great importance to the science of fluids as a whole. For example turbulence frequently occurs in the field of aerodynamics [18, 19] with turbulent effects found to influence the performance of certain aerofoils, Bose-Einstein Condensates and superfluids [20, 21, 22] as a peculiar form of turbulence is found in such phases of matter that is of particular interest to the current work. Turbulence is also commonly found in geophysical fluid dynamics, for example considering the Planetary Boundary Layer Reynolds numbers are typically very large, ordinarily a sure sign of fully developed turbulence; in this sense turbulence even has been found to have applications in the study of air pollution as air contaminant particles are dispersed by geophysical turbulent flows. A great overview of this particular field is given in [23]. The complexity and chaotic nature in turbulent systems is such that a deterministic solution cannot be feasible, as such description of these systems requires the use of alternative approaches such as statistical analysis [24, 25, 26] (where the long-term evolution of mean properties of the fluid flow is examined) or the focus of the current work; vortex dynamics [5, 27, 28].

Among the defining features of this turbulent flow is the dominance of strongly non-linear eddy currents and vortices throughout the flow. These vortices can informally be considered as objects in the fluid that cause surrounding fluid particles to follow circle-like orbits about them. Mathematically we can define vortices as elements in the fluid with vorticity, that is the

quantity determined as the curl of velocity.

$$\boldsymbol{\omega} = \nabla \times \boldsymbol{u}, \tag{1.3}$$

where here ∇ represents the differential operator common throughout vector calculus:

$$\nabla = \left(\frac{\partial}{\partial x}, \frac{\partial}{\partial y}, \frac{\partial}{\partial z} \right),$$

and $\boldsymbol{u} \equiv \boldsymbol{u}(x, y, z, t) \in \mathbb{R}^3$ is the velocity of the fluid at position (x, y, z) at time t. Here $\boldsymbol{\omega} \in \mathbb{R}^3$ gives in essence a measure of the local rotational movement of the surrounding fluid at a point, mainly developed through fluid interaction with boundary layers, and it is this vorticity that is responsible for the foundational structures of turbulence; eddy currents and vortices. Turbulence being made up of these vortices and eddies can be demonstrated to be observed even as early as the drawings of Da Vinci [29] and provides an alternative method of analysing turbulence by investigating dynamics of vortex structures rather than of the fluid motion directly. In turbulence, these vortices and eddy currents are known to decay into ever smaller vortices and eddy currents in what is known as Richardson cascade, this flow of energy to smaller length scales continues until the energy is dissipated by the viscous forces present [17]. These viscous forces, in other words the friction forces between layers of fluid within the flow, are often critical in the evolution of fluid flow as a whole.

Indeed, if we consider the standard general equations describing incompressible (constant density within a fluid parcel) fluid motion, and thus also turbulence, we have the incompressible Navier-Stokes equations. Assuming an incompressible Newtonian fluid with constant density ρ and constant viscosity μ, the velocity distribution of the flow $\boldsymbol{u} \equiv \boldsymbol{u}(x, y, z, t) \in \mathbb{R}^3$ is given as the solutions of

$$\frac{\partial \boldsymbol{u}}{\partial t} + (\boldsymbol{u} \cdot \nabla)\boldsymbol{u} = -\frac{1}{\rho}\nabla p + \frac{\mu}{\rho}\nabla^2 \boldsymbol{u} + \boldsymbol{g}, \tag{1.4}$$

$$\nabla \cdot \boldsymbol{u} = 0, \tag{1.5}$$

where (1.4) gives the Navier-Stokes momentum equations and (1.5) gives the usual incompressibility condition of divergent-free velocity [30]. Note here $\boldsymbol{g} \equiv \boldsymbol{g}(x, y, z) \in \mathbb{R}^3$ represents an

external field acting on the fluid (for example a gravitational field), $p \equiv p(x, y, z, t)$ is a scalar function representing pressure, and similarly we define ∇^2 as the Laplacian:

$$\nabla^2 = \nabla \cdot \nabla = \frac{\partial^2}{\partial x^2} + \frac{\partial^2}{\partial y^2} + \frac{\partial^2}{\partial z^2}.$$

The chaotic, aperiodic motion, and highly unstable nature of turbulence means solving these equations either analytically or numerically is extremely complicated, Nevertheless, turbulence has been successfully investigated using Navier-Stokes simulations in various works [31, 32, 33]. Examining the Navier-Stokes term by term we see the standard convection derivative familiar throughout fluid dynamics $D\boldsymbol{u}/dt = \partial \boldsymbol{u}/\partial t + (\boldsymbol{u} \cdot \nabla)\boldsymbol{u}$ representing the change of the velocity of a fluid particle as it "moves through the fluid", this essentially describes the acceleration, and thus shows the Navier-Stokes as the fluid dynamics equivalent of the Newton equation $\boldsymbol{F} = m\boldsymbol{a}$. It is important to note the non-linear advection term $(\boldsymbol{u} \cdot \nabla)\boldsymbol{u}$, this causes great computational cost in Navier-Stokes simulations, and emphasizes the struggle in finding exact solutions to such an equation. On the right-hand side of the equality we have the inertial terms contributing to the change in momentum, namely the pressure gradient $-\nabla p/\rho$ and the external body field $\boldsymbol{g}$, also we observe the $(\mu/\rho)\nabla^2\boldsymbol{u}$ term representing the difference between velocity of a point in the fluid compared to the velocity of a small surrounding volume, hence this term corresponds to the diffusion of momentum created by the viscous forces present [30], and we see fluid motion thus described as a momentum balance equation between two inertial terms and one viscous term.

The first studies of turbulence by Reynolds [6] involved such velocities in the case of turbulence, leading to the discovery of the Reynolds number that is now considered inseparable from descriptions of turbulent flow. Given a characteristic fluid velocity U, a characteristic length L and the kinematic viscosity defined as $\nu = \mu/\rho$ where μ is the coefficient of viscosity particular to the fluid in question and ρ is the density of the fluid (we again assume the fluid here is incompressible) then we define the Reynolds number as the ratio $\mathrm{Re} = UL/\nu$. The numerator UL can be shown to be of the order of the inertial forces in the fluid flow, and the same is true regarding the ν term and the viscous forces respectively [34]; the Reynolds number can then be thought of as giving an indication of the relative magnitudes of the inertial and viscous components of a fluids motion. Dynamics of a fluid flow is dependent upon this Reynolds number,

and a fluid expresses much different motion and general characteristics depending on the magnitude of the Reynolds number [30]. For fluid flows where the Reynolds number is very small, either due to small characteristic lengths/velocities or a high relative viscosity, viscous forces in effect dominate the evolution of the fluid, and the resulting dynamics can be described through the "slow fluid equations" resulting in characteristically well-ordered fluid flow. In contrast, for high Reynolds number flows, inertial forces dominate the evolution and fluid flows become frequently unstable; in this regime the chaotic velocity and pressure fluctuations that make up turbulence are observed. Thus, the transition from well-ordered laminar flow to turbulent flow is reflected in the increase from a small to a large Reynolds number. In fact there exists a critical Reynolds number Re_c particular to a given flow geometry such that if the Reynolds number of the fluid flow exceeds this value, i.e. $\mathrm{Re} > \mathrm{Re}_c$, this will result in turbulent dynamics. Turbulence can then be explained as an exhibition of inertial fluid forces dominating viscous fluid forces as predicted by a high Reynolds number.

This is similar to another dimensionless quantity in the analysis of fluid motion; the Péclet number; defining the ratio of advective transport to diffusive transport. It is defined as $\mathrm{Pe} = (Lu)/D$ where u is the fluid velocity, L is the characteristic length of the system, and D is the diffusivity coefficient, defined as the amount of a substance that diffuses across a unit area under a unit gradient, and provides a measure of how convective fluid motion conserves quantities as compared to the fluctuations due to viscous effects. As can be expected; in a turbulent system with high Reynolds number (thus less effective viscous effects compared to inertial effects) the effects of viscous transport are negligible and so we can expect a high Péclet number. This can also be recovered through the definition of the Péclet number as the product of the Reynolds and Schmidt number $\mathrm{Pe} = \mathrm{ReSc}$, with the Schmidt number defined as the ratio of momentum diffusivity and mass diffusivity $\mathrm{Sc} = \nu/D$. Thus, a high Reynolds number naturally implies a high Péclet number, and scalars are transferred mainly through fluid convection in turbulent flow [35].

With this characteristic velocity U and a characteristic length scale L, we can then introduce the new variables $\hat{\boldsymbol{u}} = \boldsymbol{u}/U$, $\hat{t} = tU/L$, $\hat{p} = p/(\rho U^2)$, $\hat{\boldsymbol{x}} = \boldsymbol{x}/L$ and $\hat{\boldsymbol{g}} = \boldsymbol{g}/g_0$ (with g_0 representing a characteristic value of $\boldsymbol{g}$) we thus attain the non-dimensional incompressible

Navier-Stokes equation.

$$\frac{\partial \hat{\boldsymbol{u}}}{\partial \hat{t}} + (\hat{\boldsymbol{u}} \cdot \hat{\nabla})\hat{\boldsymbol{u}} = -\hat{\nabla}\hat{p} + \frac{1}{\mathrm{Re}}\hat{\nabla}^2\hat{\boldsymbol{u}} + \frac{1}{\mathrm{Fr}^2}\hat{\boldsymbol{g}}, \tag{1.6}$$

where $\mathrm{Fr} = U/\sqrt{g_0 L}$ is the Froude number, another dimensionless quantity similar to the Reynolds number, except the Froude number gives a ratio of the inertial forces to the external field forces. The Navier-Stokes equations in the form of equation (1.6) reveals more clearly the role of viscous forces in the evolution of high Reynolds number fluid flows. As we allow the Reynolds number to become very large such as would be found in fully developed turbulence, the viscous term becomes negligible and the inertial terms dominate. Indeed, as we allow $\mathrm{Re} \to \infty$ the term responsible for diffusion by viscous forces $(1/\mathrm{Re})\hat{\nabla}^2\hat{\boldsymbol{u}} \to 0$ and the dimensionless Euler equations of fluid motion are recovered:

$$\frac{\partial \hat{\boldsymbol{u}}}{\partial \hat{t}} + (\hat{\boldsymbol{u}} \cdot \hat{\nabla})\hat{\boldsymbol{u}} = -\hat{\nabla}\hat{p} + \frac{1}{\mathrm{Fr}^2}\hat{\boldsymbol{g}}. \tag{1.7}$$

These equations exhibit fluid motion in the absence of viscous dissipation, and hence are simpler in nature than the aforementioned Navier-Stokes on account of the absent viscous forces, and can easily be derived from first principles [30]. However, in the absence of the viscous forces found in the Navier-Stokes equations the no-slip boundary conditions ($\boldsymbol{u} = 0$ at flow boundaries) enforced by viscous forces are not present. These no-slip boundary conditions in viscous flow create a shear layer at boundaries which then creates vorticity ω, and thus eddy currents that contribute towards turbulent velocity fluctuations. In the absence of this boundary-layer turbulence, the development of turbulent flow is due to the non-linear term in the Euler equations, and so whilst viscous forces may be considerably lessened in turbulence the presence of these forces can still have a direct effect on turbulent flow itself. Despite this, under certain circumstances convergence from Navier-Stokes solutions to Euler solutions has been shown [36].

Considering this discrepancy in Euler and Navier-Stokes dynamics, the complexity surrounding the Navier-Stokes equations, and the computational difficulty of modelling such systems (especially when considering the non-linear effects) it is clear that there are several disadvantages of modelling turbulence using the fluid dynamics equations directly. We thus seek an alternative method of analysis, which before being defined proper we first introduce some

important concepts, first the so-called circulation

$$\kappa = \oint_C \boldsymbol{u} \cdot d\boldsymbol{s} = \int_A \boldsymbol{\omega} \cdot \boldsymbol{n} dS, \tag{1.8}$$

where C is a closed curve moving with the fluid and $d\boldsymbol{s}$ is the vector differential representing a small line element on the curve C, also A is the surface bounded by the curve C and dS is a small surface element of A with outward unit normal $\boldsymbol{n}$. From the second equality (attained through application of Stokes' theorem on the line integral) we see that the circulation defined on a curve C can be thought of as the flux of vorticity through an open surface A bounded by the curve, or alternatively vorticity can be considered as the circulation through an infinitesimally small curve C [37]. Circulation is also related to another fundamental concept, namely the representation of vorticity as vortex filaments. This comes from the idea of vortex lines, defined as lines in the fluid flow tangent to the local vorticity vector; the collection of vortex lines on a closed curve then gives what are known as vortex tubes. By taking the curve to be of infinitesimal dimension, in other words located at a single point, we then realise the approximation to vorticity known as vortex filaments. It was Helmholtz who first considered this approximation of vorticity to describe fluid flow, and from this that his famed vortex theorems derive [38]. We reproduce these theorems here

1. Strength of vortex filaments are constant.

2. Vortex lines move with the fluid, and must either form a closed loop, start and end at solid boundaries in the fluid, or extend to $-\infty/\infty$.

3. Fluid elements that are initially irrotational ($\boldsymbol{\omega} = 0$) remain irrotational.

Hence, we have a description of vorticity as curves moving with the fluid with constant circulation/strength, as such vortex filaments represent a discretisation of the continuous vorticity field. The velocity imparted on the fluid as a result of a vortex filament can then be given by the vorticity equation (1.3) from inversion of the curl operator by the Biot-Savart law, given for a vortex filament of general shape as the line integral

$$\boldsymbol{u}(x, y, z) = \frac{\kappa}{4\pi} \int_C \frac{d\boldsymbol{\ell} \times \boldsymbol{r}}{|\boldsymbol{r}|^3}, \tag{1.9}$$

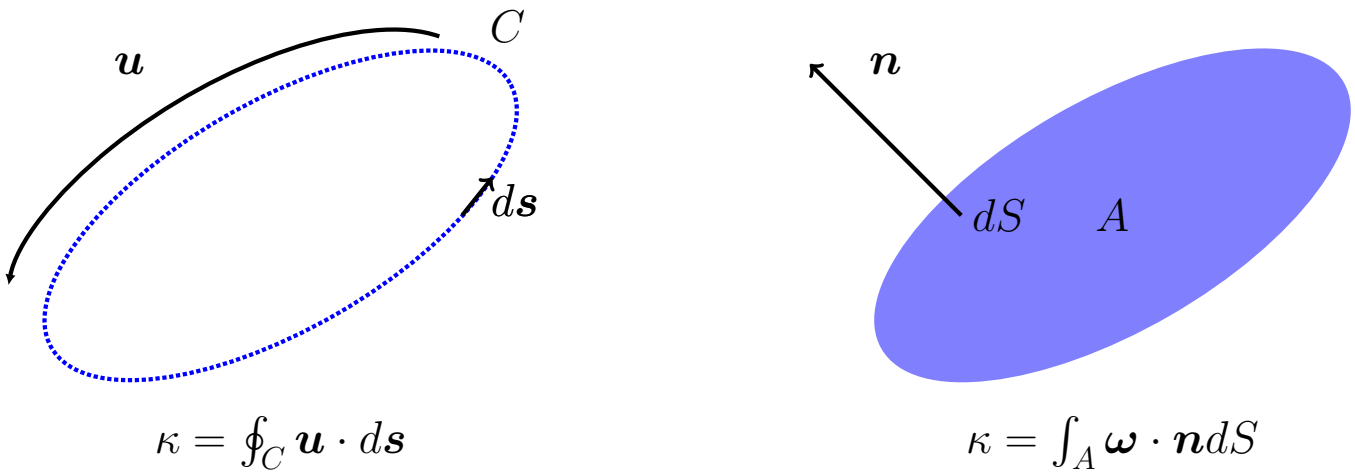

Figure 1.1: Diagrams of circulation from the two identities given by (1.8), the diagram on the left shows the original circulation definition, whereas the diagram on the right shows the result of applying stokes theorem.

with the line of integration C depending upon the shape of the vortex filament, which according to the second Helmholtz theorem must extend to either $\pm\infty$ or the region boundaries, or must form a closed curve in the fluid. Here κ is the circulation of the vortex filament, a constant according to the first Helmholtz vortex theorem, $d\boldsymbol{\ell}$ is a differential vector on the vortex filament C pointing in the direction of positive vorticity, and $\boldsymbol{r} \in \mathbb{R}^3$ is the displacement vector from the point being considered (x, y, z) to the line element $d\boldsymbol{\ell}$. Notice this is the same Biot-Savart law found in electrodynamics which gives the magnetic field generated by an electric line current [39]; this is a natural consequence of inversion of the curl operator. The velocity of a point in the fluid containing multiple vortex filaments consists of equation (1.9) summed over every vortex filament in the system. This approximation allows for a basic model of turbulent vortices where the distribution of vorticity is neglected in favour of tracking the centre point of the vorticity region. Associated vortex filament methods have proved to be successful in modelling turbulence in various situations [40, 41, 42].

It is also common in the study of turbulence to restrict study to only two dimensions. This is largely a theoretical undertaking, as turbulence in nature obviously must manifest some degree of three-dimensional dynamics; however the 2D approximation to turbulence is found to accurately describe certain (quasi)-2D physical systems such as oceans and atmospheres, where the ratio of lateral length to vertical length is very large [43]. Also in 2D turbulence we observe new phenomena not normally present, for example the inverse cascade [44], which in a restricted periodic domain can form a vortex condensate as analysed in [45]. This arises as a consequence

of the new conservation laws required for 2D turbulence, and suggests 2D turbulence as an interesting field of study not confined to a basic simplification of 3D turbulence. These energy

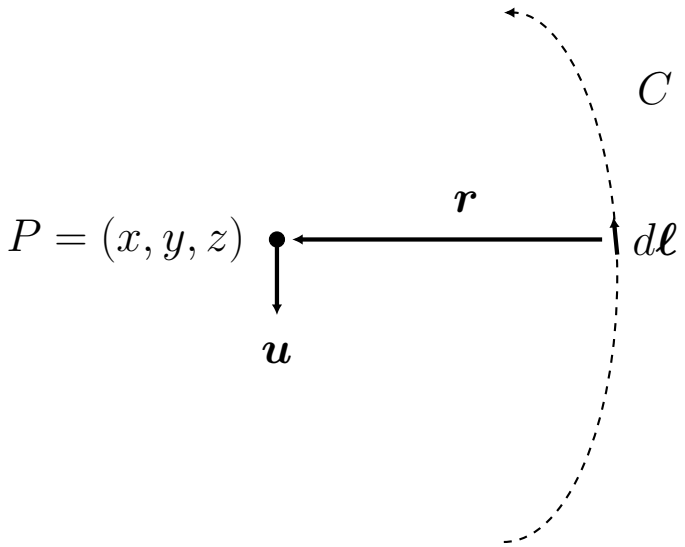

Figure 1.2: Visualization of velocity imparted from a vortex filament C on a point in the flow $P \in \mathbb{R}^3$ from the Biot-Savart law (1.9).

cascades are central to turbulent theory. Commonly understood as a typical phenomenon in turbulence according to the Kolmogorov 1941 theory [17], the standard direct cascade consists of eddies of various sizes with energy "cascading" down from the larger eddies through to smaller ones. Energy is introduced into the system through forcing at the length scale of the largest eddies, and once the energy has been transferred to the smallest length scales it is then dissipated by the viscous forces present in fluid. The intermediate range between the large scales of injection and small scales of dissipation are known as the inertial subrange, and the key result of the work of Kolmogorov is the power law defining the energy spectrum in this region

$$E(k) = C\epsilon^{\frac{2}{3}}k^{-\frac{5}{3}}, \tag{1.10}$$

where $E(k)$ is the kinetic energy contained in the wave number k, C is some constant and ϵ is the dissipation rate; the rate at which energy is transferred through length scales. The inverse cascade however is the opposite of this effect; in 2D and quasi-2D turbulence energy is instead transferred through to the largest length scales, and the same power law equation (1.10) instead dictates the flow of energy from the length scale of energy injection through to the largest length scales in the system. This inverse cascade is a key feature of 2D turbulence, and a model such

as the one we are to develop should consider this, hence we look at this in more detail later, now we examine another interesting form of turbulence.

1.3 Turbulence in quantum fluids

Now that the preliminaries of hydrodynamic turbulence have been explained we now move to consider possibly the most interesting phenomenon considered in the current work, namely the concept of quantum turbulence. We classify turbulence into two distinct types, that of the standard classical turbulence described in section 1.2, and of quantum turbulence. Whilst classical turbulence is a common occurrence that can be observed readily in nature (for example in a flowing river or stream) quantum turbulence is much rarer, only occurring in carefully designed experiment [22] or in neutron stars [46]. By quantum turbulence we refer to the turbulent flow found in a superfluid, that is, a carefully prepared fluid such that fluid flow occurs with zero viscosity. Such fluids only exist at extremely low temperature very close to absolute zero [47].

This superfluidity is thought to occur as a result of many atoms in the fluid occupying the same quantum state, and therefore will be described by the same quantum mechanical wave function and thus exhibit the same behaviour because of this. If a particle in such a state is to be scattered by another object (e.g. a particle outside the state, or a wall) this particle can not interact solely; each particle in the state must interact at once with this object as they are described by the same quantum wave function. This is obviously very improbable, and so the fluid in this quantum state flows without typical viscous forces that would cause such interactions. This is a phenomenon first found in liquid ^{4}He; as the temperature of the system is lowered, once a transition temperature now known to be $T_\lambda = 2.17K$ is reached, a transition (known as the lambda transition on account of the sharp discontinuity of the temperature graph [48]) occurs. Once this transition has occurred, the fluid has two states; "Helium I" above T_λ and "Helium II" below this T_λ. This Helium II regime was found to display unusual properties such as increased thermal conductivity [49] and ability to slip along solid walls leading to creeping effects [50], finally leading to the description of the Helium II state as superfluid [51]. Interestingly, superfluidity is also possible in ^{3}He [47]. According to the thermodynamic description, each particle occupies a so-called "quantum state" specified by a

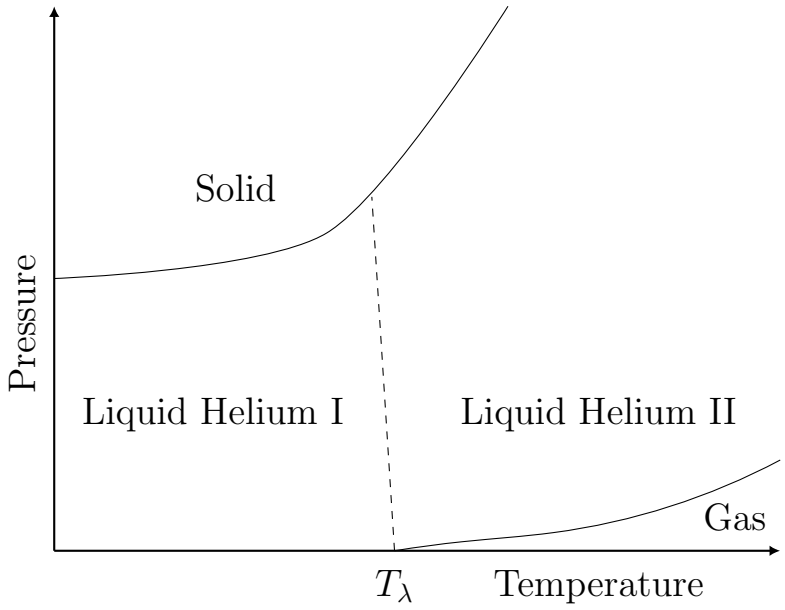

Figure 1.3: Phase diagram of ^{4}HE against temperature and pressure, with phase boundaries marked as solid lines and the λ transition temperature marked as a dashed line, showing solid and gaseous regions as well as the two liquid phases, the ordinary Liquid Helium II and the superfluid Liquid Helium II. Note the discontinuity between boundaries (no triple point).

certain energy value. Under the Pauli exclusion principle, more than one identical particles with half-integer spins (Fermions) cannot occupy the same quantum state within a system, whereas for particles with an integer spin (Bosons) this is possible [52]. These ^{3}He particles possess 1/2 and thus are considered Fermions, and occupation of a quantum state by a multitude of them should thus be impossible. However, through the work of Bardeen, Cooper and Schrieffer into superconductivity, it has been shown that a pair of electrons of opposite momenta move towards a state known as a Cooper pair (or BCS pair), where the electrons are considered bound due to having a lower energy than the Fermi energy. These Cooper pairs are said to condense into the lowest quantum state whereupon superconductivity, or the property of electrical conduction without energy loss, is observed [53]. It is these Cooper pairs which are thought to condense to the ground state thus resulting in superfluidity, or conversely, superconductivity can be viewed as the superfluidity of Cooper pairs in a crystal lattice [54]. The degrees of freedom present due to the multitude of Cooper pair states that in a zero magnetic field there are in fact two superfluid regimes that exist in ^{3}He, known as the a-phase and b-phase [55], with much more complicated effects than those found in superfluid ^{4}He, and both exhibiting zero viscosity. The superfluid phases of ^{3}He are very interesting and possess many peculiar phenomena in their own right, for example the continuous "half-quantum" vortex structures in the a-phase,

or the unusually high viscosity near the b-phase transition (due to being governed by Fermi statistics here) resulting in fluid hardly moving [54], a more detailed description into the phases of superfluid ^{3}He can be found in [56].

Most importantly, superfluids are then not subject to the previously explored viscous forces applicable to classical turbulent flow; this implies that superfluids flow without loss of energy due to the lack of these forces. Ordinarily in a classical fluid any turbulence will decay over time in the absence of external forcing due to the dissipative viscous forces present, thus in the absence of this it is then possible that the Richardson cascade that characterises turbulence mentioned at the end of the previous section, wherein energy flows from larger scales to smaller scales until they are dissipated by viscous effects, will then continue to the smallest quantum scales, where dissipation will instead be accomplished through certain quantum effects involving the radiation of sound [57]. Thus we have in effect a quantum regime for turbulence, commonly referred to as quantum turbulence, which has been theorized as early as 1955 by Feynman [58], and has been observed previously in the superfluid helium already mentioned [59]. Also, when considering the Reynolds number as defined as the ratio of inertial forces to viscous forces, this is challenging to define in the quantum domain due to the Reynolds number approaching infinity in the limit of the viscous forces approaching zero. Despite this there have been several attempts to define an effective Reynolds number and so identifying the onset of quantum turbulence [60, 57].

Of this quantum turbulence, we note several possible regimes that can possibly be observed. In the zero-temperature limit there are two types of quantum turbulence that may be observed, that of Vinen-type turbulence and that of Kolmogorov-type turbulence. These two regimes can be differentiated in the degree of quantum effects observed, with the Vinen-type being considered strictly quantum whereas the Kolmogorov-type can be said to be semi-classical [54]. For Vinen-type turbulence, we have the seemingly random highly knotted tangle of vortex lines as displayed in figure 1.5. These are the typical quantum vortices we have been considering thus far, of extremely small width and quantized circulation, and with annihilation and reconnection effects through phonon emission. A clear sign that this Vinen-type turbulence is present is associated with the decay of the turbulence itself, with the density of vortex lines in this regime decaying as according to the inverse time law $L(t) \sim 1/t$ at late times. This also results in the

"typical" quantum turbulence we consider in this section, with a Richardson cascade not being observed and fluid moving seemingly at random. Contrary to this, Kolmogorov-type quantum turbulence consists of vortex lines forming in bundles in the flow resulting in quasi-classical type vortices in quantum fluid. These quasi-classical vortices exceed the quantum length scale, and thus undergo the typical classical turbulent effects of advection and stretching, where here a Richardson cascade will be observed. Due to viscous dissipation being absent here however, this Richardson cascade will continue to the smallest length scales of vortex cores, through to Kelvin wave cascades along vortex lines until dissipation through acoustic effects [61]. This type of quantum turbulence is characterised by the vortex line density decaying as according to $L(t) \sim t^{-3/2}$ [54].

Of particular interest especially with regard to our model are the vortices found in such quantum turbulent regimes. The presence of vortices in superfluid helium has been observed and studied numerically in particular by Schwarz [62, 63, 64], and it is these vortices that make up quantum turbulence. Before considering with these quantum vortices proper, we segue to first discussing an important medium in which they can occur and has been very important to their analysis, namely the Bose Einstein Condensate(BEC). This "Bose-Einstein Condensation", first predicted by Bose in 1915 but only produced experimentally in 1995, refers to the phase transition that occurs in a dilute boson gas at ultra-low temperatures close to absolute zero. Given a Bose gas, as the temperature is lowered we see increasing occupation of the lowest energy states, until particles begin to occupy the lowest quantum state; the "ground state" a rough explanation of this can be given by the Bose distribution function

$$f^0(\epsilon_\nu) = \frac{1}{e^{(\epsilon_\nu - \mu)/kT} - 1}, \tag{1.11}$$

assuming non-interacting Bosons, where f^0 is the mean occupation number of the single-particle state ν, ϵ_ν denotes the energy of the state, μ is the chemical potential, k is the Boltzmann constant and T is the temperature of the system. Note the chemical potential is defined as a function of the total particles N and T under condition that total number of particles be equal to the sum of the occupancies of states. As the temperature becomes low, chemical potential rises and occupation numbers increase, yet the chemical potential cannot grow greater than the energy of the lowest single-particle state $\epsilon_{\min}$ otherwise this results in a negative Bose

distribution for the lowest energy state. Thus, the occupation number of any excited single-particle state has the upper bound

$$f^0(\epsilon_\nu) \leq \frac{1}{e^{(\epsilon_\nu - \epsilon_{\min})/kT} - 1}, \tag{1.12}$$

note that this constraint does not apply to the ground state, the occupation number of which may be arbitrarily large. Given the total number of particles in excited states is less than N, the remaining particles must then be accommodated in the ground state and Bose-Einstein condensation occurs [65]. The highest temperature this condensation occurs is known as the transition temperature T_c such that when $T < T_c$ the condensation process begins as boson molecules move to the lowest energy quantum state. The specific value this critical temperature T_c takes is highly dependent upon any external potentials present, the mass of particles and whether the particular gas is ideal or otherwise, and other factors [66, 67, 68]. A general form of the critical temperature can be directly from the Bose statistics description of a gas, in particular the ideal Bose gas state equation $N/V = (1/\lambda^3)\sum_{n=1}^{\infty}(f^n/n^{3/2}) + f(1/V)/(1-f)$ where N is the number of particles present in the system, V is the volume considered, λ gives the thermal wavelength $\lambda = \sqrt{2\pi\hbar^2/MkT}$ where M is the particle mass, k is the Boltzmann constant, and f the fugacity; a state function expressing the idealised partial pressure of a gas in a non-ideal gaseous mixture. Note also the summation; a monotonically increasing function of f converging only for fugacities $f \in [0, 1]$. Here, according to Bose statistics the $f/(1-f)$ term expresses the average occupation of the lowest quantum state n_0, therefore the equation of state can be rewritten as $\lambda^3\langle n_0\rangle/V = N\lambda^3/V - \sum_{n=1}^{\infty}(f^n/n^{3/2})$, and in order for a physical solution the lowest energy state cannot have a negative occupation number, so it must be that $N\lambda^3/V > \sum_{n=1}^{\infty}(1/n^{3/2})$ where the summation now gives the Riemann-zeta function such that $N\lambda^3/V > \zeta(3/2)$. This defines two regions in f, V, T space, that of the condensed and uncondensed phase, and the critical boundary defined as the two-dimensional surface $N\lambda_c^3/V = \zeta(3/2)$, through the definition of λ the critical temperature is then given as

$$T_c = \left(\frac{N}{V\zeta(3/2)}\right)^{2/3}\frac{2\pi\hbar^2}{mk},$$

note that the Riemann-zeta function has a known value $\zeta(3/2) \approx 2.6124$ such that

$$T_c \approx \left(\frac{N}{2.6124V}\right)^{2/3} \frac{2\pi\hbar^2}{mk}.$$

This gives the value at which the macroscopic occupation of the ground state known as condensation occurs [69]. These particles in the ground state have the same velocity, and can be described by the same quantum wave function. In figure 1.4 this process is displayed showing the velocity distribution of Rubidium atoms as the temperature of the Bose-gas is decreased. In the left-most frame we see the gas at a temperature slightly above the critical value T_c prior to the formation of the condensate, in the middle frame we see the condensate beginning to form, and in the right-most we see almost every atom occupying the ground-state, almost a pure condensate is observed. Bosons in this ground state coalesce into a "super-atom" with

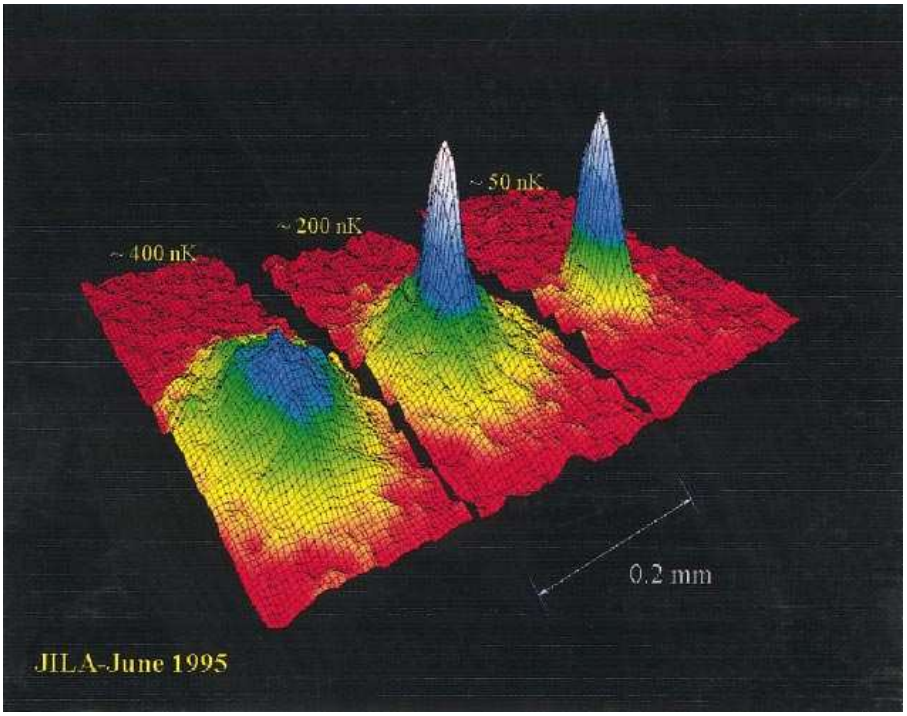

Figure 1.4: The momentum distribution of a vapour of cooled ^{87}Rb atoms. Three frames are visualized for three different temperatures of the gas with a field of view of 200μm by 270μm. Colour represents the density at each momentum, with red being the fewest and white the most. Figure taken from [1] from the original 1995 experiment by Anderson et al. [2].

its own macroscopic properties and characteristics as a new phase of matter; the Bose-Einstein Condensate (BEC) is formed [70]. These BECs are of great interest by their own characteristics, and despite the fragility of the systems considered, have proven useful in answering questions on matters of condensed matter physics and quantum mechanics [71, 72]. Of distinct interest

for our purposes is the ability of BECs to exhibit quantum turbulence.

It is clear that this peculiarity is of considerable interest, as understanding of the behaviours of BECs is then deeply tied to an understanding of quantum turbulence and thus of turbulence as a whole. Particularly interesting is the vortices that are formed in the event of quantum turbulence. By stirring or rotating a BEC for example one observes the formation of vortex lattices once a certain critical angular velocity is reached [73]. According to the Onsager-Feynmann theory, such vortices possess quantized circulation; in other words the circulations of such vortices must be an integer multiple of the quantum value $\kappa = h/m$ [74]. Also, rotational motion is only sustained through these vortices, i.e. fluid is irrotational, $\boldsymbol{\omega} = 0$ at all points other than the vortices in question. Hence, we find the Helmholtz laws of vortex motion to be satisfied in the case of quantum vortices, and as vortex widths are incredibly small (of the order of a few angstroms in ^{4}He for example [75]) we find that quantum vortices are then analogous to the vortex filaments found in the last section. Quantum turbulence can be thought of as a tangle of identical quantized vortex filaments as shown in figure 1.5; here instead of a loose approximation vortex filaments now represent the regions of vorticity completely. This is remarkably demonstrated by Bustamante and Nazarenko [76], where it is shown explicitly that vortices in quantum fluid can be described as vortex filaments; starting at the Hamiltonian form of the non-linear Schrödinger equation(NLS) $i(\partial\psi/\partial t) = \partial H/\partial\psi^*$, with ψ the complex wave function of the fluid such that $|\psi|^2 = \rho$, and the Hamiltonian giving the total energy as

$$H = \int \left[|\nabla\psi(\boldsymbol{x}, t)|^2 + \frac{1}{2}(|\psi(\boldsymbol{x}, t)|^2 - 1)^2 \right] d\boldsymbol{x},$$

by considering the NLS in its hydrodynamic form (to be discussed later), and then finding the Hamiltonian in terms of vortex lines, given some extra manipulation and the assumptions of large vortex curvature and spacing when compared to vortex size we have the following result

$$H = \frac{\kappa^2}{16\pi} \int_{|\boldsymbol{s}-\boldsymbol{s}'|>\xi^*} \frac{d\boldsymbol{s} \cdot d\boldsymbol{s}'}{|\boldsymbol{s} - \boldsymbol{s}'|},$$

which is the Biot-Savart equation as seen in the previous section defined in Hamiltonian form, describing the motion of vortex filaments. Thus, the approximation of quantum vortices by the aforementioned vortex filaments can be rigorously justified as the description of slow motions

of the more general NLS equation by the Biot-Savart law, a key approximation commonly used in the analysis of BECs.

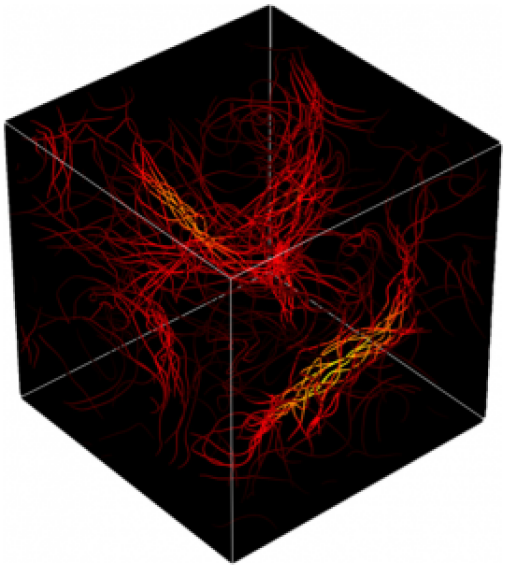

Figure 1.5: Snapshot of a simulation of a quantum vortex tangle, with vortex lines coloured according to the normalized magnitude of $\boldsymbol{\omega}$. Reproduced from [3].

To examine the theory of BECs (and thus quantum turbulence), here we consider a 2D BEC, assuming that the gas is "fully-condensed"; given a gas of N particles in the zero temperature limit $T \to 0$ the full condensation has occurred and all N particles occupy the ground state. In occupying the lowest quantum state of the Bose gas, according to the Hartree approximation, each atom in this state can be described by the same wave function ψ with the total wave function Ψ described as the product of these. This is not necessarily the case in the true wave function as the zero temperature limit can never be reached in physical systems, and due to correlations at small separations some atoms will occupy different states, although through experiment it is observed this occurs at a negligible rate for low T compared to T_c. The total wave function of the system Ψ can then be given as

$$\Psi(x_1, y_1, x_2, y_2, ..., x_N, y_N, t) = \psi_1(x_1, y_1, t)\psi_2(x_2, y_2, t)...\psi_N(x_N, y_N, t), \tag{1.13}$$

with $\boldsymbol{r}_i$ representing the position vector of the ith particle, and t representing time, and ψ_m the wave function of the mth particle. This approximation assumes a fully developed condensate, therefore an extremely low temperature close to absolute zero. By experiment (an example of which shown in figure 1.4) this is shown to be of the order of several nano-kelvins. By

considering the many body Hamiltonian in addition to the Schrödinger equation, one can attain the time-dependent Gross-Pitaevskii equation(GPE) here given in dimensionless form

$$i\dot{\psi} = -\nabla^2\psi + |\psi|^2\psi + \mu\psi, \tag{1.14}$$

with the scalar differential operator Laplacian $\nabla^2 = (\partial/\partial x)^2 + (\partial/\partial y)^2$, where here $\psi = \psi(\boldsymbol{r}, t) \in \mathbb{C}$ is a complex field that represents the ground state wave function, with $|\psi(\boldsymbol{r}, t)|^2$ giving the density of the condensate at a particular point in space $\boldsymbol{r}$ and time t. The parameter μ is the chemical potential of the system, the change of energy of the system per additional particle introduced with a fixed volume.

This equation of motion describes the dynamics of the ground state of a bosonic gas, so effectively models the motion of the condensate itself. The GPE is also known as the "Non-linear Schrödinger equation" on account of the resemblance to the position-space Schrödinger equation governing the wave function of a quantum mechanical system, with the addition of the non-linear $|\psi|^2\psi$ term, the contribution from particle pair interactions as the BEC evolves. Usually also in the GPE the external potential term $V(\boldsymbol{r})\psi$ is included to model the traps used to confine the condensate such that the extremely low temperatures required can be reached, these frequently are harmonic traps in order to model the magnetic trapping frequently used [77] (although different trapping forms of potential have been used, for example the uniform potential optical box trap [78] or random potentials [79]) however due to the periodic boundary conditions we use this term can be neglected in this case.

What is perhaps one of the most interesting properties of the BEC is the hydrodynamic representation; under certain transforms the dynamics of BECs can be shown to approximate fluid motion. If the wave function in this case is represented in terms of its amplitude and phase such that $\psi = \sqrt{\rho}e^{i\phi}$, the so-called "Madelung transform" [80]; by comparing real and imaginary parts of the resulting equation we recover the equations of motion for the condensate in a familiar hydrodynamic form

$$\dot{\rho} + \nabla \cdot (\rho \boldsymbol{v}) = 0, \tag{1.15}$$

$$\dot{\boldsymbol{v}} + (\boldsymbol{v} \cdot \nabla)\boldsymbol{v} = -\frac{\nabla^2\rho}{\rho} + \nabla\left(2\frac{\nabla^2\sqrt{\rho}}{\rho}\right), \tag{1.16}$$

this represents the familiar Euler equations of motion for a fluid of zero viscosity, with the addition of a quantum pressure term, describing the forces due to spatial variations in magnitude of the wave function [65]. Importantly, the velocity of the system is given in terms of the gradient of the scalar phase $\boldsymbol{v} = 2\nabla\phi$, and so the standard physical velocity of the condensate can be attained from the wave function

$$\boldsymbol{v} = i\frac{\psi\nabla\psi^* - \psi^*\nabla\psi}{|\psi|^2}, \tag{1.17}$$

due to the gradient definition of the velocity now this implies that for such a fluid $\omega = \nabla \times \boldsymbol{v} = \nabla \times (2\nabla\phi) = 0$ thus the flow in general is irrotational, except where the velocity is singular i.e. points where $\psi = 0 \implies \rho = 0$, around these points the circulation can be given as a multiple of 2π

$$\kappa = \oint \boldsymbol{v}.d\boldsymbol{l} = 2\pi l, \tag{1.18}$$

with $l \in \mathbb{Z}$. Noting that we are still in units of $\hbar/m$, this then demonstrates the appearance of quantized vortices with circulations in units of $2\pi\hbar/m$ when the Madelung transformation is considered. The GPE then allows for the formation and propagation of sound waves as already discussed and in the formation of quantized vortices similar to the point vortices considered elsewhere in the current work, said vortices can interact both with each other and with the propagating sound waves in the condensate. Integral to the definition of vortices in BECs using this description is the notion of the healing length

$$\xi = \frac{1}{\sqrt{8\pi na}}, \tag{1.19}$$

this length represents the minimum distance at which the condensate can heal, i.e. the distance at which the condensate grows from a density of 0 to n, where a is the s-wave scattering length. Essentially this represents a minimum length scale of the system, and thus a "resolution" of the BEC. This quantity is relevant for turbulence in particular, providing the size of vortex cores, as it gives the distance from the zero density vortex centre to the density of the surrounding fluid. Vortices coming within range of the healing length typically annihilate, a process that is common throughout quantum turbulence and is key to the development of a coherent condensate.

Corresponding to the equivalency of quantum turbulence to the intriguing quantum-hydrodynamic Euler equations in (1.16), the quantum vortices found in the Hamiltonian formulation of quantum turbulence (using the non-linear Schrödinger equation) from equation (1.18) is found to have a velocity profile

$$\boldsymbol{u}(x,y,z) = \frac{2}{r}\hat{\boldsymbol{\theta}}(x,y,z), \tag{1.20}$$

where r is the separation from the vortex to point (x,y,z) and $\hat{\boldsymbol{\theta}}$ is the azimuthal unit vector [81], also the density according to quantum vortices are found to have the profile

$$\frac{d^2R}{dr^2} + \frac{1}{r}\frac{dR}{dr} - \frac{1}{r^2}R + (1-R^2)R = 0, \tag{1.21}$$

with boundary conditions $R(0) = 0$ and $R(r) \to 1$ as $r \to \infty$ and $R(r) = \sqrt{\rho(r)}$.

Under the assumptions of well-separated initial vortices, and equal numbers of positive vortices to identical negative vortices, it has been found that from these profiles (1.20-1.21) the point vortex model can be derived [81], which directly occurs as a consequence of the point vortex model as weak solutions of the 2D Euler equations such as the quantum hydrodynamic equations (1.16); we now consider the point vortex model proper.

1.4 Point vortex analogy

We now move to the foundation of the current work, namely the "point vortex" model (PVM). The PVM is a particular model of 2D turbulent plane flow, wherein perfectly straight infinitely thin vortex line filaments are perpendicular to the plane in question, thus vortices in such 2D turbulent flow are represented by an assembly of discrete points, and through the Kelvin circulation theorem each point has a constant circulation which can informally be thought to describe the "strength" of a given point vortex. In this way we move from a continuous ever-shifting vorticity distribution which hence implies continuous vortices to a simpler model of vorticity where vortices are represented as simple interacting particles. Hypothetically, the PVM can informally be thought of as a combination of the previously mentioned turbulence approximation methods, with parallel straight vortex filaments being "sliced" perpendicularly

by the plane, hence resulting in a 2D turbulent flow described by the point vortex particles already mentioned. We can thus formulate the motion of such point vortices directly by considering the 3D analogue. As circulation around vortex filaments is constant, it must be the case that circulation around point vortices is constant (a direct consequence of both the Helmholtz theorems and Kelvin's theorem). The velocity field imparted by such point vortices are then also as a result of these vortex filaments, and is thus recoverable by the Biot-Savart law (1.9) by considering a point whose position vector from the vortex filament is perpendicular to the vortex filament itself, this gives the velocity field of an isolated point vortex from th Biot-Savart law as

$$u_\theta = \frac{\Gamma}{2\pi r}, \quad u_r = 0, \quad u_z = 0. \tag{1.22}$$

This is expressed in cylindrical coordinates, i.e. in terms of the radius from the vortex filament $r = \sqrt{x^2 + y^2}$, some angle around the vortex filament $\theta = \tan^{-1}(y/x)$, and position along the vortex filament z equivalent to the z coordinate in Cartesian case. With the cylindrical velocities then defined as $u_\theta = d\theta/dt$, $u_z = dz/dt$ and $u_z = dz/dt$, and Γ some constant considered the strength of the vortex filament (this will be examined later). As $u_z = 0$ this means motion of the particle is constrained to the same plane as result of the vortex filament. If it happens that u_z is not zero such that $u_z = c$, symmetry in z is broken, and point vortex motion in the plane now becomes uniformly translating 3D fluid motion. Here the constant c velocity in the z direction can be thought as a timescale of 2D point vortex motion, and the resulting fluid trajectories around vortex filaments now replicate the Poynting vector of Laguerre-Gaussian modes commonly used in the modelling of optical vortices [82, 83].

From equation (1.22), we also note the angular velocity having finite value at every point in the plane, except for the limiting case where $r \to 0$ and the angular velocity becomes a singularity. Hence, a fluid particle on the 2D follows a circular orbit about the point vortex maintaining the same separation of r. Using (1.3) and the cylindrical coordinate form for ∇, we can then find the vorticity distribution as the curl of the above:

$$\boldsymbol{\omega} = \left[\left(\frac{1}{r}\frac{\partial u_z}{\partial \theta} - \frac{\partial u_\theta}{\partial z} \right), \left(\frac{\partial u_r}{\partial z} - \frac{\partial u_z}{\partial r} \right), \frac{1}{r}\left(\frac{\partial}{\partial r}(r u_\theta) - \frac{\partial u_r}{\partial \theta} \right) \right] = (0,0,0) \quad \text{for } r \neq 0. \tag{1.23}$$

Hence fluid is irrotational as $\boldsymbol{\omega} = 0$ at all points except for where $r = 0$, which is of zero

measure. These correspond to the positions of the point vortices in question, where we have a singularity in the vorticity distribution due to the singularity found in the angular velocity u_θ. At singularities in the angular velocity u_θ we find the vorticity in this case always appears as a scalar field, as ω_z exists as the only vorticity component, i.e. vorticity vectors are perpendicular to the x, y or r, θ plane, and thus motion imparted by this vorticity is restricted to this plane. We can also form the point vortex in question in terms of a Rankine vortex. The equations of motion for a fluid in the presence of a Rankine vortex is given [30]:

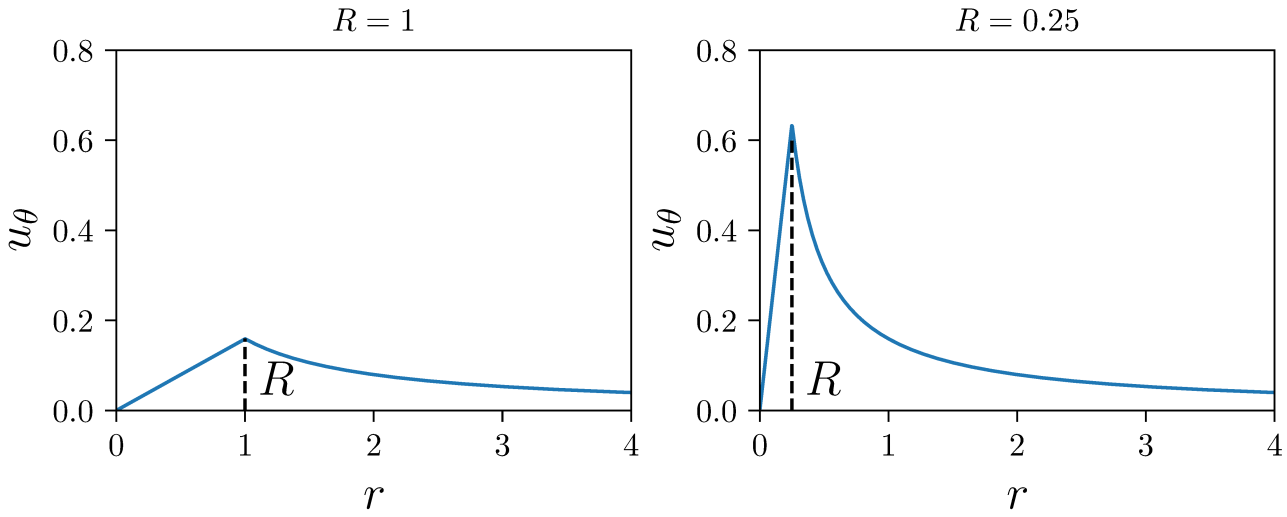

Figure 1.6: Plot of the angular velocity of the fluid with respect to r in the presence of a Rankine vortex with $\kappa = 1$ showing two cases of R, with the point $r = R$ annotated and marked by a dashed line. Note the maximum magnitude at $r = R$ and how this tends to infinity as $R \to 0$.

$$\boldsymbol{u}_\theta = \begin{cases} \frac{\kappa r}{2\pi R^2} & \text{if } r \leq R, \\ \frac{\kappa}{2\pi r} & \text{if } r > R, \end{cases} \tag{1.24}$$

$$\boldsymbol{u}_r = \boldsymbol{u}_z = 0, \tag{1.25}$$

where here we have R representing the radius of the isolated Rankine vortex in question. We observe in figure 1.6 the resulting angular velocity. We see here a solid body rotation proportional to r inside the radius of the vortex, and the angular velocity imparted by a point vortex outside this radius, with maximum velocity at $r = R$; the boundary of the vortex core to the surrounding fluid. Thus, when $R \to 0$, we see the velocity of the point vortex (1.22) being recovered. We also see in figure 1.7 the effect on vorticity of having $R \to 0$, we observe that the vorticity approaches infinity at $R = 0$ hence the point vortex represents a singularity

in the vorticity distribution. Therefore, by considering a fluid flow in terms of point vortices,

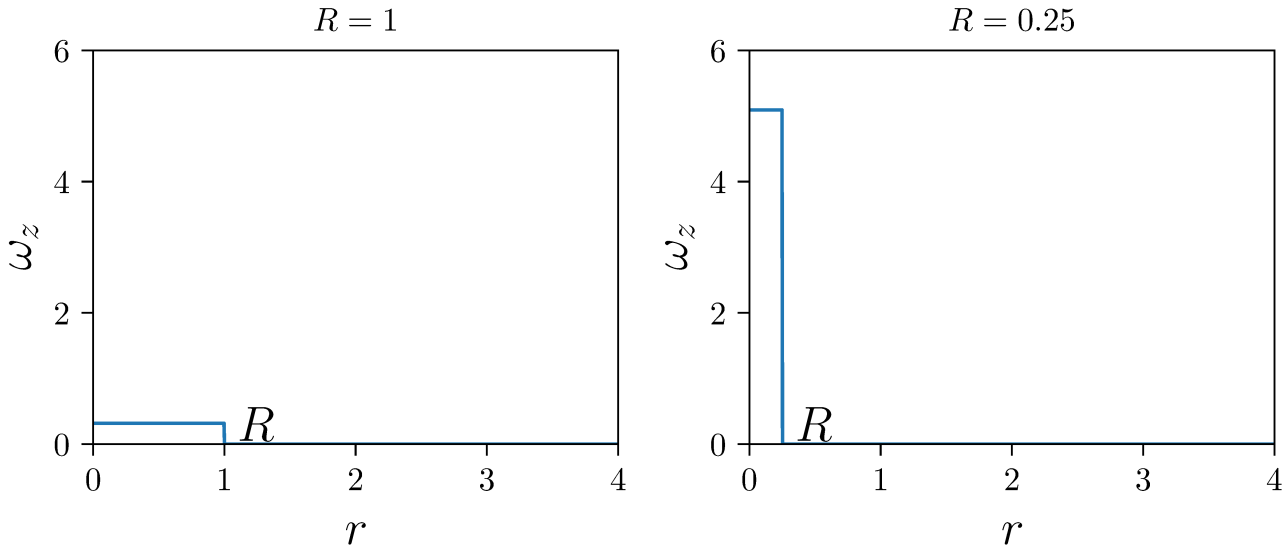

Figure 1.7: Plot of the vorticity of the fluid with respect to r in the presence of a Rankine vortex with $\kappa = 1$ showing two cases of R, with the point $r = R$ annotated and marked by a dashed line.

we are essentially ignoring the structure and evolution of the underlying vorticity distribution in favour of easily approximating the regions of maximum vorticity, usually the vortex cores. Such an approximation of course finds varied success, and the applicability of the point vortex model largely depends upon the particular flows to be considered, however methods involving the point vortex model have found success with a large variety of fluid flows [84, 85, 86]. Clearly, the approximation by point vortices is best used to model cases where vortex width is already very small in comparison to the relative distances of vortices from each other, in order that point vortex dynamics remain faithful to original hydrodynamic vortices as much as possible. In particular the point vortex model has been found to serve a great approximation to quantum turbulence which we will explore later. Now we give some more explicit theory of the point vortex model.

1.5 Basic theory of the point vortex model

We can analyse the dynamics of the system using a Hamiltonian formulation. We start by expressing the equations of motion of the point vortex model as done by Kirchhoff [87]. Here

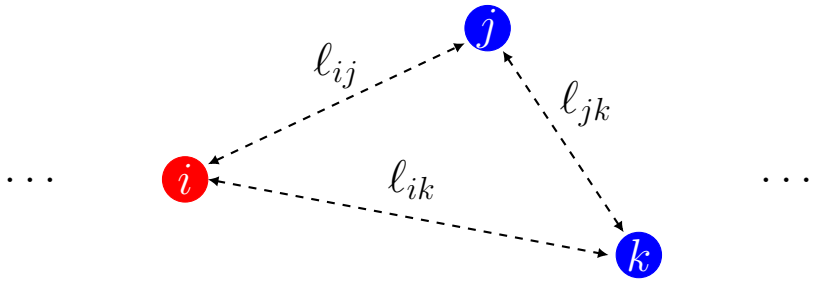

Figure 1.8: Diagram showing the fundamental vortex separations which the equations of motion are defined in terms of, expressed with arbitrary vortices i, j and k. Vortices are coloured to show difference in the sign of circulation possessed by each vortex, and inter-vortex separations are annotated and marked by dashed lines.

$\dot{x}_i$ represents the x velocity of vortex i and $\dot{y}_i$ represents the y velocity of vortex i as such:

$$\dot{x}_i = \frac{d}{dt} x_i(t),$$

where here (x_i, y_i) are the Cartesian x and y coordinates of vortex i and so on for other vortices $i = 1, 2, \ldots, N$ in the system. Note that from here we will use the shorthand $[x_i(t), y_i(t)] = (x_i, y_i)$. First, according to the Helmholtz-Hodge decomposition the fluid velocity of the flow in $\mathbb{R}$ can always be decomposed into two terms, an irrotational scalar velocity potential and a solenoidal vector potential ψ as

$$\boldsymbol{u} = \nabla\phi + \nabla \times \boldsymbol{\psi}, \tag{1.26}$$

taking the curl of this gives

$$\omega = \nabla(\nabla \cdot \boldsymbol{\psi}) - \nabla^2\boldsymbol{\psi} = -\nabla^2\boldsymbol{\psi}, \tag{1.27}$$

where the final equality is a result of the solenoidal (i.e. divergence-free) vector potential. Equation (1.27) gives a Poisson equation, which through standard techniques [88] can be solved in terms of the Green's function $\boldsymbol{\psi} = \int G(\boldsymbol{x} - \boldsymbol{r})\omega(\boldsymbol{r})d\boldsymbol{r}$, with $G(\boldsymbol{x}) = -1/(2\pi)\ln|\boldsymbol{x}|$ and $\boldsymbol{r}$ a point in the plane. Given we now consider a point vortex, we have vorticity defined as discrete singularities in the flow, with a single vortex i at $\boldsymbol{x}_i$ having vorticity distribution $\omega(\boldsymbol{x}) = \kappa_i\delta(\boldsymbol{x_i})$ where here κ_i is the scalar circulation of vortex i. This is often considered the "strength" of the point vortex. According to the definition of circulation (1.18) considered around a single

vortex filament perpendicular to a plane of otherwise irrotational fluid any closed curve in the plane around the vortex filament can be deformed to a circle without changing the value of circulation. Hence, using the velocities defined in (1.22)

$$\kappa = \oint_C \boldsymbol{u} \cdot d\boldsymbol{s} = \oint_{C^*} \boldsymbol{u} \cdot d\boldsymbol{s} = \int_0^{2\pi} \frac{\Gamma}{2\pi r} r d\theta = \Gamma,$$

where C^* is the circle of radius r containing the vortex from deformation of the initial curve (thus velocity tangent to this curve then is given by u_θ), which is possible without loss of generality as $\oint_{C-C^*} \boldsymbol{u} \cdot d\boldsymbol{s} = \int_A \boldsymbol{\omega} \cdot \boldsymbol{n} dS = 0$ due to the area A not containing the vortex and thus vorticity in this region is zero everywhere. Note the above integral of the circulation is independent of the radius of the deformed circle, even as $r \to 0$, thus the vorticity flux due to a point vortex is intrinsic to the vortex itself and does not change based on the curve C considered, and κ is considered the strength of the vortex.

The solution of equation (1.27) as a result of vortex i can then be given

$$\psi_i(\boldsymbol{x}) = -\frac{1}{2\pi} \int \kappa_i \ln |\boldsymbol{x} - \boldsymbol{r}| \delta(\boldsymbol{x_i} - \boldsymbol{r}) dr = -\frac{\kappa_i}{2\pi} \ln |\boldsymbol{x} - \boldsymbol{x}_i|. \tag{1.28}$$

As fluid motion in the point vortex model is purely due to velocity imparted by vortices (in other words the solenoidal potential in equation (1.26)), we have velocity due to this single vortex $\boldsymbol{u} = \nabla \times \psi_i(\boldsymbol{x})$, and therefore since the velocity-vorticity relation is linear the velocity imparted by a system of N point vortices is given as $\boldsymbol{u} = \sum_{i=1}^{N} \nabla \times \psi_i(\boldsymbol{x})$, and finally by taking the curl and examining separate components of $\boldsymbol{u}$ we have the equations of motion found by Kirchoff [87, 34, 37]

$$\dot{x}_i = -\frac{1}{2\pi} \sum_j{}' \frac{\kappa_j y_{i,j}}{\ell_{i,j}^2}, \quad \dot{y}_i = \frac{1}{2\pi} \sum_j{}' \frac{\kappa_j x_{i,j}}{\ell_{i,j}^2}, \tag{1.29}$$

with $x_{i,j} = x_i - x_j$, $y_{i,j} = y_i - y_j$, and with $\ell_{i,j}$ representing the length of the line segment spanning vortex i and vortex j, therefore:

$$\ell_{i,j}^2 = x_{i,j}^2 + y_{i,j}^2. \tag{1.30}$$

These quantities are displayed in figure 1.8. The above equations of motion (1.29) fit Hamilton's

canonical equations [5]:

$$\kappa_i \dot{x}_i = \frac{\partial H}{\partial y_i}, \quad \kappa_i \dot{y}_i = -\frac{\partial H}{\partial x_i}. \tag{1.31}$$

With the Hamiltonian H given by:

$$H = -\frac{1}{4\pi} \sum_{i,j}^{N\prime} \kappa_i \kappa_j \ln(\ell_{i,j}), \tag{1.32}$$

where κ_i represents the circulation of vortex i. Note that here and throughout the remainder of this work we will use the shorthand sum notation given:

$$\sum_{\substack{j=1 \\ i \neq j}}^{N} \sum_{j=1}^{N} = \sum_{i,j}^{N\prime}.$$

It is clear that the above equations of motion are consistent with the Hamiltonian and canonical equations. This then forms the point vortex system in full, so in order to solve the point vortex system we must solve the above equations of motion. It can be observed that the relative dynamics of a particular set up of vortices is the same irrespective of how they are oriented on the plane, i.e. we observe the same relative behaviour regardless of translation or rotation of the system. We use Noether's theorem which states that symmetric properties of the Hamiltonian imply the existence of conserved quantities, where here we refer to Hamiltonian invariance under a transform as a symmetry. Hence, according to Noether's theorem there exists three constants of motion in our system, linear momentum (in the x and y direction) and angular momentum are conserved [89]. These quantities are given as:

$$P = \sum_{i=1}^{N} \kappa_i x_i, \quad Q = \sum_{i=1}^{N} \kappa_i y_i, \quad M = \sum_{i=1}^{N} \kappa_i (x_i^2 + y_i^2). \tag{1.33}$$

We can combine these to form a conservation law that is only dependent upon the relative lengths between vortices as such:

$$R = \frac{1}{2} \sum_{i,j}^{N\prime} \kappa_i \kappa_j \ell_{i,j}^2 \equiv \left(\sum_{i=1}^{N} \kappa_i \right) M - P^2 - Q^2. \tag{1.34}$$

Note also we can define a point that is constant in the fluid, here referred to as the centre of

vorticity $\boldsymbol{x}_\Gamma = (x_\Gamma, y_\Gamma)$, which can be thought of as the unique point in the flow that is the average of vortex positions weighted by the individual vortex circulations. It is easy to make analogies from this to the centre of mass found in classical mechanics, as this is essentially the point vortex equivalent. We define the centre of vorticity mathematically as such:

$$(x_\Gamma, y_\Gamma) = \frac{1}{\sum_{i=1}^{N} \kappa_i}(P, Q), \tag{1.35}$$

note that as both P, Q, and $\sum_{i=1}^{N} \kappa_i$ are invariant with respect to time, the centre of vorticity remains as a fixed point with respect to time.

Summarising, the $N \geq 1$ point vortex dynamics is defined as a $2N$ dynamical system with four conserved quantities, the Hamiltonian and the integrals of motion above. This gives $2N-4$ degrees of freedom. Alternatively, it is possible to define the system in terms of relative motion of vortices, where we examine the vortex separations rather than absolute vortex positions. In the relative length description the system is defined as an $N(N-1)/2$ dynamical system with two constants of motion, the Hamiltonian H and the combined integral of motion R. Such a system of relative lengths has $N(N-1)/2-2$ degrees of freedom, hence whilst a system of $N = 3$ vortices has one degree of freedom when considering the previous coordinate length description and so is integrable, whereas an assembly of vortices with $N > 3$ generally is not [27], making the case $N = 3$ of particular significance.

1.6 Thesis outline

Throughout the current thesis we then will consider the point vortex model against a backdrop of the aforementioned systems of classical and quantum turbulence, in the hopes of developing the preliminary foundation for a larger statistical theory of point vortex motion and of how it may relate to turbulence as a whole. We first speculate that an encompassing theory of arbitrary point vortex motion will be grounded in the fundamental interactions between point vortices and more specifically the interactions of vortex dipoles, Thus in chapter 2 we analyse the effects of these interactions between the fundamental point vortex structures of vortices and dipoles. We first examine the scattering angles and periapsis separations of the dipole-vortex collision; we also extend this by considering the extremum values of dipole separation.

Also analysed here are the dipole-dipole collisions in both integrable and non-integrable cases, including the possibility of larger or smaller dipoles being created through these interactions. We seek to form a complete description of the effects of such interactions such that they may potentially be used to describe the statistical evolution of larger systems in a future work.

In chapter 3 this study is extended into the interactions of vortex clusters, and seek to show why this is important to standard turbulent systems and how the point vortex model relates to them. Beginning with checking the interactions of vortex dipoles with different sizes of rotating vortex clusters, solving for key quantities such as the scattering angles and regimes of dipole creation, we also consider the possibility of approximating large vortex cluster by single point vortices of an equivalent circulation. Later in this chapter the 2D turbulent phenomenon of the inverse energy cascade is considered with respect to the point vortex model, namely how the inverse energy cascade may be realised through the point vortex model.

Lastly, in chapter 4 compressible effects are finally considered. With the dynamics of quantum turbulent systems in mind in particular, the dynamics of a dipole with respect to sound are considered here. Specifically we seek to find evidence for the common notion that a dipole in the presence of sound gradually decreases in size until the quantum phenomenon of vortex "annihilation" is observed (more on this later), and we seek an explanation for why this may occur and under what particular conditions.

Chapter 2

Fundamental collisions of vortex dipoles

2.1 Introduction: dipoles as the agents of point vortex evolution

First we consider the evolution of point vortex systems as a result of the interaction of the fundamental point vortex structures. As discussed, it is often useful to model a continuous vorticity field as a point vortex cloud, especially in the case of BECs, as the point vortex assembly is a very close approximation to quantum vortices in this case. Also point vortex systems constitute weak solutions of the 2D Euler equations [90], another demonstration of the close relationship between 2D classical turbulence and point vortices [43]. The model's usefulness to describe ideal 2D flows arises from the fact that vortices in 2D behave like point-like objects advected by the resulting velocity field. Fundamentally, it is our hypothesis that the vortex gas dynamics of the point vortex system can be characterised as a series of scattering collisions between vortex structures. Indeed, the evolution of a large assembly of point vortices will consist of many smaller interactions but only a few interactions have an actual high/ probability of occurring, and so the effects of these collisions will have the largest degree of importance to dynamics of larger systems, and regarding these we will focus our attention. Here it is argued that of all vortex structures it is the vortex dipole that is most paramount to this picture of basic collisions, and so to the evolution of a large system as a whole.

This relies upon a statistical description of turbulence reduced to the fundamental collisions between vortex structures; as such this could only hold in certain regimes. Firstly it must be assumed in such a system that the width of vortex cores are considerably smaller than the distance between vortices. Whilst in the point vortex model this assumption is easily fulfilled due to infinitesimally small vortex widths, in real physical systems vortices have finite width, so this condition must hold in order that true dipoles and other vortex structures can form. As corollary to this the vortices in the system must be dilute; i.e. the number of vortices in the system should not be too high, again in order that vortex structures can form and interact instead of a many-vortex interaction being observed. Also, through our investigation we will only consider vortices of identical circulation, therefore in order to faithfully replicate the effects of real systems with our model it must be that this holds as much as is possible (an example of this would be the quantized vortices in quantum turbulence).

We then consider vortex dipoles interacting with other vortex structures within the fundamental interactions in this chapter. In section 2.2 we begin investigating the scattering of a dipole via a third isolated vortex and consider the dipole periapsis during the scattering process. We extend this study to the four vortex system of two interacting dipoles in section 2.3 in both the integrable and non-integrable cases to examine the non-trivial properties of the dipole dynamics during evolution.

2.2 Three vortex system: dipole-vortex collisions

The most basic interaction of a dipole with another vortex structure that can occur in the point vortex model is that of a dipole with a single isolated point vortex, the interaction of the two simplest vortex structures other than the trivial $N = 2$ cases of a vortex-vortex and vortex-anti-vortex (i.e. a dipole). Although this in theory represents the simplest vortex structure interaction, especially compared to the interactions considered later in this chapter, when considering turbulent flows composed of a dilute system of point vortices, it can be speculated that this should be the most common interaction due to comprising the simplest interaction constituents possible (a dipole and a vortex) and so this is the most important in terms of evolution of larger point vortex systems. In theory this interaction is then the most likely to occur and so the dynamics of this interaction is of prime importance to the evolution

of larger systems.

Hence we here consider the interaction of a vortex dipole with a lone vortex with circulation of the same magnitude of the constituent dipole vortices. This is a specific case of the more general three vortex motion that has been shown to be integrable, and has been characterised in both the cases of identical circulations by Novikov [28] and arbitrary circulations by Aref [5]. Both gave a phase space analysis of said three vortex interactions and examined certain possible interactions in such systems. Aref in particular conducts a basic study into this three vortex assembly, wherein the scattering angles for the dipole-vortex collision are given and a region of periodic motion is briefly mentioned and investigated. Our interest is in the examination of the particular three vortex interaction of a vortex dipole interacting with third isolated point vortex that has thus far not been developed in great detail. We will briefly review and follow their mathematical analysis, with a full derivation of the scattering angle of the dipole (with an unseen mistake corrected) to be given. Also, new results on the evolution of the dipole size during interaction will be given in terms of the Aref formalism.

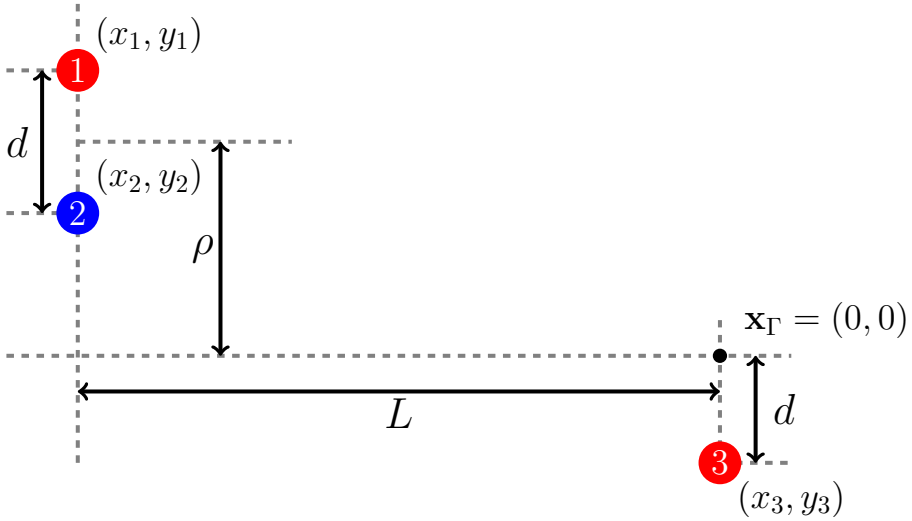

Figure 2.1: The initial setup of the dipole-vortex interaction. The red circles indicate positions of the positive circulation κ point vortices, while the blue circle indicates the negative circulation $-\kappa$ point vortex, and the particular numbering of vortices chosen is marked on each vortex. The parameters defining the system d, ρ, L are annotated and marked as solid lines, with vortex positions and the centre of vorticity x_Γ also being annotated.

We consider an initial vortex dipole propagating towards a lone point vortex situated in an infinite 2D domain, i.e. $(x_i, y_i) \in \mathbb{R}^2$ represents the position of vortex i with $i = 1, 2, 3$. The dipole-vortex arrangement can then be fully characterised by the setup depicted in figure 2.1. Vortices 1 and 2 are oppositely signed vortices of equal strength forming the dipole with circu-

lations $\kappa_1 = -\kappa_2 = \kappa > 0$, this dipole is situated a horizontal distance $L \in \mathbb{R}$ away from the isolated point vortex 3 with circulation $\kappa_3 = \kappa$. We limit ourselves to vortices with circulations of equal magnitude to keep our analogy with quantum vortices in Bose-Einstein condensates. Vortices 1 and 2 of the vortex dipole are a vertical distance $d \in \mathbb{R}$ from each other, and we define the impact parameter $\rho \in \mathbb{R}$ quantifying the vertical distance from the midpoint of the vortex dipole to the centre of circulation which we set as the origin of our coordinate frame $\mathbf{x}_\Gamma = (0, 0)$. As the initial position of each vortex in the system can be described in terms of these initial parameters, the conserved quantities are fixed in terms of these parameters, so the Hamiltonian H gives

$$H = -\frac{\kappa^2}{2\pi} \ln\left(\frac{l_{13}}{l_{12}l_{23}}\right) = -\frac{\kappa^2}{4\pi} \ln\left\{\frac{L^2 + \left(\rho + \frac{3d}{2}\right)^2}{d^2\left[L^2 + \left(\rho + \frac{d}{2}\right)^2\right]}\right\} \underset{L\to\infty}{\to} \frac{\kappa^2}{4\pi} \ln\left(d^2\right).$$

If vortices are initialised too close together, the three vortices will interact immediately, and we will observe an effective three vortex interaction that does not correspond to proper dipole-vortex dynamics. Therefore, to ensure a proper propagation of the initial dipole we must consider the interaction in the limits of $d, \rho \ll L$ to ensure that initially the dipole is unaffected by the presence of the third isolated vortex, and so the dipole can propagate for some time until interaction takes place and a true collision is observed, rather than a full three vortex interaction when $t = 0$. We take the limit as $L \to \infty$ which gives the final equality here. At this limit the initial position of the dipole is infinitely isolated from the stationary vortex, thus the dipole-vortex interaction makes no contribution to the Hamiltonian, the value of the Hamiltonian will solely be due to the isolated dipole (as a stationary vortex has no energy contribution) and thus the Hamiltonian of the dipole-vortex collision converges to the Hamiltonian of a propagating dipole as $L \to \infty$ as L becomes very large.

The linear and angular momentum are also given in terms of these initial parameters

$$\mathbf{P} = (0, 0), \qquad M = \kappa(d^2 + 2\rho d),$$

leading to the conserved value of R given by

$$R = \kappa^2(d^2 + 2\rho d), \tag{2.1}$$

where we have used the total circulation $\sum_i \kappa_i = \kappa$. It is important to note that as the three lengths between the vortices form a triangle, we must also have the inter-vortex separations satisfying the following triangle inequalities

$$l_{12} \leq l_{13} + l_{23}, \qquad l_{13} \leq l_{12} + l_{23}, \qquad l_{23} \leq l_{12} + l_{13}. \tag{2.2}$$

According to the analysis of Aref there are two types of interaction possible in this case, depending upon the magnitude of the impact parameter relative to the dipole separation d. Given ρ is sufficiently large compared to the initial separation d, the dipole propagates past vortex 3 at a large enough separation such that the initial dipole persists once interaction is complete and will only acquire a slight deflection in the direction of propagation due to the far field effects of the isolated vortex, this phenomenon will hence from here be referred to as *direct scattering*. Alternatively given that ρ is small comparable to d, the dipole approaches sufficiently close to the lone vortex 3 such that an exchange in vortices takes place between the positive vortices 1 and 3, leading to a new dipole being formed between vortices 2 and 3 and propagating off to infinity with vortex 1 remaining as the final stationary vortex. This process will hence be titled *exchange scattering*. The two distinct interaction types are then concretely differentiated by the particular vortices forming the final dipole as $t \to \infty$. Through the dynamics there are two key points in time which we consider important. *The exchange point* is the moment in time in which the two positive vortices have exactly equal separations from the anti-vortex and we have $l_{12} = l_{23}$ at this point. At this point the initial positive dipole-vortex becomes the isolated vortex and vice versa. We also define the important *critical point* as the point in time during the evolution in which the minimum separation between positive vortices is reached.

This point is of particular interest as this can be considered the point during the interaction during which the dipole is closest to the isolated vortex, and so it is the point during the interaction at which the strongest effects will occur. By definition, we can then determine the critical point exactly by computing the critical values of the differential equation (1.29). The other inter-vortex separations are also of particular interest at this point, as this may provide clues towards when more interesting interactions occur in more complicated interactions, for example annihilation in quantum turbulence. We represent these lengths as l^*_{ij}. Because of

the simple nature of the dipole-vortex collision, the exchange point and the critical point occur simultaneously, but in more complicated collisions involving more than three point vortices this may not be the case. In the case of direct scattering, the critical point of the interaction arises when all three point vortices become collinear with the value of the area of the triangle spanned by the three vortices A_{123} vanishing, as either $l_{13} = l_{12} + l_{23}$ when $\rho > 0$ or $l_{23} = l_{12} + l_{13}$ when $\rho < 0$. At the interface between the boundaries of direct and exchange scattering we expect that the three vortices will be trapped in a bounded state of constant rotation as shown by Aref [5], this corresponds to the negative vortex being trapped between the two regimes of direct and exchange scattering; the impulse imparted by each positive vortex is exactly equal and so the anti-vortex remains locked in interaction with both, with all three vortices rotating about the center of circulation in an equilateral triangle configuration.

Here we will extend the mathematical formalism using dimensionless variables found in works of Aref and Novikov [28, 5], we use variables defined as the ratio of squares of the inter-vortex lengths with the newly defined parameter C, defined by Aref as the timescale of relative vortex motion [5]. This is derived from the previous conserved quantity R (2.1),

$$R = \kappa^2 l_{13}^2 - \kappa^2 l_{12}^2 - \kappa^2 l_{23}^2 = -3\kappa^3 C, \tag{2.3}$$

such that $C = -R/(3\kappa^3)$. Thus, we rescale the inter-vortex lengths resulting in variables b_i for $i = 1, 2, 3$ representing dimensionless vortex separations. This then results in

$$b_1 = \frac{l_{23}^2}{\kappa C}, \qquad b_2 = -\frac{l_{13}^2}{\kappa C}, \qquad b_3 = \frac{l_{12}^2}{\kappa C}, \tag{2.4}$$

also from the geometric constraints in 2.2 the variables b_i must satisfy the constraint $b_1^2 + b_2^2 + b_3^2 \leq 2(b_1 b_3 - b_1 b_2 - b_2 b_3)$. The b_i variables defined in this way constitute a set of generalized coordinates that must satisfy the geometric constraint $b_1 + b_2 + b_3 = 3$. Similarly, we can define the non-negative quantity θ in terms of the dimensionless variables b_i, this represents the dimensionless Hamiltonian as the l variables in the original definition are shifted into dimensionless b space, and so constant quantities of θ

$$\frac{|b_2|}{b_1 b_3} = \kappa |C| \exp\left(-\frac{4\pi H}{\kappa^2}\right) = \theta, \tag{2.5}$$

then represent trajectories in phase space; varying θ thus gives different dynamics in real space. To examine the motion of the three vortex collision we express the vortex separation equation of motion (1.29) in terms of these dimensionless variables. In particular the equation of motion of the variable b_2 is of interest, as it is this variable that expresses the dimensionless separation of the two positive vortices. As these vortices can never be a part of the same dipole one must always remain as the stationary vortex once the interaction is complete (which positive vortex in particular is left over depends upon whether we have direct or exchange scattering). Hence, the equation of motion of the dimensionless b_2 variable can be used to encapsulate the dynamics of the interaction as a whole.

Using the evolution equation for the relative vortex motion (1.29), the definition of the dimensionless variables b_1, b_2, b_3 (2.4), and the conservation laws of the point vortex interaction, one can show that

$$\dot{b}_2 = \left(-\frac{1}{C}\right)\frac{2}{\pi}\kappa_2\epsilon_{ijk}A_{123}\left(\frac{1}{l_{23}^2}-\frac{1}{l_{13}^2}\right) = \pm\frac{2}{C^2\pi}A_{123}\left(\frac{b_3-b_1}{b_1b_3}\right), \tag{2.6}$$

where A_{123} is the area of the triangle spanned by the three vortices and ϵ_{123} is the Levi-Civita symbol that indicates the orientation of the labelling of the triangle vertices. The area A_{123} can also be expressed in terms of the vortex separations l_{12}, l_{13}, l_{23} by Heron's formula $A_{123} = \sqrt{r(r-l_{12})(r-l_{23})(r-l_{13})}$ where $r = (1/2)(l_{12}+l_{13}+l_{23})$. This reduces to $A_{123} = (1/4)\sqrt{4l_{12}^2l_{23}^2-(l_{12}^2-l_{13}^2+l_{23}^2)^2}$. By replacing with the dimensionless b_1, b_2, b_3 variables and using the constraints $b_1+b_2+b_3 = 3$ and (2.5) the area A_{123} can be expressed in terms of variable b_2 only:

$$A_{123} = \frac{1}{4}\sqrt{4C^2b_1b_3-(Cb_3+Cb_2+Cb_1)^2} = \frac{C}{2\sqrt{\theta}}\sqrt{|b_2|-\frac{9}{4}\theta}.$$

In the same manner, the $(b_3-b_1)/b_1b_3$ term appearing in equation (2.6) can be expressed as

$$\begin{aligned}\frac{b_3-b_1}{b_1b_3} &= \frac{\theta}{|b_2|}\sqrt{(b_3-b_1)^2} = \frac{\theta}{|b_2|}\sqrt{(b_1+b_2+b_3)^2-b_2^2-4b_1b_3-2b_1b_2-2b_2b_3},\\ &= \frac{\theta}{|b_2|}\sqrt{(3-b_2)^2-4\frac{|b_2|}{\theta}}.\end{aligned}$$

Combining these results together gives us the dynamical equation for b_2 in terms of the variable

b_2 alone

$$\dot{b}_2 = \pm\frac{2}{C^2\pi}A_{123}\left(\frac{b_3 - b_1}{b_1 b_3}\right) = \pm\frac{\sqrt{\theta}}{C\pi b_2}\sqrt{(|b_2| - \frac{9}{4}\theta)\left[(3-b_2)^2 - 4\frac{|b_2|}{\theta}\right]}. \tag{2.7}$$

Note the expression under the radical is a cubic in b_2, if b_2 is equal to the roots of this cubic we have that $\dot{b_2} = 0 \implies \dot{l_{13}^2} = 0$ and thus if b_2 ever reaches these values we have reached the critical point in the dynamics and so will observe the most interesting dynamics. These roots have an important correspondence to real space point vortex dynamics, thus we label them as such; for the case of $C > 0$ we give

$$\alpha(\theta) = -\frac{9}{4}\theta, \quad \beta(\theta) = -\frac{1}{\theta}\left(1 - \sqrt{1-3\theta}\right)^2, \quad \gamma(\theta) = -\frac{1}{\theta}\left(1 + \sqrt{1-3\theta}\right)^2, \tag{2.8}$$

and for the case that $C < 0$ roots are given as $\bar{\alpha}(\theta) = \alpha(-\theta)$ and so on, i.e.

$$\bar{\alpha}(\theta) = \frac{9}{4}\theta, \quad \bar{\beta}(\theta) = \frac{1}{\theta}\left(1 - \sqrt{1+3\theta}\right)^2, \quad \bar{\gamma}(\theta) = \frac{1}{\theta}\left(1 + \sqrt{1+3\theta}\right)^2. \tag{2.9}$$

Then we can re-express the b_2 equation of motion in terms of these roots.

$$\dot{b}_2 = \begin{cases} \pm\dfrac{\sqrt{\theta}}{C\pi b_2}\sqrt{(\alpha - b_2)(\beta - b_2)(\gamma - b_2)} & \text{for } C > 0, \\ \\ \pm\dfrac{\sqrt{\theta}}{C\pi b_2}\sqrt{(b_2 - \bar{\alpha})\left(b_2 - \bar{\beta}\right)(b_2 - \bar{\gamma})} & \text{for } C < 0. \end{cases} \tag{2.10}$$

The functional relationships of the above roots (2.8) and (2.9) are plotted verses θ in figure 2.2. One should interpret the roots of (2.10) as follows: as $t \to -\infty$ the initial setup in real space is of an isolated dipole infinitely far away from a third isolated point vortex, the dipole and the vortex are not interacting here, and we have in effect a vortex dipole completely isolated from the stationary point vortex. In the case of $C > 0$, $b_2(-\infty) = -\infty$, while for $C < 0$, $b_2(-\infty) = \infty$ where the value of C depends on the initial configuration (and hence value of the conserved quantity θ or in real space the impact parameter ρ). As the system evolves, the value of b_2 reduces continuously in magnitude (representing the dipole approaching the stationary vortex), this continues until it reaches the first root of (2.10) at which point it undergoes the corresponding scattering process as dictated by the initial condition. As can be determined

from figure 2.2, for $C > 0$ and $\theta < 1/3$ the first root is $b_2 = \gamma$ or for $C < 0$ and $\theta < 8/3$, $b_2 = \bar{\gamma}$ meaning that the condition $l_{12} = l_{23}$ is satisfied, and the three vortex configuration undergoes an exchange scattering process. If the value of θ is $\theta > 1/3$ for $C > 0$ or $\theta > 8/3$ for $C < 0$ then the first critical point reached by b_2 is either α (for $C > 0$) or $\bar{\alpha}$ (for $C < 0$) respectively. At these values, the vortex configuration reaches a physical boundary equivalent to the limit of the triangle inequality, i.e. either $l_{23} = l_{12} + l_{13}$ for $C > 0$ or $l_{13} = l_{12} + l_{23}$ for $C < 0$ meaning that the three vortices are in a collinear configuration and a direct scattering process occurs. From

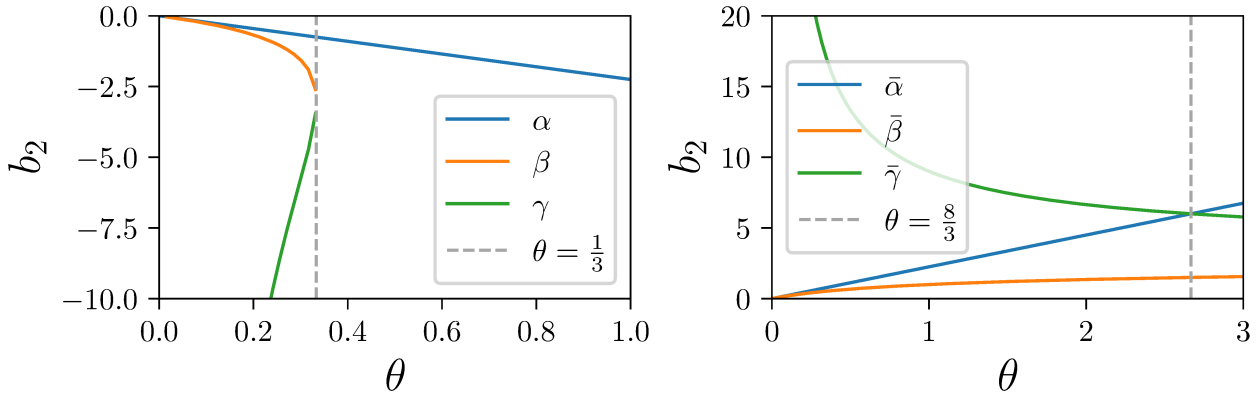

Figure 2.2: (Left) Plot of the roots α, β, γ against θ for $C > 0$ of (2.10). Roots β and γ become imaginary for $1/3 < \theta$, with this transition marked as a grey dashed line. (Right) Roots $\bar{\alpha}, \bar{\beta}, \bar{\gamma}$ for $C < 0$. All roots are positive, where $\bar{\gamma}$ is the largest root until $8/3 < \theta$ in which root $\bar{\alpha}$ becomes greatest. The region boundary again is marked by a grey dashed line.

consideration of which root is encountered first by the variable b_2 (i.e. the root of the largest magnitude) from the initial state defined at $t \to -\infty$ we can determine the boundary of the scattering conditions with respect to the parameter θ or alternatively ρ/d. This is displayed in table 2.1. This of course assumes that once a root b_2^* is reached the magnitude of b_2 will then begin increasing as the dipole propagates off, due to the simplicity of the three vortex interaction this will always be the case, as according to figure 2.2 in order for b_2 to continue decreasing in magnitude an exchange scattering and direct scattering process would occur in the same interaction, an impossibility (or in the case that $C > 0$, $\theta > 1/3$ we have $b_2 \to 0$, an obvious impossibility as this implies $l_{12} \to 0$).

Note also that the roots β and $\bar{\beta}$ also correspond to what would be considered an exchange scattering process where at the critical point $l_{12} = l_{23}$, the other two sets of roots are always greater in magnitude than these, and so b_2 will always reach an alternative root and propagate

off to infinity before this root is reached. The roots β, $\bar{\beta}$ correspond to a region of bounded periodic motion achievable by initialising the vortices in proximity, thus these dynamics can not generally be reached when considering a dipole-vortex setup, except in the special cases where $\theta = 1/3$, $C > 0$ and $\theta = 8/3$, $C < 0$ where $\beta = \gamma$ and $\bar{\beta} = \bar{\gamma}$ respectively. In these cases the point vortices form a quasi-stable equilateral triangle or collinear structure that exhibits rigid-body rotation about the center of circulation (confirmed by our numerical computations).

Table 2.1: Parameter ranges of both ρ, d and θ corresponding to scattering types of the three regions of the three vortex interaction defined in figure 2.1. Region II has been split into two subregions defined by the sign of C, although the same scattering type is observed in these regions.

Region	C Range	θ Range	Impact Parameter Range	Scattering Type
I	$C > 0$	$1/3 < \theta < \infty$	$-\infty < \rho/d < -1$	Direct
IIa	$C > 0$	$0 < \theta < 1/3$	$-1 < \rho/d < -1/2$	Exchange
IIb	$C < 0$	$0 < \theta < 8/3$	$-1/2 < \rho/d < 7/2$	Exchange
III	$C < 0$	$8/3 < \theta < \infty$	$7/2 < \rho/d < \infty$	Direct

2.2.1 Dipole-vortex scattering

Aref [5] used the formalism presented above to determine analytical results for the dipole scattering angle after interaction with the third isolated point vortex in the case of circulations $\kappa_1 = \kappa_2 = -\kappa_3 = 1$. We derive the scattering angle in appendix A.1 including correcting some previous errors in Aref's calculations. The integrals in question are not reducible to elementary functions but instead will take the form $\int R(x, y)dx$, where y^2 is a cubic in x and $R(x, y)$ is a rational function. This is what is known as an elliptic integral, a full treatment and explanation of which is given by Abramowitz [91]. These integrals in question can not be expressed in terms of elementary functions, and must instead be reduced to simpler forms to make for easier computation. Briefly we can summarise this process as such; first consider the polar angles of the vortices ϕ_i for $i = 1, 2, 3$ defined as the angle spanned from the horizontal to the line segment joining the center of circulation and the vortex i, then we define the scattering

angle of vortex 2 as

$$\Delta\phi_2 = \lim_{t\to\infty}\phi_2(t) - \lim_{t\to-\infty}\phi_2(t) = \int_{-\infty}^{\infty}\dot{\phi}_2 dt = \int_{L_1}^{L_2}\dot{\phi}_2\left(\frac{1}{\dot{b}_2}\right)db_2,$$

here the last equality arises from the transformation from physical space to our phase space description, where the limits L_1, L_2 depend upon the particular dynamics of the interaction, in other words what region of table 2.1 we are considering will change the dynamics of the variable b_2 and thus provide different values for L_1, L_2. The equation of motion for the polar vortex angle can be found simply through cosine laws for vortex separations

$$\dot{\phi}_2 = \frac{\theta}{4\pi C}\frac{9 - 3b_2 + \frac{4}{\theta}|b_2|}{(6-b_2)|b_2|}, \tag{2.11}$$

see Appendix A or the original derivation by Novikov for details [28]. By substituting the equations of motion for ϕ_2 (2.11) and b_2 (2.10) into the above scattering angle integral we then attain the scattering angles in each case in the form of $\Delta\phi_2 = \int_{L_1}^{L_2}[\chi(b_2)/y]db_2$, where $\chi(b_2)$ is a rational function of b_2 and $y = \sqrt{(b_2-\alpha)(b_2-\beta)(b_2-\gamma)}$ if $C > 0$ or $y = \sqrt{(b_2-\bar{\alpha})\left(b_2-\bar{\beta}\right)(b_2-\bar{\gamma})}$ if $C < 0$, thus by the definition given above we have recovered the scattering angles as elliptic integrals. Through established theory of elliptic integrals [91], these can be reduced to some linear combination of the basic forms

$$\int_{L_1}^{L_2}\frac{db_2}{y}, \qquad \int_{L_1}^{L_2}\frac{b_2}{y}db_2, \qquad \int_{L_1}^{L_2}\frac{(b_2)^2}{y}db_2, \qquad \int_{L_1}^{L_2}\frac{db_2}{(b_2-c)y},$$

with c some constant. Through simple substitutions such as those found in Labahn and Mutrie [92] we finally reduce the scattering angles into linear combinations of Legendre's complete normal forms of the first and third kind

$$K(k) = \int_0^{\pi/2}\frac{d\phi}{\sqrt{1-k^2\sin^2\phi}}, \qquad \Pi(n,k) = \int_0^{\pi/2}\frac{d\phi}{(1-n\sin^2\phi)\sqrt{1-k^2\sin^2\phi}}.$$

The above Legendre integrals are often considered obsolete compared to the more modern Carlson symmetric forms [93]. However, to be consistent with the work of Aref and due to availability in numerical libraries, we use the Legendre normal forms here. The above procedure is repeated in each case such that four expressions for the scattering angle in each region is

given (A.4) and are plotted in 2.3 and compared with angles computed using direct numerical simulation of the point vortex model. Our definition of the scattering angle is only defined for modulo 2π, however in figure 2.3 we have unravelled the scattering angle to better display the meaning of the asymptotes. Positive values of $\Delta\phi_2$ indicate an anti-clockwise deflection. We observe excellent agreement between the theoretical results given by (A.4) (black dashed curve) and the numerical data (red circles).

For large values of the normalized impact parameter ρ/d we observe minimal deflection of the dipole as expected. As the impact parameter shrinks, corresponding towards a more direct propagation of the dipole towards the isolated vortex we observe two clear asymptotes, one between regions I and IIa and another between regions IIb and III indicating the boundaries between the direct and exchange scattering regions. The asymptotes correspond to locking of the three vortices into either an equilateral triangle or a quasi-stable collinear structure that undergoes continual rotation - hence the tendency towards an infinite scattering angle. Numerical instabilities in our simulations lead to the locked configurations eventually becoming unstable and so the numerical results become extremely sensitive in regions close to the asymptotes; as the locked rotating configurations are unstable equilibria, the slightest perturbation can result in the breakdown on the usual rotating dynamics, and as the vortex 2 continues to rotate in these regions we find the numerical error compounding in these regions, thus the numerical error in our simulations as compared to theory is the greatest approaching these rotating asymptotic regions (it is still very small however). Region IIa and IIb correspond to exchange scattering where we observe an almost $-\sinh$ like behaviour. We note that figure 2.3 slightly differs from what was originally presented in [5] (figure 11) due to a sign error made in that paper. These calculations have been corrected and can be found in appendix A.1.

2.2.2 Dipole size and the periapsis

As well as quantifying the angle of deflection of a dipole with a third vortex, it is also important to examine the dipole size during its propagation. Over the course of a dipole interaction the distance from the dipole-vortex to the dipole anti-vortex may either shrink or grow due to the effects of interacting with the third vortex. We are then interested in finding the degree to which the dipole may grow or shrink due to the effect of the third vortex. This is an essential piece of

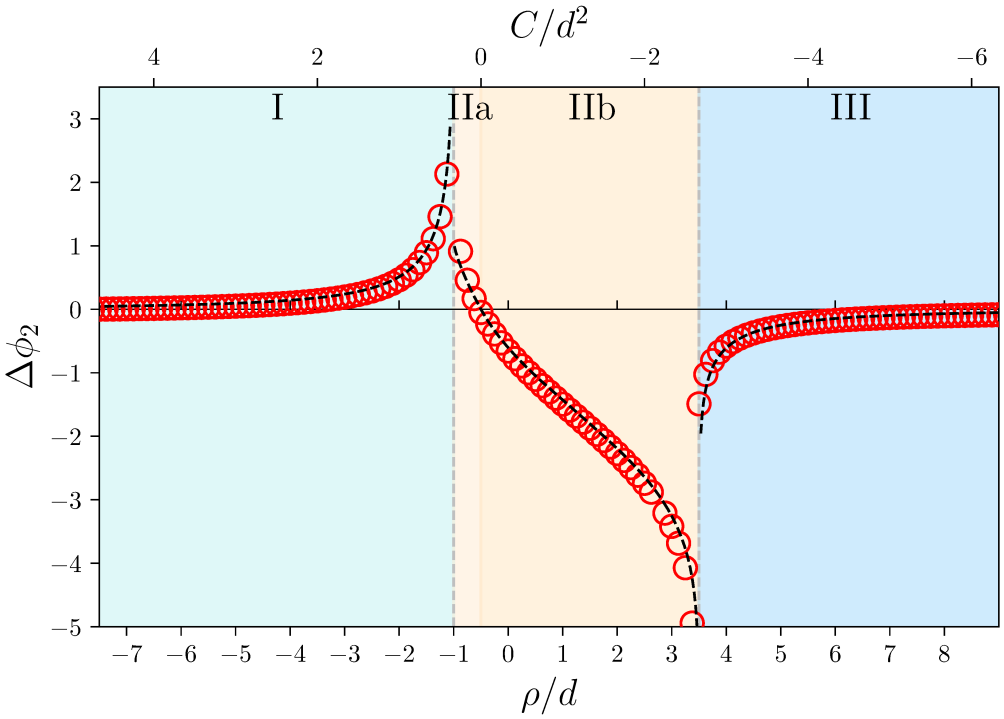

Figure 2.3: Unwinded scattering angle of the negatively signed point vortex in the dipole-vortex interaction with respect to the normalized impact parameter ρ/d. Numerical results using the point vortex model are given by red circles, while the theoretical predictions of (A.4) are plotted as the black dashed curve. Also marked are the regions corresponding to different scattering processes as presented in table 2.1.

dynamical information if one draws a connection of point vortices to quantum vortices in Bose-Einstein condensates because quantum vortices can undergo a process of annihilation if they proceed to interact within a critical distance to each other. Approximately this occurs at the order of the quantum vortex core radius or healing length $\xi \sim 1\mu m$. Consequently, the process of vortex annihilation leads to the reduction of the number of vortices and the generation of sound in Bose-Einstein condensates [94], which can dramatically change the vortex topology of the turbulence. Thus, the minimum dipole distances in the point vortex model may suggest a mechanism for this.

Subsequently, in this subsection, we will focus on two main quantities: the periapsis – a term borrowed from celestial mechanics meaning the closest point of an orbiting body to the object it is orbiting, and the final dipole size post-interaction. In the case of the dipole-vortex interaction considered here, the final dipole size (post-interaction at $t \to \infty$) will trivially equal d due to energy conservation of the system (we will see later that this is not necessarily the case when the number of vortices exceeds three). The periapsis is the point of closest approach

of the dipole to the isolated vortex. As stated before the distance from the dipole to vortex 3 can fully be encapsulated by the dimensionless variable b_2, therefore the periapsis is equivalent to the roots of (2.10), and from this we can determine the inter-vortex lengths at the periapsis, as these correspond to critical points of the differential equation for $\dot{l}_{ij}^2$ for all the inter-vortex distances. Due to the simplicity of the dipole-vortex interaction the minimum/maximum of the dipole will occur at this periapsis, depending on the interaction region we can then compute the local minimum or maximum inter-vortex lengths of the formed dipole.

When considering region I, as this is a direct scattering region the vortices will become collinear at the periapsis. A simple calculation shows that the collinearity condition in this region $l_{23} = l_{12} + l_{13}$ is equivalent to when the variable $b_2 = \alpha$, although this is slightly trivial as α is the only real root in this case, so it is obvious that the collinearity condition occurs at this root. Regions IIa and IIb are regions of exchange scattering so at the periapsis the distances between the negative point vortex and the two positive vortices are equal, i.e. $l_{12} = l_{23}$. It can then be shown this is equivalent to either of the roots γ or β for $C > 0$, and as γ is the most negative it is this root that corresponds to the exchange condition in dipole-vortex scattering (as b_2 will reach this value first). The same reasoning applies when $C < 0$ only here the exchange scattering occurs when $b_2 = \bar{\gamma}$ instead. Finally, for region III, the scattering process is direct scattering and the first root reached by b_2 is $b_2^* = \bar{\alpha}$ (the largest of three real roots) and this is indeed equivalent to the collinearity condition applied by this region $l_{13} = l_{12} + l_{23}$.

Given this b_2 value at the periapsis and the relations between the b variables (and therefore the real space l vortex separations) it is then possible to find the inter-vortex lengths at the periapsis. It is necessary also to give careful consideration to the sign of the resulting square roots, but once this is done each length at the periapsis can be expressed in terms of the parameter ρ/d and are given in the limit $\rho \ll L$ and $d \ll L$ in table 2.2. The analytical result is then compared to direct numerical simulations of the point vortex model. Results are displayed in figure 2.4 where excellent agreement is observed partly due to the analytical results given in table 2.2 being $O(\rho^2/L^2)$ and $O\left(d^2/L^2\right)$ accurate in the limit $\rho, d \ll L$. The values of the periapsis can be interpreted to give the minimum or maximum size of the vortex dipole. In figure 2.5 we plot the global minimum and maximum lengths of the vortex dipole pre- and post-interaction defined at the critical point t^*. The blue and red dashed lines are

Table 2.2: Vortex separations at the periapsis of the three vortex scattering setup given in terms of the impact parameter ρ and the initial dipole separation d for each region of interaction. Values are leading order results taken in the limits of initial far dipole separation: $\rho \ll L$ and $d \ll L$.

Region	l_{12}^*	l_{13}^*	l_{23}^*
I	$d\left(\frac{1}{4}+\frac{1}{2}\frac{\rho}{d}-\frac{1}{2}\sqrt{-\frac{7}{4}-3\frac{\rho}{d}+\frac{\rho^2}{d^2}}\right)$	$d\left(-\frac{\rho}{d}-\frac{1}{2}\right)$	$d\left(\frac{1}{4}+\frac{1}{2}\frac{\rho}{d}+\frac{1}{2}\sqrt{-\frac{7}{4}-3\frac{\rho}{d}+\frac{\rho^2}{d^2}}\right)$
IIa	$d\sqrt{1+\sqrt{2\left(1+\frac{\rho}{d}\right)}}$	$d\left(1+\sqrt{2\left(1+\frac{\rho}{d}\right)}\right)$	$d\sqrt{1+\sqrt{2\left(1+\frac{\rho}{d}\right)}}$
IIb	$d\sqrt{1+\sqrt{2\left(1+\frac{\rho}{d}\right)}}$	$d\left(1+\sqrt{2\left(1+\frac{\rho}{d}\right)}\right)$	$d\sqrt{1+\sqrt{2\left(1+\frac{\rho}{d}\right)}}$
III	$d\left(\frac{1}{4}+\frac{1}{2}\frac{\rho}{d}-\frac{1}{2}\sqrt{-\frac{7}{4}-3\frac{\rho}{d}+\frac{\rho^2}{d^2}}\right)$	$d\left(\frac{\rho}{d}+\frac{1}{2}\right)$	$d\left(\frac{1}{4}+\frac{1}{2}\frac{\rho}{d}+\frac{1}{2}\sqrt{-\frac{7}{4}-3\frac{\rho}{d}+\frac{\rho^2}{d^2}}\right)$

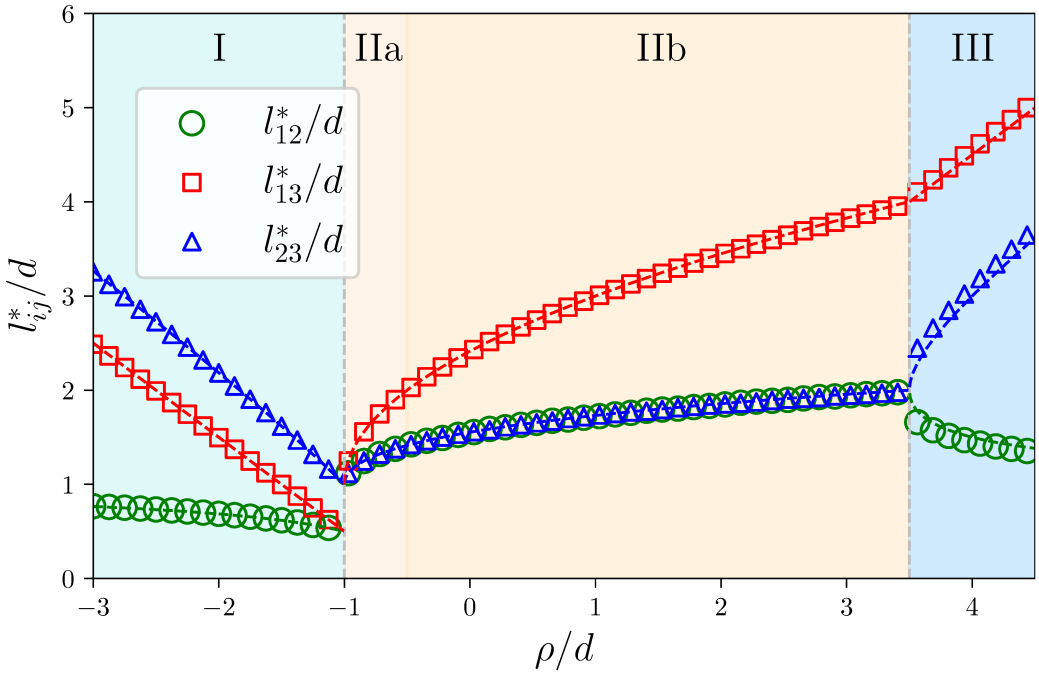

Figure 2.4: Numerical results compared with theoretical predictions of the critical lengths in the dipole-vortex interaction with respect to the normalized impact parameter ρ/d. Dashed lines represent the theoretical predictions of each length determined by the critical points of (1.29). Markers represent the numerical results for the corresponding lengths as indicated by the legend. Note the asymptotic cases at $\rho/d = -1$ and $\rho/d = 7/2$ corresponding to rigid-body motion.

numerical measurements, but agree with the theoretical critical inter-vortex distances presented in table 2.2 and verified in figure 2.4. We observe that the two figures are identical as the critical values of the dipole size are defined either at the initial or end states $= d$ or at the critical point t^*. Note that in region II, post-interaction the dipole is composed of vortex 2 and 3. What is noteworthy is that in region I, for negative impact parameters $\rho/d < -1$, the dipole distance

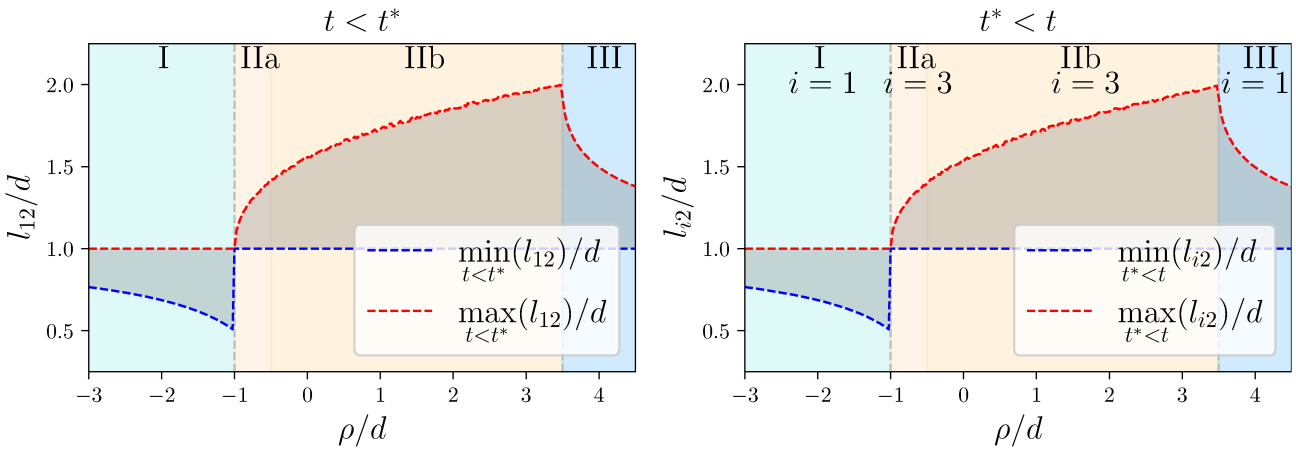

Figure 2.5: Numerical results of the minimum and maximum size of the propagating vortex dipole pre- and post-interaction with the third isolated vortex. The moment of interaction is defined via the value of t^* that indicates the critical point. In region II, the tracked vortex dipole is that composed of vortex 2 and 3.

shrinks during propagation, with the minimum distance achieved at the periapsis point with size $l_{12} = d/2$ when $\rho = -d$. This implies that the three vortex scattering process can bring dipoles closer together as much as a factor of two (although only temporarily due to energy conservation leading to the post-interaction dipole size returning to d).

Ultimately, as in quantum systems annihilation requires dipole separation becoming close to the healing length (1.19), despite vortex annihilation not being possible here (and also the healing length not being defined), the periapsis behaviour in this case could be a viable mechanism for vortex annihilation in compressible point vortex like systems such as Bose-Einstein condensates where it is possible for quantum vortex dipoles to become close enough for vortex annihilation to occur as indicated in [94]. In regions IIa and IIb we observe that $l_{12} = l_{23}$ at the critical point confirming the exchange scattering scenario described previously and that the exchange scattering occurs at the periapsis with a widening of the dipole-vortex (in this case it corresponds to maximum of the dipole distance during the complete interaction). In region III, a direct scattering interaction for positive impact parameter, the dipole size increases from its initial size d during its interaction before returning to size d. At large impact parameters (both positive and negative) the dipole passes by the third vortex at a significant distance meaning any three vortex scattering will be negligible with l_{12} remaining close to the initial value d.

Throughout investigation of the three vortex system we thus find, as demonstrated in fig-

ure 2.3, that the exchange scattering type can be considered most disruptive in larger point vortex assemblies (in other words exchange scattering will be more responsible for mixing due to dipole-vortex collisions in larger systems) with this behaviour being most extreme near the asymptotes $\rho/d = -1$ and $\rho/d = 7/2$. Additionally, through figure 2.4 we attain the closest approach between vortices at the critical point, demonstrating that it is only possible for vortices to come within the initial d separation in the first case of direct scattering near the asymptote, this indicates that if annihilation is to occur in vortex systems where this is possible it is most likely to occur in this region of direct scattering. This is further supported by the minimum/maximum plots of the pre- and post-interaction dipole separations figure 2.5. When considering vortex systems statistically, this region of direct scattering should thus take special importance in view of how the number of dipoles in the system changes over time.

2.3 Four vortex system: dipole-dipole collisions

Here we will consider the second basic point vortex collision, the interaction of a dipole with another dipole of the same size. As the dipole-vortex collision was a specific case of the more general three vortex interaction, the dipole-dipole collision is a specific case of more general four vortex dynamics. The point vortex model in general is not integrable for $N > 3$, therefore the general dipole-dipole collision is not integrable and cannot be solved by analytical methods such as those in the previous system. Despite this, the dipole-dipole collision has been extensively studied by both Aref and Eckhardt [95, 4, 96] where special regimes of integrable motion have been identified and theoretical expressions for the dipole scattering angles computed [95, 4]. There are then two specific types of interaction of a dipole with another dipole; that where the system is integrable and non-integrable, which we refer to as the integrable and non-integrable dipole-dipole collisions respectively. The integrable cases can be shown to occur when linear momentum in x and y and the total circulation mutually vanish, resulting in a parallelogram configuration in dipole-dipole collisions, and giving a three-body problem similar to that discussed in section 2.2. In the following two subsections we will discuss both the integrable and non-integrable dipole-dipole interactions.

2.3.1 Integrable dipole-dipole scattering

The idea of integrable four vortex motion was first examined by Eckhardt [95]. Following the Hamiltonian description of the point vortex model, a system with $2N$ degrees of freedom can be considered integrable if it has N independent integrals of motion H_i that pairwise commute under the Poisson bracket, in other words given a Poisson bracket $\{f, g\}$ for each pair of integrals H_i, H_j we have $\{H_i, H_j\} = 0$. Here Eckhardt defines the Poisson bracket

$$\{f, g\} = \sum_i \frac{1}{\kappa_i} \left(\frac{\partial f}{\partial x_i} \frac{\partial g}{\partial y_i} - \frac{\partial f}{\partial y_i} \frac{\partial g}{\partial x_i} \right). \tag{2.12}$$

Here equation (2.12) defines the commutation relations of the point vortex model, which upon quantization deforms to quantum commutators [97, 98]. In the case of four vortices the integrals of motion do not in general pairwise commute under this Poisson bracket, instead we have that $\{Q, P\} = \sum_i \kappa_i, \{P, M\} = -2Q, \{Q, M\} = 2P$, this Poisson bracket has the advantage of giving a clear physical basis for the above commutation relations; if there is a translation generated by linear momentums P or Q then rotation will thus mix it with a translation in Q or P respectively, the sum of circulations also then gives the average rotation and thus gives the mixing of linear momentums P and Q. Therefore, when considering the four vortex case we have 8 degrees of freedom with 4 integrals of motion H, Q, P, M. In order for this to be considered integrable we must then have that $Q = P = \sum_i \kappa_i = 0$. The total circulation vanishing is trivially satisfied when considering two identical dipoles. By considering the vanishing momentum we attain the equalities $(x_1 + x_3)/2 = (x_2 + x_4)/2$, $(y_1 + y_3)/2 = (y_2 + y_4)/2$. These equalities imply a parallelogram configuration of the four vortices in the integrable case, and as this is due to the momentum this parallelogram will hold for all t, leading to and extra geometrical constraint and thus enabling a mathematical reduction of the system to an effective three body interaction. The setup we consider is then shown in figure 2.6. This consists of two identical direct facing point vortex dipoles each of size d, and strengths $\pm\kappa$. We have several parameters defined as in the three vortex case; we have an impact parameter ρ characterising the vertical displacement between the midpoints of the initial dipole positions, the parameter L again quantifies the horizontal distance between the dipole initial positions. It is in the limit of $\rho \ll L$ and $d \ll l$ in which we consider the interaction. The parallelogram geometry lets us

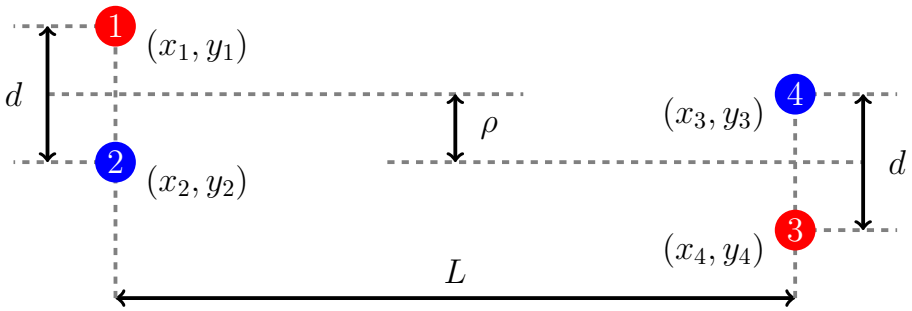

Figure 2.6: Initial setup of the integrable four vortex interaction, with each vortex marked as a circle coloured by the sign of its circulation, and with our chosen numbering marked. The initial dipole separations defined as d, and impact parameter between dipole midpoints represented as ρ, and horizontal separation between dipoles L are annotated and marked by solid lines.

exclude the fourth vortex from the equations of motion using the standard relations defining a parallelogram $l_{34} = l_{12}$, $l_{14} = l_{23}$, and $l_{24}^2 = 2l_{12}^2 + 2l_{23}^2 - l_{13}^2$ to arrive at a three body scattering problem, albeit with a much more complicated Hamiltonian taking the form

$$H = -\frac{\kappa^2}{2\pi} \ln\left(\frac{l_{13}\sqrt{2l_{12}^2 + 2l_{23}^2 - l_{13}^2}}{l_{12}^2 l_{23}^2}\right) = -\frac{\kappa^2}{2\pi} \ln\left(\frac{\sqrt{(\rho+d)^2 + L^2}\sqrt{(\rho-d^2)^2 + L^2}}{d^2(\rho^2 + L^2)}\right)$$
$$\underset{L\to\infty}{\to} \frac{\kappa^2}{2\pi} \ln\left(d^2\right),$$

The final limit of the Hamiltonian gives the energy of two isolated vortex dipoles with circulations $\pm\kappa$, giving twice the value of the Hamiltonian in the three vortex scattering problem discussed in section 2.2 in the $L \to \infty$ limit, i.e. the Hamiltonian of a single point vortex dipole, due to the isolated vortex not contributing any energy to the system. The momentum for this interaction then vanishes as it is required that $\mathbf{P} = (0, 0), M = 0$, Note that due to this $R = 0$ when considering all four vortices (this can then be considered an alternative form of the integrability condition). We can use the three vortex R as an effective relative momentum R_{eff} by considering vortices 1, 2, and 3 (the three vortices that we reduce analysis to) as the position of vortex 4 is dependent on the position of the other vortices.

$$R_{\text{eff}} = 2\kappa^2 \rho d.$$

We then follow the same strategy as in the three vortex interaction. Given two interacting point vortex dipoles, there then are two pairs of vortices of identical circulations (in other words two vortices with circulations κ and two vortices with circulations $-\kappa$) these pairs cannot propagate

off as part of the same vortex structure, so as $t \to -\infty$ and $t \to \infty$ these lengths will tend to infinity. The dynamics of the dipole-dipole scattering can then be encapsulated by following the relative distance between the like-signed pairs. As we are excluding the fourth vortex from the interaction it makes sense to consider the length of the pair comprised of vortex 1 and 3 through the dimensionless variable $b_2 = -l_{13}^2/\kappa C$, with C defined as in the three vortex case.

To express the equation of motion for the integrable four-vortex case we again use (1.29), which is a general equation for any number of point vortices, we have

$$\frac{dl_{13}^2}{dt} = \frac{2}{\pi}\kappa_2\epsilon_{132}A_{132}\left(\frac{1}{l_{23}^2} - \frac{1}{l_{12}^2}\right) + \frac{2}{\pi}\kappa_4\epsilon_{134}A_{134}\left(\frac{1}{l_{34}^2} - \frac{1}{l_{14}^2}\right), \tag{2.13}$$

$$= \pm\frac{2\kappa}{\pi}\left[A_{132}\left(\frac{1}{l_{23}^2} - \frac{1}{l_{12}^2}\right) - A_{134}\left(\frac{1}{l_{34}^2} - \frac{1}{l_{14}^2}\right)\right],$$

$$= \pm\frac{4\kappa}{\pi}A_{123}\left(\frac{1}{l_{23}^2} - \frac{1}{l_{12}^2}\right), \tag{2.14}$$

where we have used $\kappa_2 = \kappa_4 = -\kappa$, the fact that ϵ_{132} and ϵ_{134} will always be of opposite sign and the geometry of the parallelogram that implies that A_{132} and A_{134} are congruent triangles. The particular positive or negative term from the last equality will be decided by the phase of the evolution we are in, in other words are the dipoles propagating towards or away from each other. Similarly to the dipole-vortex collision, critical points of (2.13) for variable l_{13} occur when the vortex separations $l_{12} = l_{23}$ or if the three vortices $1, 2, 3$ leading to the area $A_{123} = 0$. Following the same strategy that we outlined for the three vortex interaction, it is possible to form an analogous conserved quantity θ with a slightly different formula on account of the more complicated Hamiltonian

$$\frac{\sqrt{b_2(b_2-6)}}{b_1 b_3} = \kappa|C|\exp\left(-\frac{2\pi H}{\kappa^2}\right) = \theta, \tag{2.15}$$

we also define C from the three vortex R as is given in (2.3). Using the conserved quantities C

and θ and rewriting (2.13) in terms of the dimensionless variable b_2 gives

$$\begin{aligned}\frac{db_2}{dt} &= \frac{2\sqrt{\theta}}{C\pi\sqrt{b_2(b_2-6)}}\sqrt{\left[\sqrt{b_2(b_2-6)}-\frac{9}{4}\theta\right]\left[(b_2-3)^2-\frac{4}{\theta}\sqrt{b_2(b_2-6)}\right]},\\ &= \begin{cases}\frac{2\sqrt{\theta}}{C\pi\sqrt{b_2(b_2-6)}}\sqrt{(b_2-\alpha)(b_2-\beta)(b_2-\gamma)} & \text{if } C>0,\\ \frac{2\sqrt{\theta}}{C\pi\sqrt{b_2(b_2-6)}}\sqrt{(\bar{\alpha}-b_2)\left(\bar{\beta}-b_2\right)(\bar{\gamma}-b_2)} & \text{if } C<0.\end{cases}\end{aligned} \tag{2.16}$$

As in the dipole-vortex interaction we have three sets of roots for $\dot{b}_2$, either α, β, γ or $\bar{\alpha}, \bar{\beta}, \bar{\gamma}$ depending on what sign the quantity C takes. Note that these are not the same roots as found in the dipole-vortex case, and are on the whole more complicated due to the more complicated Hamiltonian.

We have defined the roots of (2.16) as the following: for the case when $C > 0$

$$\begin{aligned}\alpha &= 3\left(1-\sqrt{1+\frac{9}{16}\theta^2}\right), \qquad \beta = 3\left(1-\frac{2\sqrt{2}}{3\theta}\sqrt{1-\sqrt{1-\frac{9}{4}\theta^2}}\right), \\ \gamma &= 3\left(1-\frac{2\sqrt{2}}{3\theta}\sqrt{1+\sqrt{1-\frac{9}{4}\theta^2}}\right),\end{aligned} \tag{2.17}$$

and when $C < 0$ the roots are given by

$$\begin{aligned}\bar{\alpha} &= 3\left(1+\sqrt{1+\frac{9}{16}\theta^2}\right), \qquad \bar{\beta} = 3\left(1+\frac{2\sqrt{2}}{3\theta}\sqrt{1-\sqrt{1-\frac{9}{4}\theta^2}}\right), \\ \bar{\gamma} &= 3\left(1+\frac{2\sqrt{2}}{3\theta}\sqrt{1+\sqrt{1-\frac{9}{4}\theta^2}}\right).\end{aligned} \tag{2.18}$$

The boundaries between different scattering regimes (direct and exchange) in the dipole-dipole interaction can be determined as in the case of the vortex-dipole collision and are dictated by the roots of (2.16) explicitly given by (2.17) and (2.18) and plotted in figure 2.7. The symmetry of the two sets of roots around $b_2 = 3$ for either sign of C is due to the parallelogram symmetry of the problem and is confirmed in the phase diagrams of Aref [99]. For $\theta < 2/3$ we have three real roots in each case (dependent on the sign of C). Given the initial conditions where we assume $L \to \infty$ we have that the first roots reached by the variable b_2 during its evolution are γ and $\bar{\gamma}$ for $C > 0$ and $C < 0$ respectively. These roots correspond to exchange scattering

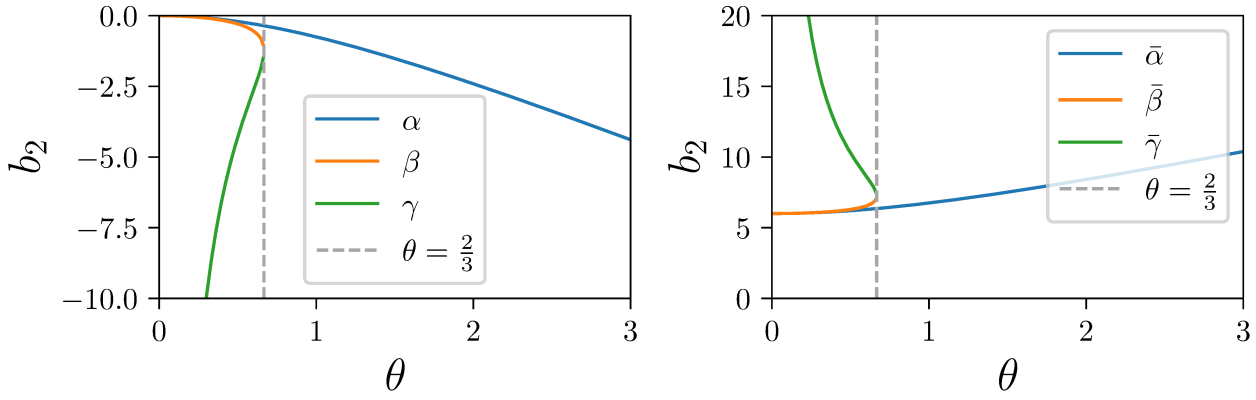

Figure 2.7: (Left) Plot of the roots α, β, γ for $C > 0$ of (2.16). Roots β and γ become imaginary for $2/3 < \theta$, we mark the boundary this occurs as a grey dashed line. (Right) Roots $\bar{\alpha}, \bar{\beta}, \bar{\gamma}$ for $C < 0$ which are the mirror images of α, β, γ in the $b_2 = 3$ plane. Roots $\bar{\beta}$ and $\bar{\gamma}$ become imaginary for $2/3 < \theta$, again marked as a grey dashed line.

where the positive vortices are exchanged by the two vortex dipoles. For $2/3 < \theta$, the roots $\beta, \bar{\beta}$ and $\gamma, \bar{\gamma}$ become complex, see figure. 2.7 for a graphical interpretation, and thus, the dipole interaction type is governed solely by the roots α and $\bar{\alpha}$ for $C > 0$ and $C < 0$ respectively that correspond to regions of direct scattering in the three vortex reduction where the three vortices become collinear.

From this we give in table 2.3 the four regions of interaction and the parameter ranges in which they apply by checking which roots are greatest in magnitude such that they will be reached first. The limiting case when $\theta = 2/3$ corresponds to the alternating ring configuration

Table 2.3: Parameter ranges of C, θ, and ρ/d by interaction region and the corresponding scattering types of the four vortex interaction, similar to 2.1. Region II has been split into two subregions defined by the sign of C with both regions IIa and IIb exhibiting exchange scattering.

Region	C Range	θ Range	Impact Parameter Range	Scattering Type
I	$C > 0$	$2/3 < \theta$	$\rho/d < -1$	Direct
IIa	$C > 0$	$0 < \theta < 2/3$	$-1 < \rho/d < 0$	Exchange
IIb	$C < 0$	$0 < \theta < 2/3$	$0 < \rho/d < 1$	Exchange
III	$C < 0$	$2/3 < \theta$	$1 < \rho/d$	Direct

as studied by Havelock [100]. Here Havelock gives equilibrium configurations consisting of an inner rotating vortex ring, and an outer rotating ring of vortices with opposite circulation, Havelock continues to analyse the stability of such systems. In the integrable dipole-dipole

collision in particular this corresponds to a bounded state whereupon vortices span a rhombus shape at interaction which continuously rotates about the center point.

The exact configuration of the rhombus can be found by the values at the periapsis, hence we find that separations between vortices of the same sign will form diagonals of the rhombus with the smaller diagonal of length $d\sqrt{2\sqrt{2}-1}$ and larger diagonal $d\sqrt{2\sqrt{2}+1}$. According to the analysis of Havelock each vortex pair will rotate with the same angular velocity (and hence the rhombus will be preserved) if the following condition holds

$$(n-1)\kappa - \frac{2np^n}{1+p^n}\kappa' = \frac{2np^2}{1+p^n}\kappa - (n-1)p^2\kappa',$$

where here n is the number of vortices contained in a vortex ring, κ is the strength of the vortices in inner ring, κ' is the strength of vortices in the outer ring, and p is the ratio of the inner ring radius to the outer ring radius. Given the values of the integrable dipole-dipole collision $\kappa = -\kappa'$, $n = 2$ and p defined through the diagonals given above this equation holds, thus each vortex rotates about the center the same constant angular velocity $\dot{\phi} = \pm(\kappa/2\pi d^2)(3+\sqrt{2})$. In real space, this parameter choice corresponds to vortices of the same sign colliding on exactly opposite trajectories, and is the result of the system being trapped between exchange and direct scattering in each case. When $C > 0$ at the limit case we have the positive signed vortices colliding along opposite trajectories, it is these vortices that then form the smaller diagonal, and we then have anti-clockwise rotation of the rhombus, thus vortices take the negative value of angular velocity. Conversely, in the case that $C < 0$ it is the negative vortices that collide on opposite trajectories, which then form the smaller diagonal, and then clockwise rotation is observed.

For both cases of C we see the exchange scattering roots γ and $\bar{\gamma}$ tending to $-\infty$ and ∞ respectively as $\theta \to 0$. This represents the root in the limit of infinite initial dipole separation; i.e. $L \to \infty$ with L defined as according to figure 2.15, and so we have for the exchange scattering root $|b_2| \to \infty$ and so this root is non-physical. By the definition of θ (2.15), if $\theta = C = 0$ we must have that either $b_2 = 0$, $b_2 = 6$, or $b_1 b_3 \to \infty$. The latter possibility $b_1 b_3 \to \infty$ implies that $|b_1| \to \infty$ (as $|b_3| \to \infty$ would imply the dipole separation is tending to infinity and thus dipole-dipole dynamics is not maintained) and thus corresponds to the previously mentioned non-physical solutions of $\gamma \to -\infty$ and $\bar{\gamma} \to \infty$. Also, the case of $b_2 = 0$

implies the dipoles occupy the same point in space and so is also a non-physical solution, hence the only physically relevant solution to the limiting case $\theta = C = 0$ is when $b_2 = 6$, corresponding to the $\bar{\beta}$ root at $\theta = 0$. In this case we find the vortex dipoles undergoing a completely "head on" collision, with vortices of opposite signs colliding along exactly opposite trajectories. These vortex/anti-vortex pairs form new dipoles and propagate off at right angles to the original dipole alignments. This interaction is analogous to a vortex ring colliding with a wall through the technique of images.

In the previously mentioned work of Eckhardt and Aref the scattering angle in the integrable dipole-dipole collision was (correctly) given and hence will not be repeated here. In figure 2.8 we plot the resulting theoretically derived scattering angle against our numerical simulation data for the scattering angle [4]. Note that Eckhardt and Aref only gave results for the case when $C < 0$, although as we have symmetry of the configuration around $C = 0$ we can extend this to include $C > 0$ by reflection about the $C = 0$ point and $\Delta\phi = 0$. For the exchange scattering cases, the results are translated by $-\pi/2$, to account for the rotation of the parallelogram configuration as a result of the exchange process. Excellent agreement is observed between both sets of results, confirming the validity of Eckhardt and Aref's derivation. We notice the asymptotes located at $\rho/d = \pm 1$ which correspond to an infinite scattering angle due to the rotating rhombus configuration already discussed. At the extremes of the impact parameter range we observe negligible scattering due to the dipoles passing at large distances from each other. We note also the scattering angle going to zero over a much smaller range than in the dipole-vortex case (figure 2.3), here the scattering angle is already at 0 for parameters $|\rho/d| > 2$. This is a consequence of interaction strength (velocity) of a dipole decaying as $\propto 1/r^2$, while for a single vortex the decay is $\propto 1/r$, leading to a much smaller degree of scattering for most of the parameter range.

Now to examine the evolution of the dipole size over the course of the integrable dipole-dipole collision. This is important for the same reasons as in the dipole-vortex collision, as in quantum turbulence, vortices that come close over the course of an interaction the separation may shrink to less than the healing length of the system and thus annihilation will occur, fundamentally changing the structures present in the evolution of a larger system. As before, we can consider the previously computed roots of the dynamics of b_2 in (2.17) and (2.18) as corresponding to

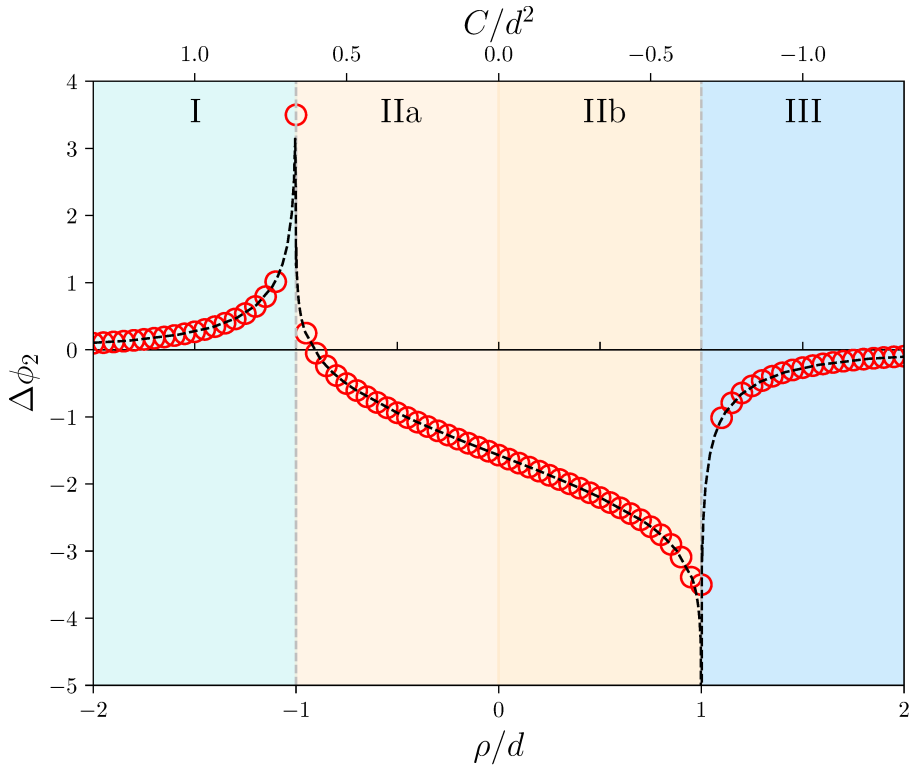

Figure 2.8: Unwinded scattering angle results of the integrable dipole-dipole collision. Analytical results of Eckhardt and Aref [4] are presented as the black dashed curve with our numerical results for comparison (red circles). The background is shaded and labelled so to show different the regions given in table 2.3 as in the three vortex case, with boundaries of exchange and direct scattering represented as the dashed grey lines.

the periapsis point, then as the system is integrable here we can use this to solve for the other inter-vortex distances at the periapsis. In the integrable dipole-dipole case the critical lengths of vortex separations occur at the same moment in time as in the dipole-vortex collision, which is to be expected as the extra parallelogram geometrical constraint reduces the system to a three-body interaction. For the same reason we do not see persistent dipole growth/shrinking here, once the interaction is complete the dipole will relax to the initial value d as otherwise energy conservation would be violated. Our results at the critical lengths of the vortex configuration are presented in table 2.4. Separations for vortices with the fourth vortex are dependent on the vortex separations between other vortices on account of the additional geometric constraints and can easily be recovered from the aforementioned conditions and so will not be reproduced here. In figure 2.9 we plot the theoretical predictions of the critical vortex separation lengths presented in table 2.4 against numerical data obtained from our simulations. We observe complete agreement between theory and numerical data across all regions of parameter space. The dipole is ascertained to shrink over the course of the interaction in regions I and III, in

Table 2.4: Critical vortex separations of the reduced three vortex system in the integrable dipole-dipole collision categorized by the regions defined in table 2.3.

Region	l_{12}^*	l_{13}^*	l_{23}^*
I	$d\sqrt{-\frac{\rho}{d}\sqrt{1+\frac{1}{4}\frac{\rho^2}{d^2}}-\frac{1}{2}\frac{\rho^2}{d^2}}$	$d\sqrt{-\frac{\rho}{d}\left[\sqrt{4+\frac{\rho^2}{d^2}}-2\right]}$	$d\sqrt{-\frac{\rho}{d}\sqrt{1+\frac{1}{4}\frac{\rho^2}{d^2}}+\frac{1}{2}\frac{\rho^2}{d^2}}$
IIa	$d\sqrt[4]{2+2\sqrt{1-\frac{\rho^2}{d^2}}}$	$d\sqrt{2\frac{\rho}{d}+2\sqrt{2}\sqrt{1+\sqrt{1-\frac{\rho^2}{d^2}}}}$	$d\sqrt[4]{2+2\sqrt{1-\frac{\rho^2}{d^2}}}$
IIb	$d\sqrt[4]{2+2\sqrt{1-\frac{\rho^2}{d^2}}}$	$d\sqrt{2\frac{\rho}{d}+2\sqrt{2}\sqrt{1+\sqrt{1-\frac{\rho^2}{d^2}}}}$	$d\sqrt[4]{2+2\sqrt{1-\frac{\rho^2}{d^2}}}$
III	$d\sqrt{\frac{\rho}{d}\sqrt{1+\frac{1}{4}\frac{\rho^2}{d^2}}-\frac{1}{2}\frac{\rho^2}{d^2}}$	$d\sqrt{\frac{\rho}{d}\left[\sqrt{4+\frac{\rho^2}{d^2}}+2\right]}$	$d\sqrt{\frac{\rho}{d}\sqrt{1+\frac{1}{4}\frac{\rho^2}{d^2}}+\frac{1}{2}\frac{\rho^2}{d^2}}$

contrast to the dipole-vortex collision which only had shrinking in region I, with the closest critical distance being attained when the impact parameter $\rho/d = -1$. The minimum dipole size across the parameter space is larger than what can be produced in the dipole-vortex interaction at a distance of $l_{12} = 0.79d$ as opposed to $d/2$. At the same value of the impact parameter $\rho/d = -1$ the two positive point vortices 1 and 3 approach even closer at a distance of $l_{13} = 0.49d$ at the points where the vortices enter the tight rotating rhombus configuration. In regions IIa and IIb, we observe exchange scattering ($l_{12} = l_{23}$) and where the two dipoles come together and exchange vortices creating two new sets of dipoles that then propagate away with both new dipoles relaxing back to their initial sizes of d as ensured by the conservation of energy. Indeed, the long-time dynamics of the system after scattering (for both direct and exchange) is that of two oppositely propagating dipoles of equal size d due to the conservation laws and the geometric constraint of the parallelogram (which we have confirmed numerically). In general, this behaviour does not occur in the non-integrable dipole-dipole collision that we will investigate in the next subsection. In figure 2.10 we show the minimum and maximum distances of the vortex dipole involving vortex 2. We observe qualitatively similar behaviour to the integrable dipole-vortex collision with the dipole shrinking during direct scattering, but growing during exchange scattering. The pre- and post-interaction symmetry arises due to the critical points occurring at the moment of collinearity or exchange (see in the next subsection that this is not necessarily the case in general).

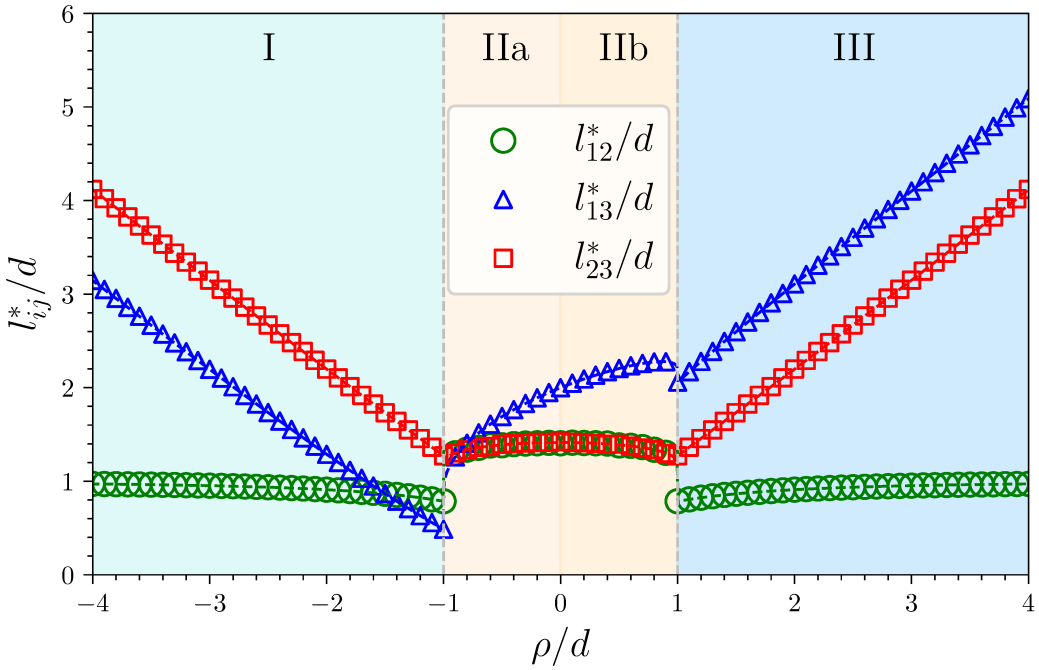

Figure 2.9: Critical vortex separation lengths in the integrable dipole-dipole interaction. Theoretical results are plotted as dashed curves given by the formulas in table 2.4 with numerical results as coloured symbols. The background is shaded and labelled according to the regions in table 2.3. Boundaries between regions represented as dashed grey lines indicate the change from exchange and direct scattering process.

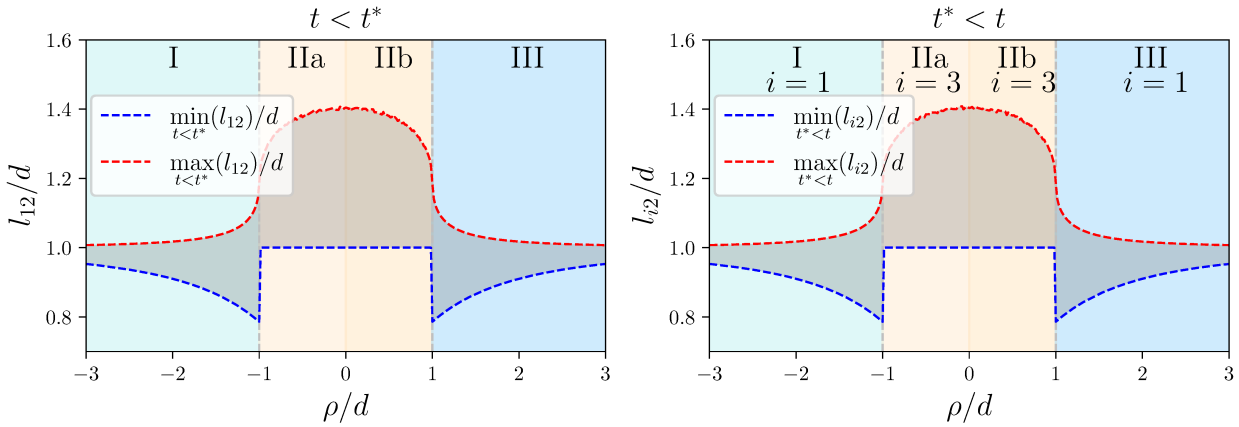

Figure 2.10: Numerical results of the minimum and maximum size of the propagating vortex dipole pre- and post-interaction defined as the moment t^* that the critical point is reached. Post-interaction we track the vortex dipole that includes the negative point vortex 2.

2.3.2 Non-integrable dipole-dipole scattering

The next fundamental collision in the point vortex model to consider is the non-integrable dipole-dipole collision, defined as two identical dipoles as in section 2.3.1, but with the necessary parallelogram integrability condition not satisfied here. The non-integrable dipole-dipole setup

as considered here is displayed in figure 2.11. This represents the general non-integrable dipole-dipole collision between two equally sized, equal circulation dipoles. The first dipole comprising vortices 1 and 2 is of separation d and is initialised from the origin by separation L_1, the second dipole of vortices 3 and 4 is also of size d and is situated from the origin by distance L_2. The two dipoles are aligned such that they propagate towards the origin, with the precise trajectory of the second dipole specified by the incidence angle $\psi \in [0, 2\pi)$. These three parameters L_1, L_2, ψ fully define the general non-integrable dipole-dipole collision. We will consider the interaction in the limit of $L_1, L_2 \to \infty$, and as such we consider the ratio $\delta_L = L_1/L_2$ as this limit is taken. Also, due to symmetry of the problem, we find that the transformation of $\psi \to 2\pi - \psi$ leads to the original configuration if vortices are relabelled such that $1 \leftrightarrow 3$ and $2 \leftrightarrow 4$.

As shown by analysis found in 2.3.1 and [96, 4], this system is non-integrable for the violation of the reflection symmetry $\psi \neq \pi$ and as such we cannot use the analytical techniques found in the previous sections. The investigation in this case is then purely restricted to a numerical basis. In [96], Eckhardt highlighted the rich dynamics of two interacting dipoles in the non-integrable case for both direct and exchange scattering scenarios. We will extend this numerical study and examine other aspects of the dipole dynamics, such as the dipole scattering angle and the evolution of the dipole size during and after the interaction. Considering the initial

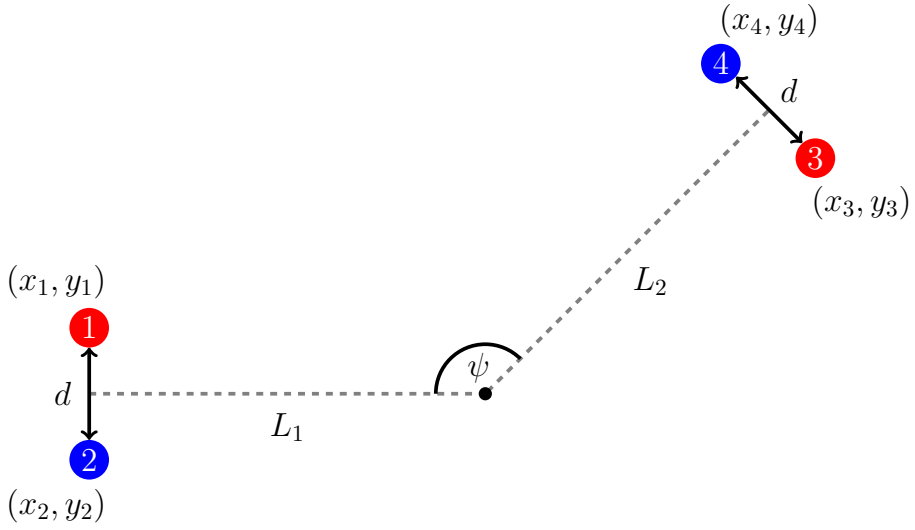

Figure 2.11: Initial setup of the non-integrable four vortex dipole-dipole collision, with each vortex coloured according to the sign of its circulation and marked according to our chosen numbering. The incidence angle and initial dipole separations (ψ and d) are marked as solid lines whereas the distance from dipole centres to the origin L_1 and L_2 are marked as dashed grey lines. The four vortices are arranged as two dipoles of size d with both orientated such that trajectories intersect at the origin.

vortex configuration as given in figure 2.11 gives the following conserved quantities in the limit $L_1, L_2 \to \infty$:

$$H = -\frac{\kappa^2}{2\pi}\left[\ln\left(\frac{2\sqrt{\left[L_1 - L_2\cos(\psi) + \frac{d}{2}\sin(\psi)\right]^2 + \frac{1}{4}[d\cos(\psi) - d + 2L_2\sin(\psi)]^2}}{d^2\sqrt{d^2 + 2(L_1^2 + L_2^2) + (d^2 - 4L_1L_2)\cos(\psi) - 2d(L_1 + L_2)\sin(\psi)}}\right)\right.$$
$$\left. + \ln\left(\frac{\sqrt{\left[L_1 - L_2\cos(\psi) - \frac{d}{2}\sin(\psi)\right]^2 + \frac{1}{4}[d - d\cos(\psi) + 2L_2\sin(\psi)]^2}}{\sqrt{d^2 + 2(L_1^2 + L_2^2) + (d^2 - 4L_1L_2)\cos(\psi) + 2d(L_1 + L_2)\sin(\psi)}}\right)\right]$$
$$\underset{L_1, L_2 \to \infty}{\to} \frac{\kappa^2}{2\pi}\ln\left(d^2\right),$$

which in the limit of $L_1, L_2 \to \infty$ leads to the usual value of the Hamiltonian of two dipoles of size d infinitely separated. The linear momentum in this setup is given as

$$\mathbf{P} = \{-\kappa d\sin(\psi), -\kappa d\left[1 + \cos(\psi)\right]\},$$

note that for the parameter $\psi = \pi$ we have $= (0, 0)$ and so the integrability condition is recovered for this value of ψ (in fact this corresponds to the $C = 0$ vortex ring collision as described in section 2.3.1). Also, for this setup we have the angular momentum $M = 0$ and these momentum expressions can be combined to give

$$R = -2\kappa^2 d^2\left[1 + \cos(\psi)\right].$$

The conserved quantities of the system are then completely dependent upon the orientation of the right-hand dipole in the upper half plane, and can be varied by a simple translation of ψ. We perform a series of numerical simulations of the point vortex model with initial conditions as presented in figure 2.11 for several values in the parameter space of ψ and δ_L with $L_1, L_2 \gg d$.

Due to the non-integrability of the system, we cannot identify the type of scattering observed analytically; instead this must be done numerically. We first track the motion each dipole and monitor what vortices the final dipoles consist of at the final long-time limit. Typically, the two dipole will approach each other, interact, and then eventually propagate away remaining as two coherent dipoles. Through this we present a map of the interaction types observed in figure 2.12. We observe a majority of exchange scattering occurring in the central star shaped region (yellow) centred on $\psi = \pi$ and $\delta_L = 1$. This is consistent, as the value $\psi = \pi$ corresponds

to the integrable $C = 0$ case (i.e. exchange scattering) regardless of the value of δ_L, whereas the value of $\delta_L = 1$ implies $L_1 = L_2$ (dipoles are separated from the origin by the same distance) and so will engage in a very close interaction for any value of ψ. The exchange scattering "star" can then be thought of as perturbations from these parameter values, in other words exchange scattering is likely wherever either or both $\delta_L \approx 1, \psi \approx \pi$. Outside this internal star region we observe direct scattering (light blue) where dipole propagation paths are such that extreme collisions are very unlikely. Hence, a direct scattering process occurs with slight deflection of propagation paths without destabilizing the initial dipole structures. Interestingly, there are regions of exchange scattering close to $\psi = 0$ and $\psi = 2\pi$ that swoop out towards the center. These "shark-fin" regions of exchange scattering begin at the boundaries of our considered interaction and reach towards the central "star" through very thin tails, seemingly of smaller width than the resolution of our simulations. These regions are an artefact of simulating over the entire parameter range, including parameter regions where the two dipoles happen to be initialised very close to each other, these artefacts are not representative of true dipole-dipole collisions but nevertheless present novel dynamics such as dipole chasing and dipoles phasing through the centre of the ahead dipole.

In figure 2.12 we identify six specific interactions (a-f) in the parameter space to demonstrate the interactions that occur in these regions. In figure 2.13 we plot the evolutions of each vortex over the course of the interaction given these parameter sets. Figure 2.13(a) shows a typical direct scattering process, with the two dipoles missing each other with very little deflection due to the small value of $\delta_L \approx 0.7$.

Figures 2.13(b-c) are two types of exchange scattering where a pair of vortices are exchanged between the dipoles. For figure 2.13(b) we have the typical exchange scattering as may have been observed in the previous section 2.3.1 with dipole vortices simply exchanging and dipoles propagating off to infinity. However, we notice a much more complicated exchange process in figure 2.13(c) (which is situated close to the boundary between direct and exchange scattering) displaying a complicated rotation between the two dipoles close to the moment of exchange, reminiscent of the Havelock ring rotation identified at the exchange/direct boundary in the integrable case. This then gives an idea of the boundary dynamics between direct and exchange scattering, and given a hypothetical interaction occurring at the exact boundary between direct

and exchange scattering (with no numerical error) this rotating Havelock ring formation will rotate indefinitely as the system is trapped between direct and exchange scattering regimes.

Interestingly, if we take another point close to the direct and exchange boundary figure 2.13(d) we observe similar but more prolonged four vortex dynamics composed of a rotational dance before the two dipoles propagate away. We see three vortices (vortices 1, 2 and 3) forming their own rotating vortex structure, which will possess its own mean circulation of κ, which when paired with the remaining anti-vortex 4 produces in effect a "pseudo-dipole" which shortly propagated before this rotating structure breaks down and dipoles propagate away as expected. It is this swirling motion that leads to extremely large values of scattering angle for the interaction. This then should represent another boundary case, and given parameters at the exact interface between direct and exchange scattering this rotation will continue indefinitely as the vortices are trapped in this configuration between direct and exchange scattering. It is interesting why this new boundary behaviour occurs here and not the rotating Havelock rings as seen in figure 2.13(c), but is more than likely due to which "leg" of the star the parameters are located; boundary cases along the $\psi \approx \pi$ legs give the Havelock ring configuration and boundary cases along the $\delta_L \approx 1$ branches will result in the pseudo-dipole boundary configuration (this explanation also answers why this behaviour was not observed in the integrable dipole-dipole collision). The points in parameter space on the boundary lines at which a figure 2.13(c) type interaction becomes a figure 2.13(d) type interaction (and the dynamics exactly at these points) is an interesting open question. Moreover, notice in the figure 2.13(d) case that the relative sizes of the two dipole have changed after undergoing the direct scattering which was something banned in the integrable cases. In figures 2.13(e) and (f) we take two sets parameters close to the $\psi = 0$ and $\psi = 2\pi$ boundaries. This means that both dipoles in both realisations are close to propagating along the same axis. We observe in figure 2.12 that both (e) and (f) border the swooping exchange regions that meaning that the type of orientation is sensitive to the scattering process, as (e) can be described as exchange scattering whereas (f) is clearly direct scattering. In both (e) and (f) the second dipole actually starts behind the initial dipole at a very small incidence angle, i.e. each dipole is almost propagating along the same path. Here we observe an interesting "slipstream" effect where the dipole behind, despite being identical to the dipole in front, propagates faster than the front dipole to the point where

as the system evolves the trailing dipole eventually catches up and we observe a four vortex interaction. If parameters are such that they reside on one of the swooping "shark-fin" curves, we then observe exchange scattering as observed in (e). Otherwise, if parameters are off these curves in these regions we instead observe the two dipoles being deflected as a result of this process with no change in the initial dipole structure. An example of this is seen in (f) with the trailing dipole actually passing through the two front dipole vortices and then both dipoles propagating off in what can be considered a direct scattering process. We already see here in the last three cases (d-f) a clear change in the final dipole sizes that remains post-interaction, with one dipole increasing and one dipole decreasing in size. The relative change of the dipole sizes is controlled by the conservation of the Hamiltonian as the final state when the dipoles are infinitely separated must still lead to $H = (\kappa^2/2\pi)\ln(d^2)$ (we will discuss more on this later).

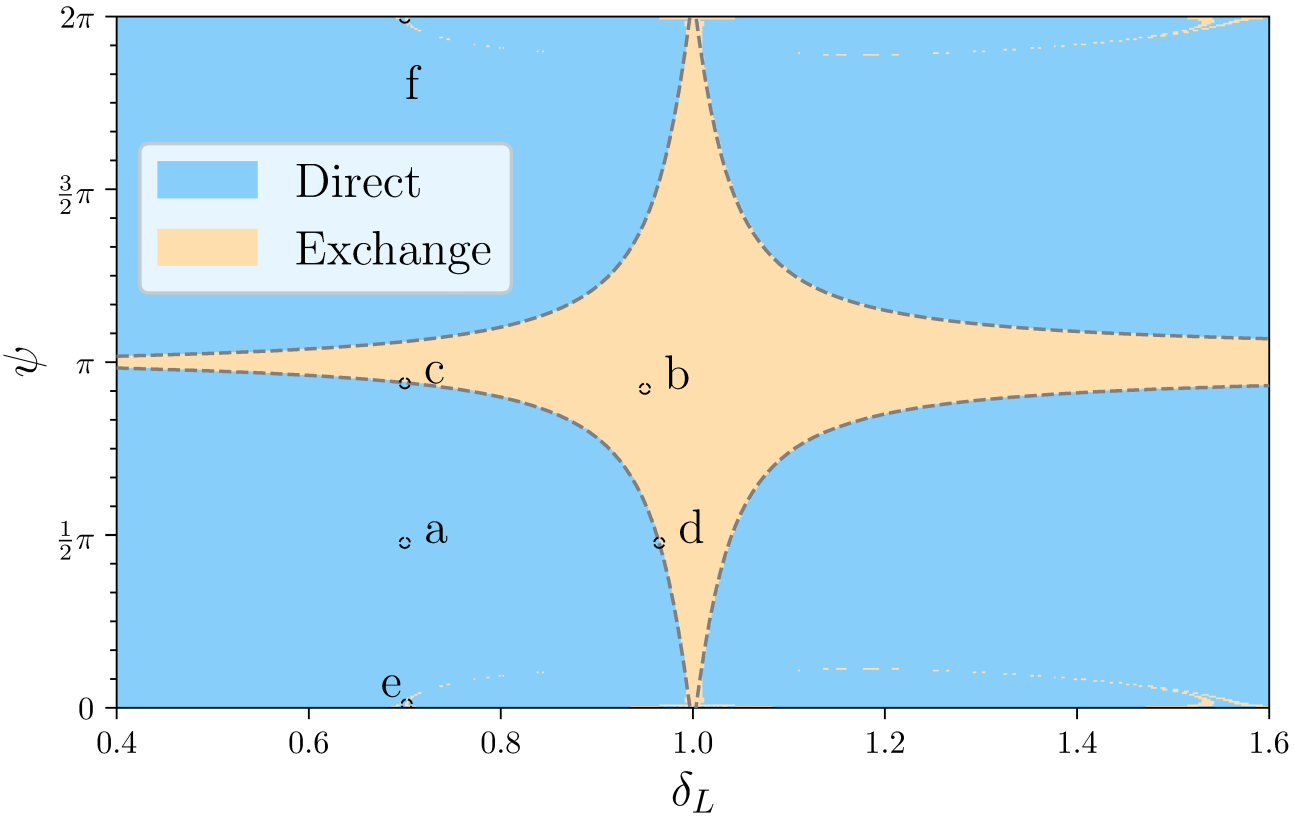

Figure 2.12: Colourmap of the type of interaction observed in the non-integrable dipole-dipole collision across the parameter space $\psi \in (0, 2\pi)$ and $\delta_L \in [0.4, 1.6]$. Light blue regions indicate parameter regions of direct scattering while regions of yellow correspond to exchange scattering where the initial dipoles exchange vortices during the interaction. Six particular regions of interest have been highlighted and labelled (a-f), the particular evolutions at these points are illustrated in figure:2.13. The boundary between main direct and exchange scattering regions are marked by grey dashed curves.

As in previous cases, we then solve for the scattering angles of the system using our numerical

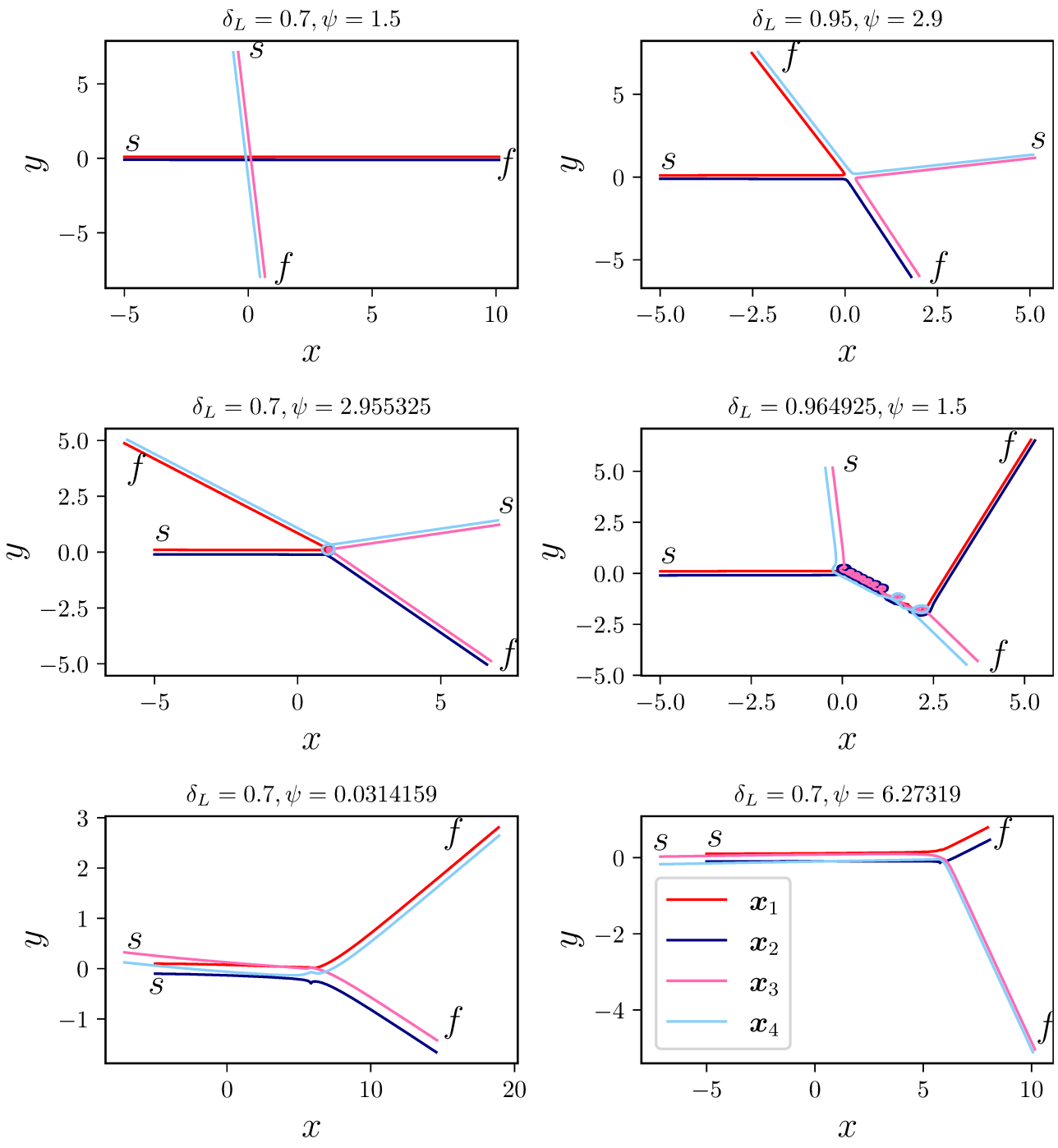

Figure 2.13: Vortex trajectories from six parameter sets (top row, left to right) (a) $\psi = 1.5, \delta_L = 0.7$, (b) $\psi = 2.9, \delta_L = 0.95$ (middle row, left to right) (c) $\psi = 2.955325, \delta_L = 0.7$, (d) $\psi = 1.5, \delta_L = 0.964925$,(bottom row, left to right) (e) $\psi = 0.0314159, \delta_L = 0.7$, and (f) $\psi - 6.27317, \delta_L = 0.7$. Labels s and f indicate the start and finishing points of the simulation. The dark red and blue curves correspond to vortices 1 and 2, with the pink and light blue curves vortices 3 and 4.

method, we track the direction of propagation of vortex 2 and determine the corresponding deflection angle $\Delta\phi_2 = \lim_{t\to\infty}\phi_2(t) - \lim_{t\to-\infty}\phi_2(t)$ measured only after sufficient time has elapsed post-interaction to ensure that the vortex dipole is isolated and is propagating only via self-interaction. The scattering angle results are then presented in figure 2.14. We notice in the direct scattering regions there is very little deflection of the dipole propagation direction when compared to the dipole-vortex collision. The far-field interaction of two dipoles is then weaker than that of a dipole-vortex, and so significant deflection is seen to only occur when dipoles undergo a very close interaction. Consequently, we observe the most significant dipole scattering mainly in or close to the central exchange scattering star. The inner exchange scattering region is predominantly blue meaning that after an exchange of vortices, the vortex dipole containing vortex 2 exhibits a negative angle deflection, i.e. a clockwise deflection. Interestingly this result holds for the previous cases also, with the majority of exchange scattering giving a negative deflection angle. There is however a small band of positive angle deflection along the direct-exchange border region as displayed in figure 2.13(d). A small red patch is observed in the upper left quadrant of the exchange scattering region, with a sharp transition from red to dark blue due to the 2π winding of the deflection angle, indicating the initial dipole has been scattered to a trajectory opposite its initial trajectory, and that the most consistently extreme scattering through the whole parameter space occurs here. Overall the scattering between two identical dipoles is much more regular than what is observed for a general dipole-dipole collision with dipoles of varying strengths $\kappa_1 = -\kappa_2 \neq \kappa_3 = -\kappa_4$. Analysis by Aref and Pomphrey [101] into these more general interactions shows various complex chaotic scattering dynamics that we do not observe here, although we do observe significant jumps in the scattering angle for particular parameter sets, most notable close to the direct/exchange boundary in the upper left quadrant. The dynamics of the interaction in these cases involve a longer four vortex interaction that includes repeated rotation of the vortex system, e.g. the cases presented in figure 2.13(c) and (d), and are similar in style to the integrable four-vortex case where these boundaries regions correspond to Havelock's double alternating rings [100]. Finally, we observe in the dipole-dipole collision that the direct scattering process is less effective compared to the dipole-vortex collision, and also that the exchange scattering process can be far more disruptive to the initial state, with various complicated four vortex interactions shown.

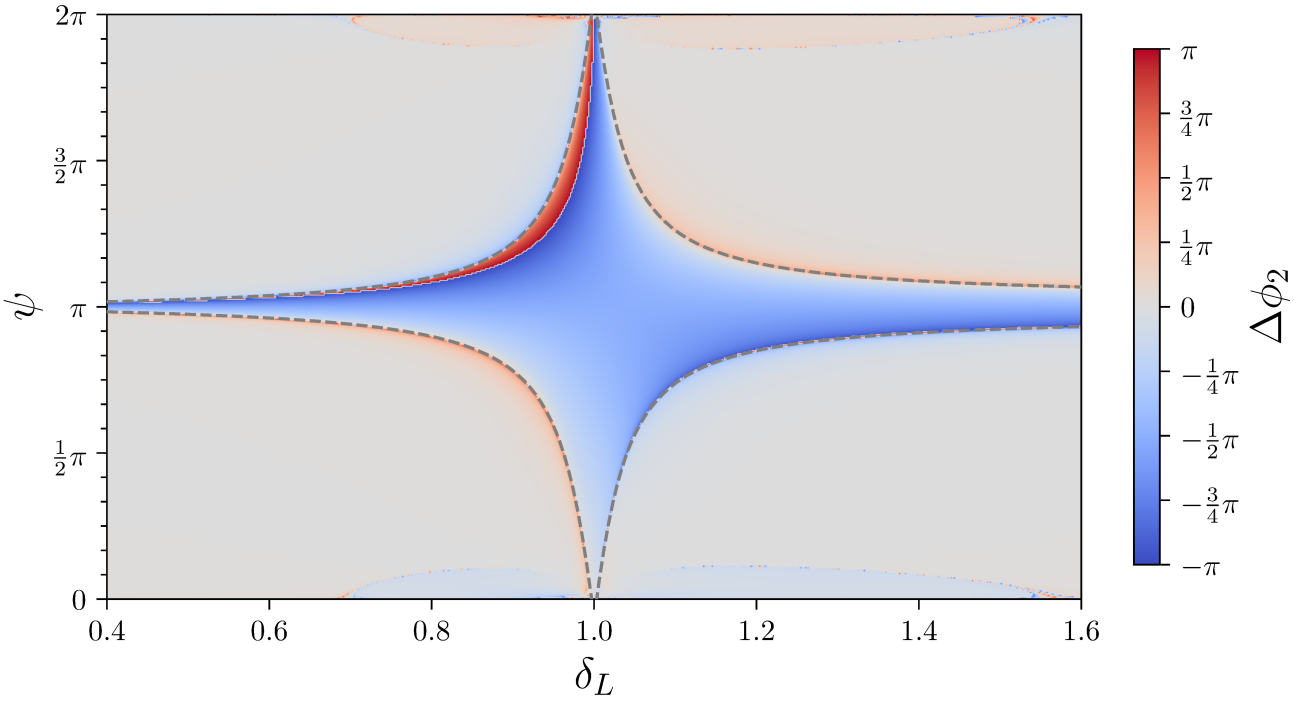

Figure 2.14: Heatmap of the scattering angle of the dipole-dipole interaction over the parameter space. Results are displayed as a colourbar centred at zero, which is taken as the horizontal original dipole trajectory. Region boundaries between direct/exchange scattering are marked by grey dashed curves.

Also, we consider the minimum and maximum dipole size before and after interaction has taken place. Note that in the non-integrable dipole-dipole collision we have two sets of same-signed vortices, vortices $1, 3$ and vortices $2, 4$, meaning here we can define the critical point as either the minimum of the length l_{13} or l_{24} (exclusion of the fourth vortex by the parallelogram geometry meant this was not the case for the integrable dipole-dipole collision). Here we will define the critical point as the point in time t^* where l_{13} is at minimum to be consistent with previous cases, although taking the minimum of l_{24} to be the critical point would give equally valid results, and should be symmetric with the results of taking l_{13} as the critical point. It is also of note that due to the added complexity of the system this is the first collision where the critical point may not necessarily correspond in time to the exchange or direct scattering process. This is illustrated in figure 2.15, where through direct numerical simulation we display the evolution of the inter-vortex lengths over a particular non-integrable dipole-dipole exchange scattering interaction. We solve numerically for the critical point (the minimum of l_{13} over the entire evolution) and mark this by a black dashed line.

We can see the course of the interaction through this, at the first part of motion where

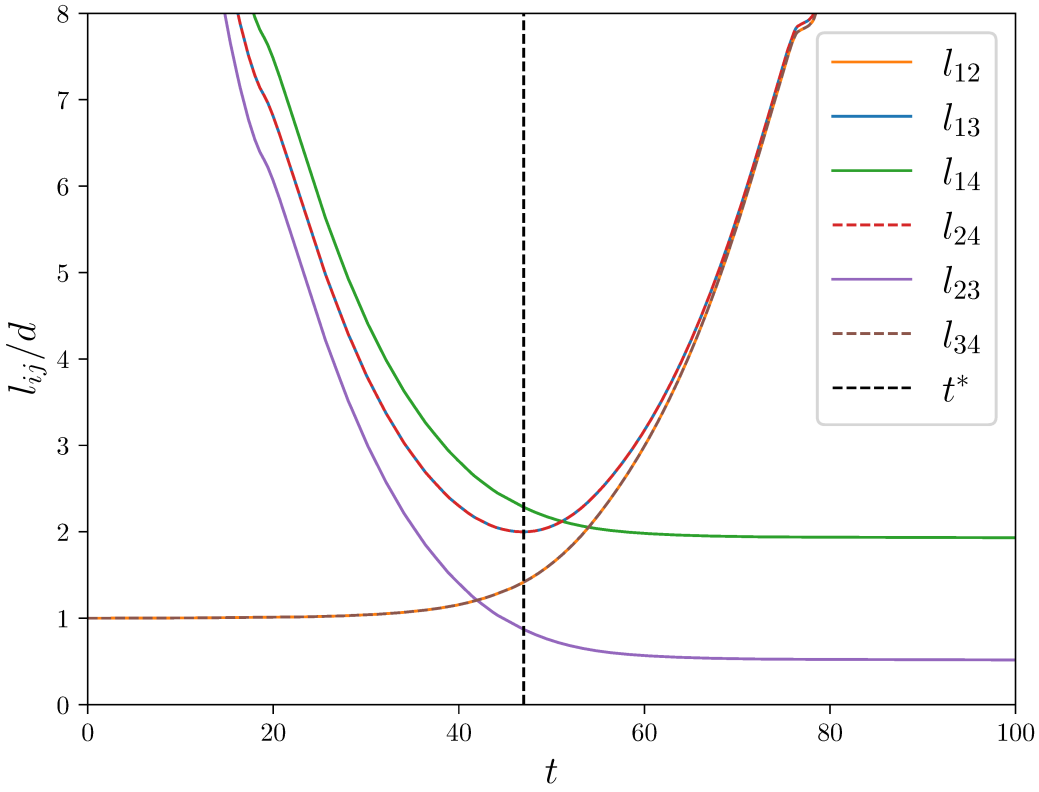

Figure 2.15: Inter-vortex separations for a sample parameter set $\delta_L = 1, \psi = 4.71239$ in arbitrary units of time t, with each inter-vortex length given as a different colour as indicated by the legend and the critical point represented as a dashed black line.

$t \leq 40$ each separation not between vortices of the same initial dipoles steadily decrease, with the separations between dipole vortices l_{12} and l_{34} increasing up to the first exchange point whereupon $l_12 = l_{23}$. Continuing to the critical point at $t \approx 46.996$ where by definition l_{13} is at minimum, and also at this point l_{24} is also at minimum. After this, there is another exchange scattering point where $l_{14} = l_{34}$. Once the second exchange scattering point is passed lengths between the new dipoles (l_{14} and l_{23}) become constant, and other lengths tend to infinity as $t \to \infty$ and the dipoles propagate off to infinity.

There are several features of interest here; firstly, whilst dipole lengths are initialised to the same value and remain identical before the exchange scattering process, once the interaction is complete at the final point in time we see two distinct dipole separations indicating a persistent change in dipole sizes as a result of this interaction. Also note that there are two different exchange points here, we see the first exchange point where $l_{12} = l_{23}$ before the critical point, and the second exchange scattering point where $l_{14} = l_{34}$ after the critical. Thus, the critical point no longer corresponds to an exchange scattering process as in the previous more simple cases, and there now occurs multiple exchange processes over the course of the interaction.

This additional complex behaviour can be seen as due to the added complexity of the equation of motion for l_{13}, as in previous cases $\dot{l_{13}^2} = 0$ implied a single exchange or point of collinearity, whereas in the non-integrable four vortex case

$$\dot{l_{13}^2} = 0 \implies A_{123}\left(\frac{1}{l_{23}^2} - \frac{1}{l_{12}^2}\right) = A_{134}\left(\frac{1}{l_{34}^2} - \frac{1}{l_{14}^2}\right),$$

then it is no longer the case that the inter-vortex minimums/maximums will occur at the critical point, so it becomes crucial to analyse the minimums/maximums over the course of the interaction.

Hence in figure 2.16 we plot the minimum and maximum dipole sizes before and after the critical point t^*, with pre-interaction defined as the phase of interaction when $t < t^*$ and post-interaction defined as the phase when $t^* < t$. As was the case in the dipole-vortex collision, we observe dipole l_{12} reducing in magnitude in the pre-interaction stage during a direct scattering process, again with extremes found near the direct-exchange scattering boundary. In the exchange scattering region, we observe that the minimal distance remains $l_{12}/d = 1$ which indicate that the dipole grows, as indicated by the red colouring in the maximal distance pre-interaction (figure 2.16 top right). Interestingly, we find post-interaction in the exchange scattering case the new dipole shrinking ($\psi \gtrsim \pi$) or enlarging ($\psi \lesssim \pi$), highlighting the possibility of dipoles of different sizes being created as a result of the non-integrable dipole-dipole collision. In figure 2.17 the final dipole sizes once interaction is complete are plotted. Numerically this is accomplished by measuring the final dipole size in the long-time limit, to ensure the interaction between dipoles is negligible and so the interaction can be considered complete. Across the entire parameter range the final vortex state is always composed of two isolated dipoles. Also, due to conservation of the Hamiltonian, and by comparing the final Hamiltonian value at $t \to \infty$ to the initial value at $t \to -\infty$, the final dipole sizes must be such that

$$H = \frac{\kappa^2}{2\pi}\ln(d^2) = \frac{\kappa^2}{2\pi}[\ln(d_1) + \ln(d_2)] \implies d^2 = d_1 d_2, \tag{2.19}$$

where d_1, d_2 are the final dipole sizes once interaction is complete. Thus, if a dipole has increased in size due to the interaction it must be true that the alternate dipole has decreased proportionally to maintain equality to d and hence conserve the Hamiltonian. This can be

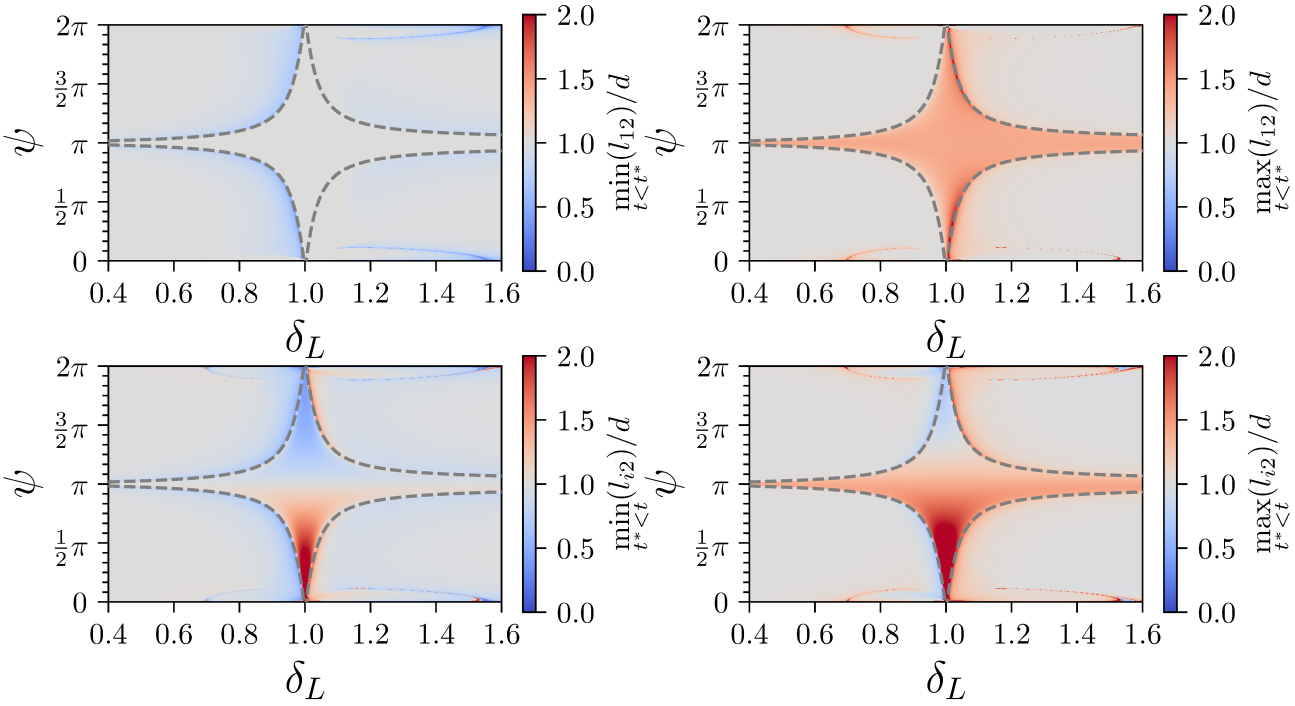

Figure 2.16: Minimum (left) and maximum (right) dipole lengths pre- (top) and post-interaction (bottom) in the non-integrable dipole-dipole collision. Results are plotted as colourbars to the right of each corresponding plot, with region boundaries marked by grey dashed lines.

observed in figure 2.17 from the symmetry of the two dipole distance, confirming that the product of normalized distance equals 1 for all values of the parameter ψ and δ_L. Moreover, we see by averaging over the parameter range there is no preference in the creation of larger or smaller dipoles, as due to the discussed conservation (i.e. equation (2.19)) the creation of a smaller dipole will inevitably lead to the creation of a larger dipole also, leading to an average final dipole separation of d. For the non-integrable dipole-dipole collision, the closest dipole we see formed over our parameter space is of size $0.016d$ at parameters $\psi = 6.28319$ and $\delta_L = 1.00188$, which is an extreme configuration of two closely chasing vortex dipoles aligned along the same axis of propagation. In summary, we found the non-integrable collision of two dipoles to be the simplest collision where dipoles can become significantly larger or smaller than the initial dipole as a result of the interaction, this was not possible in previous cases due to the integrals of motion required. These integrals of motion are maintained whilst dipoles change size after interaction by the opposing change of dipoles (in other words one dipole shrinking whilst the other expands). Moreover, we also have shown that close to the direct and exchange interaction boundary is where all the complex interactions occur. This is no more apparent than in the non-integrable dipole-dipole collision where we have shown examples of a wide

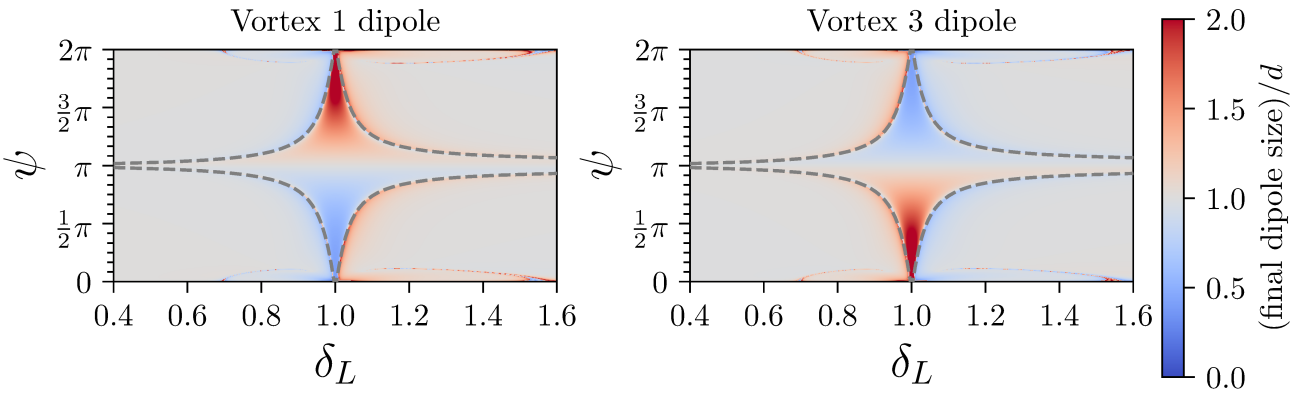

Figure 2.17: Final dipole separations post-interaction of each vortex dipole (identified by containing vortex 1 or 3). Each heatmap shows the normalized dipole size by the initial dipole separation d. The boundary between the main direct-exchange region is shown by the grey dashed curve.

array of complex interactions involving the formation of quasi-stable three vortex structures and the like. Furthermore, we have shown that direct scattering of a dipole is stronger when with an isolated vortex due to the weaker decay ($\propto 1/r$) of an isolated vortex compared to a secondary dipole $\propto 1/r^2$, note that dipole interactions are anisotropic, so specific quantities may vary given differing parameters of the interactions. We now extend this investigation to more complicated dipole interactions, as well as how they may apply to turbulence as a whole.

Chapter 3

Large N point vortex statistics

3.1 The dipole-cluster collisions

Now the final collisions that are fundamental to the evolution of larger point vortex clouds yet to be considered are the dipole-cluster collisions. Here we will consider the collision of a vortex dipole with a coherent rotating vortex structure composed of two or more same-signed vortices. We will henceforth refer to these structures as vortex clusters of size m, where m is the number of point vortices forming the vortex cluster. The most simple possible cluster is the $m = 2$ case, which when considered interacting with a vortex dipole results in a four vortex collision. By the analysis in section 2.3.1 this four vortex system cannot be integrable; the condition $\sum_{i=1}^{4} \kappa_i = 0$ can never be fulfilled assuming $\pm\kappa$ vortex circulations due to clusters being comprised of vortices of the same sign, and so we must restrict ourselves to a numerical analysis of these more complicated $m \geq 2$ cluster collisions. Also, we will restrict investigation to symmetric clusters of $m = 2, 3, 4$ vortices, each of circulation κ; we label these clusters as C_m. These interactions are then much more complicated than those already considered, so questions arise that it was not necessary to answer in previous cases. For example what new interactions may be possible? How does the introduction of clusters affect the stability of the dipole? And is the dipole changing size persistent with the addition of a cluster and if so how does this relate to the previous persistent dipole growth/shrinking in the non-integrable dipole-dipole interaction? Also, the stability of the cluster is of interest, there may be interactions that do not result in the coherent cluster persisting once interaction is complete, as due to the additional degrees of freedom present the Hamiltonian is thus more easily conserved.

There is also the possibility of approximation of these collisions as a dipole-vortex interaction similar to that found in section 2.2 (except here the isolated vortex will be of circulation $m\kappa$ to match the mean strength of the cluster). If this is possible it may greatly simplify larger point vortex systems, as these vortex-cluster collisions lead to far more complex dynamics than those examined so far, and are more relevant in larger vortex configurations that more appropriately resemble turbulent flows. Our analysis will be useful as we try to examine turbulent vortex interactions as a series of fundamental vortex collisions.

3.1.1 Dipole-cluster scattering

As is now standard we present a schematic of the initial configuration used in analysing the collision of a dipole with a C_m cluster in figure 3.1. Also, the initial configurations for the symmetric structures are given for the $m = 2, 3, 4$ cases. Similar to previous cases, the dipole is initially separated a distance d, with the dipole and C_m cluster horizontally separated a much larger distance of L. The dipole is set up to propagate towards the rotating cluster, with ρ representing the vertical distance from the center of the cluster and the dipole, with negative ρ implying the dipole center y position is lesser than the cluster y position at the initial position in time. Each C_m cluster is initialised as a regular convex m-sided polygon, appropriately sized such that the cluster rotation circumscribes a circle of diameter d. Also introduced is an additional variable ξ that represents the rotational phase of the cluster, with $\xi = 0$ taken to be the standard orientation of the cluster as displayed in figure 3.1, and hence, each cluster will have rotational symmetry isomorphic to the cyclic order of group m.

First we investigate the possibility of approximating the dipole-m-cluster collision by the appropriate dipole-m-vortex collision. To do this we perform direct numerical simulations of the dipole-m-cluster collisions using the initial setup as described in figure 3.1 using the numerical method as described in appendix A.2 and compare these to the dipole-m-vortex collisions set up similarly to figure 3.1 but with the m-cluster replaced with a single vortex of circulation $m\kappa$. This represents a generalised case of the three-vortex interaction as described in section 2.2. For large values of the impact parameter ρ it is expected that the two setups will result in similar dynamics due to the mean-field interactions of the cluster being closely approximated by an m-vortex. For more extreme collisions at lower impact parameters it is unclear how

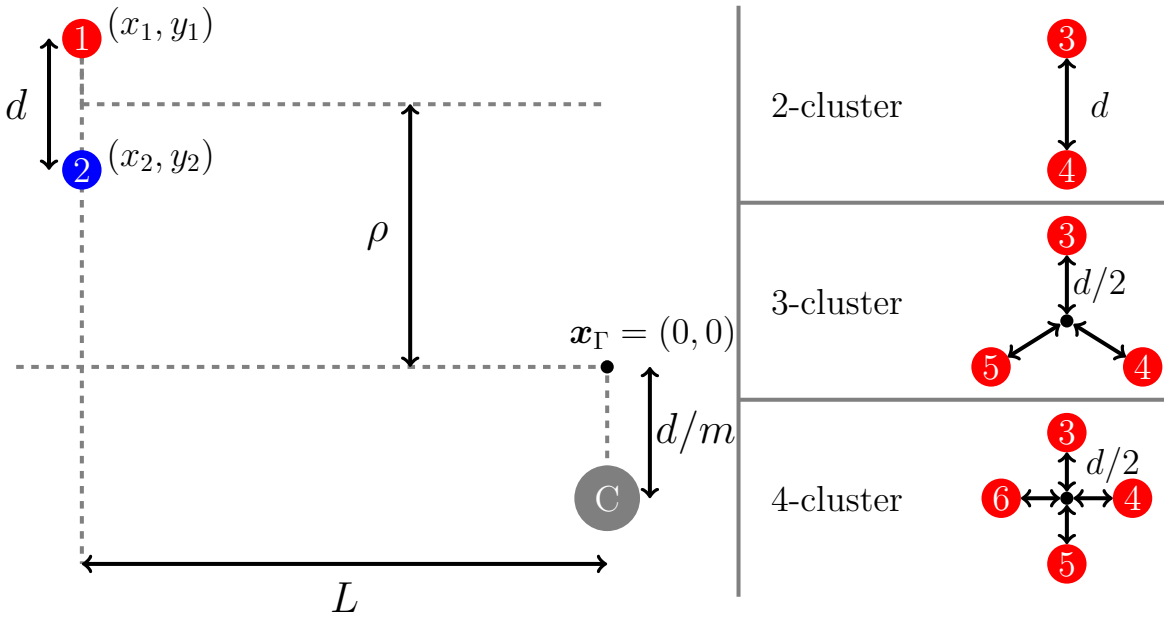

Figure 3.1: Initial setup of the dipole-cluster collision. Vortices 1 and 2 form a dipole of size d situated a distance L from the cluster C. The quantity ρ acts as an impact parameter, measuring the vertical distance from the centre of the vortex dipole to the centre of circulation. Vortices are displayed as circles with each vortex coloured according to the sign of its circulation, with each vortex marked according to our chosen numbering. The cluster is marked as a grey circle marked C. The cluster structures C_2, C_3, C_4 we use are presented on the right.

well the analogy will hold. The cluster will permit vortex stretching in the sense that cluster vortices are free to rearrange themselves, either by compression or expansion, and may in some cases separate altogether. This behaviour, dependent upon the fine internal structure of the rotating cluster, cannot be replicated by a structure as simple as a lone isolated vortex. Sample trajectories of the complex interactions observed in the vortex-cluster simulations of C_3 are presented in figure 3.2, where we observe the familiar behaviours of direct and exchange scattering in the top row, with the dipole being deflected with only minimum deflection in the case of direct scattering, and the dipole structure breaking apart and reforming with an alternate positive vortex from the cluster then propagating off in the case of exchange scattering. The bottom two trajectories demonstrate more complex interactions not previously encountered; and that are directly a result of the increased degrees of freedom due to the addition of the cluster allowing conservation of the Hamiltonian within these complex interactions. On the bottom left we see interaction of the dipole with a cluster, leading to the break-up of the vortex cluster into two distinct structures: two positively signed C_2 structures, rotating in a continual expanding spiral in long-range interaction with the isolated anti-vortex. This of course is not possible in the dipole-$m\kappa$-vortex collisions, as this "cluster disintegration" depends upon

the internal structure. This never-ending spiral expansion is reminiscent of a time-reversed trajectory of a self-similar vortex collapse such as those described in [102]. Here we see self-similar solutions of vortices spiralling logarithmically towards a center point. When considering the time-reversed trajectory of our "cluster disintegration", we see vortices (if we allow a C_2 cluster to represent a 2κ vortex) spiralling towards the center of vorticity – a potential vortex collapse – however a vortex dipole is then formed which then propagates off to infinity, possibly due to the vortex collapse being unstable, a small perturbation may disturb the vortex collapse spiral and lead to the dipole and cluster formation.

In the bottom right we have an example of what we refer to as a pseudo-exchange interaction: where the dipole undergoes a series of vortex exchanges with vortices of the cluster, but ultimately leaves the cluster as a coherent dipole composed of the same initial two vortices. We often see as part of such interactions an initial exchange interaction with the entire cluster, leading to an isolated vortex (the initial positive vortex of the dipole) and the anti-vortex propagating with the C_m in a structure similar to a dipole. However, due to the circulation disparity between the anti-vortex of strength $-\kappa$ and the C_m cluster of mean strength $m\kappa$ this structure inevitably spirals back towards the lone vortex, whereupon another exchange takes place and the original dipole is recovered. This is reminiscent of the slingshot effect found in Price [103].

In summary when considering the sample interactions presented in figure 3.2, it is only possible to replicate the direct scattering and pseudo-exchange interactions in the dipole-$m\kappa$-vortex collision, as it is these interactions that the internal structure of the cluster does not influence evolution of the system. A true exchange scattering process can never occur in the dipole-$m\kappa$-vortex interaction, due to the stronger $m\kappa$ circulation of the initially isolate vortex, any exchange must always spiral back towards the κ vortex, and so after an exchange the initial dipole is recovered in a pseudo-exchange interaction. Interestingly, the generalised dipole-$m\kappa$-vortex collision remains an integrable system, giving hope for new analytical results that are applicable for vortex-cluster collisions for large impact parameters.

In order to classify regions of scattering, in figure 3.3 we plot a colourmap indicating the parameters where the various types of vortex dynamics occur in the dipole-cluster interaction with respect to the impact parameter ρ and the cluster phase ξ. We see the majority of

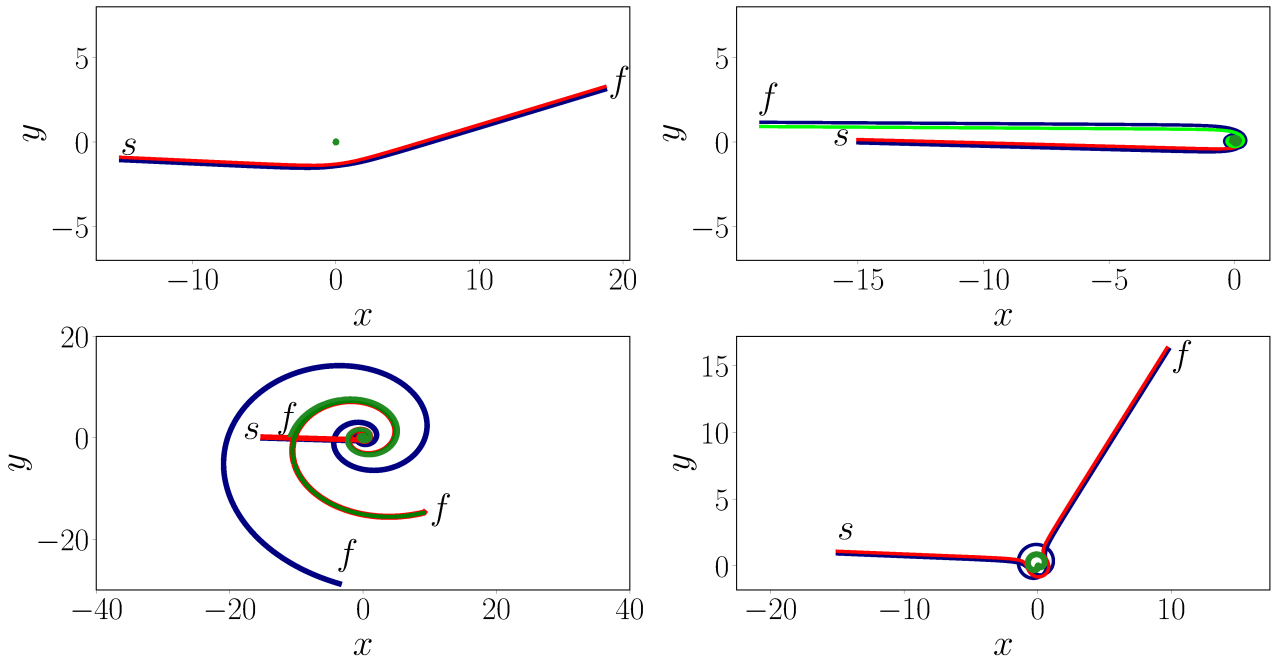

Figure 3.2: Sample trajectories of the dipole and C_3 interaction for four parameter sets. The dipole is initialised a distance of $L = 15$ in each case such that the phase of the cluster is the same for each trajectory, we then have impact parameters as such; top left $\rho/d = -5$, top right $\rho/d = 0.25$, bottom left $\rho/d = 0.275$, bottom right $\rho/d = 5$. Dipole vortices 1 and 2 are given as red and blue curves respectively, whilst the remaining 3 vortices initially forming the cluster are given as green curves. The start and finish points of the simulation in each case are denoted as s and f.

scattering as either direct or pseudo-exchange, for all values of m; we see a clear transition from direct scattering to our pseudo-exchange process that varies little across the phase ξ that echoes the type of behaviour expected to be found in the dipole-$m\kappa$-vortex collision where ρ is not close to 0, thus the dipole-cluster dynamics can be approximated by the dipole-$m\kappa$-interaction. However, note that we observe interesting phenomena near the "head-on" impact parameter value $\rho = 0$, where we see a complex band of exchange interactions as well as pseudo-exchange. The bottom row of figure 3.3 shows zoomed in images of the interaction types around this key $\rho = 0$ parameter value for each vortex size considered.

Around this value of the impact parameter we observe several complex band patterns of exchange and pseudo-exchange regions interlaced with regions of direct scattering. Note in each case there is only a single band of exchange/pseudo-exchange scattering, this band wraps around in the C_3 and C_4 cases due to the rotational periodicity of the phase ξ. As the cluster size increases this band is stretched diagonally across the parameter space, and as m increases we observe that this complex region has an extruding tail that becomes thinner meaning an

increasing majority becomes direct or pseudo-exchange scattering, so an increased probability of the outgoing dipole being comprised of the same vortices as the initial. The tail here is mottled with pseudo-exchange regions and exchange scattering, appearing at scales comparable with the resolution used to scan the parameter space, highlighting the possibility that lower resolutions could show even finer detail. It is particularly surprising in the context of the full ρ/d parameter space how small the parameter range for exchange scattering is. In each case the impact parameter range where exchange scattering is possible is a fraction of the original dipole distance d, this indicates exchange scattering is very unlikely to occur in the dipole-cluster collisions, instead it is of high probability that the original dipole remains once interaction is complete.

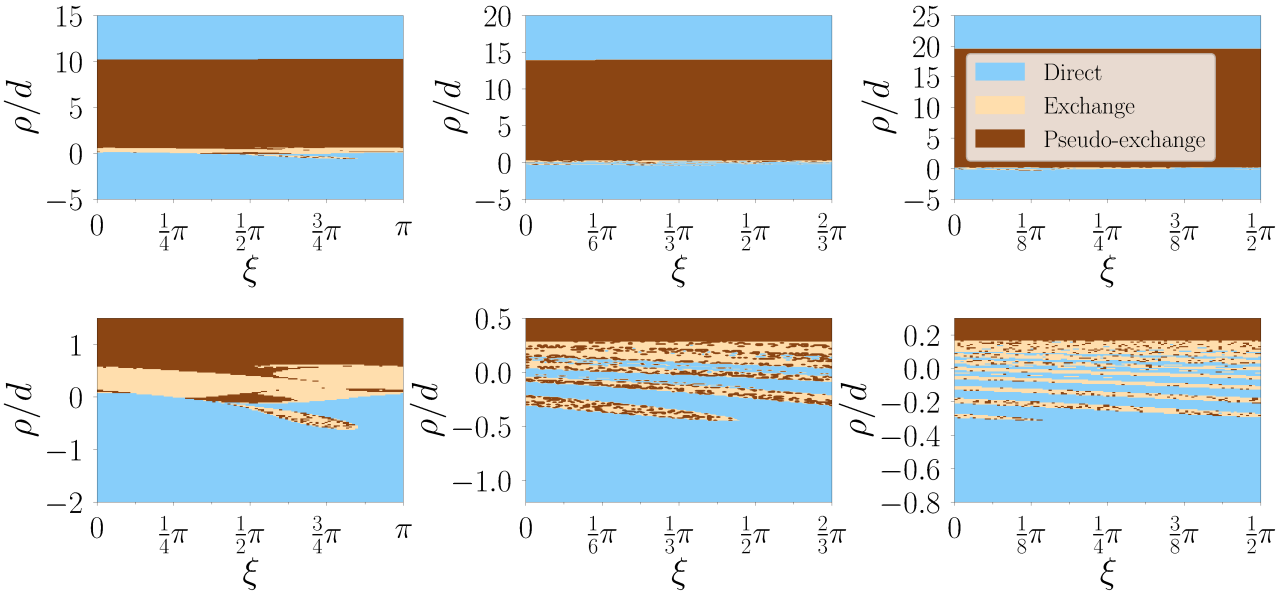

Figure 3.3: Colourmaps of the dipole-cluster interaction types across the phase ξ and ρ/d for $m = 2, 3, 4$ (left, center, right). Bottom row are zoomed images of the top row. Direct scattering and exchange scattering are marked in blue and yellow respectively, whilst the new pseudo-exchange interaction type is marked in brown.

3.1.2 Scattering angles

Here we test the approximation of a dipole-m-cluster collision with a dipole-$m\kappa$-vortex collision in the context of the scattering angles. We will compare the scattering angles in each collision and observe both the overall results and how well the approximation holds. In figure 3.4 we plot the dipole-m-cluster and dipole-m-vortex scattering angles versus the normalised impact parameter ρ/d for the prescribed cluster sizes $m = 2, 3, 4$ (left, middle, right). Three sets of

results for different cluster phases ξ are plotted and labelled C_m^ξ, with each set of ξ selected such that the three phases are equally distributed across the period of rotation; for $m = 2$ the three phases are uniformly distributed over $\xi \in [0, \pi)$, for $m = 3$, we plot three phases uniformly distributed over $\xi \in [0, 2\pi/3)$, and for $m = 4$, we plot three phases uniformly distributed over $\xi \in [0, \pi/2)$. Additionally, in each case of m the phase averaged scattering angle results $\langle C_m^\xi \rangle$ are plotted. In all data considered a coherent dipole and C_m cluster remains once interaction is complete (all cluster disintegration dynamics are excluded). Also in figure 3.4 we plot the scattering angles found in the respective dipole-m-vortex collisions as blue curves. The background colours are used to indicate regions of direct scattering (Regions I and III) and pseudo-exchange scattering (Region II) found in the dipole-$m\kappa$-vortex simulations.

Agreement between the dipole-$m\kappa$-vortex and dipole-m-cluster scattering angles is observed across virtually the entire range of impact parameters, highlighting that the approximation may be even better than first thought. Indeed, only minor discrepancies are observed in a small band of impact parameter values around the asymptotic region close to $\rho/d = 0$ of width approximately d. It is somewhat surprising how well the approximation holds even close to this band near $\rho/d = 0$, as we would expect the extra degrees of freedom enabled by the cluster vortices would allow for more exotic dynamics here. Even in the somewhat complicated pseudo-exchange interactions we observe agreement between the dipole-cluster collisions and the corresponding approximations. In the extremes of the parameter range we observe what we would expect, as here we see total agreement between results as expected with any deviations completely indistinguishable. This confirms out hypothesis that for large parameters the three vortex description is an appropriate approximation.

Summarising, we can conclude that the $m\kappa$ vortex can approximate the m-cluster even better than first thought. The only seemingly significant discrepancies between the cluster collisions and our approximations occur in a small region corresponding to a "head-on" collision of the dipole with the vortex cluster, this is perhaps explained with reference to figure 3.3, for it is only in this impact parameter range that the exchange scattering process is possible, and as this is not possible in the dipole-m-vortex collision we must indeed observe different dynamics here.

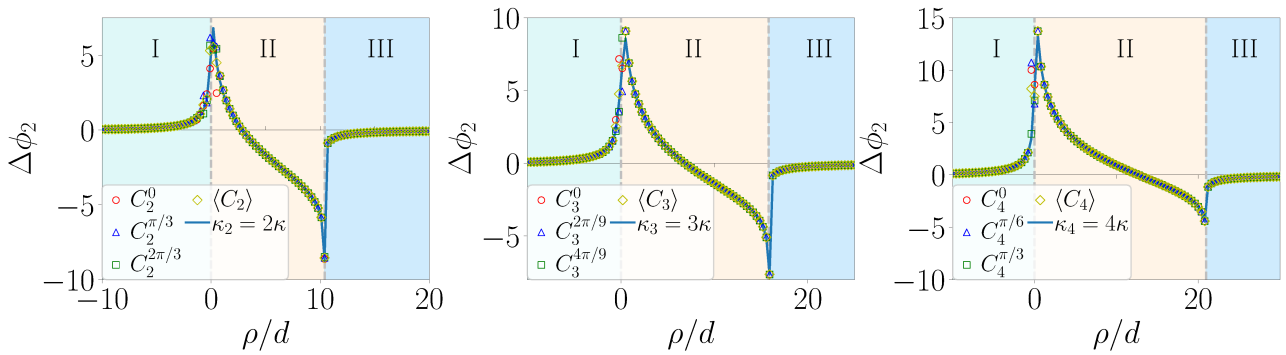

Figure 3.4: The dipole-cluster (markers indicating different phases) and dipole-$m\kappa$-vortex (solid blue curve) scattering angles compared for $m = 2, 3, 4$. Regions I and III indicate direct scattering and region II pseudo-exchange scattering in the dipole-$m\kappa$-vortex simulations. Vertical grey dashed lines indicate numerically observed boundaries between the regions of interaction.

3.1.3 Final dipole size

A natural consequence of considering vortex-cluster collisions is an increase in the number of degrees of freedom from the systems investigated in previous sections, with degrees of freedom increasing as m increases. This implies that energy conservation is more easily satisfied because of this, and so consequently it might be expected that dipole-cluster collisions can lead to a greater variety of post-interaction dipole (and cluster) sizes, as the cluster may more easily change shape to accommodate more extreme dipole growth/shrinkage. These additional degrees of freedom also result in an increased entropy of the system as a result of the increased energy (i.e. Hamiltonian (1.32)) resulting in a less ordered system.

In figure 3.5 the final separation of the post-interaction vortex dipole is plotted for each cluster that we consider. Here the dipole separation is measured once the dipole has traversed a distance such that the interaction may be considered complete, we use the value of $L + 100d$ here, although any sufficiently large value relative to the initial L and d parameters should suffice. We observe from this several band patterns similar to those seen in figure 3.3 across the same values of parameters (for larger impact parameters than what is shown we simply observe the dipole relaxing back to the original d separation). The striations show similarity to fingers of Saffman-Taylor instabilities [104], although a physical explanation for why this is the case is unclear

Note that only a small region of the parameter range is plotted, again a similar band to that found in the zoomed in images of figure 3.3, as this is the only region where variable dipole sizes

are found once interaction is complete. This is testament to the close approximation to the dipole-$m\kappa$-vortex, as in the case of the dipole-$m\kappa$-vortex persistent change of dipole separation is not possible due to energy conservation (due to being a three vortex interaction) so persistent growth in the dipole-cluster cases can only occur in the region of width approximately d about the origin $\rho/d = 0$ where the approximation breaks down. This then implies the growth or shrinking of a dipole once the interaction is completely is due to direct interaction of the dipole with the cluster core. Also, we can see through direct comparison with figure 3.3 the dipole changes size in precisely the same banding regions of interaction, and we see direct scattering correlated to a shrinking of the dipole size, and we see the dipole growing in regions of exchange scattering. This is interesting, as we observe in previous cases e.g. figures 2.4 and 2.9 the dipole also has a propensity at the critical point to become closer for direct scattering and becoming larger for exchange scattering before relaxing back to the initial d value. This is the same behaviour we then observe in the dipole-cluster scattering, except here due to the additional degrees of freedom introduced by the cluster the dipole now is not required to relax back to d once interaction is complete. Also, similar to previous cases we see that in direct scattering we only have a change in dipole size in parameter regions close to the interface between direct and exchange scattering.

When considering the interaction of the three-cluster C_3 we are faced with the cluster disintegration phenomena; an example of which has already been given in figure 3.2 (bottom left), leading to a large and expanding multi-vortex structure. There is hence no coherent dipole once interaction is complete and a concept of "final dipole size" will hence be meaningless here, hence we colour these regions black in figure 3.5. As can perhaps be expected by this point, cluster disintegration only occurs in the small parameter range about $\rho/d = 0$ where the dipole-$m\kappa$-vortex approximation breaks down, and we only observe this phenomenon in the C_3 case. We can speculate that this may be the result of the odd number of vortices present in the cluster, as the disintegration of the C_3 into two expanding C_2 cluster can be considered approximate to the time-reversed vortex collapse solution of three vortices with circulations $(-2, -2, 1)$ as found in [102]. It may be that similar collapse solutions do not necessarily exist for the C_2 and C_4, as these cannot break up into an even distribution of clusters that may be required for such cluster disintegration phenomena.

Our final dipole sizes here can be considered analogous to the critical point separation of the dipole (as there is no need for the dipole to relax here back to d it is only necessary to consider these values). Thus, the final dipole sizes can act as proxy for the dipole minimums/maximums and can show whether annihilation may be possible or not here. In our simulations, we observe that in the C_2 case we have a maximum final dipole size of $6.18d$ and minimum of $0.35d$, in the C_3 case a maximum of $4.82d$ and a minimum of $0.15d$, and in the C_4 case a maximum of $4.16d$ and a minimum of $0.11d$. This indicates that the larger the cluster the more the dipole-vortex can shrink in size. Any change in the final dipole size must be compensated by a corresponding change in the cluster configuration in order to conserve the total energy of the system. In principle, an increase of the final dipole will result in the expanding of the vortex cluster and vice-versa.

We note that with regard to the scattering angles in figure 3.4 we have significant dipole scattering through a large portion of the parameter range, for parameter values much larger than we observe the dipole growing or shrinking in size, the expansion or contraction of the dipole occurs only in a small subsection of this region. Moreover, it appears that the size of the region in which the dipole may change size after interaction decreases as the number of vortices in the cluster increases. For example, in the C_2 case the effective range for change in the dipole size is between $-1.5 < \rho/d < 0.6$ whereas in the 4-cluster case this is reduced to $-0.6 < \rho/d < 0.2$, reducing almost a third in size. This is perhaps due to the increased impulse on the dipole by the cluster reducing the ability of the internal structure of the cluster to have an effect. This is in direct contrast to the earlier phenomena observe of the dipole-dipole interaction, in which dipole creation was possible for a decently large portion of the parameter space. Hence, we can conclude that the non-integrable dipole-dipole collision is much more effective at producing a smaller or larger dipole once interaction is complete than the dipole-cluster collisions, and increasing the strength (i.e. number of vortices m) of the cluster only exacerbates this effect. Additionally, we have observed that in certain dipole-cluster collisions there may not exist a coherent dipole whatsoever once interaction is complete.

We can also check the final cluster size in the case of dipole-cluster interactions. In figure 3.6 we plot a measure of the final cluster size (3.1), across the same parameter range as figure 3.5.

The cluster size l_{C_m} is defined by first computing the center of circulation (or the center of

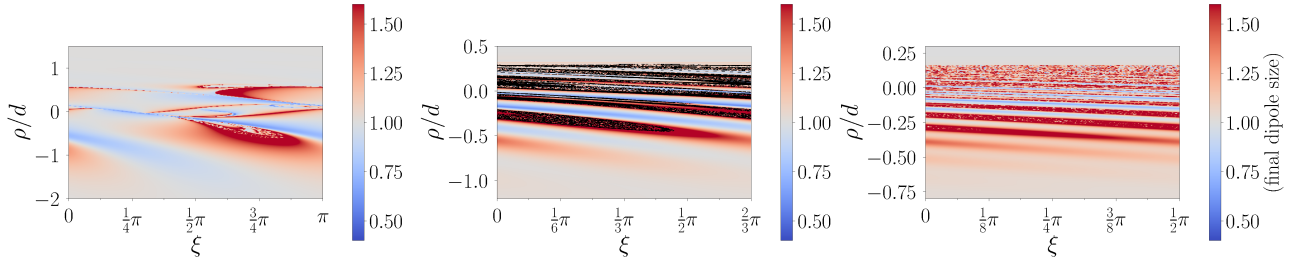

Figure 3.5: Final dipole separations normalised by the initial dipole separation d of the dipole-cluster collisions with $m = 2$ (left), 3 (center), 4 (right). Only for the $m = 3$ cluster simulations do we observe disintegration of the vortex dipole and the vortex cluster indicated by regions coloured in black.

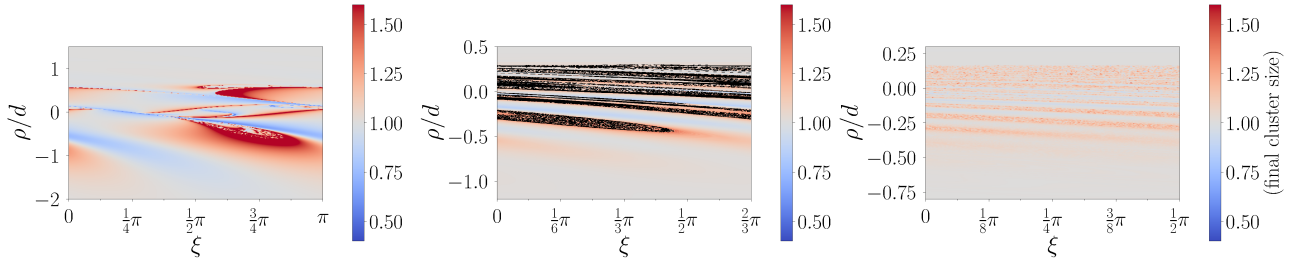

Figure 3.6: Final cluster separations normalised by the initial dipole separation d of a dipole colliding with a 2,3, and 4 cluster respectively, shown as a heatmap against the general normalised coordinates ρ/d and L/d.

the cluster in other words) and then taking average vortex separation distances of the vortices within the cluster to that center:

$$l_{C_m} = \frac{1}{m}\sum_{i=1}^{m}\sqrt{(x_i - \bar{x})^2 + (y_i - \bar{y})^2}, \tag{3.1}$$

where $\bar{x} = (1/m)\sum_{i=1}^{m} x_i$, and $\bar{y} = (1/m)\sum_{i=1}^{m} y_i$ with the summations taken only over the vortices within the cluster. We observe comparable results to those presented in figure 3.5. First examining the case of C_2 we observe exact agreement between the final dipole size and the final cluster size, this is to be expected as we have an equal number of vortices in both the dipole and the cluster, thus energy conservation requires that as $t \to \infty$ it must be that (final dipole size) = (final cluster size). In other cases where $m > 2$ this is not the case, as due to the increased number of vortices the dipole has to expand or contract less in order for energy conservation to be satisfied by offsetting the equivalent energy offset produced by an expanding or contracting vortex dipole. This comes clearly from energy conservation as required by the Hamiltonian, as the product of the lengths between vortices in the cluster must

increase proportionally to an increase in the size of the dipole, this means that as the final dipole size increases/decreases, each individual length between cluster vortices will increase/decrease to a lesser extent as the number of vortices in the cluster m increases. This behaviour is a characteristic of a dual cascade turbulent system. The vortex interaction can lead to a tightening of a vortex dipole which is an analogy of creating finer scale fluctuations (direct cascade of enstrophy) in a fluid flow. This is compensated by a more coherent vortex cluster at the largest scales (inverse cascade of energy). We speculate that these two processes occurring simultaneously is a principle outlined by Fjörtoft [105] for the development of a dual cascade between enstrophy and energy in 2D turbulence, although the extension from the current work to the Fjörtoft argument is not mathematically rigorous and is more speculative, developing this more formally may be an interesting area of future study.

Additionally, we can check the distribution of the final dipole sizes of the dipole-cluster collisions over the parameter range. Here, we use the technique of kernel density estimation, using a grid size of 1000 and a Gaussian kernel function to estimate the distribution from the final dipole values in figure 3.5. In figure 3.7 we present the results of this kernel density estimation to approximate the probability distributions of the final dipole sizes for each size cluster we are considering. Note that in the C_3 case we exclude interaction regimes where there is no coherent dipole after interaction. We must also restrict the interval of impact parameters considered, as this removes a delta-function peak situated at size d as a result of infinite states in which the dipole will propagate past the vortex cluster at far distances with no change. Thus, we restrict the impact parameter as $-1.5 < \rho < 2$ in the C_2 case, $-1.2 < \rho < 0.5$ for C_3, $-0.8 < \rho < 0.3$ in the C_4 case we get the sense of the likelihood of increase or decreasing the dipole size. We compute the expected dipole size post-interaction, the variance and skewness of

Table 3.1: Basic statistical measures of the probability distributions found in 3.7; the expected value, variance and skewness are calculated for each case of C_i.

	C_2	C_3	C_4
$\mathbb{E}$[(final dipole size/d)]	1.07	1.12	1.19
Var[(final dipole size)/d]	0.0498	0.0767	0.104
Skew[(final dipole size)/d]	4.01	2.42	1.85

the finale dipole sizes from our kernel density estimates in table 3.1 to provide a better picture

of the statistics of these distributions. We see an increase in both the mean and variance as the size of the cluster grows, perhaps due to the increased amount of the parameter space contained in the chaotic band as shown in 3.5. We also observe a positive skewness for each case that decreases as the cluster size increases, indicating the dipole size is mostly likely to grow rather than shrink as result of the scattering, although this effect is less pronounced as cluster size increases. The reason why there is a higher propensity for the dipole to grow in size is unclear, but is consistent with previous results in the dipole-vortex collision (which as discussed can provide a valid approximation to dipole-cluster dynamics) regarding the dipole minima/maxima in figure 2.5, where we see for the majority of the parameter range the dipole can only grow in size over the interaction. The dipole-cluster collision can then be considered an extension of this where the dipole size is not required to relax to the initial value here, and so dipoles are more likely to grow in size persistently than shrink. In all cases the mean values are close to unity, and the likelihood that these values contain minor errors from the parameter space resolution of our numerical procedure is strong, nevertheless we have clear evidence of a higher propensity for dipoles to grow due to the collisions considered.

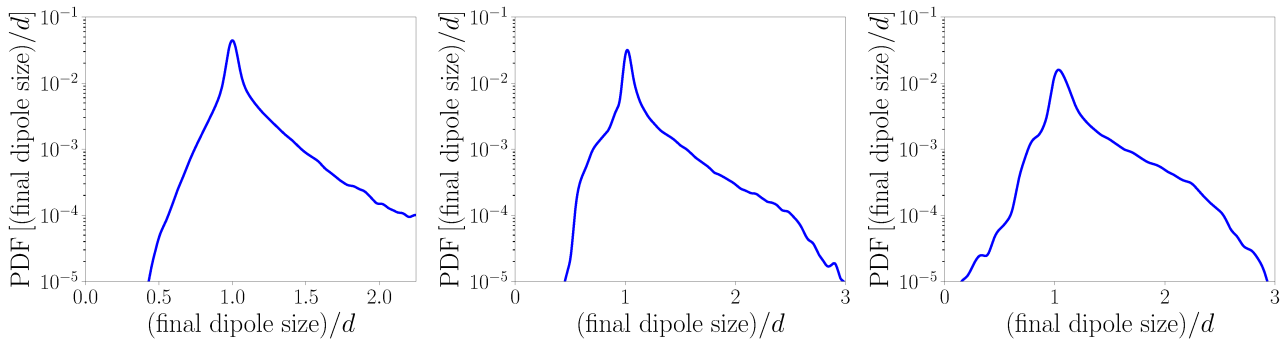

Figure 3.7: Probability density functions of the final dipole separations in the dipole-cluster interaction with C_2 (left), C_3 (middle), and C_4 (right).

3.2 Two-dimensional turbulence by the point vortex model

In chapter 2 and the previous section 3.1 we have considered the various basic dipole interactions present in the point vortex model. More specifically we have considered both the fundamental collisions of vortex dipoles with vortices, clusters, and other dipoles, with the intention of providing a framework of understanding larger point vortex assemblies. Here we will conduct a

preliminary study into large N point vortex systems to consider how they relate to turbulence as a whole. Of particular interest are how large point vortex systems relate to classical features of turbulence, and under what circumstances these features may form in the point vortex model and how they may continue to persist in the flow. Such an investigation may be invaluable for creating a greater understanding of large scale point vortex statistics as a whole.

Turbulence by and large is a certain fluid motion whereupon the idea of providing a theory precisely describing the velocity and fields (i.e. the solutions to the Navier-Stokes (1.4-1.5)) is hopeless. Hence, any theory regarding turbulence is rendered statistical in nature as an inevitability. The specific statistical theories regarding turbulence have taken many forms throughout history, such that they are beyond the scope of the current work; we hence leave description of these to such works as that by Sreenivasan [106], and instead focus upon a statistical theory now considered fundamental to turbulence, the energy cascade. We first introduce some fundamental statistical quantities of the fluid flow as given in [43].

Given the Navier-Stokes momentum equation (1.4) with the addition of a linear frictional damping term, we have:

$$\frac{\partial \boldsymbol{u}}{\partial t} + \boldsymbol{u} \cdot \nabla \boldsymbol{u} = -\nabla p + \mu \nabla^2 \boldsymbol{u} - \alpha \boldsymbol{u} + \boldsymbol{g}, \tag{3.2}$$

where the velocity field $\boldsymbol{u} = \boldsymbol{u}(x, y, t) \in \mathbb{R}^2$, the pressure term $p = p(x, y, t)$, the derivative $\nabla = (\partial/\partial x, \partial/\partial y)$ and the forcing term $\boldsymbol{g} = \boldsymbol{g}(x, y, t) \in \mathbb{R}^2$ and viscosity $\mu \in \mathbb{R}$ are similar to the previous equation (1.4), here we also have the linear damping term $-\alpha \boldsymbol{u}$ where $\alpha \in \mathbb{R}$ representing friction at large length scales. Note also it is taken that $\rho = 1$ which automatically satisfies the incompressibility condition. The stream function is then introduced $\psi(\boldsymbol{x}, t)$ so that $\boldsymbol{u} = (\partial\psi/\partial y, -\partial\psi/\partial x)$. The scalar vorticity field can then be written instead as $\omega = \nabla \times \boldsymbol{u} = -\nabla^2 \psi$ and the previous Navier-Stokes (3.2) becomes

$$\frac{\partial \psi}{\partial t} + \boldsymbol{u} \cdot \nabla \omega = \mu \nabla^2 \omega - \alpha \omega + g, \tag{3.3}$$

where the forcing term has become $g = \nabla \times \boldsymbol{g}$. Considering the invariants of the system of equation (3.3); we first have the kinetic energy $E = (1/2)\langle u^2 \rangle = (1/2)\langle \psi \omega \rangle = (1/2) \sum_{\boldsymbol{k}} |\hat{\omega}(\boldsymbol{k})|^2 / k^2$, where $\hat{\omega}(\boldsymbol{k})$ is the Fourier space representation of vorticity defined at wave vector $\boldsymbol{k} = [k_x, k_y]$,

defined through the usual 2D discrete Fourier transform

$$\hat{\omega}(\boldsymbol{k}) = \frac{1}{MN}\sum_{x=0}^{M-1}\sum_{y=0}^{N-1}\omega(x,y)\exp\left[-i2\pi\left(\frac{k_x}{M}x + \frac{k_y}{N}y\right)\right],$$

here $k = \sqrt{k_x^2 + k_y^2}$ and $\langle ... \rangle$ gives the spatial average. The Fourier space representation is advantageous to use when considering turbulent dynamics, as energy transfer amongst length scales can be considered through the energy spectrum

$$E(k) = \pi k \langle |\boldsymbol{u}(\boldsymbol{k})|^2 \rangle, \tag{3.4}$$

this is the scalar energy per unit mass possessed by the particular wave number k which then gives a picture of how energy is distributed from smaller length scales (high k) to larger length scales (small k) and from this the kinetic energy can be recovered through $E = \int E(k)dk$. The second invariant of motion is the enstrophy defined as $\Omega = (1/2)\langle\omega^2\rangle = (1/2)\sum_{\boldsymbol{k}}|\hat{\omega}|^2$, this can be informally thought of as a sort of kinetic energy equation but applied instead to the curl of velocity rather than velocity itself, and thus represents both a sort of kinetic energy of rotational movement (i.e. movement due to vorticity) and the fluid dynamics analogue of the electrodynamic Yang-Mills action [107]. The enstrophy can be recovered through the energy spectrum through $\Omega = \int k^2 E(k)dk$.

Both invariants of motion and the energy spectrum are directly connected to the dissipative effects of the fluid, we can obtain the dissipation rate of each, given the case of finite viscosity, zero friction and no external forcing, we have

$$\frac{dE}{dt} = -2\mu\int k^2 E(k)dk = -2\mu\Omega = -\varepsilon_\mu(t), \quad \frac{d\Omega}{dt} = -2\mu\int k^4 E(k)dk = -\eta_\mu(t), \tag{3.5}$$

where ε_μ and $\eta_\mu(t)$ are the scalar dissipation rate of the energy and enstrophy respectively. The enstrophy then continually dissipates with time (i.e. it has an upper bound), and so as $\mu \to 0$ it must be that $\epsilon_\mu(t) \to 0$. This is not however the case in 3D turbulence as noted by Boffetta and Ecke [43], due to other vortex stretching effects found in 3D turbulence. It is this in particular that causes the distinct differences in 2D vs 3D turbulent dynamics, and leads to the fundamental process we consider here, the direct/inverse energy cascade.

Turbulence in general can be defined through the famed energy cascade process. Alternatively termed a "Richardson cascade", this consists of the transfer of energy from larger length scales of the system through to smaller lengths of the system, in effect considering only neighbouring length scales to be interacting and the flow of energy occurring towards smaller length scales ever more rapidly without dissipation between each length scale energy transfer. This process continues until the energy of the system is dissipated through the viscous forces of the fluid motion. Energy is dispersed to smaller scales at the dissipation rate (ε) until at the smallest scales energy is dissipated by viscosity, again at the rate of ε[17]. This process of injection, energy cascade and eventual viscous dissipation is visualized in figure 3.8 again

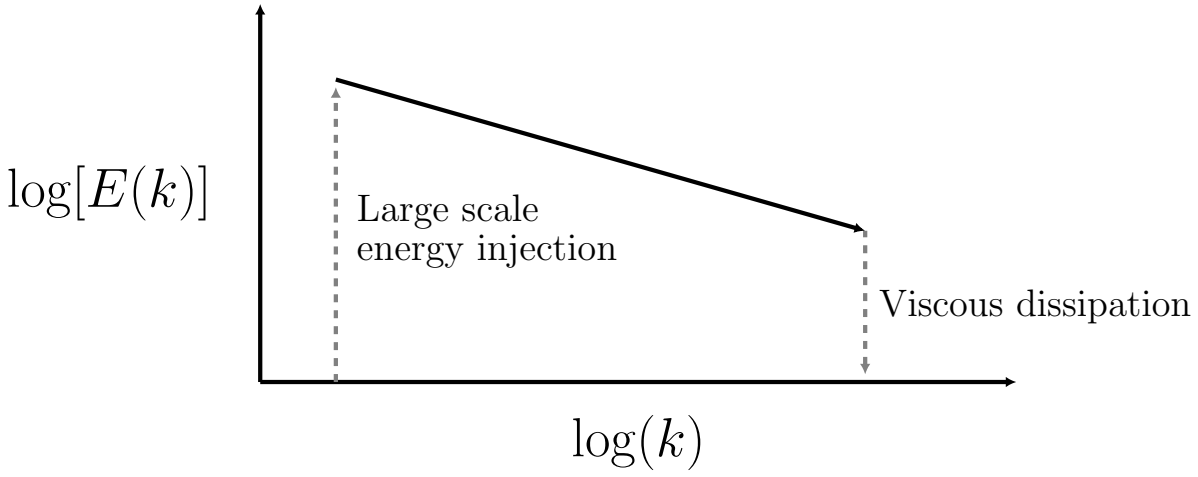

Figure 3.8: The energy cascade fundamental to turbulence. The wavenumber k is plotted log-log against the energy spectrum $E(k)$. Grey dashed lines display energy transfer due to energy injection and viscous dissipation.

with k is the wave number, the magnitude of the wavevector $\mathbf{k} \in (2\pi/L)\mathbb{Z}^3$ defined by the transform from physical space to Fourier space (with L the width of the periodic box assumed in such a transform). A smaller wavenumber implies a larger scale eddy in physical space. The range of k between the smaller wavenumbers corresponding to energy production and the larger wavenumbers corresponding to dissipation (neither of which pictured here) is termed the "inertial subrange" and is where the energy cascade is seen to take place. The energy spectrum in the inertial subrange when plotted log-log shows a straight line, implied by the 5/3 power law by Kolmogorov, a famed result in turbulence theory[17]:

$$E(k) \sim \varepsilon^{2/3} k^{-5/3}.$$

This energy cascade through the length scales can be considered fundamental to turbulence in the three-dimensional case. From the standpoint of statistical mechanics, this cascade process represents the decay of the turbulent state towards an equilibrium state of the system through two mechanisms of energy transfer; the transfer of the mechanic energy of the system to thermal energy by viscosity at higher wavenumbers, and the non-linear transfer of energy from smaller wavenumbers to higher wavenumbers.

In contrast to the case of three-dimensional turbulence, two-dimensional turbulence can be thought of not as a simplification but as an alternative special case altogether due to the behaviour implied by the dissipation equations (3.5). The reduction in dimensionality instead of simply reducing the complexity of the system rather introduces new phenomena to the system entirely, and despite the apparent idealisation of the 2D turbulent system, 2D turbulence has some relevance to actual physical systems found in nature. Two-dimensional turbulence is distinct from the normal case of turbulence, as 2D turbulence instead of holding the ubiquity in nature of 3D turbulence, instead exists as the limit of quasi-2D turbulence. Two-dimensional turbulence provides a good approximation for modelling various quasi-2D phenomena, to the point where introduction of 3D perturbation effects to the 2D turbulent picture (in other words quasi-2D dynamics) maintains the statistical properties of 2D turbulence [43], proving the applicability of the study of an otherwise idealised system. The theory of 2D turbulence in fact has many proven applications in the literature; these flows are ideal applications of two-dimensional turbulent theory due to the large discrepancy in size from the z dimension compared to the much larger x, y dimensions, hence turbulence found in these flows can be considered approximately two-dimensional. Probably the most notable and relevant examples of this are the geophysical flows of atmospheres and oceans [108, 109] where the statistical behaviour of geophysical flows are found to greatly imitate that of 2D turbulence. Also niche cases such as soap film flows exist [110], where again the z dimension of the system is highly restricted compared to that of the x and y dimensions, again showing very similar statistical effects as would be predicted by the idealised 2D turbulent theory

As noted already, the 2D turbulent case has distinctly different behaviour from that of the 3D case. Most notably, in the case of 2D turbulence we have energy transfer to smaller wavenumbers, as opposed to the transfer to larger wave numbers in 3D turbulence. This

phenomenon is known as the inverse energy cascade, where we also have a transfer of vorticity from small wavenumbers to large wavenumbers until the viscous dissipation limit is reached, this is known as an "enstrophy cascade" and was first predicted by Batchelor [111]. Together, the enstrophy cascade and the inverse energy cascade are the distinguishing features separating 2D and 3D turbulence, ensuring not only a reduced system in the 2D case but alternative statistical phenomena entirely. This specifically occurs due to the energy dissipation equations (3.5), in fully developed 2D turbulence energy instead of being dissipated by viscosity is transferred to larger and larger scales, in effect the opposite of the direct cascade, as vortices and eddy currents will continually form larger vortices and eddy currents.

Interestingly the inverse energy cascade has also been observed in 2D quantum turbulence. For example in the work of Reeves [112], where using the standard Gross-Pitaevskii equation with the addition of stationary object potentials to act as forcing and a stationary thermal cloud to act as damping in the system, there exists a regime where clusters grow ever larger as energy is transferred to higher length scales. Thus, this particular Gross-Pitaevskii equation admits an inverse cascade solution, and what has traditionally been thought of as a theory of classical turbulence has been shown to exist in quantum turbulence also, demonstrating turbulence possesses statistical features that may be found in both the classical and quantum cases. There also exists evidence of the enstrophy cascade appearing in quantum turbulence simulated by large scale point vortex simulations with the addition of dissipation and compressive effects [113]. It is then natural to ask whether the inverse cascade method is achievable in the standard point vortex model. The first description of the inverse energy cascade proper is from the work of Onsager, the famed result of large vortex cluster dominating the flow for negative values of temperature [114], with the standard Hamiltonian changed to represent the confined boundaries. This inspired the work of Kraichnan in formulating the original inverse energy cascade theories [115]. In the present day, general theories of the 2D inverse energy cascade have been found for specific point vortex systems, for example the work of Dritschel [116] in finding spectral cascades in the case of point vortices on a sphere, or in the work of [117] where an inverse cascade was found for generalised "rotor vortices" derived from the point vortex model. Here we will seek to capture the inverse energy cascade in a minimal point vortex model, and investigate the necessity of forcing and dampening in achieving this.

3.3 Numerical approach for simulation and analysis of large N point vortex statistics

We seek to analyse the cluster size statistics found in larger point vortex systems over long periods of time under certain forcing conditions such that the inverse cascade can be observed. Under these forcing conditions it is hoped that the inverse cascade is realised and that the energy can be seen propagating to lower wave numbers.

In order to do this we now consider point vortices not in the infinite domain but under periodic boundary conditions. The resulting large N point vortex evolution then forms a closed system where it is impossible for vortex dipoles to propagate off to infinity, thus the number of vortices in a closed box remains constant such that a "true" large N evolution can be observed without dissipation of the system due to dipoles propagating off from the remaining vortices.

In order to do this we utilise a different set of equations for periodic point vortex motion than in the standard infinite domain case, found by summing over the infinite image vortices of the system produced by the periodicity of the region boundaries.

We utilise the equations produced in [118], where the periodic equations of motion are recovered from the infinite domain equations of point vortex motion (1.29), by choosing appropriate limits for the periodic boundaries (scaled such that the box is of height and width 2π) the equations of motion for point vortex i in the system are recovered as an infinite sum

$$\begin{bmatrix} \dot{x}_i \\ \dot{y}_i \end{bmatrix} = \frac{1}{2\pi} \sum_{j=1}^{N} \kappa_j \begin{bmatrix} -S(y_{ij}, x_{ij}) \\ S(x_{ij}, y_{ij}) \end{bmatrix}, \tag{3.6}$$

where the infinite sum function S in 3.6 is given by

$$S(x, y) = \sum_{m,n=-\infty}^{\infty} \frac{x - 2\pi n}{(x - 2\pi n)^2 + (y - 2\pi m)^2},$$

where n are the periodic images in the x dimension and m the periodic images in the y dimension. Noting that the sum in m is absolutely convergent whilst the sum in n is conditionally convergent, by using Laplace transforms and treating the remaining integrals asymptotically and taking the limit to infinity of the partial sums that are independent of the order of the

limit gives for the M and Nth partial sum

$$S_{M,N} = \frac{1}{2}\sum_{m=-\infty}^{M} \frac{\sin(x)}{\cosh(y-2\pi m)-\cos(x)} + \frac{x}{2\pi} - \frac{x}{\pi^2}\tan^{-1}\left(\frac{N}{M}\right), \tag{3.7}$$

all that is left is to decide the physically consistent definition of the limit $M, N \to \infty$. By imposing the condition then that it is necessary for equidistant image vortices to cancel, thus it is necessary that the y velocity on vortex i from vortex j with x_{ij} is 0, and so it must be that $S(\pi, y) = 0$. This implies that the final infinite sum must be chosen such that $S_{M,N}(\pi, y) = 1/2 - (1/\pi)\tan^{-1}(N/M) = 0$, therefore

$$S(x,y) = \lim_{M\to\infty}\left[\lim_{N\to\infty} S_{M,N}(x,y)\right] = \frac{1}{2}\sum_{m=-\infty}^{\infty} \frac{\sin(x)}{\cosh(y-2\pi m)-\cos(x)}. \tag{3.8}$$

By choosing units of time to absorb constants from (1.29) and (3.8) and to rescale κ to unity, we retrieve the following equations of motion

$$\dot{x}_i = \sum_{\substack{j=1\\ j\neq i}}^{N} \kappa_j \sum_{m=-\infty}^{\infty} \frac{-\sin(y_{ij})}{\cosh(x_{ij}-2\pi m)-\cos(y_{ij})}, \quad \dot{y}_i = \sum_{\substack{j=1\\ j\neq i}}^{N} \kappa_j \sum_{m=-\infty}^{\infty} \frac{\sin(x_{ij})}{\cosh(y_{ij}-2\pi m)-\cos(x_{ij})}, \tag{3.9}$$

This is useful due to the speed at which the infinite sum in (3.9) converges, due to how rapidly terms in the sum become small at large $|m|$ in our numerical simulations we are able to truncate the sum to allow calculation without compromising accuracy. This confines the vortices to a 2π periodic box in the x and y directions such that each vortex will have coordinates $x_i, y_i \in [-\pi, \pi)$, here we also assume identical circulations such that $\kappa_i = \pm 1$. We consider N point vortices, where vortices have random positions uniformly distributed in the x and y directions. $N/2$ vortices are initialised possessing circulations of 1 and the other $N/2$ vortices are initialised possessing circulations of -1. This generates the initial condition for the large N simulations, with the system then solved according to the numerical code in section A.2, applied to the periodic equations of motion (3.9).

We evolve the system in each case alone according to these equations, as well as with an additional forcing through the use of a vortex annihilation and reinjection mechanism. If this annihilation and reinjection is included, then at each calculated time step in the system

the data is checked for any vortex dipole within a critical annihilation distance, this dipole is then removed from the system and the dipole vortices are reinjected at random positions under the constraint that the reinjected vortices are separated by the inter-vortex separation $\ell = \sqrt{4\pi^2/N}$. This results in forcing at a wave-number of $k_f = 2\pi/\ell = \sqrt{N}/2\pi$, and a dissipative effect dependent upon the tolerance at which the dipole annihilation is considered at; though these simulations we annihilate dipoles at a separation of $l/4$, meaning dissipation occurs at wavenumber $k_d = (2\pi)/(\ell/4) = 2\sqrt{N}/\pi$.

Once the subsequent time step is calculated we employ a simple cluster finding algorithm. This is defined in terms of two key parameters; the dipole tolerance tol_d and the cluster tolerance tol_c, both of which we set to half the intervortex separation $\ell/2$. Any opposite-signed circulation vortices with a separation within tol_d will be considered a dipole, and any like-signed circulation vortices within tol_c will be considered a cluster. The algorithm is then based on a simple process. Firstly, opposite-signed circulation vortex separations are compared with tol_d such that dipoles are identified. These dipoles are then removed from consideration, i.e. these dipole vortices can never be a constituent of a vortex cluster. We then compare the remaining vortices like-signed circulations with the cluster tolerance tol_c, such that any within the assigned tolerance are considered as clusters, with any remaining vortices not found to be part of either a dipole or a cluster marked as a C_1 structure (in other words a cluster of size 1). Finally, the clusters found are examined, and any two vortices that are not considered part of the same cluster but share cluster vortices are joined into the same cluster. For an example to illustrate this; if like-signed vortices 1 and 3 are not within tol_c of each other but are both within tol_c of vortex 2 (resulting in vortex clusters 1,2 and 2,3) these three vortices are then considered as one cluster on account of both forming clusters with vortex 2. We are then left with the full vortex assembly classified into dipoles and clusters.

Given the time step is calculated, we also calculate the energy spectrum of the point vortex assembly by taking fluid velocity on a mesh grid of 256×256 points as according to equation (3.9) with (x_i, y_i) here corresponding to the grid point coordinates, and then through the Fourier transform of these velocities the energy spectrum can be calculated as $E(k) = |\hat{\dot{x}}(k_x, k_y)|^2 + |\hat{\dot{y}}(k_x, k_y)|^2$ with $k = \sqrt{k_x^2 + k_y^2}$.

As a side note we also utilise both time and ensemble averaging in solving for the quantities

required in order to reduce the random fluctuations encountered as much as possible. In each case several point vortex simulations in each case with different random initial positions are performed such that averaging is possible across trajectories for both cases with and without annihilation. Additionally, a time averaging step is performed whereupon quantities of interest within a certain time step interval are averaged over the interval.

3.4 Results

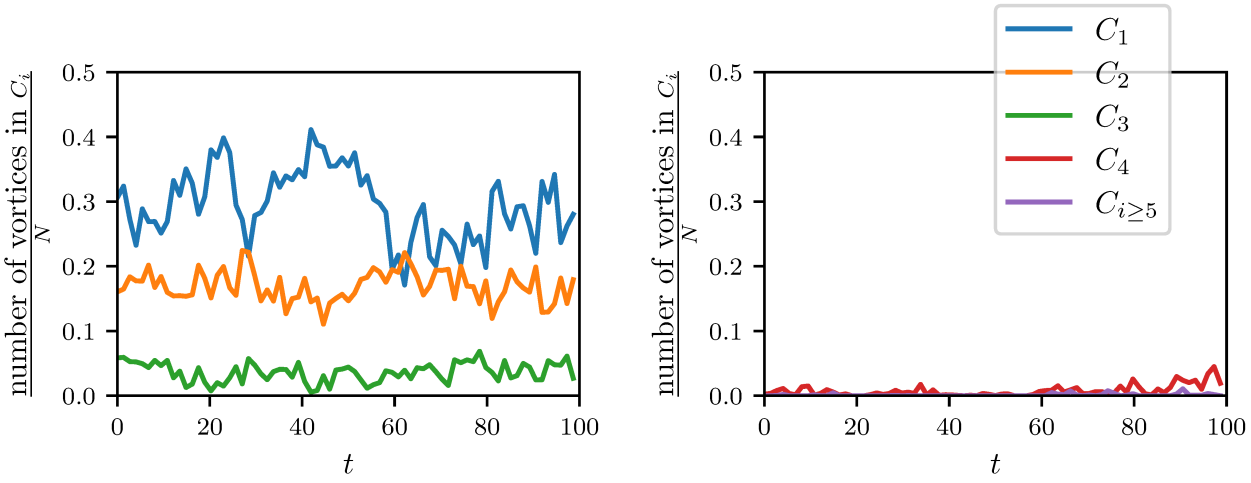

Figure 3.9: Number of vortices in each cluster C_i where i is the number of vortices in the cluster up to $C_{i\geq 5}$ normalised by the total number of vortices $N = 20$ with no annihilation/reinjection mechanism present showing how the number of clusters in the system evolve over time.

We first begin by simulating the evolution for periodic $N = 20$ vortices using the point vortex model already described, and by plotting the number of clusters over time we attain figure 3.9. We specifically track the evolution of the smaller cluster structures with respect to time, i.e. C_1, C_2, C_3, C_4 and $C_{i\geq 5}$ where i is any number greater than or equal to 5. The cluster numbers are seen to display quite chaotic behaviour between time steps, with random walk like fluctuations such as those found in chapter 4 over discrete cluster size values over very small time steps, highlighting the necessity of time and ensemble averaging. Turning our attention to the data itself, we see in 3.9 no noticeable persistent trend in the cluster numbers in each case, with each cluster line remaining relatively horizontal (other than the large fluctuations in the C_1 case, yet this still does not noticeably trend away from the initial proportion), suggesting there is no general persistent change of increase or decrease in the number of vortices in each particular

structure over the course of the interaction. Any movement away from the starting cluster number seems to return very quickly the starting value. The largest amount of movement in cluster number found appears to be the case of C_1 clusters, or in other words lone vortices. This is perhaps to be expected, as in a system without a tendency to form larger vortex structures such as dipoles or clusters these lone vortices would predominate and be most sensitive to fluctuations in other cluster structures, for example a C_2 structure disintegrating by similar processes such as that in section 3.1 increases the C_1 clusters by 2 and so on, explaining the larger fluctuations in the C_1 case. Note also the very small proportion of vortices in the C_4 and $C_{i\geq 5}$ cases. In any case we can speculate that due to the non-persistence of any significant change in cluster numbers there is no inverse cascade occurring here. By an examination of

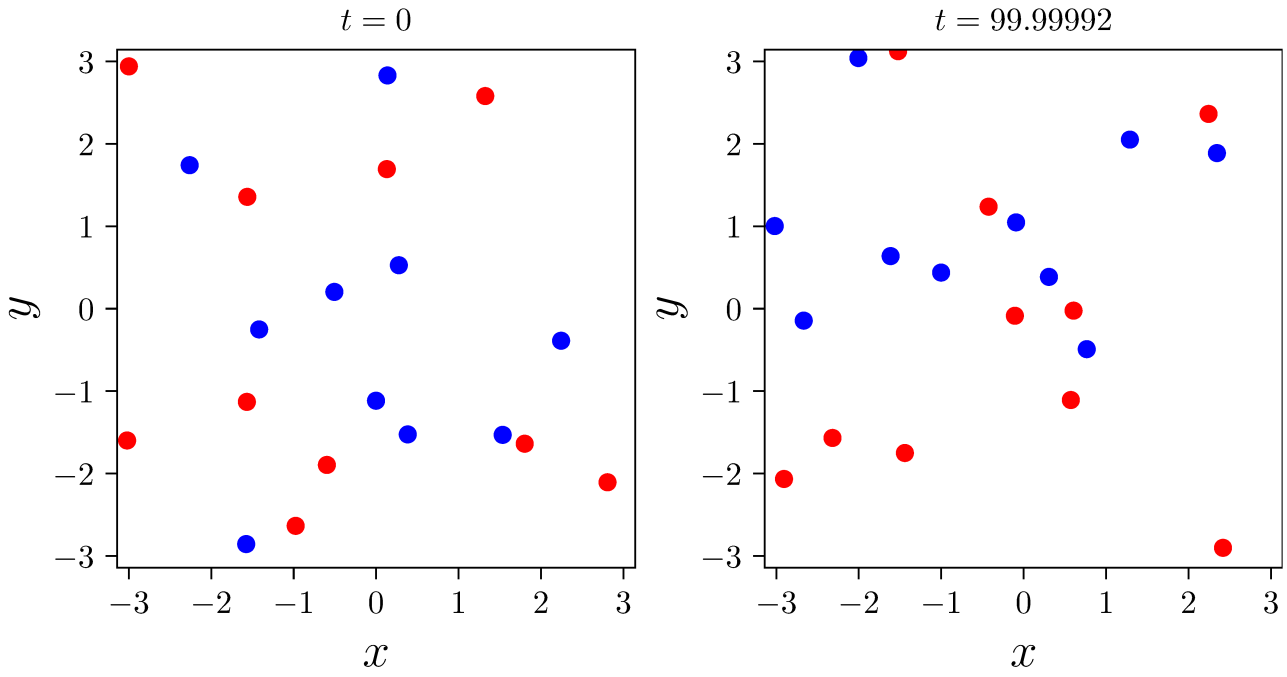

Figure 3.10: Position of vortices in one of the $N = 20$ simulations without annihilation/reinjection, negative signed circulation vortices are marked as blue circles whereas positive signed circulation vortices are marked red. Left shows vortices at the initial time point in the simulations whereas right shows vortex positions at the final time point.

the actual vortex positions at the first and last time steps in one of the simulations we average over as found in figure 3.10, we can definitively ascertain that the inverse cascade is not to be observed here. Visually it is obvious there is no fundamental persistent change of vortex structures observed here from time $t = 0$ to time $t = 99.99992$, the two "super-vortices" considered typical of the inverse cascade cannot be seen here. It could perhaps be argued that the simulation time has to be longer in order to observe the cascade, but from the results in

figure 3.9 this is unsubstantiated, as here we see no kind of trend to indicate inverse cascade is occurring even at longer time steps. In any case we can conclude that there are no obvious signs of an inverse cascade occurring. The same simulation is run with the exception of the

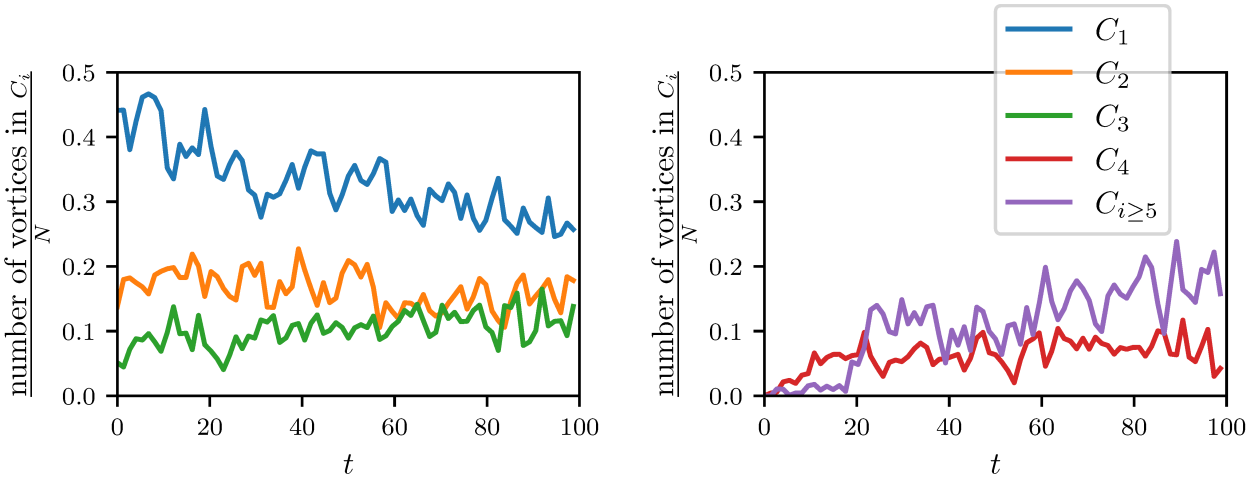

Figure 3.11: Number of vortices in each cluster C_i where i is the number of vortices in the cluster up to $C_{i\geq 5}$ normalised by the total number of vortices $N = 20$ with the annihilation/reinjection mechanism present showing how the number of clusters in the system evolve over time.

annihilation and reinjection mechanism being considered in the dynamics. In other words once a vortex and anti-vortex are very close to each other, they are removed from the system and are randomly reinjected at a separation of the inter-vortex separation. The results are plotted in figure 3.11, where markedly different behaviour is observed here on account of the annihilation and reinjection mechanism.

First, we notice with comparison to figure 3.9 that C_1 clusters, or lone vortices, have a noticeably negative trend. Also, the proportion of vortices in the larger C_3, C_4 and $C_{i\geq 5}$ cases all noticeably trend upwards with the most extreme example being the largest $C_{i\geq 5}$ clusters we consider. This is clear evidence of the formation of large scale clusters; what is essentially occurring is smaller clusters either disintegrating or merging with other cluster structures, lowering the cluster number of lone vortices not associated with clusters whilst slowly increasing the number of $i \geq 5$ clusters, as energy moves towards lower wavenumbers vortices move towards forming ever-denser clusters, culminating in two very large clusters made up of every vortex in the system (in this case each with $N = 10$ for each super-vortex). Given a long enough time frame we would expect the proportion of $C_{i\geq 5}$ vortices to slowly converge towards the value 1 to represent all vortices being contained within these final super-clusters, with other cluster

proportions converging to zero, as these would be absorbed into the final clusters. Similar to

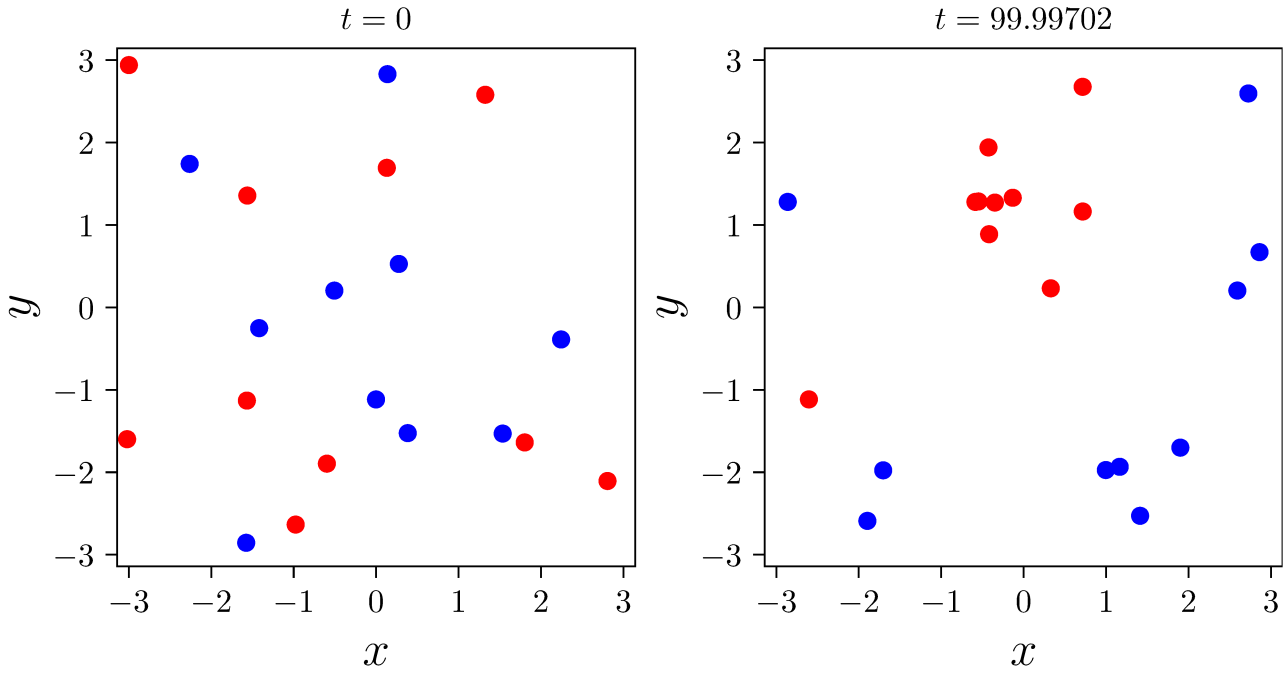

Figure 3.12: Position of vortices in one of the $N = 20$ simulations with annihilation/reinjection processes included, negative signed circulation vortices are marked as blue circles whereas positive signed circulation vortices are marked red. Left shows vortices at the initial time point in the simulations whereas right shows vortex positions at the final time point.

the case without annihilation and reinjection, we plot the first and last time step over one of the evolutions of the annihilation/reinjection case. Figure 3.12 shows the actual vortex positions in this case. Here we see a much different picture for the final time step vortex plot, as vortices have become concentrated into clusters of like-signed vortices, with very few vortices isolated from same-signed clusters.

Another possible measure of the clustering dynamics is the cluster separation used in the previous section, equation (3.1). By taking an average over time of this value we can form a picture of if vortex clusters on average are increasing in size over the interaction, highlighting the formation of clusters at large length scales if this is occurring. This is plotted in figure 3.13, where we plot the normalised average cluster separations over time in both cases. In the case where our forcing and dissipation mechanism is not present we see the cluster separations acting as a random walk with no overall trend to be observed. In the case with annihilation present however, an upward trend in the average cluster separation is easily observed, with the average separation at the final time point approximately three times the size at the initial time point; concrete evidence of cluster formation at increasing length scales as expected.

Clearly the addition of the annihilation and reinjection processes causes this behaviour, and this is the exact behaviour that is expected to be observed in the case of the inverse cascade, as vortices are slowly forming ever-larger clusters soon to result in the two super-vortices we expect. Further experiments with this number of vortices could involve running the simulation until the inverse cascade is detected to be complete, as the two large vortex clusters signifying a fully realised inverse cascade are not seen yet even at this late time point. Also interesting would be simulations of differing initial conditions, It is possible the statistics observed are sensitive to the chosen initial configurations, so additional ensembles may be interesting.

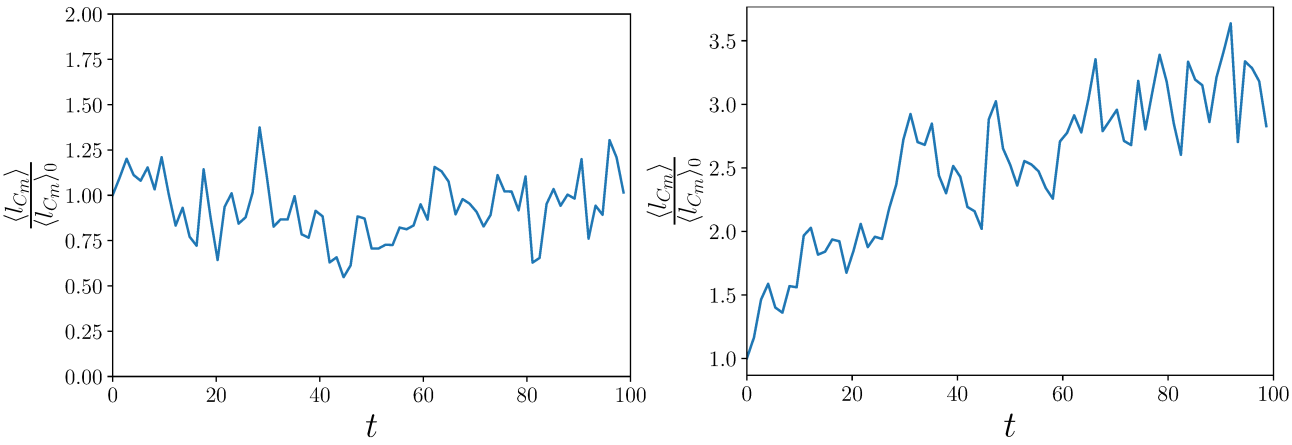

(a) Without Annihilation

(b) With Annihilation

Figure 3.13: Average cluster separations over the simulations with $N = 20$ without the annihilation and reinjection process (left) and with this process (right). Separations are normalised by the average cluster separation at the first time point $\langle l_{C_m}\rangle_0$.

Whilst the inverse cascade most probably has been realised in the $N = 20$ case, we also check the results of this applied to a higher N, such to better simulate large vortex systems. As in previous cases the number of vortices in each vortex cluster is plotted in figure 3.14. The effect of the increase in vortices is not very noticeable when compared to figure 3.9, with the proportion of vortices in each cluster size staying relatively constant throughout the simulations, with cluster proportions even taking similar values as in figure 3.9. The only noticeable differences are the lack of violent C_1 fluctuations, and a slightly higher (although still very small) proportion of vortices in C_4 and $C_{i\geq 5}$ cases. This is likely and effect of the much greater number of vortices. Other than this the end result is the same with cluster numbers experiencing fluctuations, but in each cluster case this is not consistent, and fluctuations return close to the original value at the start of the simulation. Similarly, to confirm this we plot the vortex positions at the first and last time step as before in figure 3.15. Again there is no noticeable move towards larger

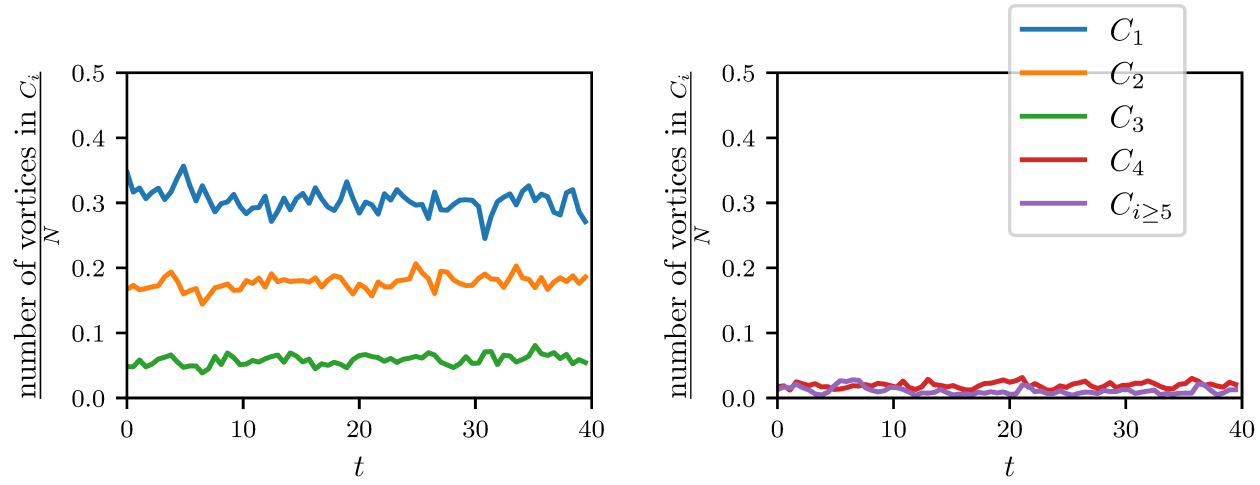

Figure 3.14: Number of vortices in each cluster C_i where i is the number of vortices in the cluster up to $C_{i\geq 5}$ normalised by the total number of vortices $N = 128$ without the annihilation/reinjection mechanism present showing how the number of clusters in the system evolve over time.

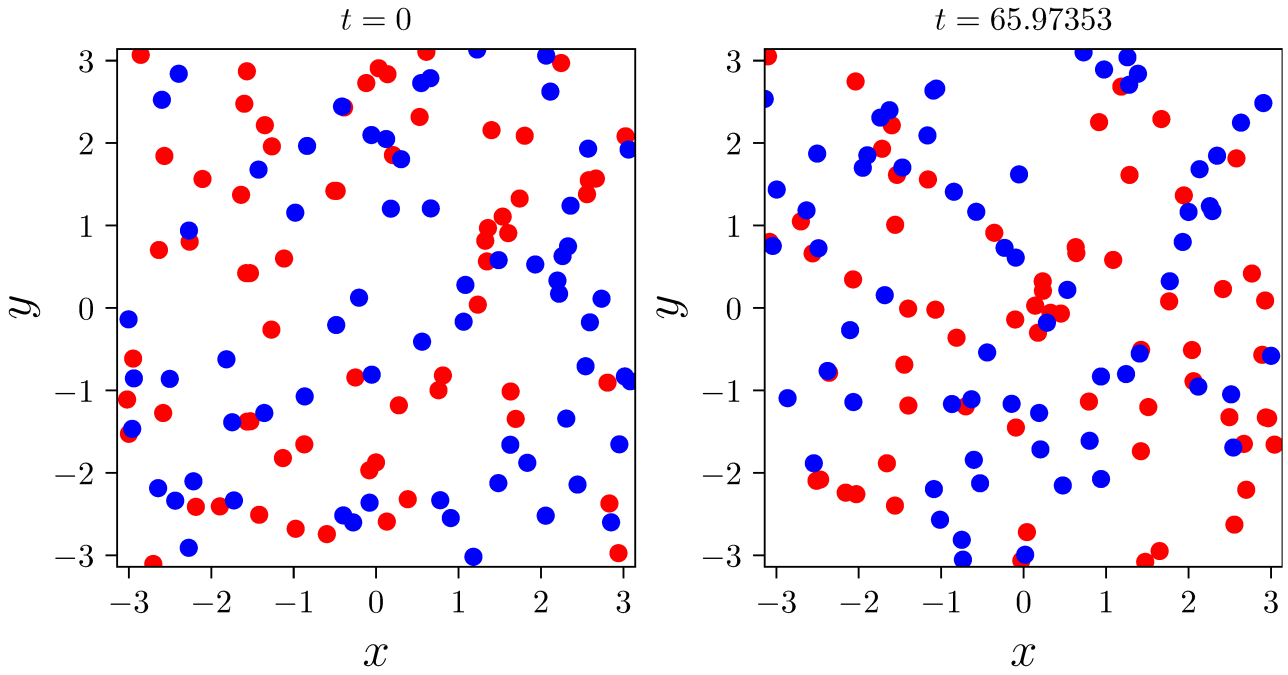

Figure 3.15: Position of vortices in one the $N = 128$ simulations without annihilation/reinjection, negative signed circulation vortices are marked as blue circles whereas positive signed circulation vortices are marked red. Left shows vortices at the initial time point in the simulations whereas right shows vortex positions at the final time point.

length scales, even more clearly than the $N = 20$ case there is no large macro clusters being formed here. Hence, it is obvious that in the case of $N = 128$ with no annihilation/reinjection there is no inverse cascade occurring here, especially when compared to the cluster numbers in figure 3.14, there is no clear trend in cluster numbers and no clear macro clusters being

formed by the final time step. Again we plot the cluster numbers for the case of $N = 128$

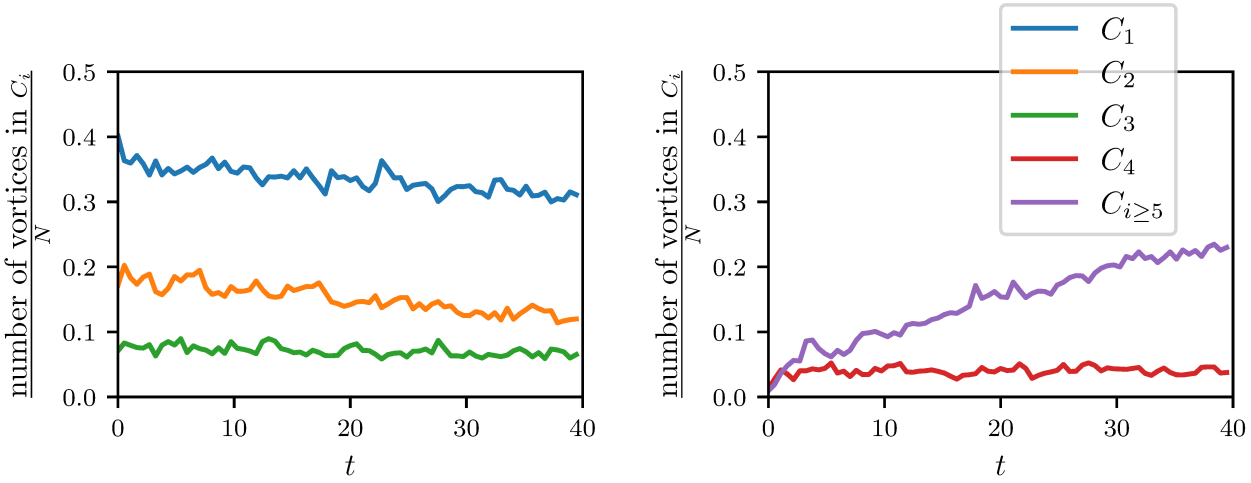

Figure 3.16: Number of vortices in each cluster C_i where i is the number of vortices in the cluster up to $C_{i\geq 5}$ normalised by the total number of vortices $N = 128$ with the annihilation/reinjection mechanism present showing how the number of clusters in the system evolve over time.

vortices with the annihilation/reinjection mechanism. Comparison to the previous case of no annihilation/reinjection clearly shows a deviation in the behaviour of the cluster sizes from the no annihilation/reinjection case 3.14. This difference does not seem to be as pronounced as the $N = 20$ simulations, perhaps on account of the smaller timescale of the simulation. There is however a noticeable difference in the total clusters C, the lone vortices C_1 are the most pronounced difference in dynamics from the no annihilation/reinjection case, interestingly cluster numbers seem to actually increase during the start of the evolution, with perhaps a small negative trend in cluster numbers starting to occur towards the end of the simulation. This is potentially a numerical consideration, as due to the increased number of vortices in the system clusters may not be as persistent during these earlier time steps, and due to the increased number of vortices in the system the separation tolerance between like-signed vortices such that they can be considered a cluster must be smaller, thus it is possible some C_1 clusters may actually be contained in larger clusters that are not realised numerically. In order to confirm this as before we examine the first and last time step of the interaction of $N = 128$ vortices with annihilation/reinjection. This is shown in figure 3.17. The difference observed here from the first to the last time step here is striking, in particular compared to the $N = 20$ case, the effect of introducing the annihilation and reinjection mechanisms are most noticeable here. More specifically, we see the random disordered vortices at $t = 0$ coalesce almost fully into

two super-clusters at the top-left and bottom-right of the bounding box, it is exactly these super clusters that we expect to observe in the inverse cascade. It is somewhat surprising the final super-clusters have been realised so quickly, compared to the previous $N = 20$ case with annihilation, we observe the final clusters we expect to observe in the case of an inverse cascade in figure 3.12 are not as developed as the vortices found here despite the simulation being run over a much larger time. This is particularly interesting as it would seem reasonable that the final super-vortices would take longer to be realised in the case of a larger vortex number, yet it seems from theses results the opposite is true. Again the average cluster separation over time

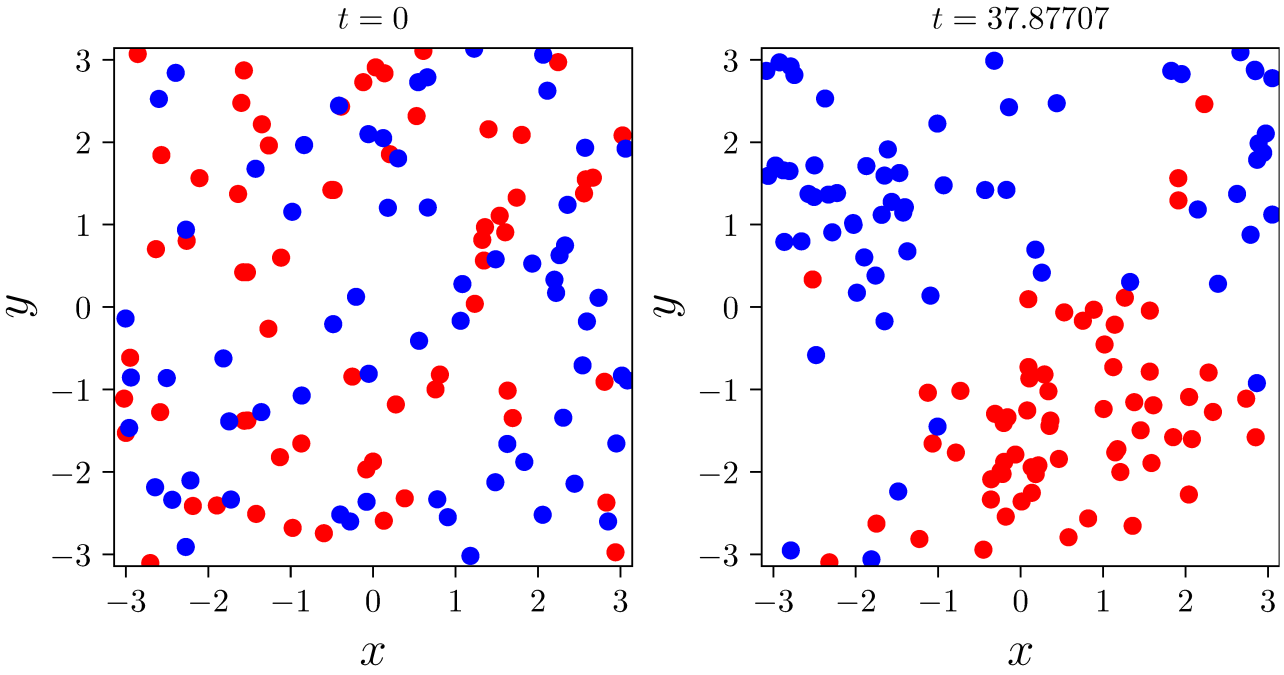

Figure 3.17: Position of vortices in one of the $N = 128$ simulations with annihilation/reinjection processes included, negative signed circulation vortices are marked as blue circles whereas positive signed circulation vortices are marked red. Left shows vortices at the initial time point in the simulations whereas right shows vortex positions at the final time point.

is examined in figure 3.18. Similar results as the $N = 20$ case is observed here, with the case where annihilation and reinjection is not present showing the same behaviour as a random walk with no noticeable trend, and the case with annihilation and reinjection showing an upward trend, and thus demonstrating large-scale clustering as the result of the introduction of this mechanism. What is perhaps unusual in this case is the amount to which the average cluster increases in size, with only an increase by a factor of approximately two from the first time step to the last. This is most probably due to the definition of the cluster tolerance used, as basing this upon the intervortex separation implies higher N systems will have much smaller

tolerance on what are considered clustered vortices, and so vortices that may be considered part of clusters but are of greater separation than this tolerance are thus not considered in the clustering separation measurement. Nevertheless, a clear growth of the average cluster occurs. Again longer simulations are required here, as well as comparison of differing initial conditions and perhaps a more sophisticated cluster finding algorithm.

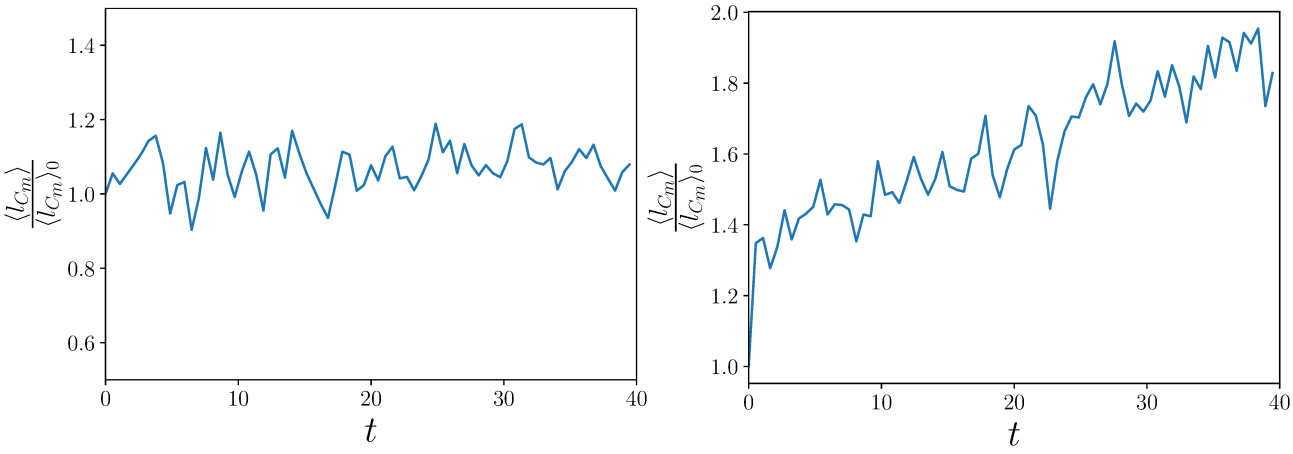

(a) Without Annihilation

(b) With Annihilation

Figure 3.18: Average cluster separations over the simulations with $N = 128$ without the annihilation and reinjection process and with this process. Separations are normalised by the average cluster separation at the first time point $\langle l_{C_m} \rangle_0$.

There is then comprehensive evidence of energy moving towards larger length scales as a result of the addition of the annihilation and reinjection mechanism into standard point vortex dynamics. However, critical to the classification of an inverse cascade in particular is the observation of a $k^{-5/3}$ power law in the energy spectra, hence energy spectra ensemble-averaged over our simulations with $N = 128$ vortices is plotted in figure 3.19. We restrict this analysis to the $N = 128$ as the large scale clustering is more obviously realised at the final time point as shown by figure 3.17. Here the average energy spectrum at the initial time point is plotted; where the energy spectrum is expected to be identical between cases with reinjection and without as clustering has not been allowed to develop yet, and we plot energy spectrum averaged over final time points denoted as t_{end}; where we expect the inverse cascade to be realised where annihilation and reinjection is possible. We see in each case the energy at each wavenumber $E(k)$ decreasing as the wavenumber k increases, as expected more energy is held at larger wavenumber in every case. In the case of no annihilation or reinjection we see no noticeable change over time in the energy spectra, with similar scaling proportional to k^{-1} as is

expected in point vortex spectra [116] at both time points. However, in the case of annihilation and reinjection being present, we see at the final time point a noticeable change in scaling at lower wavenumbers $k < k_f$ more closely resembling a $k^{-5/3}$ power law here as expected of the inverse cascade. This demonstrates the inverse cascade as energy is injected at k_f, and is dynamically transferred to large scales in the inverse cascade region $k < k_f$ until length scales become the size of the bounding box, and outside the inverse cascade range $k > k_f$ we recover the k^{-1} point vortex scaling. Over the course of this investigation we see in both the $N = 20$

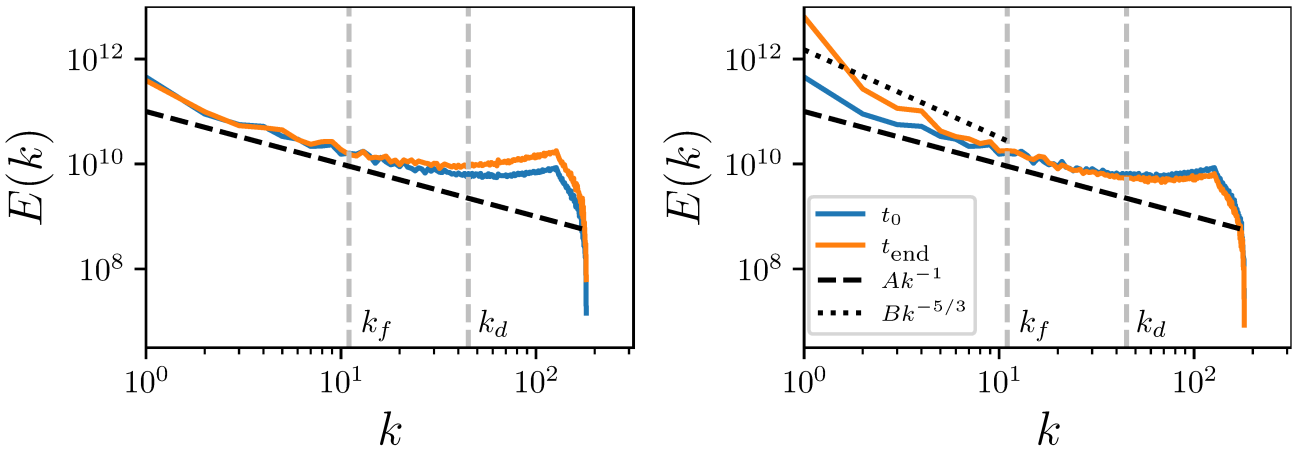

Figure 3.19: Log-log plot of the energy spectra averaged across simulations in the case of $N = 128$ dynamics for the case where annihilation and reinjection is not present (left) and where it is present (right). The energy spectra for the initial and final time points are plotted in each case, with additional lines proportional to k^{-1} (dashed) and $k^{-5/3}$ (dotted) plotted to show scaling and wavenumbers $k_f = 11$, $k_d = 45$ annotated

and $N = 128$ cases the inverse cascade is observed precisely because of the addition of the forcing due to vortex reinjection and dampening due to vortex annihilation. Thus, we have conclusively shown the minimal system of the point vortex model with procedures of dipole annihilation and vortex reinjection we present here can significantly change the statistics of the periodic vortex system, such that the inverse cascade can now be observed as occurring in the point vortex system whereas before this was not possible. Now we examine some further applications of the point vortex model in determining behaviour of turbulent systems, namely point vortices applied to sound.

Chapter 4

Effects of sound on point vortex dynamics

4.1 Vortices in the presence of sound

Here we move to considering an important aspect of how point vortex dipoles interact in turbulent systems, namely the dynamic effects of added sound on point vortex dipoles. This is especially an important area when considering point vortices in the presence of compressible effects, in particular when considering point vortices used to model 2D quantum turbulence, as it is these turbulent flows where the idealised point vortices most reflect the dilute quantum vortex dynamics found in mediums such as Bose-Einstein condensates, and also where there are also propagating sound waves through such systems that will interact with such quantum vortices.

The evolution of a turbulent flow where the point vortex model may be applied can be considered as a culmination of the various fundamental vortex-to-vortex interactions such as those found in chapters 2 and 3.1, and the effects due to density fluctuations in the underlying medium (i.e. sound waves). The sound waves present in mediums such as Bose Einstein condensates have been shown to be crucial to the dynamical evolution of the underlying flow, especially in the context of interactions with vortices, and the addition of sound and compressibility allows vortices to undergo more complex behaviours than can normally be seen.

An example of such complex behaviours is the phenomenon of annihilation found in turbulent flow. Given a vortex dipole composed of quantum vortices of width of the healing length ξ,

if the separation value of a vortex dipole becomes close to the healing length ξ, "annihilation" may occur where the vortex profiles are destroyed and propagation continues as a single dark soliton wave, whereupon it then bursts creating a shock [94, 119]. This process is so important it has been found to be crucial in the development of a coherent Bose Einstein condensate [120]. This process has also been found to be related to the reconnection to vortex filaments in three dimensions [121], whereupon the quantum vortex filaments approach locally, twist until they are antiparallel, then change topology instantly at a point and propagate off; this behavior is also followed by a sound emission. Such reconnections and annihilations should be common in a large 3D vortex tangle due to the large amount of vortices in the system resulting in many vortex pair interactions.

The sound waves present in such systems can also interact and scatter by these quantum vortices directly [122], with sound even being emitted in such cases as a rotating cluster of two vortices [123]. Of particular interest is recent work by Reeves et al. into a "noisy" point vortex model to investigate the relaxation of quantum turbulent states towards equilibrium; where the emergence of microcanonical equilibrium states in two-dimensional vortex gas is demonstrated. A point vortex model is then implemented with additional noise and damping added that faithfully reproduce these results [124]. Clearly the effects of sound are key to the development of turbulent systems where these compressible effects are possible, and these effects are absolutely linked to the dynamics of the vortices turbulence are comprised of. Thus, in considering the evolution of vortex systems regarding vortex dipoles, the effect of sound on vortex dipoles must be considered. Specifically the main area of interest when considering larger statistical systems is how sound may affect the underlying dipole structure, in particular, can sound create newly sized dipoles and can the annihilation mechanisms be observed under such regimes? It is this that we consider in this chapter. We first consider the numerical method used to implement such a compressible system in section 4.2, we then consider the results of such simulations in 4.3.

4.2 Numerical method

4.2.1 Padé approximants

In order to model the effects of sound on a vortex dipole, we first initialise a vortex anti-vortex pair in a 2D periodic box with coordinates $x \in [0, 2\pi), y \in [0, 2\pi)$, this is common in numerical simulations of the GPE and in effect ensures trapping of the "condensate" and thus the trapping forces which ordinarily necessitate the use of the trap potential $V(\boldsymbol{x})$ are no longer required (and also allows us to neglect any potentially complicated phenomena at the boundary of a condensate), this equates to solving equation (1.14) for the value of the wave function ψ. The vortex dipole is initialised with x coordinates $x_1 = x_2 = \pi$, with y coordinates $y_1 = 7\pi/8$ and $y_2 = 9\pi/8$, giving an initial dipole separation of $d = \pi/4$. An initial condition for this is first formed within the condensate using the technique of Padé approximants.

Given a function to be approximated, the Padé approximant gives an approximation to this function in terms of a rational function derived as the ratio of two power series. This approach is often superior to an approximation by Taylor series when functions contain poles, due to the representation as a rational function, thus suiting approximation of the dipole vortices. Formally, a $[N, M]$ Padé approximant is then an approximation to our function by a polynomial of $P(z)$ of degree M divided by a polynomial $Q(z)$ of degree N with $z \in \mathbb{C}$. Coefficients in such polynomials can be attained thus; given a function $f(z)$ with $z \in \mathbb{C}$ that we wish to approximate about $z = 0$ we have that $f(z)Q(z) - P(z) = Az^{M+N+1} + Bz^{M+N+2} + \cdots$, and $Q(0) = 1$. Solving these equations yields the Padé approximant of f so required [125]. The application of Padé approximants in the case of the GPE was first found by Berloff [126]. Here Berloff begins by finding the approximant of a single vortex in a uniform condensate, this is found by solution of the steady GPE equation first found by Pitaevskii [127], given the single vortex solution written in the form $\psi = R(r)e^{in\theta}$ where r is the separation from the vortex to the point (x, y) and θ is from the horizontal to the line spanned from the point to the vortex and is $n = 1, 2, 3...$ the winding number. The steady GPE equation given as

$$\frac{d^2R(r)}{dr^2} + \frac{1}{r}\frac{dR(r)}{dr} - \frac{n^2}{r^2}R(r) + [1 - R^2(r)]R(r) = 0,$$

has a solution of which can be approximated by a Padé approximant the density profile of

which can be recovered by $\rho \approx R(r)^2$. Once this has been done the wave function of a more complicated vortex assembly can be calculated through the superposition (i.e. the product) of these single vortex solutions, so the initial condition of an N vortex system in the GPE can be approximated by

$$\psi(x, y, t = 0) = \prod_{j=1}^{N} R_j(x, y) e^{i n_j \theta_j(x,y)},$$

where R_j is the amplitude of the jth single vortex wave function, ϕ_j the phase and n_j the winding number of the jth vortex. With this in mind, given a vortex dipole with initial positions $(\pi, 7\pi/8)$ and $(\pi, 9\pi/8)$, and single vortex Padé approximants R_0 and R_1 respectively, the density at a point (x, y) at separations r_0, r_1 from each vortex can be approximated as

$$\sqrt{\rho(x,y)} \approx R_0(r_0)R_1(r_1) = R\left(\sqrt{(x-\pi)^2 + \left(y - \frac{7\pi}{8}\right)^2}\right) R\left(\sqrt{(x-\pi)^2 + \left(y - \frac{9\pi}{8}\right)^2}\right), \tag{4.1}$$

with the function R given as the fourth order Padé approximant of the single vortex density function from [128]

$$R(r) = \sqrt{\frac{a_1 r^2 + a_2 r^4 + a_3 r^6 + a_4 r^8}{1 + b_1 r^2 + b_2 r_4 + b_3 r^6 + a_4 r^8}}, \tag{4.2}$$

with the a_i and b_i coefficients found in the appendix of [128]. The initial phase of the system is also then given as $\phi = \theta_1 + \theta_2$, therefore

$$\begin{aligned} \phi(x, y) &= \arctan\left(\frac{y - \frac{9\pi}{8}}{x - \pi}\right) - \arctan\left(\frac{y - \pi + \frac{\pi}{8}}{x - \pi}\right), \\ &= \arctan\left(\frac{\pi - x}{\frac{4}{\pi}\left[(x-\pi)^2 + (y-\pi)^2\right] - \frac{\pi}{16}}\right), \end{aligned} \tag{4.3}$$

then the initial condition for the wave function of the condensate can be fully expressed through (4.1-4.3) as $\psi(x, y, t = 0) = \sqrt{\rho} e^{i\phi}$.

4.2.2 Imaginary time propagation

The main drawback of the above generation of the initial condition by Padé approximants is the lack of "true" solution of the GPE equation, in effect the Padé approximant is an idealisation of the density field and phase fields which may lead to certain unwanted dynamics if we allow the GPE to propagate on the Padé approximate "as is". In other words what is attained from the Padé approximant is a numerical approximation of the associated density field, which when used with the GPE as it is not a proper solution results in the violent emission of sound waves and vortex stretching. Additionally, the phase field (4.3) in the current form is not 2π periodic, and so also cannot be considered a proper starting point for the GPE simulations. To combat this, a common approach is the use of imaginary time propagation. Here the substitution $t \to it$ is used, transforming the GPE into the dissipative Gross-Pitaevskii equation (DGPE) as such $\dot{\psi} = \nabla^2\psi - |\psi|^2\psi - \mu\psi$, this DGPE does not conserve energy of the system, instead as $t \to \infty$ in the DGPE ψ minimizes the total energy and corresponds to a stationary solution of the GPE, thus a particular wave function profile can be applied in the DGPE in order to find a fixed point of the GPE. This is of great interest, as then the Padé approximant can be applied in the DGPE to dissipate to the "true" GPE solution. However, obviously the propagation of the vortex/anti-vortex pair does not correspond to a stationary solution of the GPE, and so if the Padé approximant profile is applied in the DGPE in this form then the wave function will converge to a flat, uniform distribution where $|\psi|^2 = 1$ everywhere. In order to attain the dipole solution as a stationary solution of the GPE, we translate the DGPE into the co-moving reference frame using the Galilean transform $\psi(x, y, t) \to \bar{\psi}(x - ct, y, t)$ where c is the speed of the propagating dipole, which we take from the point vortex analogue as $c = \kappa/2\pi d = 2/\pi^2$, where here we let $\kappa = 1$. This gives $\dot{\bar{\psi}} = (\partial\bar{\psi})/(\partial t) - (2/\pi^2)(\partial\bar{\psi})(\partial\bar{x})$, where the new coordinate $\bar{x} = x - (2/\pi^2)t$. Finally, the DGPE in the moving reference frame is then given

$$\frac{\partial\bar{\psi}}{\partial t} = \nabla^2\bar{\psi} - |\bar{\psi}|^2\bar{\psi} - \mu\bar{\psi} + \frac{2}{\pi^2}\frac{\partial\bar{\psi}}{\partial\bar{x}}, \tag{4.4}$$

where the propagating vortex dipole now minimizes the total energy, and thus is a stationary solution of the GPE in this reference frame. The numerical process for generating the initial condition can thus be summarised. First the initial density field for the dipole is approximated

using the superposition of Padé approximants for the vortices using (4.1-4.2), coupled with the phase (4.3) this leads to an approximation of the wave function as $\psi = \sqrt{\rho}e^{i\phi}$. This approximate wave function is then evolved in the DGPE in the moving reference frame, equation (4.4), which then relaxes the unrealistic approximant to a true stationary solution of the GPE in the moving reference frame. This can then be utilised as the initial condition of the original GPE equation (1.14), where now the violent sound wave emission and stretching at the start of simulation does not occur. The heatmap of the resulting initial condition is shown in figure 4.1.

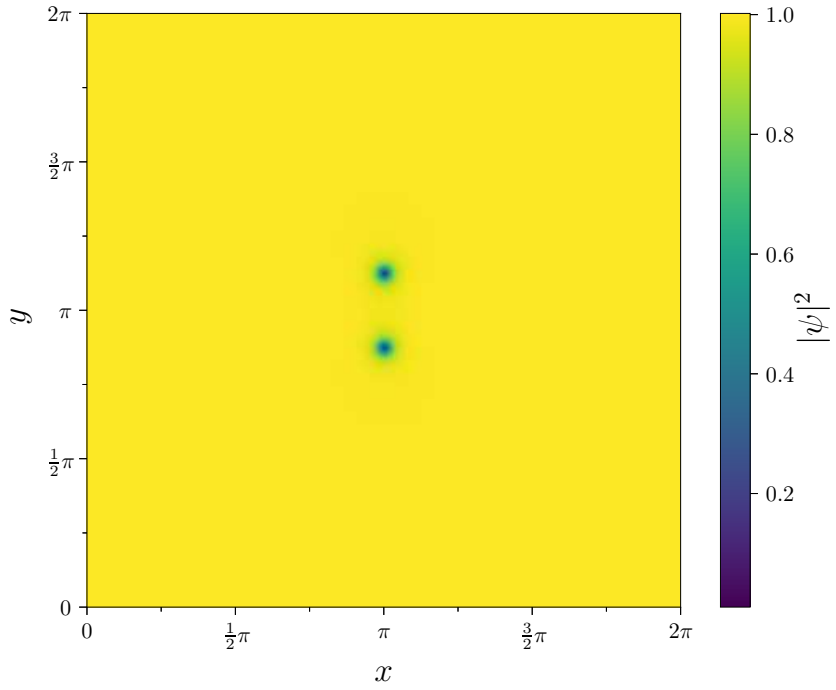

Figure 4.1: Amplitude of the wave function initial condition plotted as a heatmap in the case of no sound over the x, y coordinate space, showing the vortex dipole located at $x = \pi$ with midpoint $y = \pi$ as defects in the condensate with $|\psi|^2 = 0$.

4.2.3 Inputting sound into the system

Once the appropriate dipole solution in the GPE is found all that is left is to inject the particular sound distribution and then allow the system to evolve. Given ψ_{dipole}, the particular dipole solution already found in previous sections, we then impose a sound distribution through superposition as $\psi = \psi_{\text{dipole}}(1 + \psi_{\text{sound}})$. The particular form of the sound solution to the GPE ψ_{sound} depends upon the sound distribution chosen. We consider three primary choices for the sound distribution; the simplest case of no sound waves present in the system, the case of

Rayleigh-Jeans distributed sound, and the case of sound concentrated at a specific mode. The most basic that could be considered is the case of no sound waves, whereupon the superposition of the sound distribution solution onto the dipole solution simply reduces to the dipole density field found by evolving the Padé approximated solution in imaginary time, i.e. the initial condition is given as $\psi = \psi_{\text{dipole}}$. Whilst somewhat trivial the no sound case presents an important reference of the effects of the system before sound is added in order to compare effects of the following sound distributions. The second type of sound we consider is the Rayleigh-Jeans distributed sound distribution where sound is equipartitioned across modes. In order to find a particular distribution, first we assume sound is in thermodynamic equilibrium, then the level of sound will be appropriately equipartitioned across all wavenumbers k. Given the total number of particles and the Hamiltonian, the two conserved quantities of the GPE, given as

$$N = \int |\psi|^2 dxdy, \quad H = \int \frac{1}{2}|\nabla\psi|^2 - \frac{\mu}{2}|\psi|^2 + \frac{g}{4}|\psi|^4 dxdy, \tag{4.5}$$

by only considering the linear contribution of H and applying Parseval's theorem we then have

$$N = \sum_k |\hat{\psi}_k|^2, \quad H = \frac{1}{2}\sum_k k^2 |\hat{\psi}_k|^2. \tag{4.6}$$

Thus, in order for equipartitioned N it must hold that for low wave numbers $|\hat{\psi}_k|^2 \sim C$ with C some constant and for equipartitioned sound on H it must hold that for large wavenumbers $|\hat{\psi}_k|^2 \sim 1/k^2$. These conditions are appropriately satisfied by the Rayleigh-Jeans distribution

$$|\hat{\psi}_k|^2 = T/(\mu + k^2), \tag{4.7}$$

describing waves in thermodynamic equilibrium. Here μ and k are the chemical potential and the wavenumber as before, and T is the temperature of the system, acting as a parameter through which we can produce differing sound intensities. This gives an amplitude of $|\hat{\psi}_k|^2 \sim T/\mu$ for small wavenumbers k, and $|\hat{\psi}_k|^2 \sim T/k^2$ when wavenumbers become very large, thus satisfying the equipartition conditions, and giving a sound wave distribution in total thermodynamic equilibrium. An additional type of sound distribution that may be considered is that of an out-of-equilibrium distribution, or in other words a sound distribution

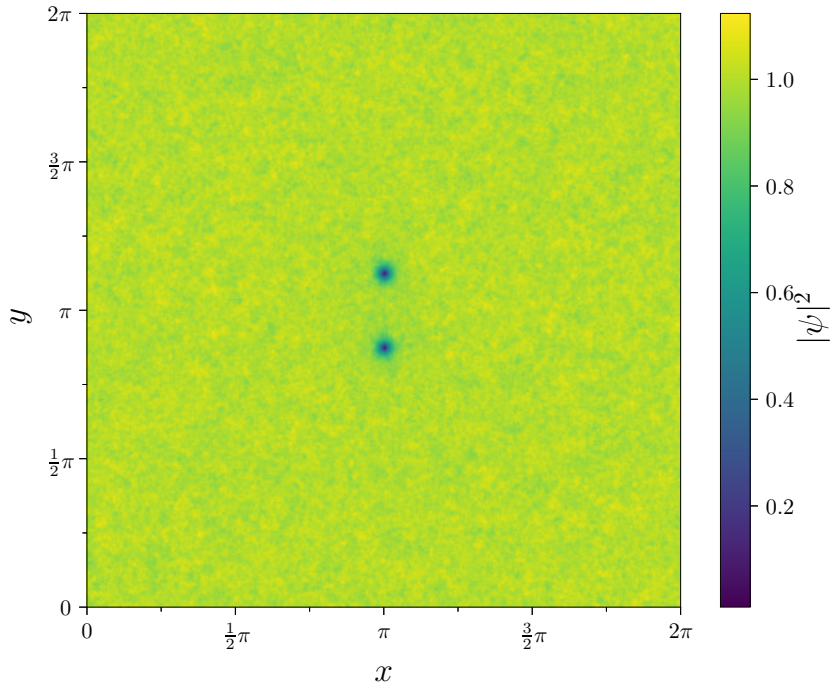

Figure 4.2: Amplitude of the wave function initial condition plotted as a heatmap with Rayleigh-Jeans distributed sound with $T = 1 \times 10^{-4}$ injected into the system over the x, y coordinate space. The vortex dipole at $x = \pi$ about $y = \pi$ is visible, as well as the sound profile created by the superposition of the sound solution.

where the energy is not equipartitioned across wave numbers. This is important in order to analyse the effect of equilibrium sound against non-equilibrium sound on such a system. A simple regime that we will consider is that of Gaussian distributed sound, with sound concentrated at a certain wavenumber k_f rather than equipartitioned. Specifically we employ the formula

$$|\hat{\psi}_k|^2 = \frac{T_G^2}{2\pi} \exp\left[-\frac{(k^2 - k_f)^2}{\sigma^2}\right], \tag{4.8}$$

where here T_G is "temperature", a parameter we adjust to alter intensity of the sound (subscripted as G to distinguish from the Rayleigh-Jeans temperatures T), here k is the wavenumber as before and k_f is the wavenumber the sound is concentrated at, in other words the mean of the Gaussian distribution we consider, in this sense we have σ as the standard deviation of the Gaussian distribution.

4.2.4 The psuedo-spectral method

In order to propagate the system the equation to be solved is a non-linear partial differential equation with periodic conditions $\psi(\boldsymbol{x}, t) = \psi(\boldsymbol{x} + 2\pi, t)$. To solve this we employ the pseudo-spectral method, common to many fluid dynamics applications. Specifically we consider the discrete inverse Fourier transform (IFT) of the ground state wave function

$$\psi(x,t) = \sum_{k=-\frac{N}{2}}^{\frac{N}{2}-1} \hat{\psi}_k(t) e^{ikx}, \tag{4.9}$$

where here N is the number of grid points in our discretization of the physical space, k is the wavenumber in Fourier space defined as $k_j = 2\pi j/L$ for $j \in \{-N/2, -N/2+1, ..., N/2-2, N/2-1\}$ and with L the length of the periodic physical space (in our case 2π) and $\hat{\psi}_k$ is the kth Fourier space representation of ψ, which may be a function of t. From substitution of the IFT (4.9) into the linear terms of the above equation to solve the dimensionless GPE (1.14) we have

$$i \sum_k \dot{\hat{\psi}}_k e^{ikx} = \sum_k k^2 \hat{\psi}_k e^{ikx} + \mu \sum_k \hat{\psi}_k e^{ikx} + |\psi|^2 \psi, \tag{4.10}$$

the dimensionless GPE has then been written in terms of the k-space Fourier representations of ψ instead of ψ directly. Employing the same method to the final non-linear term however represents a problem, as this will be a triple sum convolution in Fourier space

$$\begin{aligned} |\psi|^2\psi &= \left(\sum_{k_1} \hat{\psi}_{k_1} e^{ik_1 x} \sum_{k_1} \hat{\psi^*}_{k_2} e^{ik_2 x} \right) \sum_{k_3} \hat{\psi}_{k_3} e^{ik_3 x} = \sum_{k_1} \sum_{k_2} \sum_{k_3} \hat{\psi}_{k_1} \hat{\psi^*}_{k_2} \hat{\psi}_{k_3} e^{i(k_1+k_2+k_3)x}, \\ &= \sum_{k_1} \sum_{k_2} \hat{\psi}_{k_1} \hat{\psi^*}_{k_2} \hat{\psi}_{K-k_1-k_2} e^{iKx}, \end{aligned}$$

with $K = k_1 + k_2 + k_3$. This term is very computationally expensive to evaluate directly, and so instead we follow as is typical in the pseudo-spectral method by first calculating this term directly through the initial conditions and then transforming to Fourier space. The above equation (4.10) then becomes

$$i \sum_k \dot{\hat{\psi}}_k e^{ikx} = \sum_k k^2 \hat{\psi}_k e^{ikx} + \mu \sum_k \hat{\psi}_k e^{ikx} + \sum_k (\hat{|\psi|^2\psi})_k e^{ikx}, \tag{4.11}$$

then by matching coefficients in (4.11) we have that the kth time derivative is given as

$$i\dot{\hat{\psi}}_k = (\mu + k^2)\hat{\psi}_k + (\hat{|\psi|^2\psi})_k, \tag{4.12}$$

thus, the original GPE has been reduced from a partial differential equation to a system of N ordinary differential equations, which may be solved through standard numerical methods such as the Runge-Kutta family methods. Once the system of equations has been solved all that remains is to utilise the IFT (4.9) to attain the original values for the wave function ψ at the grid points.

In considering the Fourier transforms we must give attention to the alias errors bound to be produced, whereupon Fourier modes outside the size range we consider due to the periodicity of the problem (and as assumed by a discrete Fourier transform). This is a common error when utilising Fourier transforms of non-linear terms, such as the $(\hat{|\psi|^2\psi})$ term in equation (4.12). As a simple example we can write the $|\hat{\psi}|^2$ term in Fourier space to show this, given Fourier modes represented as $\{\hat{\psi}\}_{-N/2}^{N/2-1}$ we have the convolution

$$\begin{aligned}
|\hat{\psi}|^2{}_k &= \frac{1}{N}\sum_{n+m=k}\hat{\psi}_n\hat{\psi}^*_m = \frac{1}{N}\sum_n \hat{\psi}_n\hat{\psi}^*_{k-n}, \\
&= \frac{1}{N}\left[\sum_{-N/2<n,k-n<N/2-1}\hat{\psi}_n\hat{\psi}^*{}_{k-n} + \sum_{\substack{-N/2<n<N/2-1 \\ k-n<-N/2}}\hat{\psi}_n\hat{\psi}^*{}_{k-n} + \sum_{\substack{-N/2<n<N/2-1 \\ N/2-1<k-n}}\hat{\psi}_n\hat{\psi}^*{}_{k-n}\right],
\end{aligned} \tag{4.13}$$

The two final terms in equation (4.13) represent the aliasing error described, as due to periodicity in wave space modes with wave numbers $N/2-1 < k-n$ are aliased to $k-m-N$ modes, and vice versa as $k-n < -N/2$ are aliased to $k-n+N-1$ modes. The additional ψ product in the equation we are to solve only compounds this error.

Numerous methods exist for combating alias errors such as this; such as undersampling, where the outer $k-n < -N/2$ and $N/2-1 < k-n$ modes where aliasing occurs are not considered, or the complimentary technique of zero-padding which we implement. Here, to make the Fourier modes in the convolution free of aliasing, we extend the space to be sampled on each side by zeros, and then once convolution is complete we restrict to the original domain.

Specifically, we first compute the Fourier transform of ψ and ψ^*, which then are padded by zeros through the commonly used Orszag 2/3 rule [129], padding by $N/2$ zeros around the central region. Once this is done, we compute the inverse Fourier transform to calculate ψ and ψ^* on the extended mesh, only then do we calculate the product and take the Fourier transform of the product, finally discarding the outer values added earlier to recover the Fourier transform of the product which is now free of aliasing errors [130].

Once the wave function has been evaluated, the GPE can be considered solved. Despite this, still more work is to be done before vortex positions can be ascertained from the wave function. Vortices can be thought of as topological defects in the condensate, i.e. points where $\psi = 0$, however these points can also correspond to soliton solutions to the condensate, so instead of solving for the roots of the wave function a more sophisticated vortex tracking algorithm is required. We then utilise the "pseudo-vorticity" of the flow, defined as $\bar{\boldsymbol{\omega}} = \nabla \times (\rho \boldsymbol{v})$, where ρ is the density field and $\boldsymbol{v}$ is the hydrodynamic velocity of the flow, which can be found through the Madelung transform [80] that transforms the system to its hydrodynamic form. As already discussed the ordinarily defined vorticity is zero everywhere other than vortices, which are singularities in the vorticity distribution. In contrast, vortices represent minima and maxima of the pseudo-vorticity field and as such are easily recovered from the pseudo-vorticity distribution. Finding minimum or maximum values of this pseudo-vorticity field gives a good approximation of the vortex position. However, due to the discretization of the position space it is likely the real vortex position is not exactly located at the exact grid point of the maximum/minimum pseudo-vorticity; hence we take an average of the positions surrounding the max/min pseudo-vorticity with each position weighted by the pseudo-vorticity field of the corresponding grid points in order to get a closer approximation to the vortex position in continuous flow.

We also examine the energy over time of each particular simulation as another method to confirm results found. In particular, we consider the kinetic energy of the system, defined in [131] as $E_k = (1/A) \int (\sqrt{\rho}\boldsymbol{v})^2/2 dxdy$, where A is the area of the bounding box. According to the theory of hydrodynamic flow, we can decompose the hydrodynamic form of the velocity $\boldsymbol{v}$ into compressible and incompressible parts using the Helmholtz decomposition [132], which decomposes the flow into an irrotational part and a solenoidal part; i.e. a part where curl/vorticity

is zero and part which is divergence-free.

Thus the velocity field can be decomposed as $\sqrt{\rho}\boldsymbol{v} = (\sqrt{\rho}\boldsymbol{v})^i + (\sqrt{\rho}\boldsymbol{v})^c$ where $\nabla \cdot (\sqrt{\rho}\boldsymbol{v})^i = 0$, so here $(\sqrt{\rho}\boldsymbol{v})^i$ is the divergence-free part of the velocity field corresponding to incompressible motion and $(\sqrt{\rho}\boldsymbol{v})^c$ the irrotational part corresponding to compressible motion [133]. Further, we can decompose the kinetic energy into subsequent compressible and incompressible parts as

$$E_k^i = \frac{1}{A}\int \frac{[(\sqrt{\rho}\boldsymbol{v})^i]^2}{2} dxdy, \quad E_k^c = \frac{1}{A}\int \frac{[(\sqrt{\rho}\boldsymbol{v})^c]^2}{2} dxdy, \tag{4.14}$$

such that $E_k = E_k^i + E_k^c$. Note that E_k^i corresponds to the kinetic energy of the incompressible part of the flow, in other words the point vortices we impose, whilst E_k^c will then correspond to the kinetic energy of the sound waves in the system. By doing this we can observe how interactions occur between sound and vortices by the behaviour of E_k^i and E_k^c over time.

4.3 Results of sound on dipole evolution

We initialise vortices in several sound distributions, first we consider Rayleigh-Jeans distributed sound of several temperature values T which define the initial sound distribution Fourier space $\hat{\psi}$ representations according to (4.7). With the parameter of the chemical potential given as $\mu = 2000$ the Fourier space representations $(\hat{\psi}_k)_{\text{sound}}$ are given for each value of $k_j = 2\pi j/L$ for $j \in \{-N/2, -N/2+1, ..., N/2-2, N/2-1\}$ with $L = 2\pi$, the initial condition ψ_{sound} can then be recovered by the IFT of the Fourier space representations for each value of the temperature parameter T. We then initialise the distribution for a dipole with starting separation $d_0 = \pi/4$ according to the procedures in sections 4.2.1-4.2.2, input the ψ_{sound} distribution as according to section 4.2.3, and then continue to use the pseudo-spectral method as described in section 4.2.4 with a time step $dt = 10^{-6}$ for several temperature values T to compare how the intensity of sound affects the dynamics. We plot and compare the results of this in figure 4.3. Firstly, we notice the dipole in the case of no sound does not show any change from the original dipole size. This is to be expected, as in the case of no sound a lone propagating dipole has no mechanism for increasing or decreasing and will continue to propagate at the original dipole separation for all t. The motion of the pseudo-vorticity maximums/minimums representing quantum vortices in this case directly corresponds to the equivalent periodic point vortex motion.

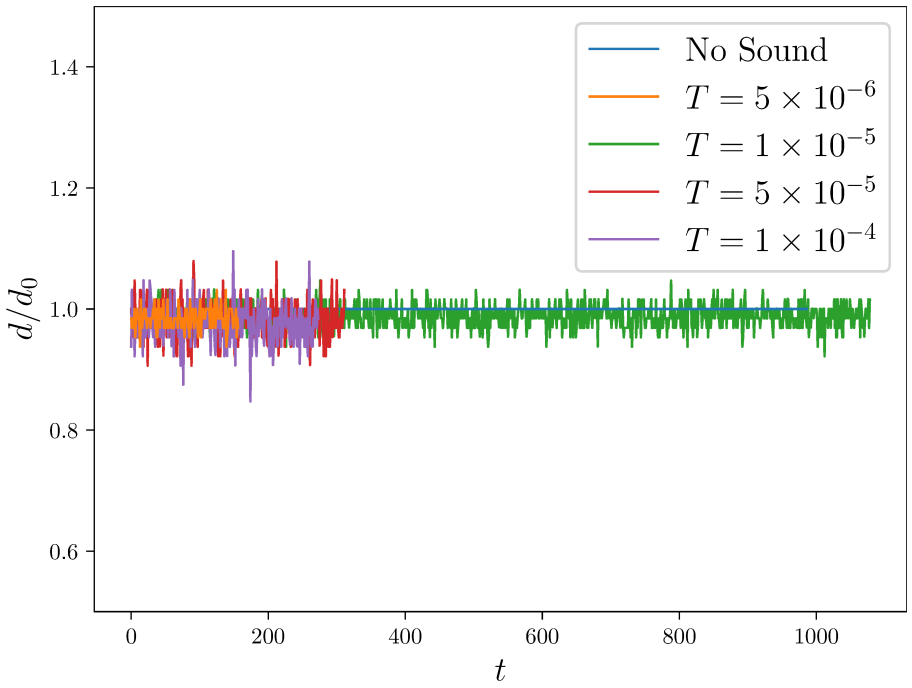

Figure 4.3: Dipole separation with respect to time for Rayleigh-Jeans distributed sound for several temperatures T. Dipole separations are normalised by the initial dipole separation in each case.

From comparison to the no sound case, it is easy to observe fluctuations in dipole size once sound is added to the system. We compare the dipole size evolution in sound for Rayleigh-Jeans distributed sound for four temperature values $T = 5 \times 10^{-6}, 1 \times 10^{-5}, 5 \times 10^{-5}$ and 1×10^{-4}. For all temperature values where sound is added to the system dipole size is affected temporarily by these sound fluctuations, with the most markedly large fluctuations occurring for the largest temperature values. This in effect shows sound having a noticeable effect on vortex dynamics. However, what is also noteworthy here is the expected behavior of the dipole shrinking in size due to the effects of the sound waves does not occur. Instead of a downward trend in dipole separation indicating dipole vortices becoming permanently closer (i.e. the dipole shrinking), perturbations to the initial dipole state always tend to relax to the original dipole separation, with the general dipole separation evolution in each case being similar to a random walk rather than a consistent downward trend. This suggests that as sound waves may collide and add energy to the vortex dipole thus causing the dipole to temporarily shrink, sound waves may also collide and take away energy from the dipole thus causing the dipole to actually grow in size, thus explaining the fluctuating dipole separation as the dipole propagates through the system and interacts with sound, with greater sizes of fluctuation corresponding to larger temperature

values and thus higher values of sound. We summarise by noting three important values in each case, scaled by the initial dipole separation. The minimum dipole separation over the interaction, the maximum, and the mean over time. For the case of no sound this identically gives $\min_t(d)/d_0 = \max_t(d)/d_0 = \langle d \rangle = 1$. The minimum, maximum and mean values are provided in table 4.1 with values from the following simulations. From this it is explicit that the mean for every T value here gives a mean ≈ 1 indicating no persistent trend, increasing the value of T only serves to increase the size of fluctuation thus giving greater minimums and maximums despite the mean not increasing or decreasing significantly We continue by separating the kinetic energy component of the flow into compressible and incompressible components as discussed for the sound distributions shown in figure 4.3. There are shown in figure 4.4, here we plot the total kinetic energy, and its compressible and incompressible components over time. A dipole decreasing in size as it approaches annihilation will thus have a greater energy. Due to this if the dipole were to decrease in size we would observe the incompressible kinetic energy increasing and the compressible decreasing. With this in mind, we examine the energy decompositions of the sound distributions also plotted in figure 4.3. In each case for each sound distribution we see energy being shown as a solid straight line, with minor fluctuations due to the noise imparted from the sound. In each case here we see the incompressible kinetic energy remaining largely horizontal throughout the entirety of the evolution. This then implies that the vortex dipole is not substantially decreasing in size over time as the incompressible kinetic energy is not increasing in any meaningful way over the time frame of evolution. This is what we would expect when considering the previous results in figure 4.3, as here we also see no noticeable consistent trend regarding the separation between dipoles. Also in each case we see the compressible kinetic energy and the total kinetic energy actually decreasing despite no corresponding increase in the incompressible kinetic part. This anomalous behavior is likely due to some kind of dissipation of the system due to numerical error compounded with the Fourier transform procedures needed to decompose the energy in this manner. Nevertheless, the data is consistent enough such that when also considering the dipole separation results we can exclude the possibility in the cases considered of dipoles becoming closer due to sound. What is perhaps unclear is why when the dipole separation encounters a fluctuation due to the sound waves, the dipole relaxes back to the original dipole size in particular, as opposed

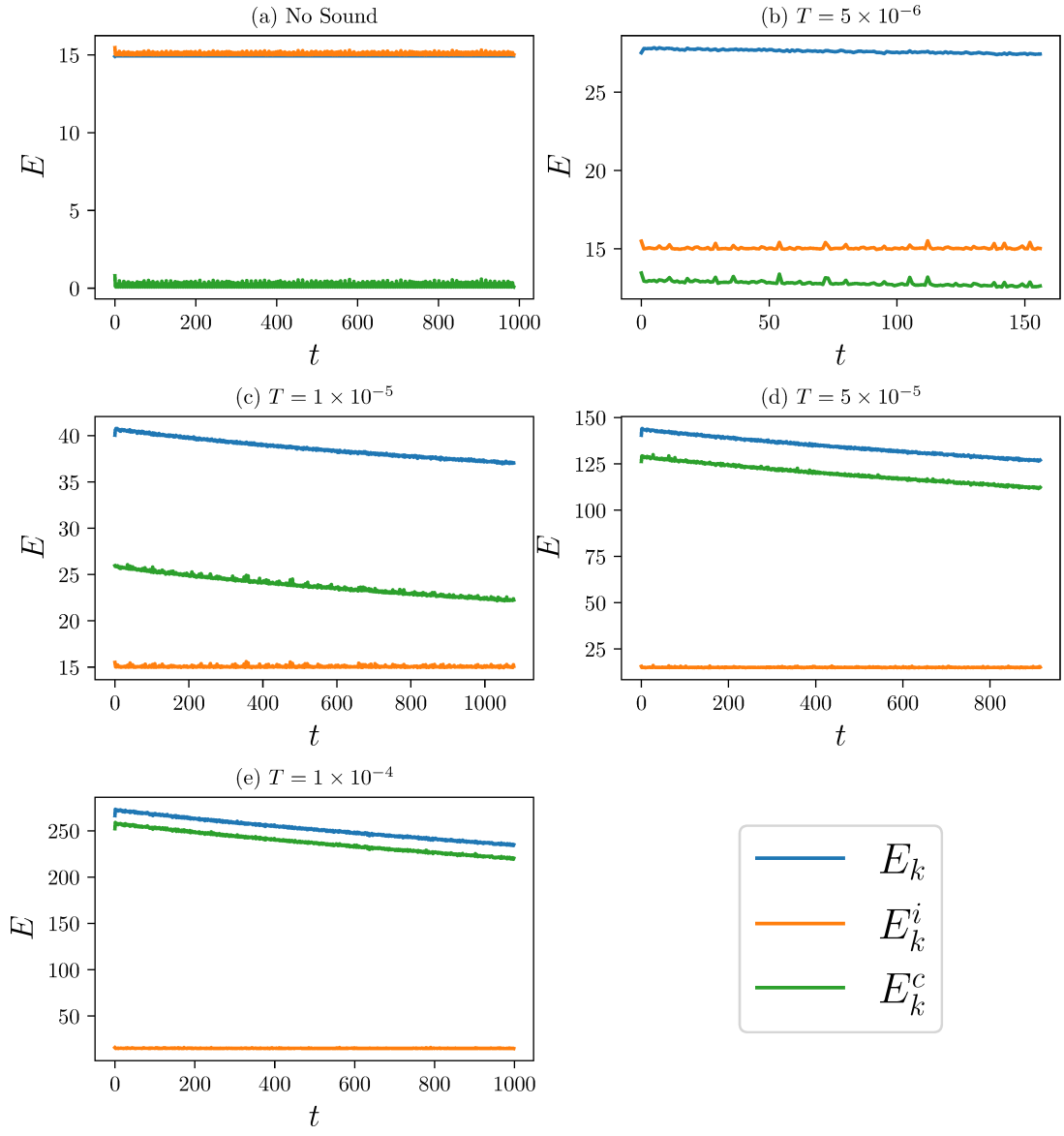

Figure 4.4: The kinetic energy decomposition for Rayleigh-Jeans distributed sound given various temperature values of T. The total kinetic energy, incompressible kinetic energy and compressible kinetic energy is plotted over the interaction for each value of T.

to any other separation value. It is speculated that this is perhaps due to the particular sound distribution used here. As the Rayleigh-Jeans distribution models sound evolution in equilibrium, thus sound is equipartitioned over all wave numbers. It may be this equilibrium across wave numbers is perhaps causing the dipole to relax back to the original separation

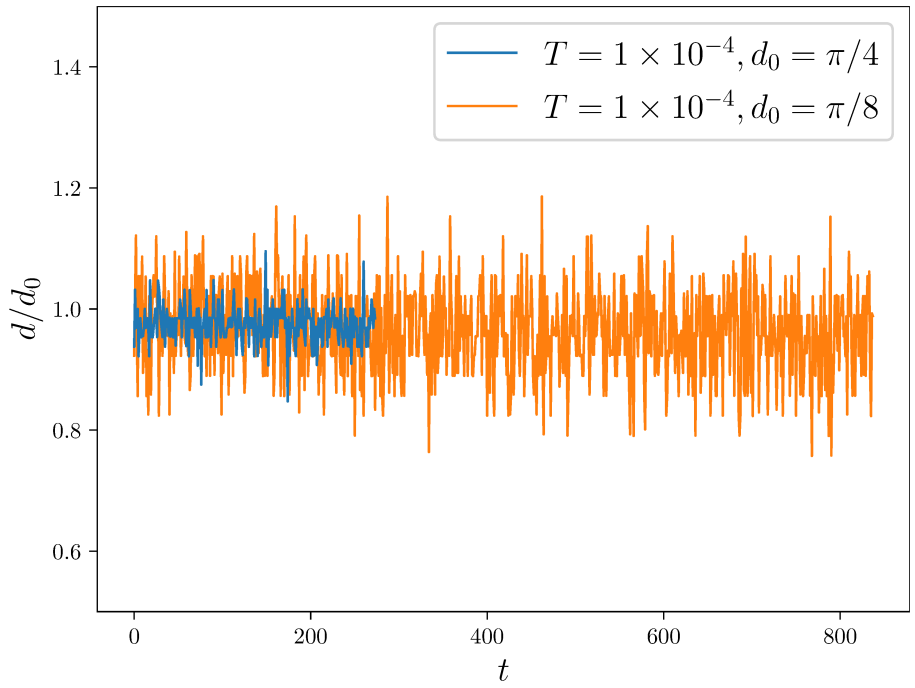

Figure 4.5: Evolution of the dipole separation over time for the same value of temperature $T = 1 \times 10^{-4}$ at different initial dipole separations $d_0 = \pi/4$ and $d_0 = \pi/8$. Dipole separations in each case are normalised by the initial dipole separations in each case.

value, as this initial separation was set as the system "equilibrium" in some sense, and thus any perturbation from this will eventually relax back to the original "equilibrium" separation. Thus, it is interesting to see whether interaction with sound that is not in equipartitioned across wavenumbers may result in the dipole reducing in size.

It also may be possible that the dipole in question may be actually trending closer together, but the initial separation of the dipole may be large and the intensity of sound weak to the extent that the shrinking of the dipole is so gradual it can not be noticed in the time frame we examine. It is thus important to consider whether a dipole that is initially much closer may display this shrinking effect, and how the initial size of the dipole may affect the dipole-sound interaction. Particularly it may be possible that even if Rayleigh-Jeans sound is not capable of reducing dipole size persistently, there however may be the possibility that the large fluctuations that occur due to the Rayleigh-Jeans sound may temporarily force the dipole within a distance smaller than the healing length ξ, and this may lead to annihilation of vortices even in systems with sound in equilibrium that does not result in a permanent dipole shrinkage.

Thus, in figure 4.5 we plot the $T = 1 \times 10^{-4}$ case for two different dipole separations, $\pi/4$ the same separation as used in figure 4.3 for reference, and new data for a dipole with initial

separation $\pi/8$, also these simulations are performed with a smaller time step in the hope of reducing the previous numerical error. We see here much the same behavior of fluctuation as found in that of figure 4.3. First we notice that there does not seem a qualitative difference between the fluctuations found in each case. This highlights that the magnitude of fluctuation in dipole size is not dependent upon the initial separation of the vortex dipole, and only depends upon the level of sound present in the system. Also, we see the same apparent random walk in dipole separation, with no permanent decrease in dipole size observed here, despite the relatively strong sound intensity in the system. In addition, what is noticeable is the small dipole sizes permitted without annihilation occurring, in particular for the $T = 1 \times 10^{-4}, d_0 = \pi/8$ case we see the dipole becomes closer. We see $\min_t(d)/d_0 = 0.82091$ for the $T = 1 \times 10^{-4}, d_0 = \pi/8$ case, and still no sign of annihilation occurring. We also observe a maximum value of $\max_t(d)/d_0 = 1.2854$ for the $T = 1 \times 10^{-4}, d_0 = \pi/8$ case and $\langle d \rangle/d_0 = 1.0453$ also for the $T = 1 \times 10^{-4}, d_0 = \pi/8$ case. Despite the fact that a consistent downward trend has yet been observed for the Rayleigh-Jeans sound, it is observed that larger values of T or smaller values of d_0 give larger relative fluctuations in dipole size, even if persistently these do not hold. It would be interesting to try even smaller initial dipoles in order to see the effects of sound as the initial separation $d_0 \to 0$, to see how dynamics may change and if annihilation will be possible through these fluctuations. Nevertheless, from the current data it is hard to justify any claim that dipoles decrease in separation persistently over time in the given cases. As

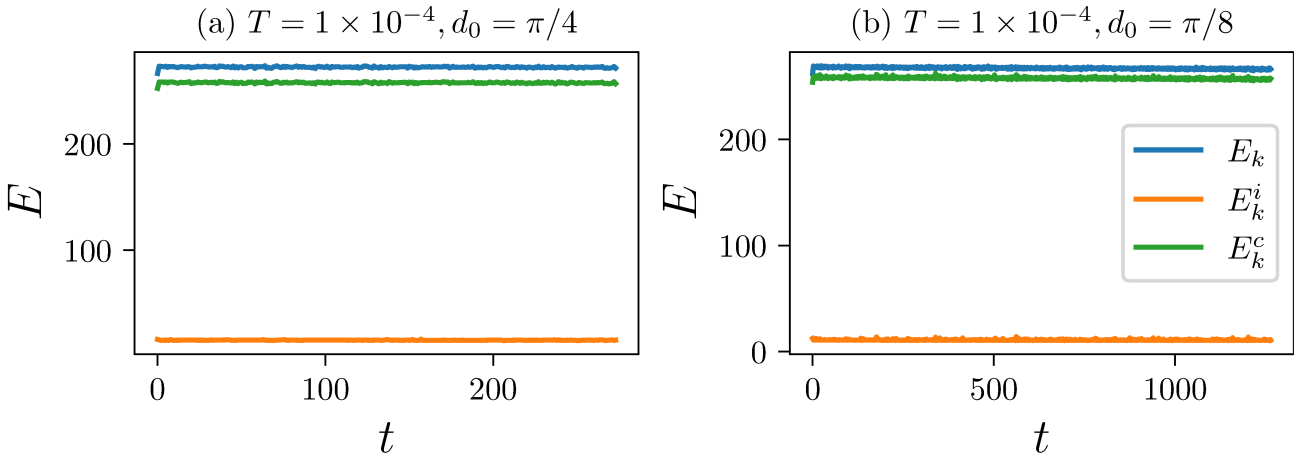

Figure 4.6: The kinetic energy decomposition for Rayleigh-Jeans distributed sound in the case of $T = 1 \times 10^{-4}$ for two initial dipole separations $d_0 = \pi/4$ and $d_0 = \pi/8$. The total kinetic energy, incompressible kinetic energy and compressible kinetic energy is plotted over the interaction for each value of d_0.

before, to confirm this we examine the kinetic energy decomposition of the above $T = 1 \times 10^{-4}$, $d_0 = \pi/4$ and $T = 1 \times 10^{-4}$, $d_0 = \pi/8$ cases. This is plotted in figure 4.6, where again we give the kinetic energy along with the compressible and incompressible parts. We see much the same results as in the previous figure 4.4, and here we see the energy is not decreasing as in the previous decomposition, highlighting indeed the numerical dissipation at work. In terms of results achieved, they are consistent with what we would anticipate given the lack of persistently decreasing dipole separation in figure 4.5, that is no transfer from incompressible to compressible energy in either case, with the only deviations of energies from their initial values being made up of the noise-like fluctuations from the sound present in the system interacting with the dipole.

Indeed, the only difference that can noticeably be observed between the two initial separation evolutions is the slightly increased incompressible kinetic energy value in the case of dipole vortices being initialised closer together. This again is to be expected as a closer dipole implies a dipole with higher velocity and thus a higher kinetic energy, this however has no bearing on the dipole increasing or decreasing in separation. Certainly if dipole shrinkage is possible due to the effect of sound it cannot be due to the simulations considered here.

Hence, if it is possible for the interaction of sound waves to permanently decrease the dipole separation and force vortices closer, it is likely not to be Rayleigh-Jeans distributed sound which causes this to occur, and thus it is necessary to consider the dipole in the presence of alternative sound distributions. As stated, the Rayleigh-Jeans method of sound distribution is a specific case of sound waves in equilibrium propagating, there are alternative distributions with sound out of equilibrium. It may be the case that it is the out of equilibrium motion of sound waves which may cause dipole shrinkage as they move towards equilibrium, rather than the motion of sound waves in equilibrium as already investigated. Hence, here we will consider alternatively distributed sound with sound waves focused at a particular wave number, and as before track the separation of dipoles as they evolve through this system.

The alternative to considering the sound distributed in an equipartitioned manner across wavenumbers is to examine the qualities of a system where sound is initially concentrated around a particular wavenumber. We consider a Gaussian distributed noise as defined in (4.8) around a particular wavenumber k_f, for all further simulations we choose $k_f = 32$ and the

standard deviation $\sigma = 8$. In figure 4.7 we see the dipole separation d plotted against the time

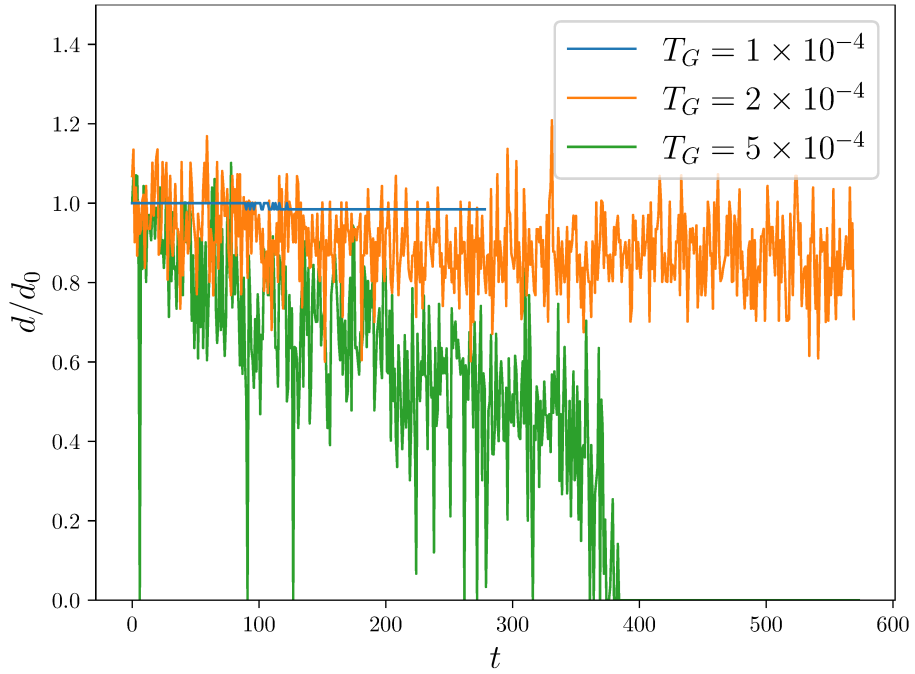

Figure 4.7: Evolution of the dipole separation over time given Gaussian distributed sound for several values of T_G. Dipole separations are normalised by the initial dipole separation.

t. We consider varying levels of intensity (with temperatures here represented as T_G in order to differentiate from the temperature values used in the Rayleigh-Jeans simulations) assuming Gaussian distributed sound waves, namely $T_G = 1 \times 10^{-4}$, $T_G = 2 \times 10^{-4}$ and $T_G = 5 \times 10^{-4}$. The $T_G = 1 \times 10^{-4}$ simulation is initialised with initial dipole separation $d = \pi/4$. The other temperature values are initialised with an initial dipole separation of $d = \pi/8$.

It can be observed that the various sound distributions considered show very different effects depending upon the intensity of the sound waves present. For example, we see no fluctuation whatsoever in the lowest sound level $T_G = 1 \times 10^{-4}$, this is remarkably different from the $T = 1 \times 10^{-4}$ sound effects that we see in for example figure 4.5, with no discernible fluctuations in this case as was observed before. The dipole separation appears to remain relatively constant, at least at the scale visualized by figure 4.7. This peculiarity, in effect, highlights the differences between the Rayleigh-Jeans and Gaussian distributed sound regimes. In the Rayleigh-Jeans case, we have $T = 1 \times 10^{-4}$ sound equipartitioned across all wave numbers, whereas in the case of Gaussian distributed sound we have a concentration at a particular mean wavenumber which quickly dissipates the further a particular wavenumber is from this mean value. As the $T_G = 1 \times 10^{-4}$ sound is concentrated at a particular wave number rather than distributed

equally across wave numbers the effects in this case are much weaker than the equivalent Rayleigh-Jeans distribution. Thus, the sound in this case is so weak the interaction with the vortex dipole has no noticeable effect on the dipole separation, and so is completely negligible. By examining the data directly we attain the minimum and maximum dipole sizes over the course of the interaction as $\min_t(d)/d_0 = 0.98438$ and $\max(d)/d_0 = 1.0001$, and with an average dipole separation of $\langle d \rangle = 0.99037$. Clearly the sound distribution has some effect on the dipole separation, although extremely small.

The effects of sound are however markedly different for the larger temperature values we consider here. We consider larger temperature values than in the previous Rayleigh-Jeans distributions, as already discussed these would be much weaker than the equivalent temperature in the Rayleigh-Jeans case. These higher temperatures result in large fluctuations in the dipole size as we would expect to see and as before observed in the Rayleigh-Jeans simulations. For the $T_G = 2 \times 10^{-4}$ case we observe a similar random walk type pattern localized about the initial dipole separation d_0, with extremely large fluctuations when compared to the seemingly constant dipole separation in the $T_G = 1 \times 10^{-4}$ case. This further reinforces the $T_G = 1 \times 10^{-4}$ case being too weak to observe the corresponding fluctuations, as for a larger temperature value the fluctuations are visibly much larger. For this particular temperature value we have a minimum dipole separation over the interaction of $\min_t(d)/d_0 = 0.56223$. The largest dipole separation over the interaction is $\max_t(d)/d_0 = 1.1314$ with a mean separation over the time considered as $\langle d \rangle/d_0 = 0.83425$. Here it is observed that over the course of the interaction the dipole reduces to nearly half of the initial dipole separation ($\pi/8$), the effect of the sound in this case is much stronger than has been observed previously in the current work, and from comparison to the maximum dipole size we see that the fluctuations present in the current simulation tend to produce greater shrinkage rather than growth in the separation, suggested by the relatively small maximum value compared to minimum and notably decreased mean. Most interestingly, the average dipole separation value is noticeably lesser than the initial dipole separation, suggesting that over time the mean value of the dipole separation will decrease. It is possible that over a longer time period we would observe an even lower mean value, and perhaps over a long enough time frame vortex annihilation may be observed. Hence, a longer time frame simulation of the evolution would be a particularly interesting area of future study.

The $T_G = 5 \times 10^{-4}$ case finally presents the most interesting of the results thus far in the Gaussian distributed sound distributions. Here the same random walk type fluctuations as in the previous $T_G = 2 \times 10^{-4}$ case can be observed here, although fluctuations appear much larger than we would expect (just as the fluctuation size difference between the $T_G = 2 \times 10^{-4}$ and $T_G = 1 \times 10^{-4}$ cases demonstrated). It is possible to observe values of 0 for the dipole separation distance, these are specific points in the system evolution where no vortices have been detected by the numerical method we employ. This implies fluctuations are so great that it is sometimes uncertain where the actual maximum of vorticity can be found, a more sophisticated numerical method may be required to determine vortex positions for these simulations. Nevertheless, the results we find for the dipole show interesting phenomena. Namely, this is the first case we have examined where a clear downward trend is visible, with the dipole separation decreasing continually until eventually converging to a value of 0. This 0 value then persists through the remaining simulation time, indicating the numerical method has not found any vortices for the remainder of the simulation. This behavior cannot be explained by the limitations of the numerical method as explained previously, and taken with the downward trend observed we must conclude that the results we observe is due to the phenomena of vortex annihilation that we have been anticipating.

As shown by the data the dipole must continually decrease in size due to the strong sound fluctuations. Then over the continued dipole size decrease the dipole sizes reaches below the critical annihilation value, whereupon dipole annihilation must occur. This results in a system with no dipoles remaining for the rest of the simulation, giving a zero dipole separation as the evolution continues.

We include the extremum values for this particular case for completeness. For the minimum value in this case before annihilation occurs we have $\min_t(d)/d_0 = 0.033315$, suggesting the critical length for annihilation to occur is ≈ 0.03 unit of the original dipole separation.

For the maximum dipole separation over the course of the interaction we have that $\max_t(d)/d_0 = 1.0994$, another low maximum value compared to the harsh shrinkage occurring in this case. Also, the mean value of the separations whilst the dipole still exists $\langle d \rangle / d_0 = 0.1509272$. All results of the min/max separations over the course of this investigation is given in table 4.1. The mean value is substantially lower than the initial value, and is lower than that of the

previous temperature value. This implies that as the intensity of the Gaussian sound increases the mean value of the dipole separation over time decreases more rapidly, as we would perhaps expect, as the stronger intensity sound waves provide a stronger impulse upon the vortex dipole and thus the vortex dipole shrinks more quickly. Crucially, this investigation of the effect of sound on the vortex dipole is principally concerned with the idea of vortex annihilation, we have shown that this is in effect possible with a particular temperature value and sound distribution. To see the effect of this sound upon the energy decompositions found we plot figure 4.8.

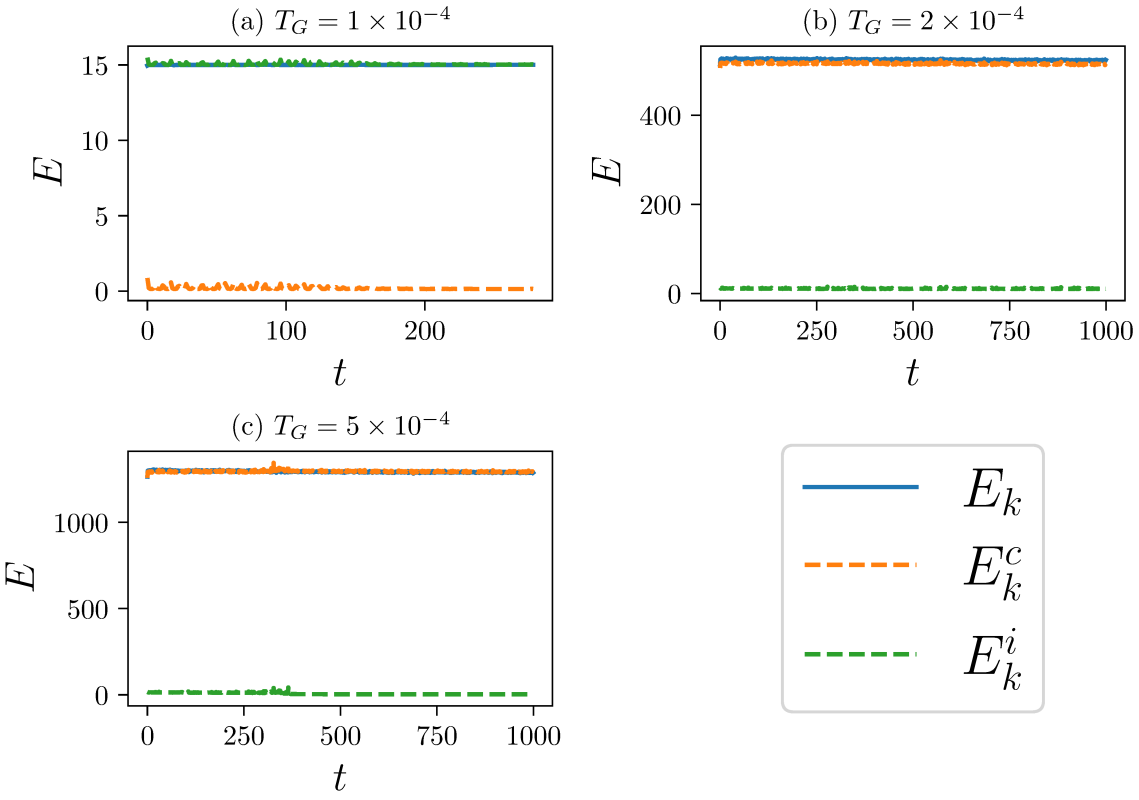

Figure 4.8: The kinetic energy decomposition for Gaussian distributed sound for $T_G = 1 \times 10^{-4}$, $T_G = 2 \times 10^{-4}$ and $T_G = 5 \times 10^{-4}$. The total kinetic energy, incompressible kinetic energy and compressible kinetic energy is plotted over the interaction for each value of T_G.

We notice here small fluctuations in the energy values in each case, and more interestingly, these fluctuations appear to stop after certain time. For example in the $T_G = 1 \times 10^{-4}$ case we see that the compressible energy E_K^c is barely above zero at $t = 0$, after this during the initial stages of the interaction we see fluctuations in the energy of both E_k^c and E_k^i whilst the total kinetic E_k appears to remain constant. This would imply that these fluctuations are then

due to the dipole interacting with the sound surrounding it and thus the incompressible and compressible energies are being passed from each other due to these interactions. During the remainder of the evolution however, we see these fluctuations relax and a relatively horizontal energy follows. It is hard to see whether this occurs in the $T_G = 2 \times 10^{-4}$ case, probably due to the increased y-axis scale these relatively small fluctuations are hard to observe. However, in the $T_G = 5 \times 10^{-4}$ case even at the large y-axis scale we see very violent fluctuations near the point in time when dipole separation $d \to 0$ was seen to occur in figure 4.7, whereupon the fluctuations stop, and it seems that after this point in time we have that $E_k^i = 0$ and $E_k = E_k^c$, in other words vortices have annihilation. The fact that this behavior was not observed in the cases of Rayleigh-Jeans sound is significant, as it highlights the possibility that this relaxation (and thus the mechanism of annihilation) is due to the movement from an out-of-equilibrium state to an equilibrium state such as those Rayleigh-Jeans distributed simulations. This implies that the annihilation of vortices represent a particular equilibrium of such as system, and we can speculate that the out-of-equilibrium states examined here must either experience vortex annihilation or relax to an equilibrium including the vortex dipole such as the Rayleigh-Jeans states studied previously, and the particular equilibrium the system finds must be on account of the initial condition, i.e. the values of T, d_0 and the particular sound distribution chosen. Thus

Table 4.1: Min/Max, and average separation lengths over the course of each evolution in both the Rayleigh-Jeans and exponentially distributed sound cases in units of the original dipole separation in each case.

T	$\min_t(d)/d_0$	$\max_t(d)/d_0$	$\langle d \rangle / d_0$
(no sound)	1	1	1
5×10^{-6}	0.95251	1.0477	1.0005
1×10^{-5}	0.93651	1.064	1.0041
5×10^{-5}	0.90625	1.0791	0.98106
$1 \times 10^{-4}, d_0 = \pi/4$	0.90372	1.1684	1.0398
$1 \times 10^{-4}, d_0 = \pi/8$	0.82091	1.2854	1.0453
T_G	$\min_t(d)/d_0$	$\max_t(d)/d_0$	$\langle d \rangle / d_0$
1×10^{-4}	0.98438	1.0001	0.99037
2×10^{-4}	0.56223	1.1314	0.83425
5×10^{-4}	0.033315	1.0994	0.63799

we have established the fundamental relation between the sound distribution chosen and the

effects observed upon the vortex dipole, in other words the choice of particular distribution of energy across wave numbers can significantly influence the dynamics of the system. We realise this in several ways, firstly the size of vortex fluctuations is specifically due to the intensity of sound upon the system (notably this may be due also to the numerical method being unsure of where the actual vorticity maximums are due to the high amount of noise present due to the intense sound), second we have shown the particular behaviour of the vortex dipole separation is due to the particular distribution of sound energy across wavenumbers, with the Rayleigh-Jeans distributed sound not producing any noticeable trend over time other than the random walk like dipole size fluctuations already mentioned. However, in Gaussian sound distributed with a focus on a particular wave number, we notice a persistent decrease in dipole size over the course of the interaction, with the most intense sound distributions resulting in the more rapid dipole separation decrease. This in particular highlights that it is not the effect of sound alone that induces a persistent change in dipole size, as in even the most intense of Rayleigh-Jeans sound no downward trend in dipole separation can be observed with any certainty. Yet in the Gaussian distributed case this downward trend is obvious, with the most intense of sound even leading to vortex annihilation. Thus, it is not the sound waves causing the dipole size decrease but the out of equilibrium movement of sound towards an equilibrium solution, that of either vortex annihilation or relaxation towards a Rayleigh-Jeans like state. This also echoes the previously mentioned work of Reeves et al. where instead of the realisation of equilibrium states by the near-equilibrium motion of noisy point vortices we establish this through the initialisation of point vortex like dipoles explicitly [124].

The results thus far convincingly demonstrate the effect on a vortex dipole due to sound in both the Rayleigh-Jeans equilibrium and the Gaussian distributed cases. However, there are various areas here which could be developed. Longer time simulations in each case would be useful in reinforcing results on the behaviour of each state, for example the $T_G = 2\times10^{-4}$ case to ensure significant shrinkage or annihilation does not occur. Given a larger array of simulations for longer times more detailed Gaussian sound results could be extracted, for example how the time to annihilation depends upon the initial dipole separation and the temperature T_G. Such results are critical to forming a kinetic theory where these sound interactions may be taken into account. In addition to this it may be prudent to more systematically vary the initial

dipole separations for each sound intensity/distribution for comparison purposes, as it is clear from figure 4.5 a change in initial dipole size has a noticeable effect on the level of fluctuations, although it is arguable if such simulations would be worth the high computational cost as the results attained in the cases already examined seem to reinforce the conclusions enough. In particular what is required in furthering this investigation is longer-time simulations and more varied sound intensities in the out of equilibrium cases, to ensure an equilibrium (either the Rayleigh-Jeans or annihilation) is actually being reached and persisting over time, assuming this is what occurs. Also, longer time evolutions in these cases would be useful in considering what occurs in the Gaussian simulations for lower sound intensities in figure 4.7, to conclusively show if the behavior seen here persists for longer times. Additionally, in examining the conclusions here, it is an open question how alternative distributions of sound may affect the dynamics, for example, do there exist more complicated out of equilibrium solutions that do not relax towards either the Rayleigh-Jeans sound or annihilation? If the conclusions we speculate are correct this should not be possible, unless there may be some other equilibrium sound distributions that may be reached. Finally, assuming the conclusions we have here are correct it must be asked, is it possible to determine a priori whether an out of equilibrium solution relaxes to a Rayleigh-Jeans/equilibrium sound or whether it annihilates? Given the preliminary results in figure 4.7, this seems to depend on both the sound intensity T_G and the initial separation d_0, but we also note the mean wavenumber k_f that we have taken as constant through these simulations. Regimes of motion leading to Rayleigh-Jeans relaxation or annihilation could then be mapped to regions of the (T_G, d_0, k_f) parameter space.

Chapter 5

Conclusion

5.1 Results and findings regarding Aref, Novikov, and Eckhardt

Through the current work we have presented a full exploration of the fundamental dipole interactions in point vortex and point vortex adjacent systems, in part inspired by the seminal works of Aref and Novikov into three body point vortex dynamics [5, 28], where we follow a similar formalism in order to fully explore the basic point vortex collisions. The work of Novikov in particular is responsible for the approach of the dimensionless b_i variables found in chapter 2, although the work of Novikov is restricted to three point vortices of identical circulation, so for an analysis of dipole interactions the remainder of this work is not strictly relevant. The appendix of the work of Aref however contains a basic analysis of the first fundamental dipole collision we consider; the dipole-vortex collision. To be more specific, Aref gives and analysis of three point vortices with circulations $\kappa_1 = \kappa_2 = -\kappa_3$, including a regime of periodic motion that is not reachable in a true dipole collision (see chapter 2 section 2.2 regarding the β root for more details), again not relevant compared to our work of focused around dipoles. However, Aref then continues to examine the scattering angles of the dipole-vortex collision, including reduction into the elliptic integrals. However, Aref does not provide the forms of the elliptic integrals in full, and through derivation and numerical analysis of these scattering angles we prove a sign error is present within the results of Aref, this is displayed in the comparison of our results to Aref's in figure 5.1, clearly demonstrating the error in the $\rho/d > 7/2$ region in

Aref's results.

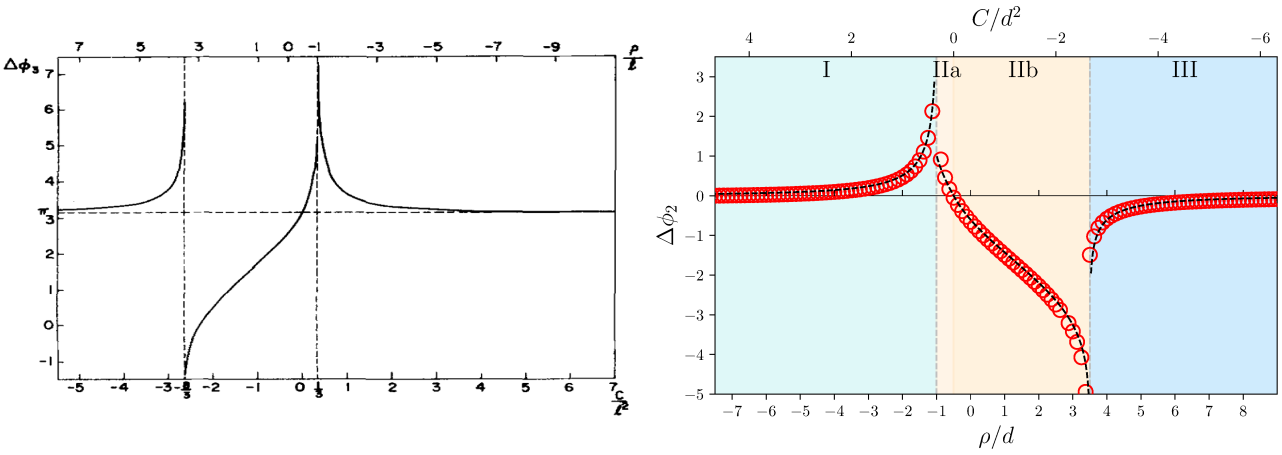

Figure 5.1: Dipole-vortex collision scattering results of Aref compared (left) to results of the current work in chapter 2 (right). Where Aref has labelled the negative vortex as 3 we have labelled this as vortex 2, i.e. $\Delta\phi_3$ in Aref and $\Delta\phi_2$ in the current work refers to the same quantity, and where Aref has denoted the initial dipole separation as l we denote this d. Left plot reproduced from the original work by Aref [5].

We continue this using the Novikov/Aref formalism to give an analysis of the full dynamics of the dipole-vortex collision; including investigating the dipole periapsis and the maximum/minimum dipole separations throughout the interaction, neither of which has been accomplished previously.

Continuing to the four vortex interactions we also consider the dipole-dipole interaction in the non-integrable and integrable cases. A phase space analysis of the integrable motion of four vortices (of which the integrable dipole-dipole collision is a subset) is given by Eckhardt [95], and analytic expressions for the scattering angle of the integrable dipole-dipole collision are given in a subsequent work by Eckhardt and Aref [4]. No such error as in the dipole-vortex case is found here, so we avoid from reproducing these derivations and instead extend these results to the $C > 0$ regime and provide a plot of this with our numerical results with which we see total agreement in figure 2.8. We continue as before to derive the dipole periapsis and the maximum/minimum dipole separations in the integrable dipole-dipole interaction, again which has not been done previous to this work.

In the work of Eckhardt and Aref non-integrable dipole-dipole dynamics is also considered [4], however this is concerned with capturing the chaotic dynamics of non-identical vortex pairs with regard to scattering times, and is not relevant to our work concerning non-integrable

dynamics of identical dipoles where we provide a numerical analysis of the regions of interaction, scattering angles, minimums/maximum dipole separations over the interaction, and dipole lengths post-interaction. Again, none of this has been accomplished previous to the current work.

5.2 Final Thoughts

In chapter 1, we first introduced the phenomenon of turbulence, that is central to much research into fluid dynamics. We give a historical basis for turbulence, detailing the work of past dynamicists such as Reynolds and Kolmogorov, including their theories of early turbulence as it was first introduced by Reynolds and furthered by Kolmogorov's famous power laws. Continuing, we also introduce the basic notions that this work (and fluid dynamics as a whole) relies on in vorticity and the equations of motion, and introduce the Helmholtz vorticity laws that have a great bearing on vortex motion as a whole.

Also in this chapter we review the interesting phenomenon of quantum turbulence. We summarise the idea of turbulence in a fluid with zero viscosity, providing explanations for several mediums through which we can observe quantum turbulence, namely that of superfluid helium and Bose-Einstein condensates. Through this we examine turbulent flow in non-viscous fluid i.e. quantum turbulence. We then visit the Gross-Pitaevskii equation as a model of the fully-developed condensate, and hence can be used to model quantum turbulence. Of notable interest in quantum turbulence are the quantum vortices we see within these simulations, these vortices are identical, of very small core size and have quantized circulations. These vortices are of great interest, as they are the closest realisation of the idealised point vortices which we then introduce in the remainder of the introduction. This model of turbulent flow is integral to the work as a whole, we thus continue to describe in great detail the point vortex system. The theory of the point vortex system as a Hamiltonian system is visited, as well as the natural idea of the point vortex as the limit of the Rankine vortex. Also through Noether's theorem the conserved quantities of the point vortex system are given.

In chapter 2 we consider the point vortex system in more detail, here we examine the fundamental interactions of point vortex structures, noting their importance to large scale flow as a whole in both point vortex and non-point vortex systems, including the quantum Bose-

Einstein turbulent flow and standard hydrodynamic turbulence. An overview is provided of previous works on these fundamental interactions such as those by Aref and Novikov. We begin by introducing the most fundamental of vortex structure interactions, that of a dipole with a stationary vortex. The idea of the dipole periapsis is here reproduced, and the inter-vortex separations at the dipole periapsis are found. This is important in the phenomenon of vortex annihilation, and we find that the dipole separation only becomes significantly less than the initial separation during the first region of direct scattering, highlighting that perhaps annihilation is most likely in the first region in the limit of the impact parameter $\rho \to -1$ in systems where annihilation is possible. Here also given are the minimum and maximum dipole sizes of the point vortex dipole, as this has an important bearing on the statistical evolution of larger systems. Results attained are not dissimilar from the periapsis lengths, with a dipole minimums/maximum separations frequently occurring at the dipole periapsis. We again see the smaller dipole sizes occurring in region I, the first direct scattering region. We also give the scattering angles of the three vortex collision both numerically and theoretically in terms of elliptic integrals, with excellent agreement. The scattering angles in this case are very important, as it is the scattering angles that are responsible for the mixing of larger turbulent systems, in other words it is the scattering angle which determine which future interactions are going to occur, and with the dipole-vortex collision being the most likely to occur this importance is two-fold.

Also in this chapter we give a full analysis of the dipole-dipole collisions as we investigate the effects of a dipole colliding with an identical sized vortex dipole, starting with the integrable collision. The dipole-dipole collision is found to be non-integrable except in the specific case where linear momenta vanish, that is: $P = Q = 0$, and the total circulation of the system is zero: $\sum_{i=1}^{4} \kappa_i = 0$ reducing the problem to a three body interaction. This in effect is impossible to observe in larger systems due to the linear momentum requirements requiring the dipoles to collide on exactly opposite trajectories, which is unlikely to ever occur. Nevertheless, the integrable case gives an insight into the more complicated non-integrable case, so it is here that we started our investigation. Here the scattering angles given by Aref and Eckhardt [4] are numerically found to be completely accurate in this case as opposed to the erroneous three-vortex scattering angles, hence we omit the derivation of the scattering angles in this case and

refer the reader to [4] regarding these. We again find the separations at the dipole periapsis in this case also. As is to be expected, this gives a similar picture to the dipole-vortex periapsis lengths found previously, within the exception that here we achieve vortex separations smaller than the initial dipole size in both regions of direct scattering here. In addition the amount of dipole shrinkage is much less here, possibly due to the impulse of the fourth vortex in the system ensuring dipoles do not attain such proximity at the periapsis. Also, we examine the dipole minimum/maximum separations of the dipole containing vortex 2 over the course of the interaction, In particular noting the symmetry about $\rho/d = 0$ in this case. We again see the dipole reaching minimum/maximum primarily at the periapsis.

The next section exploring the non-integrable dipole-dipole collision is the first time in the current work where we examine a non-integrable vortex interaction. The non-integrable dipole-dipole collision, defined as any identical dipole-dipole collision where the conditions $P = Q = 0$ and $\sum_{i=1}^{4} \kappa_i = 0$ do not hold, can be thought of as the simplest case of non-integrable motion, and thus plays an important part in the larger systems. This interaction is considered with both dipoles propagating towards a fixed target point with separations L_1, L_2 spanning from the target point to each dipole midpoint, with each spanning line being separated by an angle of incidence of ϕ. Here due to the non-integrablility of the problem the regions of exchange/direct scattering are not so clearly defined as in the previous interactions. Hence, first a numerical study is undertaken to identify the different regions, where we find direct and exchange scattering arranged in a star-shape, with exchange scattering occupying the central region where the most intense scattering effects should be observed, as we would expect. Through this we also identify several dynamics which we do not observe in previous cases, such as the "leap-frogging" of one dipole from behind another and the propagation of a vortex with a spinning three-vortex configuration. Once again in this case we solve for the scattering angles of the interaction, finding the majority of scattering once again occurring during exchange scattering, and most acutely occurring in regions of exchange scattering approaching the boundary between direct and exchange scattering. We find even in the direct scattering regions the deflection is much less than previously seen, it is concluded that this is due to the far-field interaction being weaker in this case as the velocity decays as $\sim 1/r^2$ in this case as opposed to $\sim 1/r$ as in previous cases. We also see the majority of the scattering being negative in this case with a small region

of positive scattering in the upper left quadrant. Here we again plot the minimal and maximal dipole separations with respect to the dipole containing vortex 2. As is congruent to previous cases, we find in the pre-periapsis $t < t^*$ stage of interaction the dipole becoming smaller than its initial separation t_0, with the minimum in the exchange scattering case being equal to the initial dipole separation showing as in previous cases that the dipole only grows in size during the pre-periapsis stage. Interestingly we also find post-interaction the new dipole growing or shrinking, highlighting the possibility of a persistent change in dipole size post-interaction. Hence, we investigate this possibility of persistent dipole change, plotting the final dipole size for each dipole at large enough t that the interaction can be considered completed and the effect of dipoles upon one another can be considered negligible. It is easily observed that these final plots contain dipole sizes that are much greater/smaller than the initial size, making the non-integrable dipole-dipole collision the first interaction we have observed in which persistent growth/shrinkage is possible. Moreover, the change in each dipole has a direct relation with one another where if one dipole is to expand the other is then to contract, and through the integrals of motion the final dipole sizes can be found to obey the relation $d = d_1 d_2$ where d is the original dipole separation and d_1, d_2 the separation of dipoles 1 and 2 respectively. Overall, this dipole growth/shrinkage is of great importance in terms of statistical dynamics, as it is thought this shrinkage/growth that different sized dipoles can be created, thus the statistical make-up of a system at some point in the future is in part dependent upon how dipoles are created in such systems, and we find the non-integrable dipole-dipole case the most simple interaction in which this is possible. In chapter 4 we momentarily move away from the "vortex against vortex" interactions to consider another fundamental type of interaction that occurs upon dipoles in turbulent systems. Specifically we considered the effect of sound on a vortex dipole, in particular how the outer impulse of the sound can affect (or not affect) the separation of dipoles. So we inject dipoles into the Gross-Pitaevskii equation in order to measure how the separation changes as the system evolves. This is done for a variety of different sound distributions, sound intensities, and initial dipole separations. We first examine the effects of varying intensities in the case of Rayleigh-Jeans distributed sound. This in effect represents the sound in thermodynamics equilibrium, with energy equi-partitioned across wave numbers. Through numerous simulations we find the Rayleigh-Jeans distributed sound causes marked fluctuations

in the dipole-size, resembling a kind of random walk as the sound waves cause increases or decreases the dipole size. However, we see there is no general trend in this case, and on average the dipole remains around the initial dipole separation at $t = 0$. It is speculated that through initialising the dipole vortices closer together, the fluctuations observed may be able to push dipole vortices towards becoming closer than the healing length and thus annihilating, although when considering the case of $T = 1 \times 10^{-4}$ at initial dipole separations $d_0 = \pi/4$ and $\pi/8$ we do not observe this. Finally, we consider the case of Gaussian distributed sound for several temperature values, and finally we observe the dipole shrinkage and annihilation phenomena for the largest temperature value in this case. This suggests that it is in fact the out-of-equilibrium nature of the sound present that causes this dipole shrinkage and annihilation to occur, suggesting that the regime after annihilation can be considered an equilibrium of the system that the system relaxes to, and hence underlining why this process was not observed in the Rayleigh-Jeans sound cases.

The current work has served to be a thorough investigation into the fundamental dynamics of vortex dipoles. The dynamics of vortex dipoles are of critical importance to the dynamics of larger systems as a whole, through this we theorize that a preliminary understanding of the most basic of vortex dipole interactions can be used in future to formulate a theoretical statistic formulation of the larger systems of vortex motion, one in which the statistical agents are not simple point vortices but instead are the vortex dipoles formed through the mutual interaction of a vortex and anti-vortex. With this in mind we have considered the interactions of the simplest vortex structures, as it is these that are most likely to occur in larger systems (one potential avenue of future study is to formally consider the prevalence of certain interactions over others) with this aim we consider the dipole-vortex and dipole-dipole interactions, in theory the two collisions that have the highest probability of occurring. We have studied key quantities such as the possible mixing of systems through the scattering angles as a result of these interactions, as well as the possibility of larger or smaller sized dipoles being created through these interactions as it is through this that dipoles may be created in larger N vortex systems. This study is then extended into the more complicated vortex structures as we consider the interactions of vortex clusters, we note the accuracy in dynamics of approximating the vortex cluster with an equivalent strength point vortex, whilst continuing to investigate the crucial phenomena of

dipole creation and the scattering of the system. Also, here we begin to consider the relevance of the point vortex model to more classical turbulent systems, finding the possibility of an inverse cascade in the point vortex model given certain forcing and dampening mechanisms. Finally, we consider point vortices in the case of compressible effects, i.e. dipoles in the presence of sound. In standard turbulence these kinds of interactions are likely to occur and so an understanding of dynamics is crucial to forming a larger theory of turbulent motion through point vortices. We then see under what sound distributions annihilation may occur and finally speculate of the annihilation solution as a final statistical equilibrium of the system, no doubt an important result when considering how an over-arching theory of turbulence due to vortex dipoles may be implemented.

Through this study we thus develop the beginnings of a potential future statistical model of dipole dynamics in the point vortex model, and prove the viability of capturing the dynamics of larger turbulent systems through this. To recap; a natural requirement of such a model is the presence of dipole dynamics in the turbulent system implying dilute vortices are present; the distance between vortices is much greater than the core size of the vortices themselves. Typical examples of systems fulfilling this requirement would be quantum turbulent regimes, and quasi-2D classical regimes (the reduction to 2D dynamics is also a necessary requirement for use of such a model, as could be expected of a model based around point vortex dynamics). If this is fulfilled the system can then be thought of as a series of interactions between vortex structures rather than a many body interaction of the numerous vortices in the system, and we hypothesise that it is advantageous to model the development of such a system in terms of the effects of vortex dipoles in such systems. This could be used to predict the various quantities involved in the evolution of turbulent flow; for example the evolution of vorticity by a kinetic equation as according to Chavanis [26], and various statistical quantities such as the number of dipoles/clusters in the system over time. Additionally, in chapter 3 we appear to capture the inverse cascade through the dipole effects we introduce, an extension of this study could potentially model the development of the inverse cascade according to the interactions undergone by dipoles. If development of such a model is accomplished, we are provided with a much more computationally efficient method of modelling turbulent dynamics, as the necessary computations are reduced from solving for every point vortex in a given system

to only modelling relevant quantities regarding the most common of dipole interactions, and large-scale point vortex clusters can also be approximated by point vortices of appropriate strength, greatly simplifying the computations required. This computational advantage will be most noticeable as the number of point vortices in the flow to be modelled becomes very large.

Appendix A

Appendix

A.1 Dipole-vortex scattering angles

In the appendix of [5] Aref computed the dipole-vortex scattering angles in the three vortex system. In this appendix, we will derive the scattering angles in this case due to is importance and relevance in the current work, and in doing so, we will correct a mistake in the original derivation. We follow as in [5]: consider the dipole-vortex collision as depicted in figure 2.1, we will utilise the evolution equation for b_2 (2.10), (note that Aref used the labelling b_3) to determine the scattering angle of the vortex dipole, or specifically the negatively signed point vortex labelled as vortex 2. The reason for tracking vortex 2 is that this point vortex will always be part of the final vortex dipole pair being the only negatively signed point vortex. Therefore, we will use its direction of propagation as a proxy for the dipole scattering angle. Following Aref, we express the point vortex model in terms of polar coordinates (r_i, ϕ_i), emanating from the origin (or center of circulation), defined by $x_i = r_i \cos(\phi_i), \quad y_i = r_i \sin(\phi_i)$, where r_i presents the distance of vortex i from the centre of circulation $\mathbf{x}_\Gamma$, and ϕ_i is the azimuthal angle. Then the Hamiltonian equation of motion of the point vortex system can be transformed into polar coordinates leading to

$$\kappa_i r_i \dot{r}_i = \frac{\partial H}{\partial \phi_i}, \qquad \kappa_i r_i \dot{\phi}_i = -\frac{\partial H}{\partial r_i}. \tag{A.1}$$

Following the initial strategy outlined by Novikov [28], we can transform our system from Cartesian coordinates to polar coordinates using the conservation laws (1.32) and (1.34), and

simple cosine laws for computing vortex separation around the centre of circulation, with the result for the dynamics of b_2, the equations (2.10). This leads to an evolution equation for $\dot{\phi}_2$ in terms of the variable b_2 giving

$$\dot{\phi}_2 = \frac{\theta}{4\pi C}\frac{9 - 3b_2 + \frac{4}{\theta}|b_2|}{(6-b_2)|b_2|}.$$

The scattering angle from the three vortex interaction can be subsequently defined by

$$\Delta\phi_2 = \lim_{t\to\infty}\phi_2(t) - \lim_{t\to-\infty}\phi_2(t) = \int_{-\infty}^{\infty}\dot{\phi}_2(t)\,dt.$$

Using (2.11) for $\dot{\phi}_2$ and (2.10) enables us to define the scattering angle in terms of elliptic integrals with respect to b_2:

$$\begin{aligned}\Delta\phi_2 &= \int_{-\infty}^{\infty}\dot{\phi}_2(t)\,dt = \int_{-\infty}^{\infty}\dot{\phi}_2(t)\frac{1}{\dot{b}_2(t)}\,db_2, \qquad (A.2)\\ &= \pm\frac{\sqrt{\theta}}{4}\int_{L_1}^{L_2}\frac{b_2(9-3b_2+\frac{4}{\theta}|b_2|)}{|b_2|(6-b_2)\sqrt{(|b_2|-\frac{9}{4}\theta)\left[(3-b_2)^2-\frac{4}{\theta}|b_2|\right]}}\,db_2,\\ &= \begin{cases}\mp\frac{\sqrt{\theta}}{4}\int_{L_1}^{L_2}\frac{9-(3+\frac{4}{\theta})b_2}{(6-b_2)\sqrt{(\alpha-b_2)(\beta-b_2)(\gamma-b_2)}}\,db_2 & \text{if } C>0,\\ \pm\frac{\sqrt{\theta}}{4}\int_{L_1}^{L_2}\frac{9-(3-\frac{4}{\theta})b_2}{(6-b_2)\sqrt{(b_2-\bar{\alpha})(b_2-\bar{\beta})(b_2-\bar{\gamma})}}\,db_2 & \text{if } C<0.\end{cases} \qquad (A.3)\end{aligned}$$

Here $L_1 = b_2(t\to-\infty)$, and $L_2 = b_2(t\to\infty)$ which will depend upon the parameter C and θ. The sign of the integrals will be determined by the sign of $\dot{b}_2$ during the evolution of b_2. We find that we have to consider the approach of the dipole pre-scattering separately from the evolution post-scattering. What we find is that the path taken by b_2 during the scattering process continuously evolves from the value of L_1 towards the first real root of the equation for $\dot{b}_2$ (2.10). This root corresponds to the periapsis of b_2 in which we can formally define as the critical point. After which we must consider separately the evolution of b_2 towards L_2 (we shall see that this corresponds to a change of sign of $\dot{b}_2$). We can simplify the above result by considering the dipole-vortex setup in each of the scattering regions (I, II, III) separately. In each case this will specify the sign of C and the integral limits L_1 and L_2 and enable us to perform the integral leading to an explicit formula for the scattering angle in terms of Legendre forms of elliptic integrals.

A.1.1 Region I ($C > 0$, $1/3 < \theta$)

In region I, the impact parameter ρ is large and positive and the scattering process will be of direct scattering type. For the values of the parameters $L_1 = \lim_{t\to-\infty} b_2 = -\infty$. As the evolution progresses, the value of b_2 will increase until the first real root of $\dot{b}_2$ is reached. For the values of C and θ in region I implies that roots β and γ are both complex meaning, so as b_2 must be real by definition, b_2 must increase from $-\infty$ until it reaches the physical boundary α, whereupon it again rebounds back to $-\infty$. This implies that the scattering angle is given by the value of the integral:

$$\begin{aligned}
\Delta\phi_2 &= \frac{\sqrt{\theta}}{4}\int_{-\infty}^{\alpha} \frac{9-(3+\frac{4}{\theta})b_2}{(6-b_2)\sqrt{(\alpha-b_2)(\beta-b_2)(\gamma-b_2)}}\, db_2 \\
&\quad - \frac{\sqrt{\theta}}{4}\int_{\alpha}^{-\infty} \frac{9-(3+\frac{4}{\theta})b_2}{(6-b_2)\sqrt{(\alpha-b_2)(\beta-b_2)(\gamma-b_2)}}\, db_2, \\
&= \frac{\sqrt{\theta}}{2}\int_{-\infty}^{\alpha} \frac{9-(3+\frac{4}{\theta})b_2}{(6-b_2)\sqrt{(\alpha-b_2)(\beta-b_2)(\gamma-b_2)}} db_2, \\
db_2 &= \frac{\sqrt{\theta}}{2}\left[\left(3+\frac{4}{\theta}\right)\int_{-\infty}^{\alpha}\frac{1}{y}\, db_2 + \left(9+\frac{24}{\theta}\right)\int_{-\infty}^{\alpha}\frac{1}{(b_2-6)y}\, db_2\right],
\end{aligned}$$

where $y = \sqrt{(\alpha-b_2)(\beta-b_2)(\gamma-b_2)}$. Note that coefficients for the first expression are determined by whether each particular integral is regarding the stage of the interaction before or after scattering, e.g. in the first integral corresponds to b_2 from $-\infty$ to α, and so we expect $\dot{b}_2 > 0$ hence this fixes the sign (+ in this case) arise in the $\dot{b}_2$ equation. The above integrals can be reduced to their Legendre Normal forms by simple substitutions found in Labahn and Mutrie [92]. The Legendre forms for the first and third complete elliptic integrals are given by (note we are using the *characteristic* n, given with an inverse sign than the usual third complete elliptic integral):

$$K(k) = \int_0^{\pi/2}\frac{1}{\sqrt{1-k^2\sin^2(\mu)}}\, d\mu, \qquad \Pi(n,k) = \int_0^{\pi/2}\frac{1}{(n\sin^2(\mu)+1)\sqrt{1-k^2\sin^2(\mu)}}\, d\mu.$$

To show this reduction, define a parameter $A = \sqrt{(\beta-\alpha)(\gamma-\alpha)}$ and split the first integral in the scattering angle expression into two with b_2 ranging from $-\infty$ to $\alpha - A$ and then $\alpha - A$ to

α,

$$\int_{-\infty}^{\alpha} \frac{1}{y}\, db_3 = \int_{-\infty}^{\alpha-A} \frac{1}{y}\, db_2 + \int_{\alpha-A}^{\alpha} \frac{1}{y}\, db_2,$$

and now consider the first integral on the right-hand side. Using the following substitutions

$$\sin^2(\mu) = \frac{8A(\alpha - b_2)}{(\alpha + A - b_2)^2}, \quad k^2 = \frac{2A + 2\alpha - \beta - \gamma}{4A},$$

this substitution gives a quadratic equation in b_2, the correct root depends upon whether the integral is from $-\infty \to \alpha - A$ or $\alpha - A \to \alpha$, using the positive root we can reduce the first integral to the following elliptic integral

$$\int_{-\infty}^{\alpha-A} \frac{1}{y}\, db_2 = \int_{0}^{\pi/2} \frac{1}{\sqrt{A}\sqrt{1 - k^2 \sin^2(\mu)}}\, d\mu = \frac{1}{\sqrt{A}} K(k).$$

The same is done for the second part from $\alpha - A$ to α, using the same expressions for A, k and $\sin(\mu)$ and the negative root for b_2 leading to the second integral reducing to

$$\int_{\alpha-A}^{\alpha} \frac{db_2}{y} = \int_{\pi/2}^{0} \frac{-1}{\sqrt{A}\sqrt{1 - k^2 \sin^2(\mu)}}\, d\mu = \frac{1}{\sqrt{A}} K(k).$$

The final expression for the first integral becomes

$$\int_{-\infty}^{\alpha} \frac{1}{y}\, db_2 = \int_{-\infty}^{\alpha-A} \frac{1}{y}\, db_2 + \int_{\alpha-A}^{\alpha} \frac{1}{y}\, db_2 = \frac{2}{\sqrt{A}} K(k).$$

The second integral can be similarly reduced by splitting the integral into two parts: one with limits from $-\infty$ to $\alpha - A$ and a second with limits from $\alpha - A$ to α

$$\int_{-\infty}^{\alpha} \frac{1}{(b_2 - 6)y}\, db_2 = \int_{-\infty}^{\alpha-A} \frac{1}{(b_2 - 6)y}\, db_2 + \int_{\alpha-A}^{\alpha} \frac{1}{(b_2 - 6)y}\, db_2$$

using the same substitutions as before with $n = -(\alpha + A - 6)^2/[4A(\alpha - 6)]$ gives

$$
\begin{aligned}
&= \frac{1}{\sqrt{A}} \int_0^{\pi/2} \frac{\sin^2(\mu)}{\left[(\alpha + A - 6)\sin^2(\mu) + 2A + 2A\cos(\mu)\right]\sqrt{1 - k^2\sin^2(\mu)}}\, d\mu \\
&+ \frac{1}{\sqrt{A}} \int_0^{\pi/2} \frac{\sin^2(\mu)}{\left[(\alpha + A - 6)\sin^2(\mu) + 2A - 2A\cos(\mu)\right]\sqrt{1 - k^2\sin^2(\mu)}}\, d\mu, \\
&= \frac{2}{\sqrt{A}(\alpha + A - 6)} \int_0^{\pi/2} \frac{(\alpha + A - 6)^2\sin^2(\mu) - 2A(\alpha + A - 6)}{\left[\sin^2(\mu)(\alpha + A - 6)^2 - 4A(\alpha - 6)\right]\sqrt{1 - k^2\sin^2(\mu)}}\, d\mu, \\
&= \frac{2}{\sqrt{A}(\alpha + A - 6)} \left[K(k) + \frac{1}{2}\left(\frac{A}{\alpha - 6} - 1\right)\Pi(n, k)\right].
\end{aligned}
$$

Subsequently, the full expression for the region I scattering angle can be simplified to

$$
\Delta\phi_3 = \sqrt{\frac{\theta}{A}}\left[\left(3 + \frac{4A}{\theta(\alpha + A - 6)}\right)K(k) + \frac{(\alpha - A - 6)}{\theta(\alpha + A - 6)}\Pi(n, k)\right].
$$

A.1.2 Region IIa ($C > 0$, $0 < \theta < 1/3$)

Region IIa corresponds the case where $C > 0$ and $0 < \theta < 1/3$ leading to exchange scattering and as such the evolution of the variable b_2 will evolve from the $t \to -\infty$ limit $-\infty$ until it reaches its periapsis at the root $b_2 = \gamma$ where the vortex interaction reaches the configuration with $b_1 = b_3$. At this point, an exchange interaction occurs and b_2 decreases towards $-\infty$ again (see phase point diagrams in [5] for clarification of this). Therefore, the scattering angle for vortex 2 becomes

$$
\begin{aligned}
\Delta\phi_2 &= \frac{\sqrt{\theta}}{4} \int_{-\infty}^{\gamma} \frac{9 - (3 + \frac{4}{\theta})b_2}{(6 - b_2)\sqrt{(\alpha - b_2)(\beta - b_2)(\gamma - b_2)}}\, db_2 \\
&- \frac{\sqrt{\theta}}{4} \int_{\gamma}^{-\infty} \frac{9 - (3 + \frac{4}{\theta})b_2}{(6 - b_2)\sqrt{(\alpha - b_2)(\beta - b_2)(\gamma - b_2)}}\, db_2, \\
&= \frac{\sqrt{\theta}}{2} \int_{-\infty}^{\gamma} \frac{9 - (3 + \frac{4}{\theta})b_2}{(6 - b_2)\sqrt{(\alpha - b_2)(\beta - b_2)(\gamma - b_2)}}\, db_2 \\
&= \frac{\sqrt{\theta}}{2} \left[\left(3 + \frac{4}{\theta}\right)\int_{-\infty}^{\gamma} \frac{1}{y}\, db_2 + \left(9 + \frac{24}{\theta}\right)\int_{-\infty}^{\gamma} \frac{1}{(b_2 - 6)y}\, db_2\right].
\end{aligned}
$$

Again where we have defined the variable $y = \sqrt{(\alpha - b_2)(\beta - b_2)(\gamma - b_2)}$. To reduce the above formula into normal form, we begin by applying the substitution

$$\sin^2(\mu) = \frac{\alpha - \gamma}{\alpha - b_2}, \qquad k^2 = \frac{\alpha - \beta}{\alpha - \gamma},$$

to both integrals. Then the first integral becomes

$$\int_{-\infty}^{\gamma} \frac{1}{y}\, db_2 = \frac{2}{\sqrt{\alpha - \gamma}} K(k),$$

while the second integral becomes

$$\begin{aligned}
\int_{-\infty}^{\gamma} \frac{1}{(b_2 - 6)y}\, db_2 &= \frac{2}{\sqrt{\alpha - \gamma}} \int_0^{\pi/2} \frac{\sin^2(\mu)}{[(\alpha - 6)\sin^2(\mu) - (\alpha - \gamma)]\sqrt{1 - k^2 \sin^2(\mu)}}\, d\mu, \\
&= \frac{2}{(\alpha - 6)\sqrt{\alpha - \gamma}} \left[K(k) - \int_0^{\pi/2} \frac{1}{\left[n \sin^2(\mu) + 1\right] \sqrt{1 - k^2 \sin^2(\mu)}}\, d\mu \right] \\
&= \frac{2}{(\alpha - 6)\sqrt{\alpha - \gamma}} \left[K(k) - \Pi(n, k) \right],
\end{aligned}$$

where the parameter $n = (\alpha - 6)/(\gamma - \alpha)$. Finally, returning to the full expression for the scattering angle for region IIa, we have

$$\Delta\phi_2 = \sqrt{\frac{\theta}{\alpha - \gamma}} \left[\left(\frac{3\alpha + \frac{4\alpha}{\theta} - 9}{\alpha - 6} \right) K(k) - \left(\frac{9 + \frac{24}{\theta}}{\alpha - 6} \right) \Pi(n, k) \right] = \sqrt{\frac{\theta}{\alpha - \gamma}} \left[3K(k) + \frac{4}{\theta} \Pi(n, k) \right].$$

A.1.3 Region IIb ($C < 0$, $0 < \theta < 8/3$)

For region IIb, $C < 0$ with $0 < \theta < 8/3$ and therefore at the initial condition when the dipole is far from the isolated point vortex, the variable tends towards $b_2 \to \infty$ as $t \to \infty$. As the vortex system evolves, then b_2 reduces until it reaches it periapsis at the largest root of the $\dot{b}_2$ equation for this parameter region, i.e. $b_2 = \bar{\gamma}$. Once at the periapsis point, the positive vortices exchange in the dipole and the dipole propagates away with the variable b_2 increasing back towards ∞. Therefore, initially b_2 is decreasing (hence $\dot{b}_2 < 0$) pre-scattering, while post-scattering we have

$\dot{b}_2 > 0$. This defines the signs to take in the scattering angle formula:

$$\begin{aligned}
\Delta\phi_2 &= -\frac{\sqrt{\theta}}{4}\int_{\infty}^{\bar{\gamma}} \frac{9-(3-\frac{4}{\theta})b_2}{(6-b_2)\sqrt{(b_2-\bar{\alpha})(b_2-\bar{\beta})(b_2-\bar{\gamma})}}\,db_2 \\
&+ \frac{\sqrt{\theta}}{4}\int_{\bar{\gamma}}^{\infty} \frac{9-(3-\frac{4}{\theta})b_2}{(6-b_2)\sqrt{(b_2-\bar{\alpha})(b_2-\bar{\beta})(b_2-\bar{\gamma})}}\,db_2 \\
&= \frac{\sqrt{\theta}}{2}\int_{\bar{\gamma}}^{\infty} \frac{9-(3-\frac{4}{\theta})b_2}{(6-b_2)\sqrt{(b_2-\bar{\alpha})(b_2-\bar{\beta})(b_2-\bar{\gamma})}}\,db_2 \\
&= \frac{\sqrt{\theta}}{2}\left[\left(3-\frac{4}{\theta}\right)\int_{\bar{\gamma}}^{\infty}\frac{db_2}{y} + \left(9-\frac{24}{\theta}\right)\int_{\bar{\gamma}}^{\infty}\frac{db_2}{(b_2-6)y}\right],
\end{aligned}$$

where again we have defined a variable $y = \sqrt{(b_2-\bar{\alpha})\left(b_2-\bar{\beta}\right)(b_2-\bar{\gamma})}$. We reduce both integrals in the same way as before, using the substitutions

$$\sin^2(\mu) = \frac{b_2-\bar{\gamma}}{b_2-\bar{\alpha}}, \quad k^2 = \frac{\bar{\alpha}-\bar{\beta}}{\bar{\gamma}-\bar{\beta}},$$

The first integral subsequently becomes

$$\int_{\bar{\gamma}}^{\infty}\frac{1}{y}\,db_2 = \frac{2}{\sqrt{\bar{\gamma}-\bar{\beta}}}K(k),$$

and the second integral becomes

$$\begin{aligned}
\int_{\bar{\gamma}}^{\infty}\frac{1}{(b_2-6)y}\,db_2 &= \frac{2}{\sqrt{\bar{\gamma}-\bar{\beta}}}\int_0^{\pi/2}\frac{\sin^2(\mu)-1}{\left[(\bar{\alpha}-6)\sin^2(\mu)+6-\bar{\gamma}\right]\sqrt{1-k^2\sin^2(\mu)}}\,d\mu \\
&= \frac{2}{(6-\bar{\gamma})\sqrt{\bar{\gamma}-\bar{\beta}}}\int_0^{\pi/2}\frac{\sin^2(\mu)-1}{[n\sin^2(\mu)+1]\sqrt{1-k^2\sin^2(\mu)}}\,d\mu, \\
&= \frac{2}{(\bar{\alpha}-6)\sqrt{\bar{\gamma}-\bar{\beta}}}\left[K(k)-\frac{\bar{\alpha}-\bar{\gamma}}{6-\bar{\gamma}}\Pi(n,k)\right],
\end{aligned}$$

where we have introduced a new parameter $n = (\bar{\alpha} - 6)/(6 - \bar{\gamma})$. Then the final full expression for the scattering angle in region IIb is

$$\begin{aligned}\Delta\phi_2 &= \sqrt{\frac{\theta}{\bar{\gamma} - \bar{\beta}}}\left[\left(\frac{3\bar{\alpha} - \frac{4\bar{\alpha}}{\theta} - 9}{\bar{\alpha} - 6}\right)K(k) - \left(\frac{\left(9 - \frac{24}{\theta}\right)(\bar{\alpha} - \bar{\gamma})}{(\bar{\alpha} - 6)(6 - \bar{\gamma})}\right)\Pi(n,k)\right] \\ &= \sqrt{\frac{\theta}{\bar{\gamma} - \bar{\beta}}}\left[3K(k) - \frac{4}{\theta}\frac{(\bar{\alpha} - \bar{\gamma})}{(6 - \bar{\gamma})}\Pi(n,k)\right].\end{aligned}$$

A.1.4 Region III ($C < 0$, $8/3 < \theta$)

For region III, the final case corresponding to direct scattering with $C < 0$ and $8/3 < \theta$, we have that in the limit of $t \to -\infty$, $b_2 \to \infty$, with b_2 initially decreasing until it reaches the periapsis point of $b_2 = \bar{\alpha}$, where the sign of $\dot{b}_2$ changes post-scattering and increases back up towards ∞. Therefore, the scattering angle integral (A.2) becomes (here the sign of each integral is determined by the sign of $\dot{b}_2$ pre- and post-scattering)

$$\begin{aligned}\Delta\phi_2 &= -\frac{\sqrt{\theta}}{4}\int_{\infty}^{\bar{\alpha}} \frac{9 - (3 - \frac{4}{\theta})b_2}{(6 - b_2)\sqrt{(b_2 - \bar{\alpha})(b_2 - \bar{\beta})(b_2 - \bar{\gamma})}}\, db_2 \\ &\quad + \frac{\sqrt{\theta}}{4}\int_{\bar{\alpha}}^{\infty} \frac{9 - (3 - \frac{4}{\theta})b_2}{(6 - b_2)\sqrt{(b_2 - \bar{\alpha})(b_2 - \bar{\beta})(b_2 - \bar{\gamma})}}\, db_2, \\ &= \frac{\sqrt{\theta}}{2}\int_{\bar{\alpha}}^{\infty} \frac{9 - (3 - \frac{4}{\theta})b_2}{(6 - b_2)\sqrt{(b_2 - \bar{\alpha})(b_2 - \bar{\beta})(b_2 - \bar{\gamma})}}\, db_2 \\ &= \frac{\sqrt{\theta}}{2}\left[\left(3 - \frac{4}{\theta}\right)\int_{\bar{\alpha}}^{\infty}\frac{db_2}{y} + \left(9 - \frac{24}{\theta}\right)\int_{\bar{\alpha}}^{\infty}\frac{db_2}{(b_2 - 6)y}\right],\end{aligned}$$

with $y = \sqrt{(b_2 - \bar{\alpha})(b_2 - \bar{\beta})(b_2 - \bar{\gamma})}$. The substitution in this case is given as:

$$\sin^2(\mu) = \frac{b_3 - \bar{\alpha}}{b_3 - \bar{\gamma}}, \qquad k^2 = \frac{\bar{\gamma} - \bar{\beta}}{\bar{\alpha} - \bar{\beta}},$$

which leads to the integrals simplifying to

$$\int_{\bar{\alpha}}^{\infty}\frac{1}{y}\, db_2 = \frac{2}{\sqrt{\bar{\alpha} - \bar{\beta}}}\int_0^{\pi/2}\frac{1}{\sqrt{1 - k^2\sin^2(\mu)}}\, d\mu = \frac{2}{\sqrt{\bar{\alpha} - \bar{\beta}}}K(k),$$

and

$$\int_{\bar{\alpha}}^{\infty} \frac{1}{(b_3-6)y}\, db_3 = \frac{2}{\sqrt{\bar{\alpha}-\bar{\beta}}} \int_0^{\pi/2} \frac{\sin^2(\mu)-1}{\left[(\bar{\gamma}-6)\sin^2(\mu)+6-\bar{\alpha}\right]\sqrt{1-k^2\sin^2(\mu)}}\, d\mu,$$
$$= \frac{2}{(\bar{\gamma}-6)\sqrt{\bar{\alpha}-\bar{\beta}}} \left[K(k) - \frac{\bar{\gamma}-\bar{\alpha}}{6-\bar{\alpha}}\Pi(n,k)\right].$$

Where we have defined the parameter $n = (\bar{\gamma}-6)/(6-\bar{\alpha})$. Subsequently, the final scattering angle expression in Legendre normal form is given as

$$\Delta\phi_2 = \frac{\sqrt{\theta}}{(\bar{\gamma}-6)\sqrt{\bar{\alpha}-\bar{\beta}}} \left\{ \left[\left(3-\frac{4}{\theta}\right)\bar{\gamma} - 9 \right] K(k) + \frac{4(\bar{\gamma}-\bar{\alpha})}{\theta}\Pi(n,k) \right\}.$$

A.1.5 Summary of the dipole-vortex scatting angle normal form reduction

In summary, the dipole-vortex scattering angle calculation is given by the solution to (A.2), where the path along which the integral is taken is defined by the values of variable $L_1 = b_2(t \to -\infty)$ and $L_2 = b_2(t \to \infty)$ via the periapsis of b_2. This means in (A.2), we must consider the approach and departure of the dipole separately. For the approach, we must use 2.10 with the appropriate sign corresponding to the sign $\dot{b}_2$ for our region, while after scattering the angle will be determined by (A.2) using the other sign of (2.10) as in all cases the value of $b_2(t \to -\infty) = b_2(t \to \infty)$. For each case we have shown that the scattering angle formulae correspond to the following integrals:

$$\Delta\phi_2 = \begin{cases} \dfrac{\sqrt{\theta}}{2}\displaystyle\int_{-\infty}^{\alpha} \frac{9-\left(3+\frac{4}{\theta}\right)b_2}{(6-b_2)\sqrt{(\alpha-b_2)(\beta-b_2)(\gamma-b_2)}}\, db_2 & \text{in region I,} \\ \dfrac{\sqrt{\theta}}{2}\displaystyle\int_{-\infty}^{\gamma} \frac{9-\left(3+\frac{4}{\theta}\right)b_2}{(6-b_2)\sqrt{(\alpha-b_2)(\beta-b_2)(\gamma-b_2)}}\, db_2 & \text{in region IIa,} \\ \dfrac{\sqrt{\theta}}{2}\displaystyle\int_{\bar{\gamma}}^{\infty} \frac{9-\left(3-\frac{4}{\theta}\right)b_2}{(6-b_2)\sqrt{(b_2-\bar{\alpha})(b_2-\bar{\beta})(b_2-\bar{\gamma})}}\, db_2 & \text{in region IIb,} \\ \dfrac{\sqrt{\theta}}{2}\displaystyle\int_{\bar{\alpha}}^{\infty} \frac{9-\left(3-\frac{4}{\theta}\right)b_2}{(6-b_2)\sqrt{(b_2-\bar{\alpha})(b_2-\bar{\beta})(b_2-\bar{\gamma})}}\, db_2 & \text{in region III.} \end{cases} \tag{A.4}$$

These can then be further simplified in the form of linear combinations of the Legendre complete forms of elliptic integrals.

$$\Delta\phi_2 = \sqrt{a_1}\left[a_2 K(k) + a_3 \Pi(n,k)\right], \tag{A.5}$$

where each constant coefficient a_1, a_2, a_3 and parameters k and n are given in table A1.

Table A1: Coefficients a_1, a_2, a_3 and parameters k and n for the dipole-vortex scattering angle are presented by region of interaction. The full scattering angle of the integrable case is determined from the Legendre normal form equation (A.5). Note that in region IIa we have defined an auxiliary parameter $A^2 = (\gamma - \alpha)(\beta - \alpha)$.

Region	a_1	a_2	a_3	k^2	n
I	$\dfrac{\theta}{\alpha-\gamma}$	3	$\dfrac{4}{\theta}$	$\dfrac{\alpha-\beta}{\alpha-\gamma}$	$\dfrac{6-\alpha}{\alpha-\gamma}$
IIa	$\dfrac{\theta}{A}$	$3+\dfrac{4}{\theta}+\dfrac{9+(24/\theta)}{\alpha+A-6}$	$\dfrac{[A/(\alpha-6)-1]\,[9+(24/\theta)]}{2(\alpha+A-6)}$	$\dfrac{A-(\beta+\gamma)/2+\alpha}{2A}$	$-\dfrac{(\alpha+A-6)^2}{4A(\alpha-6)}$
IIb	$\dfrac{\theta}{\bar{\gamma}-\bar{\beta}}$	3	$-\dfrac{[9-(24/\theta)]\,[\bar{\alpha}-\bar{\gamma}]}{(\bar{\alpha}-6)(6-\bar{\gamma})}$	$\dfrac{\bar{\alpha}-\bar{\beta}}{\bar{\gamma}-\bar{\beta}}$	$\dfrac{\bar{\alpha}-6}{6-\bar{\gamma}}$
III	$\dfrac{\theta}{\bar{\alpha}-\bar{\beta}}$	$\dfrac{3\bar{\gamma}-(4\bar{\gamma}/\theta)-9}{\bar{\gamma}-6}$	$-\dfrac{[9-(24/\theta)]\,[\bar{\gamma}-\bar{\alpha}]}{(\bar{\gamma}-6)(6-\bar{\alpha})}$	$\dfrac{\bar{\gamma}-\bar{\beta}}{\bar{\alpha}-\bar{\beta}}$	$\dfrac{\bar{\gamma}-6}{6-\bar{\alpha}}$

A.2 Numerical code

In this section we detail the numerical methods used to solve the point vortex system. The importance of solving the system numerically is two-fold; firstly it allows us to cross-examine our theoretical results to ensure reliability, second it gives a framework for solving systems comprising more than three vortices, which is in general not possible to solve analytically as already stated. Technically, the point vortex model as described previously consists of a system of differential equations based on Hamilton's canonical equations and the conserved Hamiltonian H. This is essentially an initial value problem with the initial vortex coordinates as the initial conditions. It is then natural to assume that any standard algorithm for solving this kind of problem, such as a standard Runge-Kutta method of order 4, will suffice here. When running basic simulations on the point vortex equations using this method however we quickly find that the supposed conserved quantities actually do not remain constant with respect to time in the numerics. This is due to the phenomenon where dipole vortices being close together leads to

faster dipole travel and so over a fixed time step gives a greater error. Clearly we are in need of a more sophisticated method for solving the system.

In order to determine where the error lies we must first examine the Runge-Kutta family of algorithms in detail. To begin we briefly examine the widely known fourth order Runge-Kutta, or "RK4", method. The RK4 method and following theory is reproduced from Burden and Faires [134]. Given an ordinary differential equation and also initial value, beginning at time $t = a$ and ending at $t = b$:

$$\dot{y} = f(t, y), \quad y(a) = y_0, \quad a \leq t \leq b.$$

Note that in this case our f refers to the original equations of motion for the point vortex system, whereas the y in our case would be the original vortex positions. Here $y_i = y(t_i)$ is the unknown we wish to find. Using a step size $0 < h < 1$ such that $t_{i+1} = t_i + h$ we approximate y_{i+1} as:

$$y_{i+1} = y_i + \frac{h}{6}(k_1 + 2k_2 + 2k_3 + k_4),$$

with :

$$\begin{aligned} k_1 &= f(t_i, y_i), \\ k_2 &= f(t_i + \frac{h}{2}, y_i + \frac{k_1}{2}), \\ k_3 &= f(t_i + \frac{h}{2}, y_i + \frac{k_2}{2}), \\ k_4 &= f(t_i + h, y_i + k_3). \end{aligned}$$

Hence, this basic Runge-Kutta method approximates y_{i+1} as the previous approximation y_i plus a weighted average of the increments k. We note the number of function calls involved in this process, i.e. the number of times it is necessary to evaluate function f at each point in time. Also, this particular Runge-Kutta method gives a local truncation error of $\mathcal{O}(h^4)$. The truncation error can be reduced by using a higher order Runge-Kutta method; however this has the effect of increasing the number of function calls required per time point whilst having little effect on conservation laws. We can also generalize the Runge-Kutta method to give order

approximations. We give the arbitrary Runge-Kutta method of s stages as:

$$y_{n+1} = y_n + h\sum_{i=1}^{s} b_i k_i, \tag{A.6}$$

where

$$\begin{aligned} k_1 &= f(t_n, y_n), \\ k_2 &= f(t_n + c_2 h, y_n + h(a_{21}k_1)), \\ k_3 &= f(t_n + c_3 h, y_n + h(a_{31}k_1 + a_{32}k_2)), \\ &\vdots \\ k_s &= f(t_n + c_s h, y_n + h(a_{s1}k_1 + a_{s2}k_2 + \cdots + a_{s,s-1}k_{s-1})). \end{aligned} \tag{A.7}$$

In order to specify the particular Runge-Kutta method to be used one must provide the number of stages s, as well as the coefficients a_{ij} known as the Runge-Kutta matrix, the coefficients b_i known as the weights, and the coefficients c_i known as the nodes.

In general, we note that approximations become more accurate as a higher order Runge-Kutta, and so a higher number of function calls, is used. This effect however becomes increasingly less prominent as $s > 5$, whereas the function calls continually increase resulting in a longer runtime as order increases. It is clear that in order to achieve a more accurate simulation we must either use a higher order system or reduce the step size to achieve a smaller error. However, if h is reduced then we will then have an increased number of time points, in other words it will take longer to reach our endpoint $t = b$ and as such this will result in more iterations of the approximation step and so more function calls overall. Also as already discussed, by increasing the order of the system increases the amount of functions calls and so is also not an attractive option. We then need a procedure that will reduce error as much as possible such that integrals of motion are conserved, whilst at the same time not reducing the time step h, or considering Runge-Kutta methods of too high an order, unless absolutely necessary.

To solve this problem, we will introduce an adaptive time stepping scheme. Essentially we will first execute a Runge-Kutta method of order 4 to attain a first approximation we will denote z_{i+1}, we will then apply a more accurate Runge-Kutta method of order 5 also. We will then allow

this fifth order solution to be our approximation of the next time point i.e. y_{i+1}. The purpose of calculating both fourth and fifth order approximations is that it allows us to calculate an error term $|y_{i+1} - z_{i+1}|$, this represents the error of the fourth order approximation with respect to the next time point approximation y_{i+1}. Now using this error term we can adjust the step size h such that the error is below a certain threshold, such that error is kept as low as possible and that invariants are hopefully conserved. Specifically we are employing coefficients from the so called "Dormand-Prince" or "RK5(4)7M" method, introduced previously by Dormand and Prince [135]. The coefficients in this method are chosen especially to ensure the highest accuracy in the fifth order approximation. Next we must decide how to adjust our time step according to the error. We will implement the commonly used local elementary controller [136]:

$$h_{i+1} = h_i \left(\frac{\epsilon}{|y_{i+1} - z_{i+1}|} \right)^{\frac{1}{5}}, \tag{A.8}$$

where ϵ is a user defined error tolerance; the larger the value of ϵ, the larger the new step size h_{i+1} will be. It is also important in such an algorithm for reasons of computational stability is to limit how much h can increase or decrease over a given time step adaption, specifically we apply a lower limit to the possible time step of $h_{min} = 10^{-7}$, an upper limit of $h_max^{0.5}$.

We now have a complete method for solving the system of point vortices numerically, where error is as small as possible. Through simulations in the current work we consistently use an error tolerance of 10^{-12}. We give the coefficients to the Dormand-Prince method in the form of a Butcher tableau, a commonly used method for displaying the coefficients used in a Runge-Kutta family method. The Butcher tableau expresses the coefficients for a Runge-Kutta method with s stages as such:

0					
c_2	a_{21}				
c_3	a_{31}	a_{32}			
$\vdots$	$\vdots$		$\ddots$		
c_s	a_{s1}	a_{s2}	$\dots$	$a_{s,s-1}$	
	b_{11}	b_{12}	$\dots$	$b_{1,s-1}$	$b_{1,s}$
	b_{21}	b_{22}	$\dots$	$b_{2,s-1}$	$b_{2,s}$

Table A2: Basic Butcher tableau showing a Runge-Kutta method of arbitrary order.

With a_{ij}, b_i, c_i corresponding to the coefficients already shown in (A.6) and (A.7). We then

express our Dormand-Prince method as:

0							
$\frac{1}{5}$	$\frac{1}{5}$						
$\frac{3}{10}$	$\frac{3}{40}$	$\frac{9}{40}$					
$\frac{4}{5}$	$\frac{44}{45}$	$-\frac{56}{15}$	$\frac{32}{9}$				
$\frac{8}{9}$	$\frac{19372}{6561}$	$-\frac{25360}{2187}$	$\frac{64448}{6561}$	$-\frac{212}{729}$			
1	$\frac{9017}{3168}$	$-\frac{355}{33}$	$\frac{46732}{5247}$	$\frac{49}{176}$	$-\frac{5103}{18656}$		
1	$\frac{35}{384}$	0	$\frac{500}{1113}$	$\frac{125}{192}$	$-\frac{2187}{6784}$	$\frac{11}{84}$	
	$\frac{35}{384}$	0	$\frac{500}{1113}$	$\frac{125}{192}$	$-\frac{2187}{6784}$	$\frac{11}{84}$	0 4th order
	$\frac{5179}{57600}$	0	$\frac{7571}{16695}$	$\frac{393}{640}$	$-\frac{92097}{339200}$	$\frac{187}{2100}$	$\frac{1}{40}$ 5th order

Table A3: Butcher tableau showing the coefficients of the Dormand-Prince method.

The absolute difference between approximations gives the error of the fourth order approximation as discussed previously.

To briefly summarise our numerical method, we express the coordinates of a particular vortex system in terms of the position vector $\boldsymbol{x}_i = (x_i, y_i)$. In order to solve a given system we apply the Dormand-Prince adaptive time step method to each $\dot{x}_i$ and $\dot{y}_i$, to then approximate both x_i and y_i values at the next time point until the time end point $t = b$ is reached. Note here we use the arbitrary formulation $\dot{\boldsymbol{x}} = f(t, \boldsymbol{x})$ with $a \leq t \leq b$ and initial condition $y(t = a) = \alpha$. Coefficients are as given in the Butcher tableau in the previous section. The pseudocode for the Dormand-Prince method is given:

set a, b

set h

set h_{min}

set h_{max}

set ϵ

set vector $\boldsymbol{x}$

set vector t

$t_0 = a$

$y_0 = \alpha$

function $f(t, \boldsymbol{x})$

    return $\dot{\boldsymbol{x}}(t, \boldsymbol{x})$

end function

function CONTROLLER(i, E)

$h = h\left(\frac{\epsilon}{E}\right)^{\frac{1}{5}}$

if $h < h_{min}$ **then**

$h = h_{min}$

end if

if $h > h_{max}$ **then**

$h = h_{max}$

end if

end function

function APPROXIMATE(i)

$k_1 = hf(t_i, \boldsymbol{x}_i)$

$k_2 = hf(t_i + c_2 h, \boldsymbol{x}_i + a_{21}k_1)$

$k_3 = hf(t_i + c_3 h, \boldsymbol{x}_i + a_{31}k_1 + a_{32}k_2)$

$\vdots$

$k_7 = hf(t_i + h, \boldsymbol{x}_i + a_{71}k_1 + a_{73}k_3 + a_{74}k_4 - a_{75}k_5 + a_{76}k_6)$

$RK4 = \boldsymbol{x}_i + b_{11}k_1 + b_{13}k_3 + b_{14}k_4 - b_{15}k_5 + b_{16}k_6$

$\boldsymbol{x}_{i+1} = \boldsymbol{x}_i + b_{21}k_1 + b_{23}k_3 + b_{24}k_4 - b_{25}k_5 + b_{26}k_6 + b_{27}k_7$

Controller(i, $|\boldsymbol{x}_{i+1} - RK4|$)

end function

$i = 0$

while $t_i < b$ **do**

Approximate(i)

$t_{i+1} = t_i + h$

$i = i + 1$

end while

This forms the complete numerical method we will use to solve the system. We will consider the most basic non-trivial cases of vortex motion both theoretically and numerically in order to determine the reliability of our numerical method. We examine the case of two identical vortices in proximity and the case of vortex and anti-vortex in proximity.

A.2.1 Identical vortex evolution

First we examine the case of identical vortices in proximity. By basic calculation we can determine velocity of each vortex in the identical vortex case. We start with two point vortices with Cartesian coordinates of vortex 1 at $(0, 0.4)$ and vortex 2 at $(0, -0.4)$ and with circulations $\kappa_1 = \kappa_2 = 1$. We calculate the velocity of each directly using (1.31) as:

$$\begin{aligned}
\dot{x}_1 &= -\frac{1}{2\pi}\frac{\kappa y_{1,2}}{\ell_{i,j}^2} = -0.19894, \\
\dot{x}_2 &= -\frac{1}{2\pi}\frac{\kappa y_{2,1}}{\ell_{1,2}^2} = 0.19894, \\
\dot{y}_1 &= \frac{1}{2\pi}\frac{\kappa x_{1,2}}{\ell_{1,2}^2} = 0, \\
\dot{y}_2 &= \frac{1}{2\pi}\frac{\kappa x_{2,1}}{\ell_{1,2}^2} = 0.
\end{aligned}$$

Each vortex in the system exerts an initial impulse upon the other giving each vortex a certain x velocity but with zero velocity in the y direction, due to starting the system with $x_1 = x_2 = 0$, however once we pass the initial time point vortex separation in the x direction $x_{ij} \neq 0$, implying each vortex will now have velocity in the y direction due to (1.31). Also it is clear from these basic calculations that $\dot{x}_1 = -\dot{x}_2$ and $\dot{y}_1 = -\dot{y}_2$ throughout the entire system. Using the length formula (1.30) we can say that:

$$\begin{aligned}
\ell_{1,2}^2 &= (x_1 - x_2)^2 + (y_1 - y_2)^2, \\
\implies \frac{d}{dt}\ell_{1,2}^2 &= 2(x_1 - x_2)(\dot{x}_1 - \dot{x}_2) + 2(y_1 - y_2)(\dot{y}_1 - \dot{y}_2), \\
&= \frac{\kappa}{\pi\ell_{1,2}^2}(-2x_{1,2}y_{1,2} + 2y_{1,2}x_{1,2}) = 0, \\
\implies \ell_{1,2}^2 = 0 &\implies \ell_{1,2} = 0.
\end{aligned}$$

The length between vortices hence remains constant, noting the individual vortex velocities this implies that vortices in such a formation rotate counter-clockwise around the center of vorticity $(0, 0)$ with constant radius $\ell_{1,2} = 0.8$. We can also deduce the angular velocity of the system

by first defining the polar angle and radius as:

$$\phi_i = \arctan\left(\frac{y_i}{x_i}\right),$$
$$r_i^2 = x_i^2 + y_i^2.$$

We see that:

$$\dot{\phi}_i = \frac{\dot{y}_i x_i - \dot{x}_i y_i}{x_i^2 + y_i^2},$$
$$\implies \dot{\phi}_1 = \dot{\phi}_2 = 0.12433,$$
$$\frac{d}{dt}r = \frac{\dot{x}_i x_i + \dot{y}_i y_i}{r_i},$$
$$\implies \dot{r}_1 = \dot{r}_2 = 0.$$

Hence, we have the same angular velocity for both vortices, so we can characterise the angular velocity of the entire rotation as $\dot{\phi} = 0.12433$. To check our numerical method we run a simulation with these starting coordinates and circulations and plot the results at each time point to achieve a trace of the motion (note that the light blue colours indicate vortex positions near the beginning of the simulation whilst the colour represents vortex positions towards the end).

The motion of the system in this case is shown in the figure A.1:

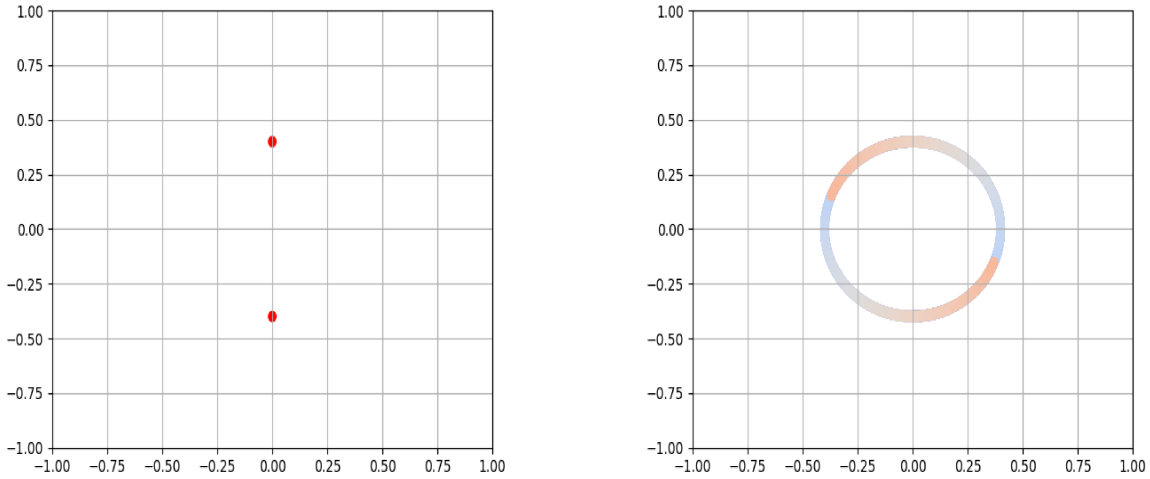

(a) Vortices at $t = 0$ (b) Vortex motion trace

Figure A.1: Demonstration of motion in the identical vortex case.

As we see the numerical results agree with our theoretical predictions. We also plot the velocity of our vortices as such:

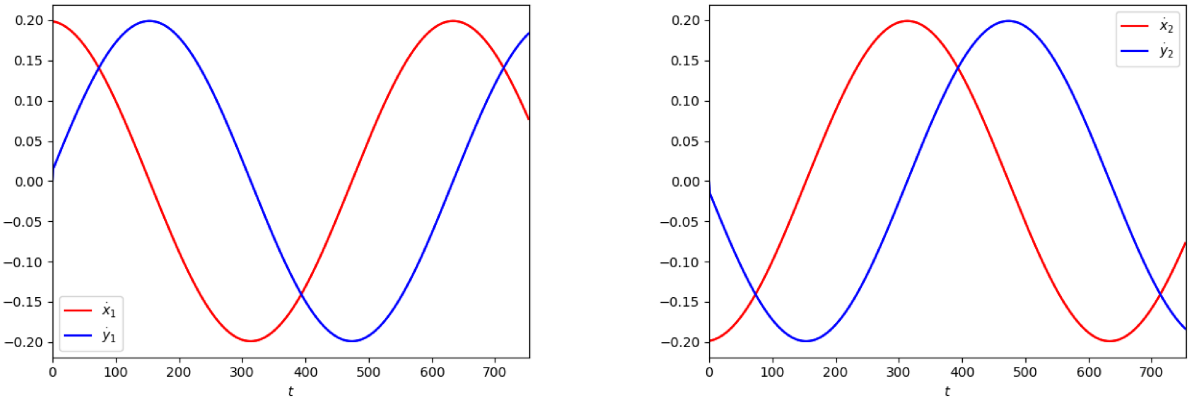

(a) Velocities of the first vortex

(b) Velocities of the second vortex

Figure A.2: Velocities of each vortex in the identical vortex case.

Continuing, we can also solve for the conserved quantities to make sure they agree with the numerics, giving the Hamiltonian and momentums as:

$$H = -\frac{2\ln(0.8)}{4\pi} = 0.035514,$$

$$P = 0,$$

$$Q = 0,$$

$$M = 0.32.$$

We then solve for the conserved quantities numerically and plot:

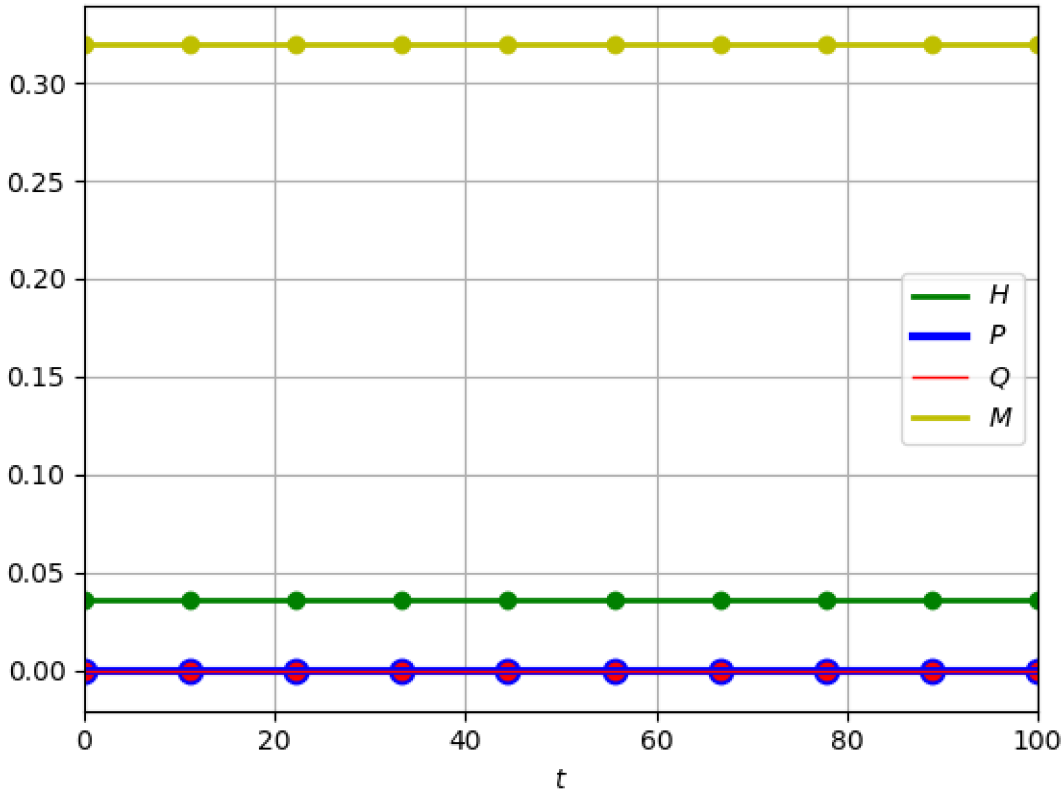

Figure A.3: Plot of the four conserved quantities in the identical vortex case.

We represent theoretical predictions as solid lines, and the results from the numerical simulations as points. In figure A.3 numerically the momenta and Hamiltonian are in agreement with our theoretical predictions and are also conserved.

A.2.2 Vortex/anti-vortex evolution

We repeat the same process for the vortex/anti-vortex pair, this particular set up is of critical importance so from here on we will refer to this as a "dipole". Starting coordinates remain the same, but the vortex at $(0, -0.4)$ now is replaced by the anti-vortex, i.e. circulation of this

vortex is $-\kappa$. We find velocities at the starting point to be:

$$\dot{x}_1 = 0.19894,$$
$$\dot{x}_2 = 0.19894,$$
$$\dot{y}_1 = 0,$$
$$\dot{y}_2 = 0.$$

We have similar results to the previous case, except here $\dot{x}_1 = \dot{x}_2$, so after the initial time point there will still be a separation of 0 in the x direction, therefore from (1.31) there will still be no velocity in the y direction after the initial time point. Examining the length derivative as before:

$$\begin{aligned}\frac{d}{dt}\ell_{1,2}^2 &= 2(x_1 - x_2)(\dot{x}_1 - \dot{x}_2) + 2(y_1 - y_2)(\dot{y}_1 - \dot{y}_2), \\ &= \frac{x_{1,2}}{\pi\ell_{1,2}^2}(y_{1,2} - y_{1,2}) + \frac{y_{1,2}}{\pi\ell_{1,2}^2}(x_{1,2} - x_{1,2}) = 0.\end{aligned}$$

So again we have a constant separation between the vortices in time. As both vortices are moving with the same x velocity, a constant separation length, and a y velocity of zero we conclude that the dipole must propagate off to infinity following a trajectory parallel to the perpendicular bisector of the vortex points. We verify this in a numerical plot as before in figure A.4:

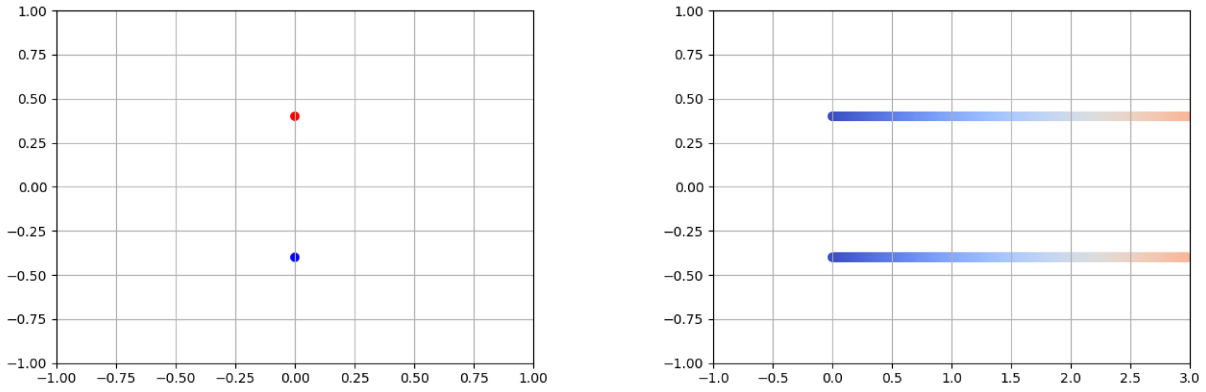

(a) Vortices $t = 0$ (b) Vortex motion trace

Figure A.4: Demonstration of motion in the dipole case.

Where here the red point represents an ordinary vortex with $\kappa = 1$ and the blue point represents the anti-vortex with $\kappa = -1$. Note that here we find the velocity is constant as predicted:

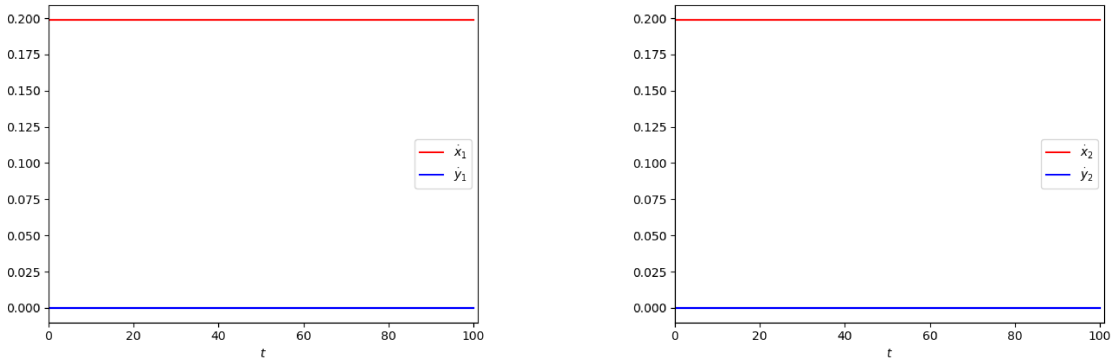

(a) Velocity of the first vortex

(b) Velocity of the second vortex

Figure A.5: Velocities of each vortex in the dipole case.

We find conserved quantities in the dipole case to be:

$$H = \frac{2\ln(0.8)}{4\pi} = -0.035514,$$

$$P = 0,$$

$$Q = 0.8,$$

$$M = 0.$$

We again plot these quantities numerically to find:

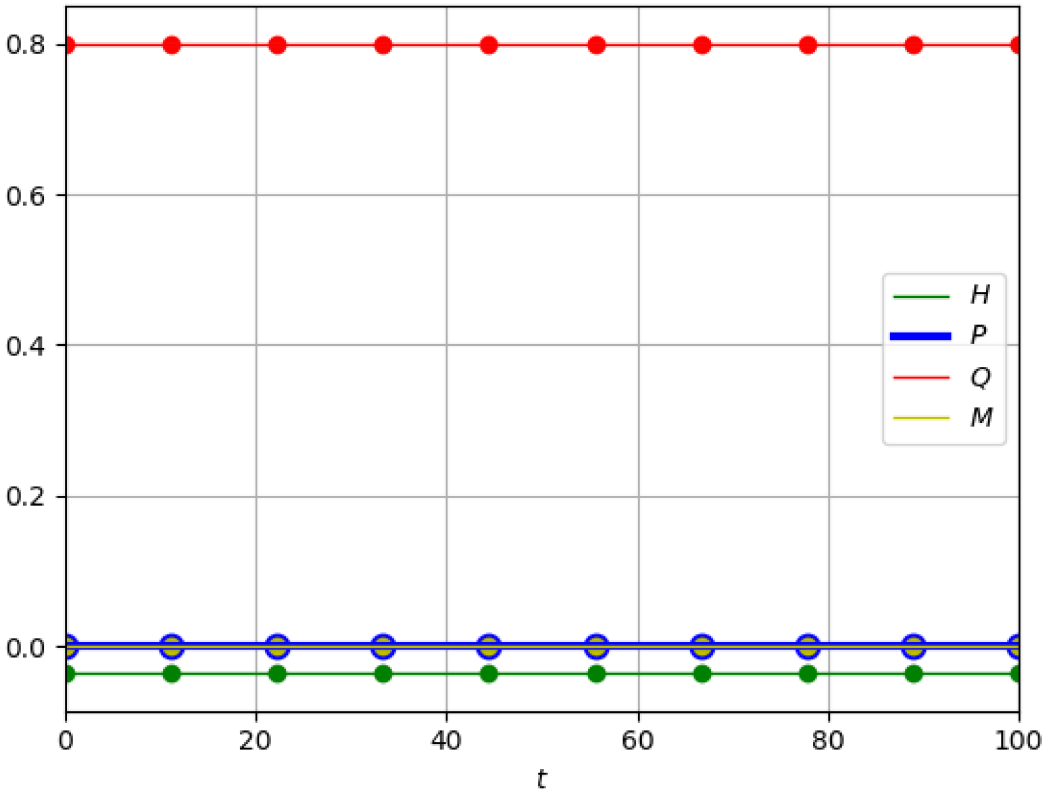

Figure A.6: Plot of the conserved quantities with respect to time in the dipole case.

As before we see that vortex trajectories and conserved quantities of the system found numerically are in agreement with our theoretical predictions. Hence, we can ensure the reliability of our numerical method, which we will now use to analyse more interesting vortex schemes.

Bibliography

[1] E A Cornell and C E Wieman. Nobel Lecture: Bose-Einstein condensation in a dilute gas, the first 70 years and some recent experiments. *Rev. Mod. Phys.*, 74(3):19, 2002.

[2] M. H. Anderson, J. R. Ensher, M. R. Matthews, C. E. Wieman, and E. A. Cornell. Observation of Bose-Einstein Condensation in a Dilute Atomic Vapor. *Science, New Series*, 269(5221):198–201, 1995.

[3] Andrew W. Baggaley, Jason Laurie, and Carlo F. Barenghi. Vortex-density fluctuations, energy spectra and vortical regions in superfluid turbulence. *Journal of Statistical Physics*, 156(6):1066–1092, September 2014. arXiv: 1207.7296.

[4] B. Eckhardt and H. Aref. Integrable and Chaotic Motions of Four Vortices II. Collision Dynamics of Vortex Pairs. *Philosophical Transactions of the Royal Society A: Mathematical, Physical and Engineering Sciences*, 326(1593):655–696, November 1988.

[5] Hassan Aref. Motion of three vortices. *The Physics of Fluids*, 22(3):393–400, March 1979.

[6] Osbourne Reynolds. An experimental investigation of the circumstances which determine whether the motion of water shall be direct or sinuous : and of the law of resistance in parallel channels. *Philosophical Transactions of the Royal Society of London*, 174:935–982, 1883.

[7] A. N. Kolmogorov. Dissipation of Energy in the Locally Isotropic Turbulence. *Proceedings: Mathematical and Physical Sciences*, 434(1890,):15–17, 1941.

[8] Lars Onager. Statistical hydrodynamics. *Il Nuovo Cimento*, 6:279–287, 1949.

[9] L. J. Campbell and Kevin O'Neil. Statistics of two-dimensional point vortices and high-energy vortex states. *Journal of Statistical Physics*, 65(3):495–529, November 1991.

[10] P. H. Chavanis and M. Lemou. Kinetic theory of point vortices in two dimensions: analytical results and numerical simulations. *The European Physical Journal B*, 59(2):217–247, September 2007.

[11] G. F. Carnevale, J. C. McWilliams, Y. Pomeau, J. B. Weiss, and W. R. Young. Evolution of vortex statistics in two-dimensional turbulence. *Physical Review Letters*, 66(21):2735–2737, May 1991.

[12] Haralambos Marmanis. The kinetic theory of point vortices. *Proceedings of the Royal Society of London. Series A: Mathematical, Physical and Engineering Sciences*, 454(1970):587–606, February 1998.

[13] N. N. (Nikolaĭ Nikolaevich) Bogolyubov. *The dynamical theory in statistical physics*. International monographs on advanced mathematics and physics. Hindustan Pub. Corp., 1965.

[14] N N Bogolyubov (Jr.) and D P Sankovich. N.N. Bogolyubov and statistical mechanics. *Russian Mathematical Surveys*, 49(5):19–49, October 1994.

[15] Michel Rieutord. *Fluid Dynamics*. Graduate Texts in Physics. Springer International Publishing, Cham, 2015.

[16] A Obukhov. Spectral energy distribution in a turbulent flow. *Izv. Akad. Nauk. SSSR. Ser. Geogr. i. Geofiz*, 5:453–466, 1941.

[17] Uriel Frisch. *Turbulence, the Legacy of A.N. Kolmogorov*. Cambridge University Press, 1995.

[18] Antti Hellsten. New Advanced k-w Turbulence Model for High-Lift Aerodynamics. In *42nd AIAA Aerospace Sciences Meeting and Exhibit*. American Institute of Aeronautics and Astronautics, 2005. _eprint: https://arc.aiaa.org/doi/pdf/10.2514/6.2004-1120.

[19] Simon Watkins, Ravi S, and Loxton B. The Effect of Turbulence on the Aerodynamics of Low Reynolds Number Wings. *Engineering Letters*, 18, August 2010.

[20] Gregory P Bewley, Daniel P Lathrop, and Katepalli R Sreenivasan. Characterisation of superfluid vortices in helium II. *arXiv preprint cond-mat/0512431*, page 7, 2005.

[21] Woo Jin Kwon, Geol Moon, Jae-yoon Choi, Sang Won Seo, and Yong-il Shin. Relaxation of superfluid turbulence in highly oblate Bose-Einstein condensates. *Physical Review A*, 90(6):063627, December 2014.

[22] L. Madeira, M. A. Caracanhas, F. E. A. dos Santos, and V. S. Bagnato. Quantum turbulence in quantum gases. *Annual Review of Condensed Matter Physics*, 11(1):annurev–conmatphys–031119–050821, March 2020. arXiv: 1903.12215.

[23] Davidson Moreira and Marco Vilhena, editors. *Air pollution and turbulence: modeling and applications*. CRC Press/Taylor & Francis, Boca Raton, FL, 2010. OCLC: ocn456728732.

[24] John Kim, Parviz Moin, and Robert Moser. Turbulence statistics in fully developed channel flow at low Reynolds number. *Journal of Fluid Mechanics*, 177:133–166, April 1987.

[25] P. H. Chavanis. Kinetic theory of point vortices: Diffusion coefficient and systematic drift. *Physical Review E*, 64(2):026309, July 2001.

[26] Pierre-Henri Chavanis. Kinetic theory of Onsager's vortices in two-dimensional hydrodynamics. *Physica A: Statistical Mechanics and its Applications*, 391(14):3657–3679, July 2012.

[27] Hassan Aref. Point vortex dynamics: A classical mathematics playground. *Journal of Mathematical Physics*, 48(6):065401, June 2007.

[28] E A Novikov. Dynamics and statistics of a system of vortices. *Journal of Experimental and Theoretical Physics*, 41(5):937–943, 1975.

[29] A. Colagrossi, S. Marrone, P. Colagrossi, and D. Le Touzé. Da Vinci's observation of turbulence: A French-Italian study aiming at numerically reproducing the physics behind one of his drawings, 500 years later. *Physics of Fluids*, 33(11):115122, November 2021. Publisher: American Institute of Physics.

[30] David Acheson. *Elementary Fluid Dynamics*. Oxford Applied Mathematics and Computing Science Series. Clarendon Press, 1st edition, 1990.

[31] Wm. T. Ashurst, A. R. Kerstein, R. M. Kerr, and C. H. Gibson. Alignment of vorticity and scalar gradient with strain rate in simulated Navier–Stokes turbulence. *Physics of Fluids*, 30(8):2343, 1987.

[32] H. J. H. Clercx and G. J. F. van Heijst. Two-Dimensional Navier–Stokes Turbulence in Bounded Domains. *Applied Mechanics Reviews*, 62(2):020802–020802–25, February 2009.

[33] Zhen-Su She, Shiyi Chen, Gary Doolen, Robert H. Kraichnan, and Steven A. Orszag. Reynolds number dependence of isotropic Navier-Stokes turbulence. *Physical Review Letters*, 70(21):3251–3254, May 1993.

[34] G. K. Batchelor. *An Introduction to Fluid Dynamics*. Cambridge Mathematical Library. Cambridge University Press, 2000.

[35] Bastian E. Rapp, editor. *Microfluidics: Modelling, Mechanics and Mathematics*. Micro and Nano Technologies. Elsevier, Oxford, 2017.

[36] R. Temam and X. Wang. The convergence of the solutions of the Navier-Stokes equations to that of the Euler equations. *Applied Mathematics Letters*, 10(5):29–33, 1997.

[37] Paul K Newton. *The N- vortex problem: analytical techniques*. Springer, New York; London, 2011. OCLC: 1063513491.

[38] H. Helmholtz. LXIII. *On Integrals of the hydrodynamical equations, which express vortex-motion. The London, Edinburgh, and Dublin Philosophical Magazine and Journal of Science*, 33(226):485–512, January 1867.

[39] David J. Griffiths. *Introduction to electrodynamics*. Pearson, Boston, fourth edition edition, 2013.

[40] Hiroyuki Adachi, Shoji Fujiyama, and Makoto Tsubota. Steady State of Counterflow Quantum Turbulence: Vortex filament Simulation with the Full Biot-Savart Law. *Physical Review B*, 81(10), March 2010. arXiv: 0912.4822.

[41] Wiiliam T. Ashurst and D. I. Meiron. Numerical Study of Vortex Reconnection. *Physical Review Letters*, 58(1632-1635), April 1987.

[42] Javier JiméNez and Alan A. Wray. On the characteristics of vortex filaments in isotropic turbulence. *Journal of Fluid Mechanics*, 373:255–285, October 1998.

[43] Guido Boffetta and Robert E Ecke. Two-Dimensional Turbulence. *Annual Review of Fluid Mechanics*, page 25, 2012.

[44] Robert H. Kraichnan and David Montgomery. Two-dimensional turbulence. *Reports on Progress in Physics*, 43(5):547, 1980.

[45] Jason Laurie, Guido Boffetta, Gregory Falkovich, Igor Kolokolov, and Vladimir Lebedev. Universal Profile of the Vortex Condensate in Two-Dimensional Turbulence. *Physical Review Letters*, 113(25):254503, December 2014.

[46] Brynmor Haskell and Armen Sedrakian. Superfluidity and Superconductivity in Neutron Stars. *arXiv:1709.10340 [astro-ph, physics:gr-qc, physics:nucl-th]*, September 2017. arXiv: 1709.10340.

[47] C. F. Barenghi, L. Skrbek, and K. R. Sreenivasan. Introduction to quantum turbulence. *Proceedings of the National Academy of Sciences*, 111(Supplement_1):4647–4652, March 2014.

[48] W. H Keesom and Miss A. P Keesom. Thermodynamic diagrams of liquid helium. *Physica*, 1(1):128–133, January 1934.

[49] W. H. Keesom and A. P. Keesom. New measurements on the specific heat of liquid helium. *Physica*, 2:557–572, January 1935. ADS Bibcode: 1935Phy.....2..557K.

[50] B. V. Rollin and F. Simon. On the "film" phenomenon of liquid helium II. *Physica*, 6(2):219–230, February 1939.

[51] P. Kapitza. Viscosity of Liquid Helium below the λ-Point. *Nature*, 141(3558):74–74, January 1938. Number: 3558 Publisher: Nature Publishing Group.

[52] Kenneth S. Krane and David Halliday. *Introductory nuclear physics*. Wiley, New York, 1987.

[53] J. Bardeen, L. N. Cooper, and J. R. Schrieffer. Theory of Superconductivity. *Physical Review*, 108(5):1175–1204, December 1957.

[54] Carlo F. Barenghi, Ladislav Skrbek, and Katepalli R. Sreenivasan. *Quantum Turbulence*. Cambridge University Press, 1 edition, September 2023.

[55] D. Vollhardt and P. Woelfle. Superfluid Helium 3: Link between Condensed Matter Physics and Particle Physics, December 2000. arXiv:cond-mat/0012052.

[56] D Vollhardt and P Wolfle. The superfluid phases of helium 3. January 1990.

[57] W. F. Vinen. How is turbulent energy dissipated in a superfluid? *Journal of Physics: Condensed Matter*, 17(45):S3231, October 2005.

[58] R.P. Feynman. APPLICATION OF QUANTUM MECHANICS TO LIQUID HELIUM. In *Helium 4*, pages 268–313. Elsevier, 1971.

[59] K. W. Schwarz. Critical Velocity for a Self-Sustaining Vortex Tangle in Superfluid Helium. *Physical Review Letters*, 50(5):364–367, January 1983.

[60] M. T. Reeves, T. P. Billam, B. P. Anderson, and A. S. Bradley. Identifying a Superfluid Reynolds Number via Dynamical Similarity. *Physical Review Letters*, 114(15):155302, April 2015. Publisher: American Physical Society.

[61] Jeffrey Yepez. Superfluid turbulence from quantum Kelvin wave to classical Kolmogorov cascades. *Physical Review Letters*, 103(8):084501, August 2009. arXiv:0905.0159 [quant-ph].

[62] K. W. Schwarz. Three-dimensional vortex dynamics in superfluid $ˆ{4}\mathrm{He}$: Homogeneous superfluid turbulence. *Physical Review B*, 38(4):2398–2417, August 1988. Publisher: American Physical Society.

[63] J. A. Geurst. Hydrodynamic theory of superfluid turbulence in He II and Schwarz's vortex modelling. *Physica A: Statistical Mechanics and its Applications*, 183(3):279–303, May 1992.

[64] K. W. Schwarz. Numerical experiments on single quantized vortices. *Physica B: Condensed Matter*, 197(1):324–334, March 1994.

[65] Christopher Pethick and Henrik Smith. *Bose-Einstein condensation in dilute gases*. Cambridge University Press, Cambridge ; New York, 2nd ed edition, 2008.

[66] Peter Grüter, David Ceperley, and Franck Laloë. Critical Temperature of Bose-Einstein Condensation of Hard Sphere Gases. *Physical Review Letters*, 79(19):3549–3552, November 1997. arXiv:cond-mat/9707028.

[67] Vanderlei Bagnato, David E. Pritchard, and Daniel Kleppner. Bose-Einstein condensation in an external potential. *Physical Review A*, 35(10):4354–4358, May 1987.

[68] J. D. Reppy, B. C. Crooker, B. Hebral, A. D. Corwin, J. He, and G. M. Zassenhaus. Density Dependence of the Transition Temperature in a Homogeneous Bose-Einstein Condensate. *Physical Review Letters*, 84(10):2060–2063, March 2000.

[69] Kerson Huang. *Statistical mechanics*. Wiley, New York, 1963.

[70] Eric A Cornell and Carl E Wieman. The Bose-Einstein Condensate. *Scientific American*, 1998.

[71] Immanuel Bloch, Jean Dalibard, and Wilhelm Zwerger. Many-body physics with ultracold gases. *Reviews of Modern Physics*, 80(3):885–964, July 2008. Publisher: American Physical Society.

[72] P. Pieri and G. C. Strinati. On the correct strong-coupling limit in the evolution from BCS superconductivity to Bose-Einstein condensation. *Physical Review B*, 61(22):15370–15381, June 2000. arXiv:cond-mat/9811166.

[73] K. W. Madison, F. Chevy, W. Wohlleben, and J. Dalibard. Vortex Formation in a Stirred Bose-Einstein Condensate. *Physical Review Letters*, 84(5):806–809, January 2000.

[74] S. K. Nemirovskii and W. Fiszdon. Chaotic quantized vortices and hydrodynamic processes in superfluid helium. *Reviews of Modern Physics*, 67(1):37–84, January 1995. Publisher: American Physical Society.

[75] Makoto Tsubota. Turbulence in quantum fluids. *Journal of Statistical Mechanics: Theory and Experiment*, 2014(2):P02013, February 2014. arXiv: 1312.0092.

[76] Miguel D. Bustamante and Sergey Nazarenko. Derivation of the Biot-Savart equation from the nonlinear Schrödinger equation. *Physical Review E*, 92(5):053019, November 2015.

[77] Franco Dalfovo, Stefano Giorgini, Lev P. Pitaevskii, and Sandro Stringari. Theory of Bose-Einstein condensation in trapped gases. *Reviews of Modern Physics*, 71(3):463–512, April 1999.

[78] Alexander L. Gaunt, Tobias F. Schmidutz, Igor Gotlibovych, Robert P. Smith, and Zoran Hadzibabic. Bose-Einstein Condensation of Atoms in a Uniform Potential. *Physical Review Letters*, 110(20):200406, May 2013.

[79] Michele Modugno. Collective dynamics and expansion of a Bose-Einstein condensate in a random potential. *Physical Review A*, 73(1):013606, January 2006. arXiv:cond-mat/0509807.

[80] E. Madelung. Quantentheorie in hydrodynamischer Form. *Zeitschrift för Physik*, 40(3-4):322–326, March 1927.

[81] Jonathan Skipp, Jason Laurie, and Sergey Nazarenko. Hamiltonian derivation of the point vortex model from the two-dimensional nonlinear Schr\"odinger equation. *Physical Review E*, 107(2):025107, February 2023. Publisher: American Physical Society.

[82] John Henry Poynting. The wave motion of a revolving shaft, and a suggestion as to the angular momentum in a beam of circularly polarised light. *Proc. R. Soc*, 82(557):560–567, 1909.

[83] L. Allen, M. W. Beijersbergen, R. J. C. Spreeuw, and J. P. Woerdman. Orbital angular momentum of light and the transformation of Laguerre-Gaussian laser modes. *Physical Review A*, 45(11):8185–8189, June 1992.

[84] Matthew Rosenzweig. Justification of the Point Vortex Approximation for Modified Surface Quasi-Geostrophic Equations. Technical Report arXiv:1905.07351, arXiv, May 2019. arXiv:1905.07351 [math-ph] type: article.

[85] Robert Krasny. A study of singularity formation in a vortex sheet by the point-vortex approximation. *Journal of Fluid Mechanics*, 167(-1):65, June 1986.

[86] Alexandre Joel Chorin. Vortex Sheet Approximation of Boundary Layers. *Journal of Computational Physics*, 27(3):428–442, May 1977.

[87] Gustav Kirchhoff. *Vorlesungen über mathematische Physik: Mechanik*. B.G. Teubner, 1876.

[88] David Borthwick. *Introduction to Partial Differential Equations*. Universitext. Springer International Publishing, Cham, 2016.

[89] Herbert Goldstein, Charles P. Poole, and John Safko. *Classical Mechanics*. Pearson Education, 3 edition, 2011.

[90] P. G. Saffman and D. I. Meiron. Difficulties with three-dimensional weak solutions for inviscid incompressible flow. *Physics of Fluids*, 29(8):2373, 1986.

[91] Milton Abramowitz and Irene Stegun. *Handbook of Mathematical Functions with Formulas, Graphs, and Mathematical Tables*. Dover Publications Inc., 1965.

[92] George Labahn and Mark Mutrie. Reduction of Elliptic Integrals to Legendre Normal Form, 1997.

[93] Bille C. Carlson. Numerical computation of real or complex elliptic integrals. *Numerical Algorithms*, 10(1):13–26, March 1995. arXiv: math/9409227.

[94] Sergey Nazarenko and Miguel Onorato. Freely decaying Turbulence and Bose–Einstein Condensation in Gross–Pitaevski Model. *Journal of Low Temperature Physics*, 146(1-2):31–46, January 2007.

[95] Bruno Eckhardt. Integrable four vortex motion. *Physics of Fluids*, 31(10):2796, 1988.

[96] Bruno Eckhardt. Irregular scattering. *Physica D: Nonlinear Phenomena*, 33(1):89–98, October 1988.

[97] J. E. Moyal. Quantum mechanics as a statistical theory. *Mathematical Proceedings of the Cambridge Philosophical Society*, 45(1):99–124, January 1949.

[98] Didier Robert. When Poisson and Moyal Brackets are equal?, March 2023. arXiv:2207.08798 [math-ph].

[99] Hassan Aref and Mark A. Stremler. Four-vortex motion with zero total circulation and impulse. *Physics of Fluids*, 11(12):3704–3715, December 1999.

[100] T.H. Havelock. The stability of motion of rectilinear vortices in ring formation. *The London, Edinburgh, and Dublin Philosophical Magazine and Journal of Science*, 11(70):617–633, February 1931.

[101] Hassan Aref and Neil Pomphrey. Integrable and chaotic motions of four vortices. *Physics Letters A*, 78(4):297–300, August 1980.

[102] Henryk Kudela. Self-Similar Collapse of n Point Vortices. *Journal of Nonlinear Science*, 24(5):913–933, October 2014.

[103] Tim Price. Chaotic scattering of two identical point vortex pairs. *Physics of Fluids A: Fluid Dynamics*, 5(10):2479–2483, October 1993.

[104] Y. Couder, N. Gérard, and M. Rabaud. Narrow fingers in the Saffman-Taylor instability. *Physical Review A*, 34(6):5175–5178, December 1986. Publisher: American Physical Society.

[105] Ragnar Fjørtoft. On the Changes in the Spectral Distribution of Kinetic Energy for Twodimensional, Nondivergent Flow. *Tellus*, 5(3):225–230, August 1953.

[106] Katepalli R Sreenivasan. Fluid Turbulence. *Reviews of Modern Physics*, 71(2):383, 1999.

[107] C. N. Yang and R. L. Mills. Conservation of Isotopic Spin and Isotopic Gauge Invariance. *Physical Review*, 96(1):191–195, October 1954.

[108] Freddy Bouchet and Eric Simonnet. Random changes of flow topology in two dimensional and geophysical turbulence. *Physical Review Letters*, 102(9):094504, March 2009. arXiv:0804.2231 [cond-mat, physics:physics].

[109] A. Pouquet and R. Marino. Geophysical turbulence and the duality of the energy flow across scales. *Physical Review Letters*, 111(23):234501, December 2013. arXiv:1309.2510 [nlin, physics:physics].

[110] H. Kellay, X-l. Wu, and W. I. Goldburg. Experiments with Turbulent Soap Films. *Physical Review Letters*, 74(20):3975–3978, May 1995.

[111] G. K. Batchelor. Computation of the Energy Spectrum in Homogeneous Two-Dimensional Turbulence. *Physics of Fluids*, 12(12):II–233, 1969.

[112] Matthew T. Reeves, Thomas P. Billam, Brian P. Anderson, and Ashton S. Bradley. Inverse Energy Cascade in Forced Two-Dimensional Quantum Turbulence. *Physical Review Letters*, 110(10):104501, March 2013.

[113] Matthew T. Reeves, Thomas P. Billam, Xiaoquan Yu, and Ashton S. Bradley. Enstrophy Cascade in Decaying Two-Dimensional Quantum Turbulence. *Physical Review Letters*, 119(18):184502, October 2017.

[114] Gregory L. Eyink and Katepalli R. Sreenivasan. Onsager and the theory of hydrodynamic turbulence. *Reviews of Modern Physics*, 78(1):87–135, January 2006.

[115] Robert H. Kraichnan. Inertial Ranges in Two-Dimensional Turbulence. *Physics of Fluids*, 10(7):1417, 1967.

[116] David G. Dritschel, Marcello Lucia, and Andrew C. Poje. Ergodicity and spectral cascades in point vortex flows on the sphere. *Physical Review E*, 91(6):063014, June 2015.

[117] Jan Friedrich and R. Friedrich. Generalized vortex model for the inverse cascade of two-dimensional turbulence. *Physical review. E, Statistical, nonlinear, and soft matter physics*, 88:053017, November 2013.

[118] Jeffrey B. Weiss and James C. McWilliams. Nonergodicity of point vortices. *Physics of Fluids A: Fluid Dynamics*, 3(5):835–844, May 1991.

[119] Cecilia Rorai, K. R. Sreenivasan, and Michael E. Fisher. Propagating and annihilating vortex dipoles in the Gross-Pitaevskii equation. *Physical Review B*, 88(13):134522, October 2013. arXiv: 1212.6389.

[120] Sergey Nazarenko and Miguel Onorato. Wave turbulence and vortices in Bose–Einstein condensation. *Physica D: Nonlinear Phenomena*, 219(1):1–12, July 2006.

[121] S. Ogawa, M. Tsubota, and Y. Hattori. Reconnection and acoustic emission of quantized vortices in superfluid by the numerical analysis of the Gross-Pitaevskii equation. *Journal of the Physical Society of Japan*, 71(3):813–821, March 2002. arXiv: cond-mat/0104255.

[122] C. Nore, M. E. Brachet, E. Cerda, and E. Tirapegui. Scattering of first sound by superfluid vortices. *Physical Review Letters*, 72(16):2593–2595, April 1994.

[123] Giorgio Krstulovic, Marc Brachet, and Enrique Tirapegui. Radiation and vortex dynamics in the nonlinear Schrödinger equation. *Physical Review E*, 78(2):026601, August 2008.

[124] Matthew T. Reeves, Kwan Goddard-Lee, Guillaume Gauthier, Oliver R. Stockdale, Hayder Salman, Timothy Edmonds, Xiaoquan Yu, Ashton S. Bradley, Mark Baker, Halina Rubinsztein-Dunlop, Matthew J. Davis, and Tyler W. Neely. Turbulent Relaxation to Equilibrium in a Two-Dimensional Quantum Vortex Gas. *Physical Review X*, 12(1):011031, February 2022.

[125] G A Baker, Jr. The Theory and Application of the Pade Approximant Method. Technical Report LA-DC-6526, Los Alamos National Lab, Los Alamos, NM (United States), January 1964.

[126] Natalia G Berloff. Padé approximations of solitary wave solutions of the Gross–Pitaevskii equation. *Journal of Physics A: Mathematical and General*, 37(5):1617–1632, February 2004.

[127] Lev P. Pitaevskii. Vortex Lines in an Imperfect Bose Gas. *Soviet Physics JETP*, 13(2):451, 1961.

[128] Marco Caliari and Simone Zuccher. Reliability of the time splitting Fourier method for singular solutions in quantum fluids. *arXiv:1603.05022 [math]*, March 2016. arXiv: 1603.05022.

[129] Steven A. Orszag. On the Elimination of Aliasing in Finite-Difference Schemes by Filtering High-Wavenumber Components. *Journal of the Atmospheric Sciences*, 28(6):1074–1074, September 1971. Publisher: American Meteorological Society Section: Journal of the Atmospheric Sciences.

[130] John P Boyd. *Chebyshev and Fourier Spectral Methods*. Number 49 in Lecture Notes in Engineering. Springer Berlin, Heidelberg, 2 edition, 2000.

[131] Giorgio Krstulovic and Marc Brachet. Energy cascade with small-scales thermalization, counterflow metastability and anomalous velocity of vortex rings in Fourier-truncated Gross-Pitaevskii equation. *Physical Review E*, 83(6):066311, June 2011. arXiv: 1010.0116.

[132] Erhard Glötzl and Oliver Richters. Helmholtz decomposition and potential functions for n-dimensional analytic vector fields. *Journal of Mathematical Analysis and Applications*, 525:127138, February 2023.

[133] C. Nore, M. Abid, and M. E. Brachet. Decaying Kolmogorov turbulence in a model of superflow. *Physics of Fluids*, 9(9):2644–2669, September 1997.

[134] Richard L. Burden, J. Douglas Faires, and Annette M. Burden. *Numerical analysis*. Cengage Learning, Boston, MA, tenth edition edition, 2016. OCLC: ocn898154569.

[135] J.R. Dormand and P.J. Prince. A family of embedded Runge-Kutta formulae. *Journal of Computational and Applied Mathematics*, 6(1):19–26, March 1980.

[136] Gustaf Söderlind and Lina Wang. Adaptive time-stepping and computational stability. *Journal of Computational and Applied Mathematics*, 185(2):225–243, January 2006.